Fanning the flames: Past and future links between climate change and fire activity across boreal forests

ANDREW ALISTAIR CLELLAND

How to cite:

CLELLAND, ANDREW ALISTAIR (2026) Fanning the flames: Past and future links between climate change and fire activity across boreal forests. Doctoral thesis, Durham University.

Fanning the flames: Past and future links between climate change and fire activity across boreal forests

Andrew A. Clelland

Thesis abstract

Boreal forests are experiencing unprecedented environmental change, with increasing fire activity posing significant ecological and climatic challenges. This thesis investigates past, present and future interactions between climate and fire across the boreal biome, combining reanalysis datasets, burned area products and machine learning to examine drivers of fire occurrence and project potential changes in future burned area. Chapter 2 evaluates the reliability of three reanalysis datasets across Siberia by comparing six climate variables related to fire activity with *in situ* observations from meteorological stations. The datasets are mostly good representations for the studied variables but also show notable regional biases and inconsistencies, highlighting the importance of bias correction in the boreal region. Chapter 3 evaluates twelve satellite imagery-derived burned area products across Arctic-boreal North America and Russia from 2001 to 2020, identifying consistent patterns in North America but major discrepancies in southern Siberia, and highlighting the strengths, limitations and suitability of each product for various research and monitoring applications. Chapter 4 develops machine learning models to project burned area across boreal and tundra biomes from 2025 to 2100 under different climate change projections using climate model outputs. Results show strong scenario- and region-dependent increases in burned area, particularly in North America, suggesting that climate change will intensify fire regimes in many areas. The final discussion chapter combines these findings, emphasising that climate-fire relationships are non-uniform and modulated by vegetation, topography and climate. It discusses the implications of increasing fire activity for carbon accounting, ecosystem resilience and climate feedbacks, and highlights the need for adaptive fire management and further research into vegetation-fire-climate feedbacks in boreal systems. Together, the thesis provides a novel approach to understanding boreal climate-fire dynamics and underscores the urgency of addressing fire risk in a warming world.

Fanning the flames: Past and future links between climate change and fire activity across boreal forests

Andrew A. Clelland

Department of Biosciences
Durham University
2025

Submitted for the degree of Doctor of Philosophy

Table of Contents

Declaration

The material contained within this thesis has not previously been submitted for a degree at Durham University or any other university. The research reported within this thesis has been conducted by the author unless indicated otherwise.

Chapter 2 has been published as:

Clelland, A. A., Marshall, G. J. and Baxter, R. (2024) Evaluating the performance of key ERA-Interim, ERA5 and ERA5-Land climate variables across Siberia. *International Journal of Climatology*. 44(7), 2318-2342.

The author contributions were as follows: A.A.C. and G.J.M. conceived the study. G.J.M. developed the methodology. A.A.C. conducted the research. A.A.C. and G.J.M. analysed the data. A.A.C. wrote the manuscript, with contributions from G.J.M. and R.B.

Chapter 3 has been published as:

Clelland, A. A., Marshall, G. J., Baxter, R., Potter, S., Talucci, A. C., Rady, J. M., Genet, H., Rogers, B. M. and Natali, S. M. (2024) Annual and Seasonal Patterns of Burned Area Products in Arctic-Boreal North America and Russia for 2001-2020. *Remote Sensing*. 16(17), 3306.

The author contributions were as follows: A.A.C., S.P. and B.M.R. conceived the study. A.A.C., G.J.M., S.P., A.C.T., J.M.R. and B.M.R. developed the methodology. A.A.C. conducted the research. A.A.C. analysed the data and wrote the manuscript, with contributions from all authors.

An adapted version of Chapter 4 is currently in preparation for submission to *Nature Communications Earth and Environment* as:

Clelland, A. A., Potter, S., Marshall, G. J., Baxter, R., Hosking, J. S., Talucci, A. C., Yang, Y., Rady, J. M., Genet, H. and Rogers, B. M. Escalating wildfire extremes across boreal forests under climate change.

The author contributions were as follows: A.A.C., G.J.M., R.B., J.S.H. and B.M.R. conceived the study. A.A.C., S.P., G.J.M., J.S.H., Y.Y., H.G. and B.M.R. developed the methodology. A.A.C. conducted the research. A.A.C. analysed the output and wrote the first draft of the manuscript, with contributions from all authors.

Andrew A. Clelland
June 2025

Acknowledgements

I am incredibly grateful to my lead supervisors, Dr Gareth Marshall at the British Antarctic Survey (BAS) and Professor Bob Baxter at Durham University, for not only spearheading and guiding the PhD, but for our formal and informal chats, academic collaboration, and being calm, approachable, friendly faces. I really cannot thank you both enough. Huge thanks too to my second BAS supervisor, Dr Scott Hosking, for all your knowledge and advice about the machine learning aspects of the PhD and always pointing me in the right direction.

I am also indebted to my collaborators at Woodwell Climate Research Center, especially to Dr Brendan Rogers for becoming an unofficial fourth supervisor and always finding time in your impossibly busy schedule to chat every fortnight and answer emails. Another enormous thank you to Stefano Potter for always being available to answer my daft coding questions with a good sense of humour. Thanks too to my other co-authors and remaining members of the fortnightly “ML fire modelling” meeting: Dr Anna Talucci, Dr Yili Yang and Dr Joshua Rady from Woodwell, and Dr Hélène Genet from the University of Alaska, Fairbanks (UAF); your contributions were invaluable.

Alongside my regular collaborators, there is a multitude of colleagues to thank at both Woodwell and UAF as part of the Permafrost Pathways project including, but not limited to, Dr Sue Natali, Dr Elchin Jafarov, Dr Ben Maglio, Andrew Mullen, Greg Fiske, Valeria Briones and Trevor Smith. Both on campus in Cape Cod and at AGU, everyone welcomed me with open arms and made my time in America so enjoyable. Thanks especially to my office mates at Woodwell over the three stints (Tiff, Marco, Mitch, Dani and Kaj), to Andie and Pat, and everyone in the Carriage House. Thanks too to Sean and his parents, Lynne and David, for hosting me and showing me the sights of New England.

In addition to my overseas colleagues, thanks to Dr Kweku Abraham from the University of Cambridge, who provided excellent statistical advice, and to Tony Phillips at BAS for his regular assistance with JASMIN. Also at BAS, thanks to Evelyn, Roseanne, Dorothea, Zelna, Rachel, Lizzie, John, Max, Millie and Bryony for the conversations and time spent together over the years, and to all my office mates and the other PhD students for providing a fun working environment. Thanks too to Ali Teague for being a friendly face behind the admin, and to the BAS 5-a-side footballers for some light-hearted, but still competitive, relief on Tuesday lunchtimes. At Durham University I'm very grateful to Emma Robinson for her administrative assistance, and to Professor Steve Willis and Dr Adrian Brennan for their support and reassurance on my progress committee.

This PhD, including the placement at Woodwell and numerous conferences abroad, was generously funded by the Natural Environment Research Council (NERC) through the IAPETUS2 DTP (grant NE/S007431/1), led by Professor John Wainwright and Professor Phil Stephens, ably assisted by Jen Gadouleau. The Iapetus cohort events were something I always really looked forward to and I learnt so much from them. Special thanks are extended to fellow students Ainsley, Dan, Nic, Maddy, Beth, Deepti, Lizzie and Sam for being all round good eggs. Thanks too to Duncan Yellowlees for his incredible training on how to make academic presentations unique and interesting, and Dr Abdou Khouakhi for leading the NERC-funded Google Earth Engine course at Cranfield University, which proved exceedingly useful for the latter half of my PhD.

Outside the office, a huge thank you to all my teammates and friends at Cambridge City Lacrosse Club. It has been incredible to be part of a close-knit team again, experiencing the massive highs (and sometimes devastating lows) together as one unit. Thanks especially to Dominika and Piotr for being my partners in crime both on and off the pitch. Also to James, Matt, Joe and Johannes, aka the "footy pub bois", and to everyone who joined us, thank you for the countless hours we spent in the pub and at the Abbey Stadium watching the football, unwinding and chatting rubbish. To my old friends in the North West and beyond, especially to Benny, Hoth and Ed, thank you for all the support and fun times we've had along the way.

Last but not least, this PhD would not have been possible without the support of my parents, Pauline and Ian, and my late Nana, Lynn. Thank you for being there through the good times and the not-so-good times, for putting up with all my antics, for being a constant source of encouragement, and for always being my number one fans. I may not always show it, but I really appreciate everything you've done for me, and I love you lots.

Dedication

This thesis is dedicated to Chris Pownall. Inspirational teachers can change the world.

Chapter 1

Introduction

Mixed-species boreal forest in the Stolby Nature Reserve, Krasnoyarsk, Russia.

Fire activity in boreal forests

Boreal forests form a vast circumpolar band across the Northern Hemisphere, spanning large portions of Alaska, Canada, Fennoscandia, and Russia. These forests represent the Earth's largest land biome and play a critical role in the global climate system (Olsson, 2009, Gauthier et al., 2015). They act as immense carbon stores, support unique biodiversity, and influence land-atmosphere energy exchanges through their seasonal albedo and evapotranspiration patterns (Potter et al., 2020, Dong et al., 2024). However, boreal ecosystems are increasingly under threat from accelerated climate change, which is driving profound shifts in disturbance regimes, particularly wildfire activity (Scholten et al., 2024), and have been identified as one of the nine global tipping points (Armstrong McKay et al., 2022). An extensive portion of boreal forests is underlain by perennially frozen ground, called permafrost, which plays a critical role in regulating soil hydrology, carbon storage, and ecosystem dynamics (Jafarov et al., 2012, Obu et al., 2019).

Throughout this thesis the extent of the boreal biome follows the definition of Dinerstein et al. (2017), comprising a mosaic of cold-adapted ecoregions shaped by long winters, coniferous vegetation, and disturbance-driven processes such as fire and permafrost dynamics. The extent of the boreal biome is shown in Figure 1.1, including areas underlain by permafrost (Brown et al., 1998).

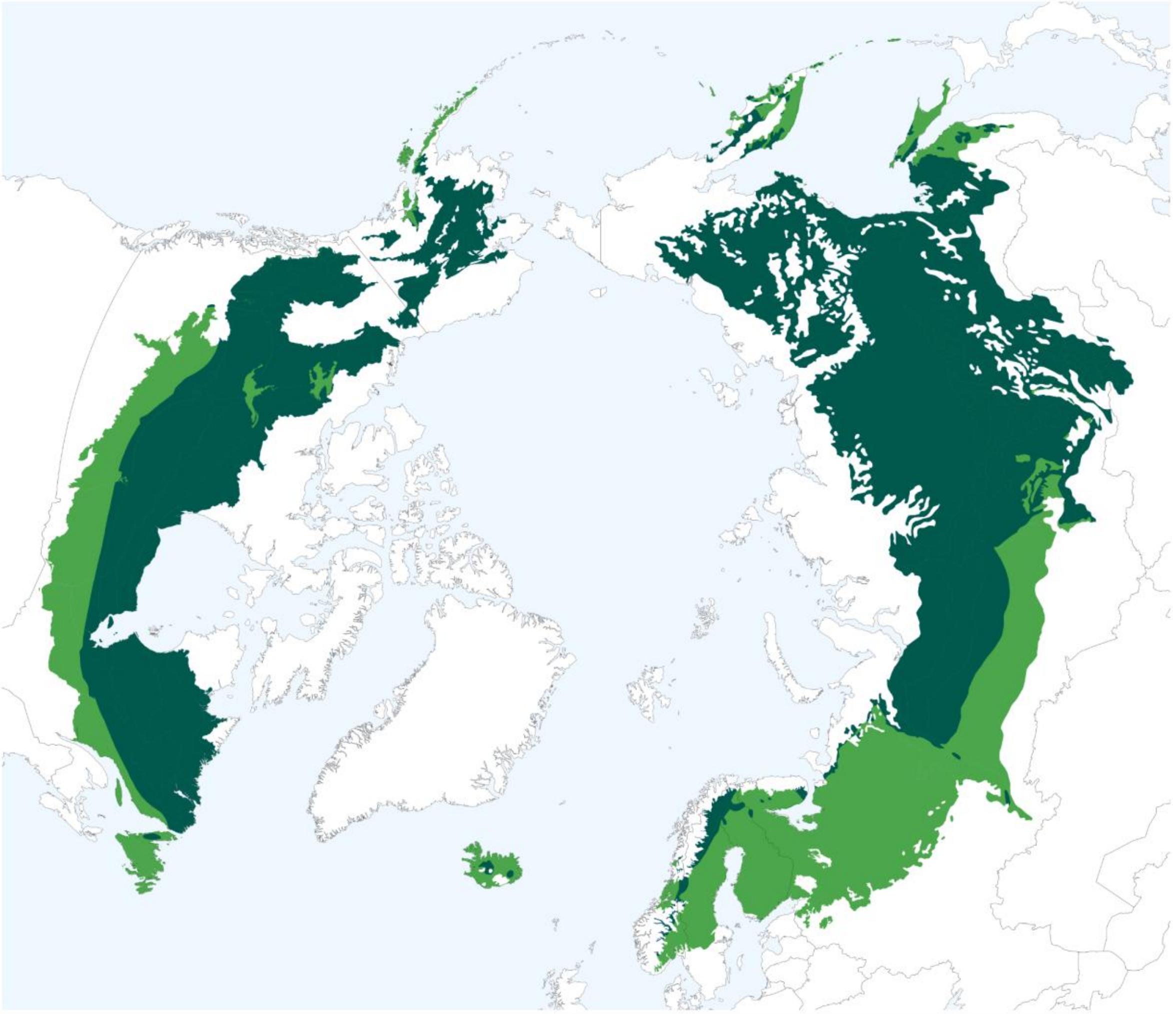

Figure 1.1. Extent of the boreal biome with areas underlain by permafrost (dark green).

Wildfires are a natural and essential component of boreal ecology, contributing to forest regeneration and landscape heterogeneity, which helps maintain diverse regeneration niches and supports species coexistence across successional stages (Olsson, 2011). Yet, recent years have seen unprecedented fire seasons in boreal regions, characterised by a greater amount of burned area, more intense fires, and increasingly unpredictable behaviour. For instance, the 2023 fire season in Canada shattered previous regional records in total burned area and emissions, with widespread impacts on air quality, ecosystems, and communities (Jain et al., 2024). These patterns are consistent with scientific expectations that boreal fire regimes are becoming more extreme under climate warming, particularly due to rising temperatures, declining relative humidity, and longer fire seasons (Rogers et al., 2015, Baltzer et al., 2021).

Understanding how climate change affects boreal fire regimes is not only a matter of academic interest; it is a pressing global challenge. Figure 1.2 shows the extent of fires in the boreal biome from 2001 to 2024. Fires in boreal forests can release massive quantities of carbon dioxide and black carbon into the atmosphere, undermining their function as carbon sinks and contributing to further warming (Zhang et al., 2024b, Janssen and Veraverbeke, 2025). Fire activity can also accelerate permafrost thaw, triggering substantial additional carbon emissions and altering hydrological systems (Li et al., 2021). At the same time, wildfires threaten infrastructure, disrupt transportation, and pose serious risks to health, especially among northern and indigenous communities who may rely on the land for very long-established cultural and subsistence practices.

Figure 1.2. Locations of fires, from the FireCCI v5.1 and MCD64A1 burned area products, in the boreal biome (red) from 2001 to 2024.

From a policy perspective, increasing boreal fire activity complicates efforts to meet climate mitigation goals and accurately account for land-use emissions (Balch et al., 2017, Rogers et al., 2020). As fire regimes change, there is an urgent need to develop better forecasting tools, long-term projections, and adaptive fire management strategies that are grounded in robust science and account for regional variation (Phillips et al., 2022). This thesis contributes to that effort by analysing climate-fire interactions across both historical and future timescales using complementary data and methods.

Despite growing recognition of the relationship between climate and fire in boreal regions, several significant gaps remain in the literature. Many long-term assessments rely on coarse indices or aggregated fire statistics that may obscure important spatial and seasonal patterns (e.g. Jones et al., 2022, Cardil et al., 2023, Watanabe et al., 2023). Furthermore, much of the existing fire science focuses either on local to national-scale studies (e.g. Michael et al., 2021, Mohajane et al., 2021, Rubí et al., 2023) or global assessments (e.g. Pausas and Keeley, 2021, Zhang et al., 2024a, Di Giuseppe et al., 2025), with limited attention to the intermediate, biome-wide scale where both climate and fire exhibit substantial heterogeneity.

While climate projections are widely used to assess future fire risk, there is often only limited validation against observational records, and relatively few studies employ data-driven approaches that can capture nonlinear interactions or spatial dependencies in fire behaviour. Additionally, while remote sensing and reanalysis datasets have become more accessible, their integration with machine learning and advanced statistical methods remains underdeveloped in fire science. Thus, there is a need for approaches that can combine historical context with predictive modelling, offering not just trend analyses but also plausible futures under climate change.

Thesis outline

This thesis tackles the aforementioned challenges by investigating how fire activity across boreal forests has responded to past climate variability and how it is likely to evolve under future warming scenarios. Specifically, the thesis addresses the following research questions:

- How have key climate indicators of fire danger changed over recent decades in boreal Eurasia?
- What patterns of fire occurrence and burned area can be observed across boreal forests using satellite data?
- How can machine learning be used to project future burned area in the boreal biome, and what do these projections suggest about regional vulnerability and the future relationship between fire activity and climate variability?

The thesis is structured around three research papers, the first two of which have been published in peer-reviewed journals, while an adapted version of the third is in preparation for submission to *Nature Communications Earth and Environment*.

- **Chapter 2** assesses how accurately six fire-relevant climate variables across Siberia are reproduced by three atmospheric reanalysis datasets compared to *in situ* meteorological observations. Reanalysis datasets provide a long-term record of past weather and climate by combining observations with model data using a consistent assimilation scheme.
- **Chapter 3** evaluates burned area products derived from satellite imagery across North America and Russia, identifying their respective strengths and limitations, and assessing their suitability for different research and monitoring applications.
- **Chapter 4** applies a machine learning framework to project future burned area across the Arctic-boreal zone using data from two climate models, evaluating how different future climate scenarios may affect fire extent and distribution.

A multi-method approach is employed in this thesis that integrates historical reanalysis data, satellite-based fire observations, a new regional land cover product, fire danger indices, and climate models from the Coupled Model Intercomparison Project Phase 6 (CMIP6) ensemble. Chapter 2 determines the most appropriate reanalysis dataset to train the machine learning models on, whereas Chapter 3 does likewise with the burned area products. In Chapter 4, all the datasets, including the most suitable datasets discovered during the previous chapters, are combined to train machine learning models. The methodological emphasis is on generating regionally-specific insights that can inform both scientific understanding and practical fire management.

Chapter 5, the final discussion chapter, synthesises all the above findings, reflects on their broader implications for climate-fire dynamics, and outlines future research priorities. Attention is given to how climate and fire interact in space and time, and how fire regimes may shift under different projected climate scenarios. Special care is taken to evaluate the strengths and limitations of the data used, and to prioritise interpretability and reproducibility in the modelling process.

Chapter 2

Evaluating climate reanalysis data across Siberia

Meteorological stations in the Kola Peninsula, Russia. *Photo credit: Gareth Marshall*

This chapter is published as: Clelland, A. A., Marshall, G. J. and Baxter, R. (2024) Evaluating the performance of key ERA-Interim, ERA5 and ERA5-Land climate variables across Siberia. *International Journal of Climatology*. 44(7), 2318-2342.

The author contributions were as follows: A.A.C. and G.J.M. conceived the study. G.J.M. developed the methodology. A.A.C. conducted the research. A.A.C. and G.J.M. analysed the data. A.A.C. wrote the manuscript, with contributions from G.J.M. and R.B.

Abstract

Reanalysis datasets provide a continuous picture of the past climate for every point on Earth. They are especially useful in areas with few direct observations, such as Siberia. However, to ensure these datasets are sufficiently accurate they need to be validated against readings from meteorological stations. Here we analyse how values of six climate variables – the minimum, mean and maximum 2-metre air temperature, snow depth, total precipitation and wind speed – from three reanalysis datasets – ERA-Interim, ERA5 and ERA5-Land – compare against observations from 29 meteorological stations across Siberia and the Russian Far East on a daily timescale from 1979-2019. All three reanalyses produce values of the mean and maximum daily 2-metre air temperature that are close to those observed, with the average absolute bias not exceeding 1.54 °C. However, care should be taken for the minimum 2-metre air temperature during the summer months – there are nine stations where correlation values are less than 0.60 due to inadequate night-time cooling. The reanalysis values of snow depth are generally close to those observed after 1992, especially ERA5, when data from some of the meteorological stations began to be assimilated, but the reanalysis snow depth should be used with caution (if at all) before 1992 as the lack of assimilation leads to large overestimations. For low daily precipitation values the reanalyses provide good approximations, however they struggle to attain the extreme high values. Similarly, for the 10-metre wind speed; the reanalyses perform well with speeds up to 2.5 ms^{-1} but struggle with those above 5.0 ms^{-1}. For these variables, we recommend using ERA5 over ERA-Interim and ERA5-Land in future research. ERA5 shows minor improvements over ERA-Interim, and, despite an increased spatial resolution, there is no advantage to using ERA5-Land.

Introduction

Siberia can be defined as the vast region of Russia and Northern Kazakhstan that extends over 13 million square kilometres, bounded to the west by the Ural Mountains and to the east by the Pacific Ocean. Much of this region comprises boreal forest, known as the taiga, which is the world's largest forest, comprising over 20 % of the planet's total forested area and 60 % of all boreal forests in the Northern Hemisphere (Zyryanova et al., 2008). Siberia is projected to experience extreme weather events more frequently during this century than the last due to the warming climate. Such events include flooding, an increase in the number and severity of forest fires, and permafrost and glacial melting, leading to biodiversity changes and increased carbon dioxide and methane emissions (Callaghan et al., 2021). Therefore, major changes to the Siberian taiga ecosystem and its ability to operate as a carbon sink will itself have a considerable effect on the magnitude of future global warming (Olsson, 2009). Such changes are already apparent: for example, in recent decades, forested areas of Northern Russia with significantly positive cumulative near-surface air temperature trends have shown the most pronounced deterioration (Shabanov et al., 2021), leading to an increase in the amount of understorey fuel (Gale et al., 2021) and thus a greater propensity to suffer fire activity.

In order to understand the drivers of Siberian climate change and to provide a baseline against which to compare future changes, we need an accurate dataset that provides coverage across the entire region. Atmospheric reanalyses are the standard tool for providing such data in remote areas such as Siberia, where there are relatively few meteorological observations. They provide a uniform multivariate record of the atmosphere and hydrological cycle. Reanalyses employ a numerical weather prediction forecast model to assimilate an historical archive of meteorological data, derived from a range of ground-based observations, radiosondes and multifarious types of satellite data. By providing gridded global fields of meteorological parameters, reanalysis data give a continuous picture of the climate. The forecast and assimilation models are kept constant in these datasets to maintain temporal homogeneity for climate change studies, unlike operational forecast systems that are regularly updated. Nonetheless, it is known that reanalyses can be affected by variations in the coverage and type of assimilated data, especially in more remote areas where there are fewer other data to constrain the reanalysis model.

New versions of reanalyses are produced regularly, following improvements in model physics and data assimilation in the operational forecast models. The current European Centre for

Medium-Range Weather Forecasts (ECMWF) reanalysis is their fifth-generation atmospheric reanalysis product (ERA5), with a 0.25° (31 km) horizontal resolution with output at an hourly timescale (Hersbach et al., 2020). ERA5 superseded ERA-Interim, where the data were produced at a reduced 80 km horizontal resolution on a 6-hourly timescale (Dee et al., 2011). Following the release of ERA5, ERA5-Land was created over the land component with the same temporal resolution but a higher spatial resolution of 0.1° (9 km) (Muñoz-Sabater et al., 2021).

It is especially important that the accuracy of reanalyses is properly evaluated to ensure the scientific validity of climate research that is based solely on these data. Several previous works have conducted validations of ERA-Interim with observed data for climate variables in remote regions of Russia.

The mean 2-metre air temperature is the most accurately reproduced climate variable in ERA-Interim, irrespective of study location, with correlation values consistently over 0.90 and mean biases of 0.80-1.50 °C (e.g. Grankina et al., 2019, Demchev et al., 2020, Lan et al., 2023). In these studies, the validations were conducted on a daily timescale before the mean was taken either seasonally (Grankina et al., 2019, Demchev et al., 2020) or annually (Lan et al., 2023). Note that we expect the correlation values to increase as the timescale increases as daily extreme maxima/minima have less overall impact on the correlations of longer periods. Klehmet et al. (2013) found that snow depth in South Siberia was generally overestimated by 20-40 %, and up to 60 % in April. ERA-Interim consistently significantly underestimated total precipitation: Riazanova et al. (2016) found that precipitation values are underestimated by 56 % in South Siberia during summer months, where the extreme high precipitation events occur associated with localised convective activity, and Dyakonov et al. (2020) stated that at the Caspian Sea the precipitation can be underestimated by up to 54 % per year.

Previous recent studies of ERA5's performance have also been conducted in remote regions of Russia: Matveeva and Sidorchuk (2020) validated the daily mean 2-metre air temperature, total precipitation and snow depth on the Yamal Peninusla from 1985 to 2019, Voropay et al. (2021) evaluated the total monthly precipitation with station data across South Siberia from 1979 to 2015, and Lan et al. (2023) used daily temperature and precipitation variables grouped at an annual timescale to compare several reanalyses datasets, including ERA-Interim and ERA5, across Northern Siberia from 2000 to 2018.

In the abovementioned three studies, the reanalyses again performed best when considering the mean air temperature, especially during summer, with correlations greater than 0.97 for ERA5 and ERA-Interim. The bias in ERA5 is consistently around 0.50 °C, whereas in ERA-Interim this increases to 0.96 °C, and ERA5 performs best during the summer months and worst during the winter months. When considering the maximum and minimum temperatures, Lan et al. (2023) found that both ERA-Interim and ERA5 perform better reproducing temperature maxima. For ERA-Interim the absolute bias of the maxima is 1.29 °C less than the minima (-1.73/3.02 °C) and the correlation is increased by 0.06 (0.90/0.84), whereas for ERA5 the absolute bias of the maxima is 0.12 °C less than the minima (-2.35/2.47 °C) and the correlation is increased by 0.08 (0.93/0.85).

There are significant variations in the skill of the reanalyses in reproducing total precipitation between the studies, highlighting the regional differences in the quality of the reanalyses. ERA5 performs worse in the northernmost region, the Yamal Peninsula, with daily correlations only between 0.50 and 0.70. Here ERA5 struggles to reproduce the extreme high precipitation events, especially during summer, where the RMSE is greatest, although the reanalyses tend to overestimate precipitation all year round. In South Siberia the correlations are on average greater than 0.70, although ERA5 again performs worse during summer than in other seasons and there are high biases and RMSE values all year round.

The new ERA5-Land dataset appears in few validation studies to date. Evaluations of ERA5-Land's performance have again been conducted on individual variables, such as temperature trends (Liu et al., 2021, Wang et al., 2022, Yilmaz, 2023) and soil temperatures (Cao et al., 2020), the latter focused on permafrost regions, including across Russia. Whereas Liu et al. (2021) and Wang et al. (2022) looked at global temperature trends, Yilmaz (2023) focussed on one specific region – Turkey – and found no significant difference between ERA5 and ERA5-Land; in fact, ERA5 tends to estimate the trends marginally better than does ERA5-Land.

The present work is, we believe, the first to compare ERA-Interim with ERA5 and ERA5-Land across a range of climate variables. In this study we conducted a validation of the three ECMWF reanalyses with observed data from 29 meteorological stations across Siberia and the Russian Far East. The validation investigates six climate variables: the minimum, mean and maximum 2-metre air temperature (MN2T, T2M, MX2T), mean snow depth (SD), total precipitation (TP) and 10-metre wind speed (WSP). These variables were chosen as this work is part of a broader project investigating how climate change has influenced forest fires in the region. In the Methodology we describe the research areas and reanalyses, before the results of the validation are presented, and the strengths and weaknesses of using these reanalysis data in Siberia, as well as which reanalysis dataset performs best for the variables studied, are discussed. The shortened variable names will be used throughout the rest of this chapter.

Methodology

Research areas and meteorological stations

The research areas were chosen based upon incorporating as many different tree types, topographies, and regional climates as possible, as part of the authors' ongoing research into forest fires. As such the regions cover areas of Scots pine (*Pinus sylvestris*), Siberian dwarf pine (*Pinus pumila*), larch (*Larix spp.*), Siberian fir (*Abies sibirica*) and birch (*Betula spp.)*, over mountainous, swampy and steppe land (Kharuk et al., 2021). The co-ordinates of the boundaries of the seven research areas are given in Table 2.1; the full list of the 29 meteorological stations used in the validation is given in Table A2.1 (p. 61) and a map showing the stations within each area is provided as Figure 2.1. Note that some meteorological stations within the research areas were not used due to a lack of available data (> 10 %) over the whole time period. Maps of the ecoregions of the study areas, as per Soja et al. (2004b), are given in Figures B2.1 and B2.2 (pp. 62-63).

Table 2.1. List of study areas with N, W, S, E boundaries and the number of usable meteorological stations within them.

Area	Name	N latitude (°N)	W longitude (°E)	S latitude (°N)	E longitude (°E)	No. of usable stations
1	NW Siberia	64.5	82.0	58.0	95.5	3
2	W Yakutsk	67.0	111.5	61.0	125.0	6
3	E Yakutsk	64.0	127.5	57.5	141.5	5
4	Amur region	58.5	123.0	52.0	134.0	5
5	SW Siberia	56.5	92.5	50.5	102.5	4
6	Verkhoyansk region	70.5	126.0	64.0	143.0	2
7	NE Sakha	69.5	144.5	62.5	162.0	4

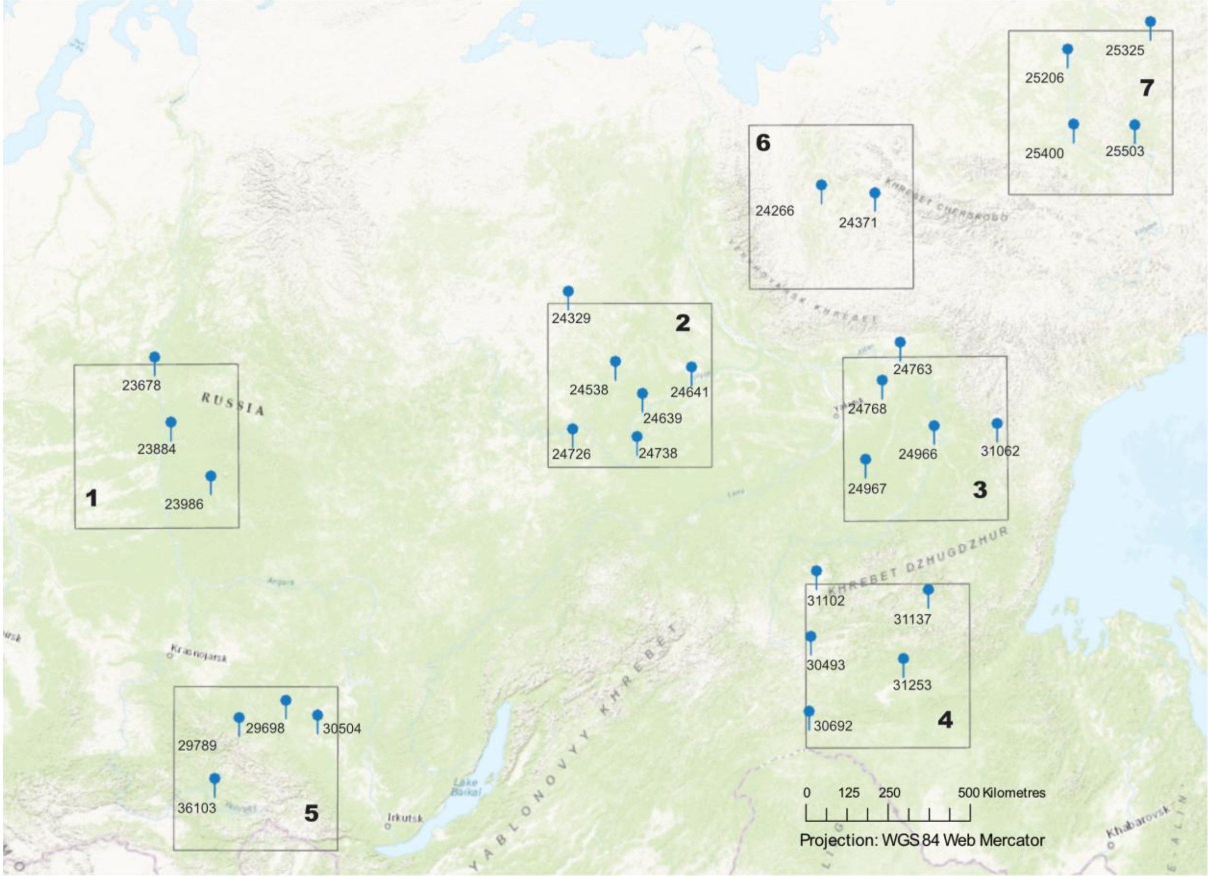

Figure 2.1. Map of the seven research areas in Siberia with pins representing the location of the 29 meteorological stations used in the validation.

ERA-Interim, ERA5 and ERA5-Land

ERA-Interim was announced in 2007 as the ECMWF's replacement for their previous reanalysis product, ERA-40 (Simmons et al., 2007). Data are available from January 1979 to August 2019 on a spectral T255 (79 km) horizontal resolution with a 6-hourly temporal resolution. ERA-Interim was produced sequentially every 12 hours using a 4D-Var data assimilation system (Dee et al., 2011). ERA-Interim was widely used and has been considered a valid alternative to observations globally (Liu et al., 2018).

ERA5 is the fifth-generation atmospheric reanalysis produced by ECMWF, replacing ERA-Interim as their latest reanalysis product. Data are currently available from 1940 onwards (Hersbach et al., 2023). ERA5 has a 0.25° (31 km) horizontal resolution, an hourly temporal resolution, and is produced using an improved four-dimensional data assimilation in ECMWF's Integrated Forecast System (Hersbach et al., 2020). ERA5's 37 post-processed pressure levels are the same as those of ERA-Interim, although the data that ERA5 assimilates better reflect observed changes in climate forcing and many new or recently reprocessed observations are used (Noël et al., 2020). The real vertical resolution is determined by the model levels from the surface up to a height of 80 km, which is 137 for ERA5, increased from 60 in ERA-Interim (Hersbach et al., 2020).

ERA5-Land was created by forcing the HTESSEL land surface component with the atmospheric model (Muñoz-Sabater et al., 2021), but without coupling them. Observations, such as those from meteorological stations, are assimilated into ERA5 but not ERA5-Land, so, despite the fact that the snow model is the same in both ERA5 and ERA5-Land, for instance, snow observations are not directly assimilated in the latter (Hersbach et al., 2020, Muñoz-Sabater et al., 2021, Urraca and Gobron, 2023). ERA5-Land has the same temporal resolution as ERA5 but at a higher spatial resolution of 0.1° (9 km). It is available from 1950 and is updated to the present time with little delay.

ERA5 is generally considered the best reanalysis product currently available (e.g. Ramon et al., 2019, Tarek et al., 2019), and as such this work assesses how ERA5 compares to its predecessor, ERA-Interim, as well as its higher resolution land-based counterpart, ERA5-Land. Daily means for the climate variables are computed for all three reanalyses using values taken at each output temporal resolution (6-hourly for ERA-Interim and hourly for ERA5 and ERA5-Land). The daily minimum and maximum values are recorded directly as the lowest/highest values over the previous 24-hour period (Hersbach et al., 2020).

This validation was conducted using the daily data, which were then analysed on a seasonal basis. The reanalysis data were linearly interpolated to the points of each meteorological station so that a direct analysis could take place.

Missing and erroneous data from meteorological stations

The full evaluation was conducted using data from 1979 to coincide with the availability of data from all three reanalysis datasets, with an additional section on how ERA5 and ERA5-Land perform from 1959 to 1978. Time periods were excluded from statistical calculations if more than 10 % of meteorological station data during that period were missing. As such, a month was excluded if there were 4 or more days of missing data, a year was excluded if there were 2 or more missing months and decadal trends were calculated subject to having 9- or 10-

years' worth of data. There are more missing data from the meteorological stations before 1979 than after.

The use of ERA5, on occasion, highlighted where there were significant errors in data from a meteorological station. For example, ERA5 highlighted curious T2M values in the years 1966-1976 at station 23986 (Figure 2.2a). Although the original reason behind this is unknown, when multiplying the positive values by 10 (Figure 2.2b), the adjusted readings appear much more realistic, and these adjusted values are used in subsequent statistical calculations.

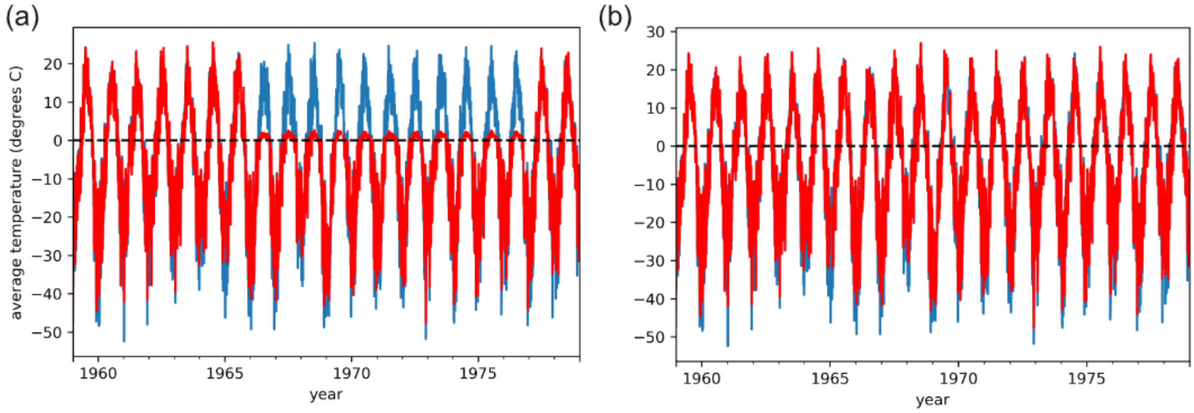

Figure 2.2. Average monthly T2M values at station 23986 (see Figure 2.1) for the years 1959-1978 before (a) and after (b) the adjusted meteorological station readings. The blue and red lines show the ERA5 and station values, respectively.

Similarly, ERA5 highlighted issues with the average SD at station 24371. Before 1984, ERA5 drastically underestimates the values from the station, although the peak in 1978 is represented, as seen in Figure 2.3. This is one of only two stations where ERA5 generally underestimates SD (along with 23986) and the meteorological station data at 24371 are never assimilated into ERA5. From 1982-1985 there is a steep drop in the meteorological station values, and from 1987 onwards the readings are as expected. Note that there are gaps in the meteorological station data where years have been excluded due to missing > 10 % of the data and the data only begin in 1966. Lobanov and Kirillina (2019) state that although the station has not changed latitude or longitude from 1942, there have been inhomogeneities in the average monthly precipitation in April and August. This leads to the possibility that there could be calibration errors at the station producing inaccurate readings.

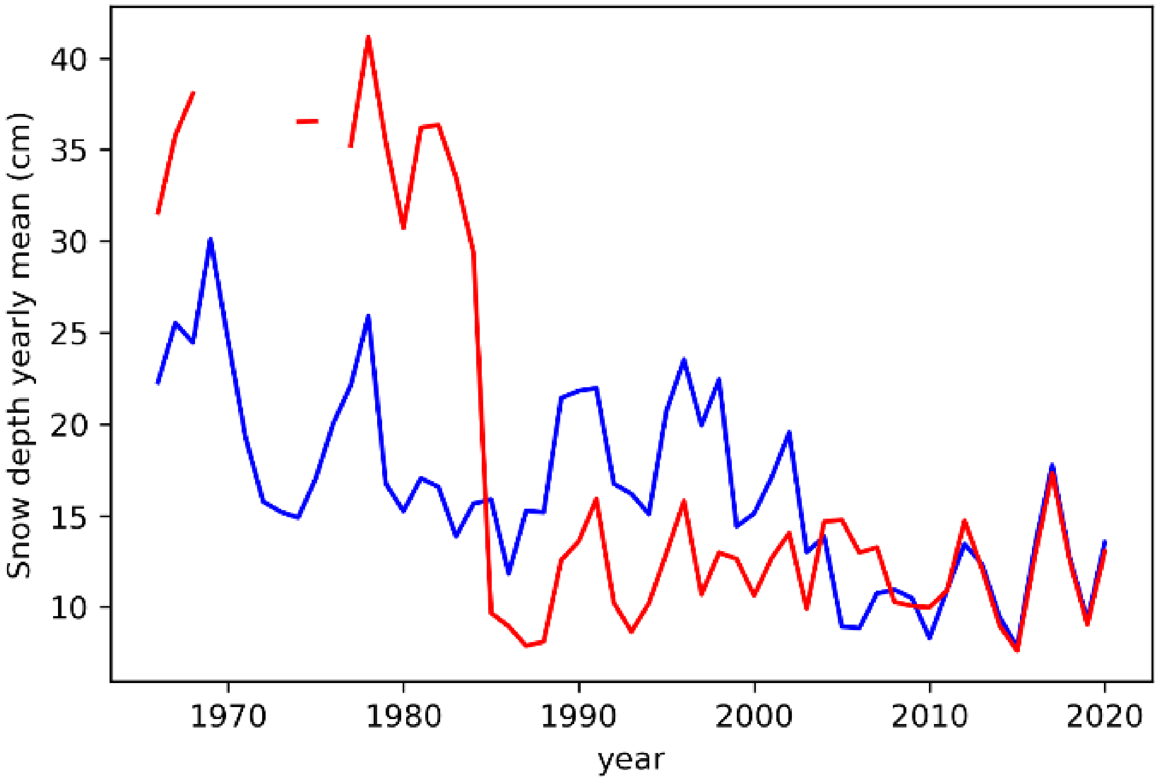

Figure 2.3. The mean yearly SD at station 24371 for the years 1966-2020. The blue and red lines show the ERA5 and station values, respectively.

Statistics used in the validation

Five statistics were used in the validation: the Pearson correlation coefficient (r), the Spearman rank correlation coefficient (ρ), variance ratio (vr), root-mean-square error (RMSE) and bias. r is used for T2M, MX2T and MN2T as these variables can attain values below zero and form normal distributions, whereas the non-parametric ρ is used for SD, TP and WSP as these values cannot attain non-positive values and do not form normal distributions. The line of best fit shown on the figures for the results is determined by the regression model $y \sim x$. The equations for calculating r, ρ, vr, RMSE and bias, respectively, are given in Equations 2.1-2.5 below.

$$r = \frac{\sum(x_i - \bar{x})(y_i - \bar{y})}{\sqrt{\sum(x_i - \bar{x})^2 \sum(y_i - \bar{y})^2}} \tag{2.1}$$

where x_i, y_i are the values of the x/y-variable in a sample and $\bar{x}$, $\bar{y}$ are the mean of the values of the x, y-variable.

$$\rho = 1 - \frac{6\sum d_i^2}{n(n^2 - 1)} \tag{2.2}$$

where d_i is the difference between the two ranks of each observation and n is the number of observations.

$$S_i^2 = \frac{\sum(x_i - \bar{x})^2}{n - 1} \tag{2.3}$$

where S_i is the sample standard deviation of variable i, x_i is the value of one observation, $\bar{x}$ is the mean value of all observations, and n is the number of observations. The variance ratio (*vr*) is then the variance of the reanalysis dataset divided by the variance of the observational data. If the *vr* is greater than 1, the variance in the reanalysis is overestimated, whereas a *vr* less than 1 indicates that the variance is underestimated.

$$RMSE = \sqrt{\frac{\sum_{i=1}^{N}(\hat{x}_i - x_i)^2}{N}} \tag{2.4}$$

where N is the number of non-missing data points, $\hat{x}_i$ is the estimated time series, and x_i is the actual observations time series. Similarly:

$$bias = \frac{\sum_{i=1}^{N}(\hat{x}_i - x_i)}{N} \tag{2.5}$$

The bias indicates whether the reanalyses overestimate or underestimate the observed parameter and by how much, whereas the RMSE finds the average error, irrespective of its sign.

Results

2-metre air temperature

T2M

T2M is the parameter studied that is most accurately reproduced by all three reanalyses. The validation statistics are given in Table 2.2.

Table 2.2. Validation statistics for daily T2M.

Reanalysis	Bias (°C)	RMSE (°C)	*vr*	*r*
ERA-Interim	0.43	2.66	0.96	0.991
ERA5	0.16	2.89	0.98	0.989
ERA5-Land	0.50	3.00	0.94	0.989

The correlations on a daily timescale are approximately 0.990, and across all the stations there is a small average warm bias, ranging from 0.16 °C in ERA5 to 0.50 °C in ERA5-Land. The average RMSE is just under 3 °C and the variance is consistently slightly underestimated across all three reanalyses. The differences in the correlations and variance ratios are negligible, with a 0.34 °C difference between both the smallest and largest biases and RMSEs. Figure 2.4 shows the performance of ERA-Interim, ERA5 and ERA5-Land against meteorological station data for daily T2M.

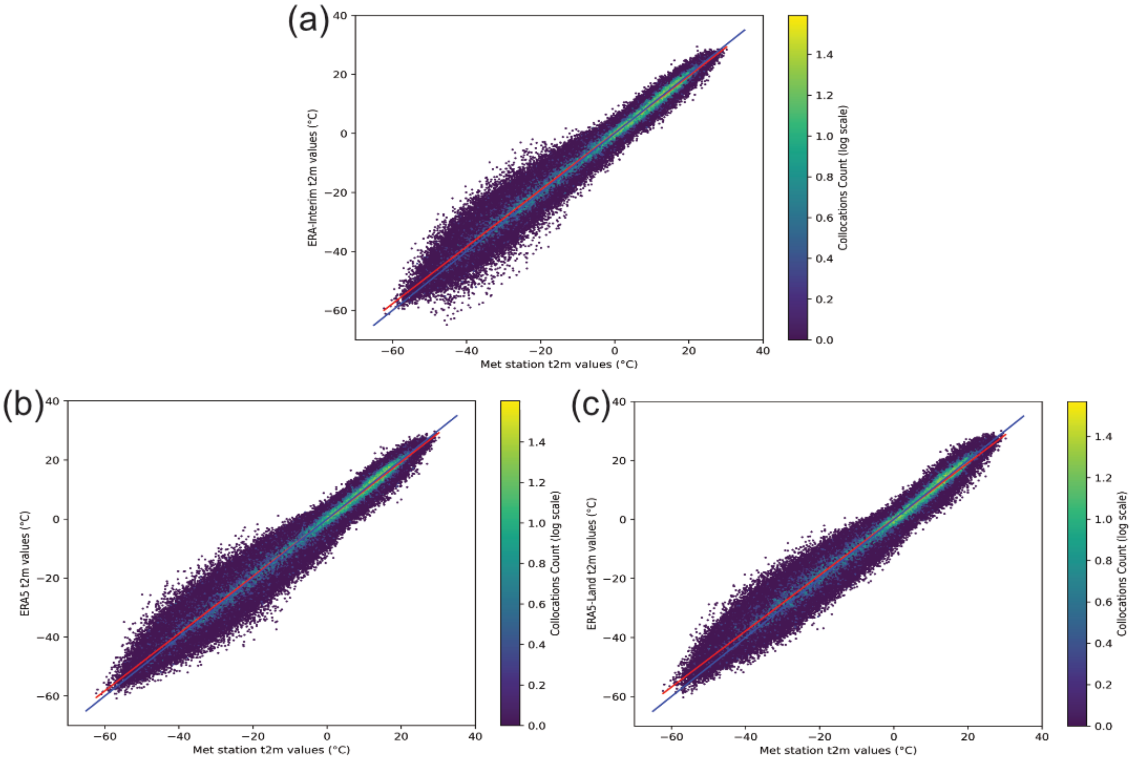

Figure 2.4. Daily T2M values from ERA-Interim (a), ERA5 (b) and ERA5-Land (c) with respect to the corresponding values from each station. The solid blue line indicates perfect agreement, and the line of best fit is in red. The pixel colour scale indicates the number of collocations of each pixel on a logarithmic scale.

The graphs in Figure 2.4 show that the same relationships between the biases and observed daily T2M values are seen across the three reanalyses: the reanalyses have the least deviation from the $y=x$ line when the temperature is around 0 °C, with the deviation increasing above the $y=x$ line as the temperature decreases, leading to a small warm bias as the reanalyses fail to attain the extreme cold temperatures. This is further highlighted in Figure 2.5, which shows that the reanalyses consistently reproduce T2M less well in winter (DJF).

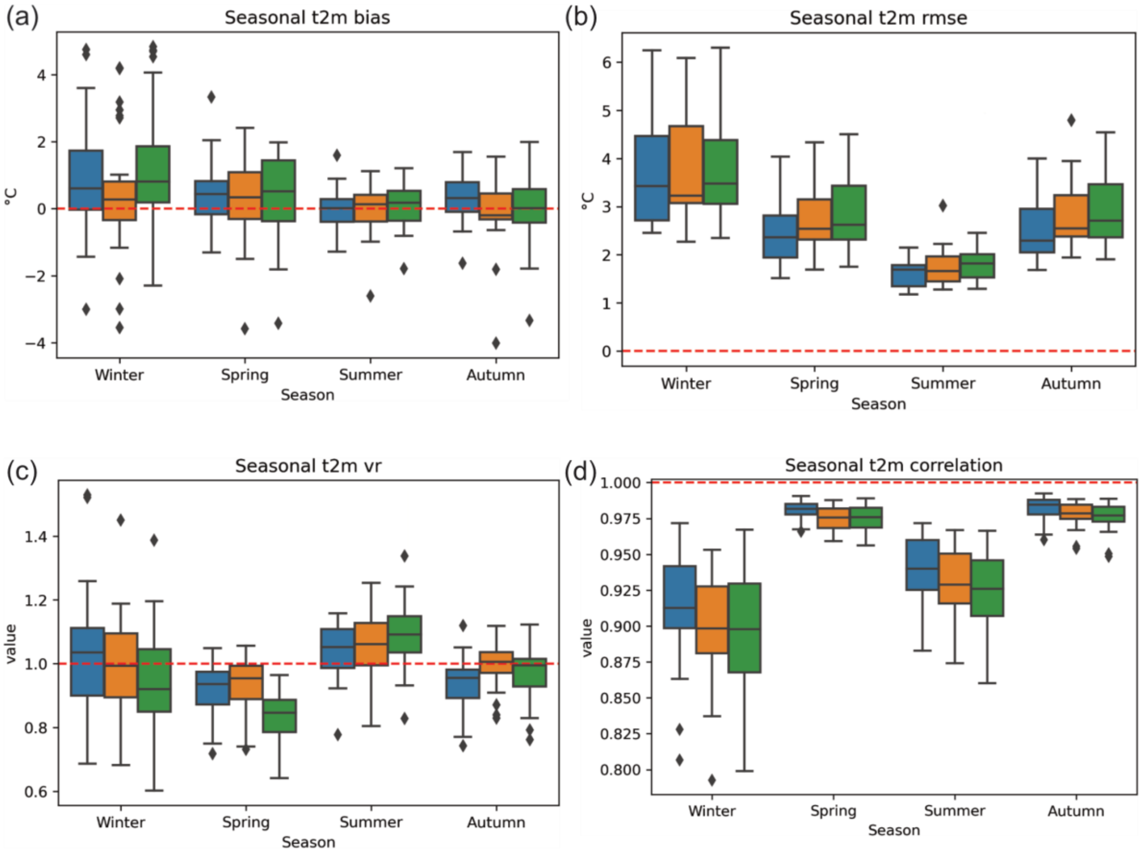

Figure 2.5 – Seasonal values of the ERA-Interim (blue), ERA5 (orange) and ERA5-Land (green) bias (a), RMSE (b), variance ratio (c) and correlation (d) statistics for T2M. The red dashed line indicates the optimum value for each statistic; the whiskers extend to a maximum of 1.5 x interquartile range (IQR).

The season has the lowest average correlation of 0.903, and the greatest mean bias and RMSE values, 0.90 °C and 3.79 °C, respectively (Figure 2.5). However, the average variance ratio is the closest to 1.00 of all the seasons. The reanalyses perform similarly strongly in spring (MAM) and autumn (SON), with a correlation over 0.975, an average absolute bias less than 0.55 °C, RMSE approximately 2.75 °C and variance ratio around 0.93. Summer (JJA) has the lowest average bias and RMSE values of 0.01 °C and 1.71 °C, respectively. Outliers lie both above and below the whiskers in winter for all three analyses for the T2M bias (Figure 2.5a), which supports the conclusions drawn from Figure 2.4 in that the maximum deviation both and above and below the y=x line occurs at temperatures between -20 and -40 °C.

Between the three reanalyses the differences between ERA-Interim and ERA5 are negligible, however ERA5-Land consistently performs marginally less well than the others. On a daily timescale the reanalyses also perform equally strongly across all the study regions, as no area stands out ahead of the others, although Verkhoyansk region has the greatest average bias and RMSE values across the three reanalyses, at 0.87 °C and 3.38 °C, respectively. In winter, spring and autumn, the reanalyses reproduce T2M best in NW Siberia and worst in Verkhoyansk region, whereas in summer there are no significant differences across the study areas.

MX2T

When considering the daily temperature extremes, the three reanalyses tend to perform slightly better at reproducing the daily maxima than the daily minima. The validation statistics for MX2T are given in Table 2.3.

Table 2.3. Validation statistics for daily MX2T.

Reanalysis	Bias (°C)	RMSE (°C)	*vr*	*r*
ERA-Interim	-1.54	3.57	0.90	0.988
ERA5	-1.49	3.42	0.93	0.989
ERA5-Land	-1.52	3.34	0.94	0.989

The reanalyses again all perform consistently well and there is little to separate them. The average correlation is 0.989, and the difference between the highest and lowest values for the bias, RMSE and *vr* are small. The correlation differences between the seven study areas are negligible, and the variance ratios are within 0.10 of each other. For the bias and RMSE values the reanalyses all perform best in Amur region and least well in SW Siberia, with a 2.39 °C and 1.93 °C difference between them, respectively.

Figure 2.6 shows the performance of ERA-Interim, ERA5 and ERA5-Land against meteorological station data for MX2T. The graphs follow the same trends as T2M, although the average cold bias for positive temperatures and the warm bias for negative temperatures are slightly more pronounced here across all three reanalyses.

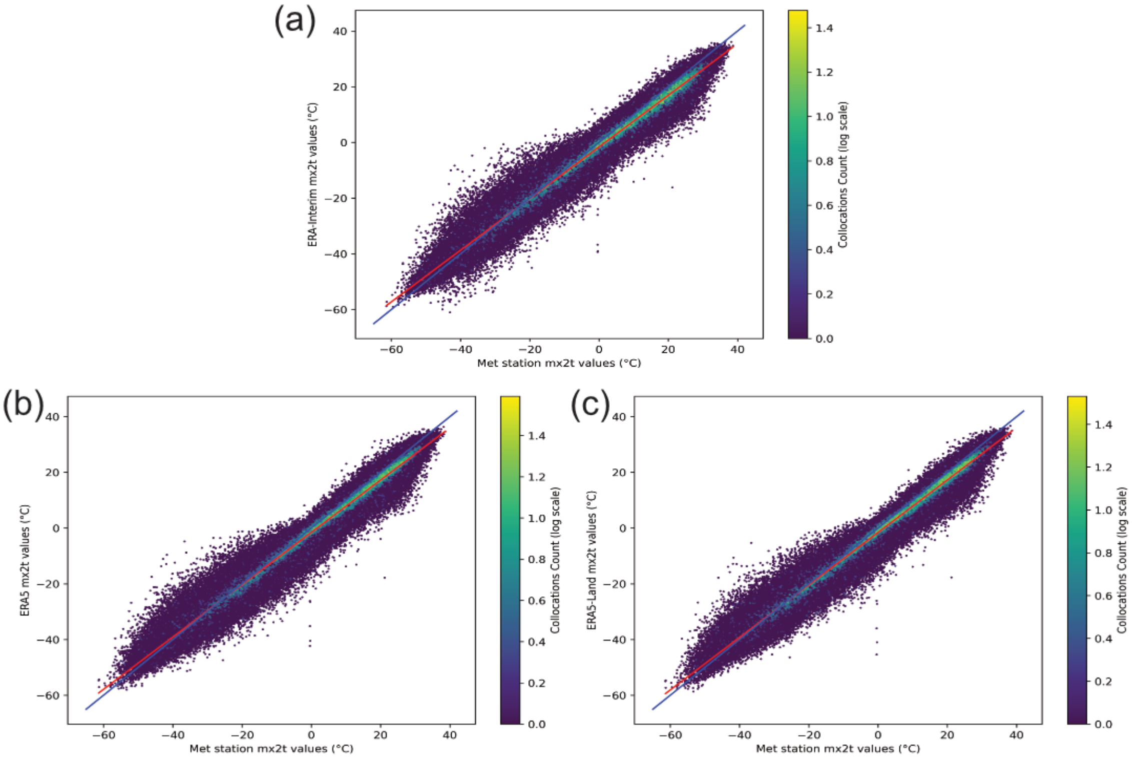

Figure 2.6. Daily MX2T values for ERA-Interim (a), ERA5 (b) and ERA5-Land (c) with respect to the corresponding values from each station. The solid blue line indicates perfect agreement, and the line of best fit is in red. The pixel colour scale indicates the number of collocations of each pixel on a logarithmic scale.

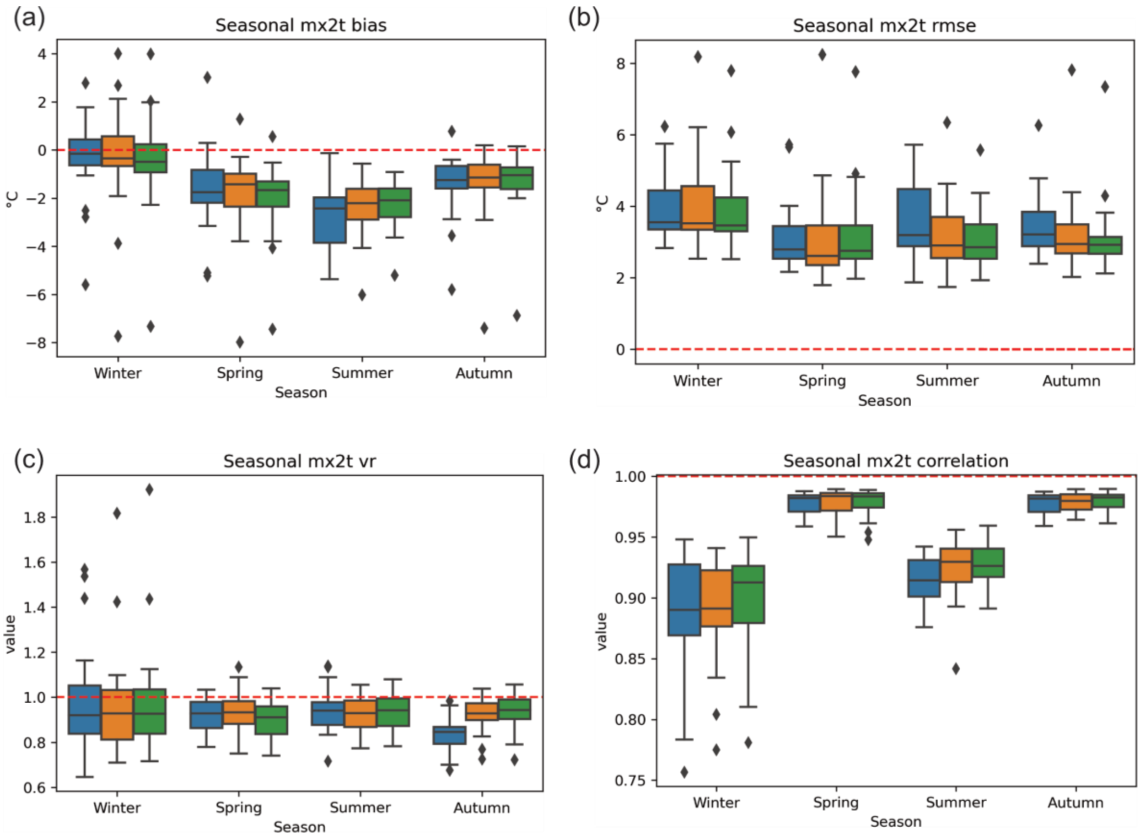

Figure 2.7. Seasonal values of the ERA-Interim (blue), ERA5 (orange) and ERA5-Land (green) bias (a), RMSE (b), variance ratio (c) and correlation (d) statistics for MX2T. The red dashed line indicates the optimum value for each statistic; the whiskers extend to a maximum of 1.5 x IQR.

There are more seasonal outliers in the MX2T statistics (Figure 2.7) than with the equivalent T2M statistics (Figure 2.5), this time throughout the year for both bias and RMSE, and in winter for *vr* and *r*. The outliers occur when the maxima hit their extreme highs and lows as the reanalyses struggle to attain these values. The average correlation ranges from 0.894 in winter to 0.978 in both spring and autumn. In contrast to T2M, the bias is smallest in winter, -0.33 °C, and largest, -2.45 °C, in summer. However the RMSE is greatest in winter, 3.94 °C, and smallest, 3.10 °C, in spring. The variance ratio is consistent, at approximately 0.93, across the reanalyses and seasons. The variance is consistently underestimated, but we note a marked improvement in ERA5 and ERA5-Land over ERA-Interim in autumn (Figure 2.7c).

The seasonal variation in the validation statistics is inconsistent between study areas, with MX2T performing least well in Verkhoyansk region during summer and winter, where the extreme maximum and minimum temperatures are seen. In winter the region has the lowest average correlation and variance ratio values, and the greatest RMSE values, at 0.808, 1.29 and 4.46 °C, respectively, whereas in summer it has the largest mean bias and RMSE values, at -3.76 °C and 4.44 °C. For spring and autumn, the biases and RMSE values are greatest in SW Siberia, at -3.80 °C and 4.63 °C respectively in spring, and -3.14 °C and 4.26 °C in autumn. Amur region is the area where the reanalyses perform best in spring and summer, with average bias/RMSE values of -0.49/2.31 °C in spring and -1.80/2.60 °C in summer. There are no other significant seasonal spatial differences.

MN2T

The MN2T values are the least well reproduced temperature values by the reanalyses, as indicated especially in the bias and RMSE statistics; however, the values are still strong compared with the other climate variables. The validation statistics for MN2T are given in Table 2.4.

Table 2.4. Validation statistics for daily MN2T.

Reanalysis	Bias (°C)	RMSE (°C)	*vr*	*r*
ERA-Interim	2.16	4.88	0.89	0.972
ERA5	1.54	4.69	0.95	0.972
ERA5-Land	1.80	4.69	0.95	0.973

The correlation between the reanalyses and the meteorological station values is also the lowest for MN2T amongst the three temperature variables. This is due to unexpectedly low correlation values of 0.650, 0.661 and 0.656, for ERA-Interim, ERA5 and ERA5-Land respectively, during the summer months (Figure 2.8d). Freychet et al. (2017) used ERA-Interim to look at MX2T and MN2T events during summer heatwaves in China and suggested that during the summer months the night-time MN2T stays too high as a result of insufficient cooling by the atmospheric moisture.

The correlations for the other seasons are also the lowest of the three temperature variables, however the differences are markedly less than in summer, with average values of 0.853, 0.921 and 0.950 in winter, spring and autumn, respectively. As with T2M, the MN2T RMSE is lowest in summer, at 3.85 °C, however the season with the highest RMSE is spring (5.49 °C). Similarly, spring has the lowest variance ratio values across the three temperature variables, with an average of 0.75, and, as with MX2T, the ERA-Interim variance ratio is noticeably lower in autumn than both ERA5 and ERA5-Land. As expected, the most pronounced bias is in winter, 2.40 °C, as the reanalyses struggle to attain the coldest minimum temperatures. The bias is smallest in autumn, at an average of 1.34 °C. Most outliers occur in winter for the bias and RMSE, again highlighting the difficulty of the reanalyses in reproducing the coldest temperatures.

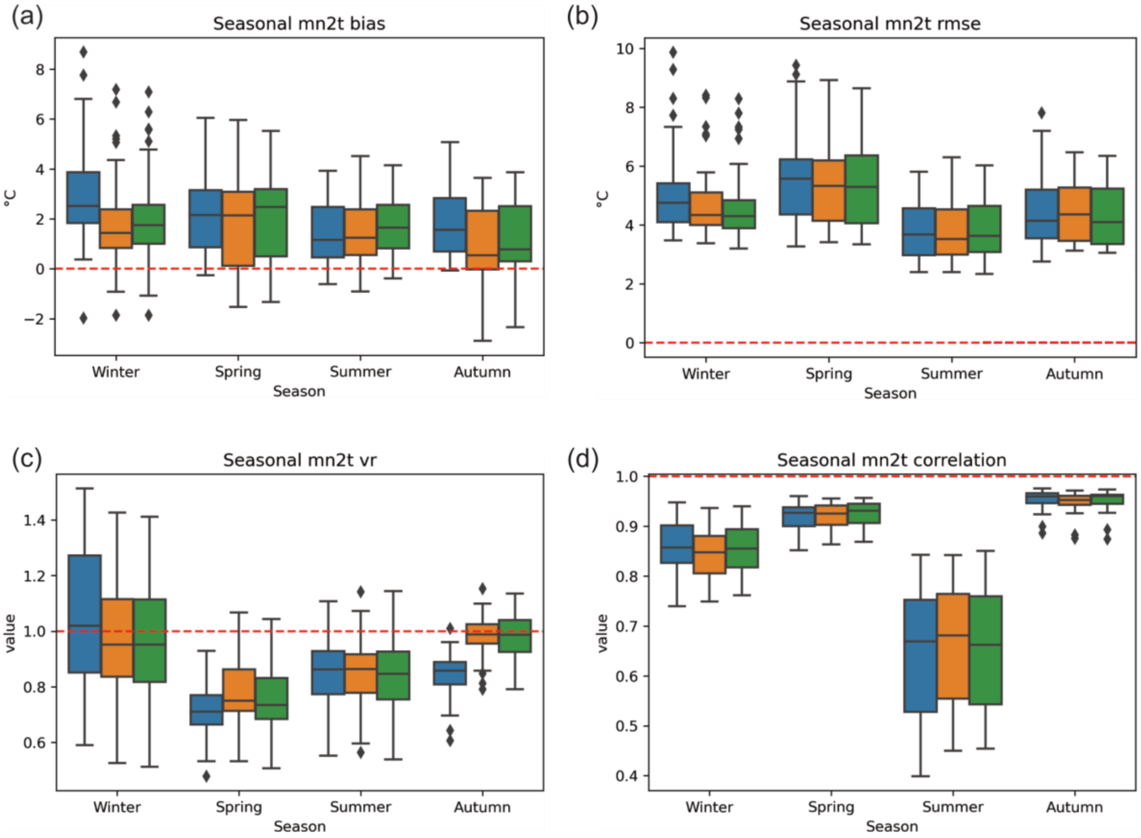

Figure 2.8. Seasonal values of the ERA-Interim (blue), ERA5 (orange) and ERA5-Land (green) bias (a), RMSE (b), variance ratio (c) and correlation (d) statistics for MN2T. The red dashed line indicates the optimum value for each statistic; the whiskers extend to a maximum of 1.5 x IQR.

There are nine meteorological stations at which the correlations with the three reanalyses are less than 0.600 in summer. These are 24329 (W Yakutsk), 24967 and 31062 (E Yakutsk), 30493 and 31137 (Amur region), 29789 and 36103 (SW Siberia), and 25325 and 25503 (NE Sakha). During summer these stations exhibit greater average biases (2.30 °C), and RMSEs (4.86 °C), and lower variance ratios (0.76) across the three reanalyses than the other meteorological stations, which have a mean bias, RMSE and variance ratio of 1.10 °C, 3.35 °C and 0.88, respectively. The stations are spread across five of the seven research areas and located at different altitudes (from 97 to 983 m above sea level). Most of these stations are surrounded by hills or mountains and at the bottom of a valley, however 24329 is located in a flat, swampy area. It is therefore likely local conditions play a significant, increased role at these stations, which cannot be picked up by the coarse spatial resolution of the reanalysis datasets.

Figure 2.9 shows the performance of ERA-Interim, ERA5 and ERA5-Land against meteorological station data for MN2T. The scatter plots are again similar to those for T2M and MX2T, however the greater number of points above the $y=x$ line below 0 °C highlights the moderate warm bias, with the reanalyses struggling to attain the coldest daily minima. Similar to the other temperature variables, there is little to differentiate between the three reanalyses. However, as with T2M, Verkhoyansk region is the area where the reanalyses perform least well, most notably in spring and autumn, and NW Sakha has the lowest bias and RMSE values of the seven areas in winter, summer and autumn. Note that Verkhoyansk region is the area with the fewest number of usable stations (only two), therefore returns the fewest number of observations, and often appears as the "weakest" area in this validation for several of the climate variables.

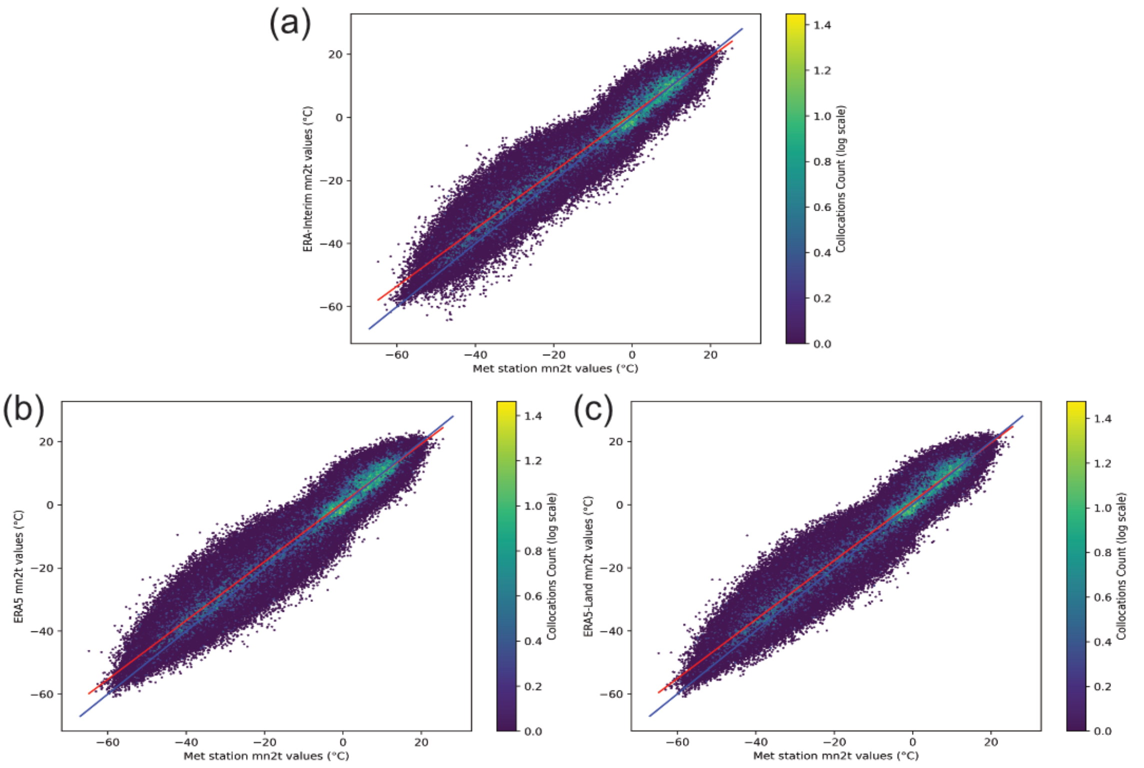

Figure 2.9. Daily MN2T values for ERA-Interim (a), ERA5 (b) and ERA5-Land (c) with respect to the corresponding values from each station. The solid blue line indicates perfect agreement, and the line of best fit is in red. The pixel colour scale indicates the number of collocations of each pixel on a logarithmic scale.

When considering the three 2-metre air temperature variables together, ERA5 performs the best, although the advantage over ERA-Interim and ERA5-Land is negligible.

SD

The daily SD provides the most interesting and variable results. In general, ERA5 only begins to correspond closely with *in-situ* observations from 1992: station data are available before this time but were not assimilated. Urraca and Gobron (2023) demonstrated an additional small correction to values in the mid-2000s associated with the introduction of the assimilation of a satellite-based binary snow cover product. Further commentary on this issue is given in the discussion. The number of assimilations at each station per year is given in the supporting material (Table D2.1; pp. 65-67). Where the data are not assimilated, ERA5 tends to vastly overestimate SD, albeit still picking up trends with a high correlation. ERA5-Land takes its boundary conditions from ERA5, so the link with values from meteorological stations is weakened (H Hersbach, 2022, personal communication, 14 July). Conversely, ERA-Interim appears to perform better in the earlier period, with a lower bias, RMSE and *vr*. The validation statistics, split into two periods, are provided in Table 2.5.

Table 2.5. Validation statistics for the daily SD for the periods 1979-1991 and 1992-2019.

	Bias (cm)		RMSE (cm)		*vr*		ρ	
Reanalysis	79-91	92-19	79-91	92-19	79-91	92-19	79-91	92-19
ERA-Interim	1.84	3.19	10.83	11.80	1.21	2.39	0.883	0.910
ERA5	5.25	1.67	12.70	6.13	2.22	1.59	0.894	0.945
ERA5-Land	7.20	5.79	14.40	11.76	2.49	2.13	0.877	0.906

The daily SD values in the reanalyses against the meteorological station readings in the two time periods are shown in Figure 2.10. Although the trends across ERA5 and ERA5-Land are broadly similar, there is an upper limit of around 140 cm in ERA-Interim in the second time period (Figure 2.10d), which is even sometimes reached when the observations demonstrate there was no snow cover.

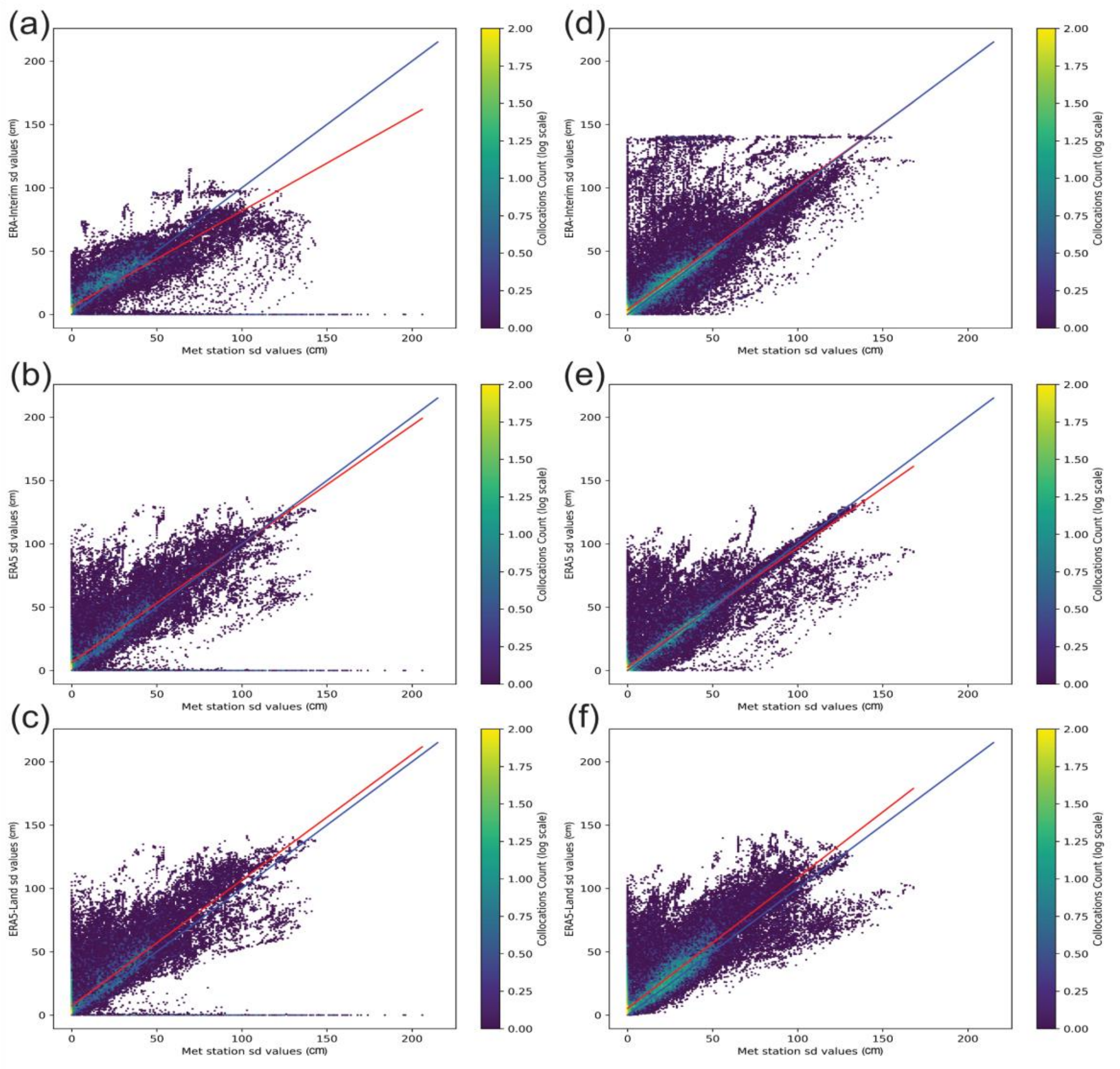

Figure 2.10. Daily SD values for ERA-Interim, ERA5 and ERA5-Land with respect to the corresponding values from each station, respectively, for the periods 1979-1991 [(a) to (c)] and 1992-2019 [(d) to (f)]. The solid blue line indicates perfect agreement, and the line of best fit is in red. The pixel colour scale indicates the number of collocations of each pixel on a logarithmic scale.

Whereas ERA5 can be used to find errors in mean near-surface temperature station data (Figure 2.2), here we found that station data can be used to find errors in ERA-Interim SD in the 1992-2019 period. Figure 2.11 highlights the four main stations where these errors occur. These graphs suggest why ERA-Interim performs better in the 1979-1991 period as the graphs spike most pronouncedly post-2000. As the SD for the reanalyses was calculated using both the ECMWF snow depth and snow density values, both values were checked for irregularities. We found that there were no irregularities with the snow density values; typical values during winter are between 285 and 299 kg m^{-3}, and these values were present during the years where the snow depth values were unusual. However, there are irregular jumps in the original reanalysis snow depth values that are inconsistent with previous years. Typical values range between 0.06 and 0.25 m of water equivalent (mwe), and on several occasions, these jump to between 0.38 and 0.42 mwe, causing the irregularities in the calculated snow depth readings.

A previous issue has been highlighted (NCAR, 2023) where, between 1 July 2003 and 23 February 2010, data locations in ERA-Interim were shifted around 100 km to the south-east, as a result of the processing of National Environmental Satellite, Data, and Information Service snow cover data. This would explain most of the inaccurate ERA-Interim values at stations 24726 (Figure 2.11a) and 25503 (Figure 2.11c), although some of the former's erroneous values occur beyond 2010, as do the errors at stations 24768 and 36103. These errors do not occur in ERA5 (and therefore ERA5-Land) as snow depth readings are assimilated from station observations using 2D-Optimal interpolation in the data assimilation – as opposed to Cressman interpolation in ERA-Interim – and an enhanced snowpack parameterisation (Hersbach et al., 2020, P Berrisford, 2023, personal communication, 30 May). This helps to represent the snowmelt runoff timing more realistically and better align the albedo to satellite products (Dutra et al., 2010).

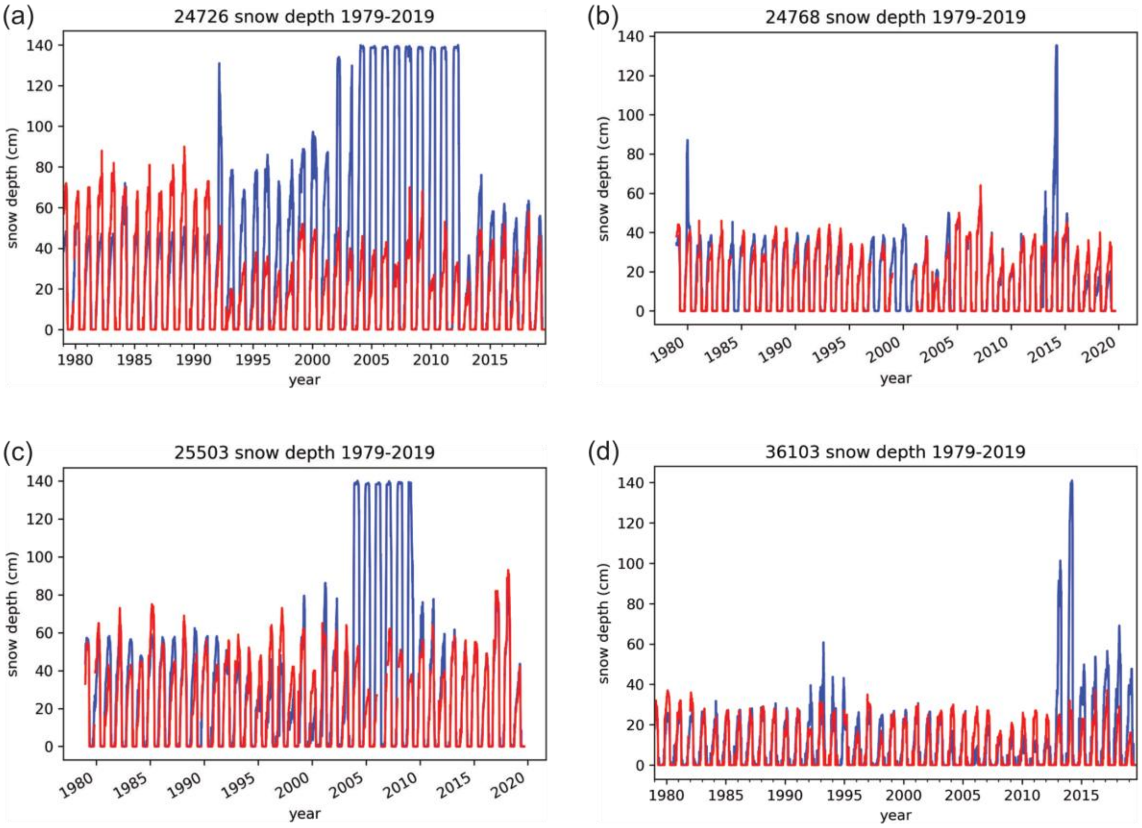

Figure 2.11. ERA-Interim (blue) and meteorological station (red) SD values, 1979-2019, for stations 24726 (a), 24768 (b), 25503 (c) and 36103 (d). Note that station 24768 has no data available in 1984, 1997, 1999 and 2000.

During the summer months SD is predominantly zero at all the study stations, and so this season was not included in the seasonal analysis (Figure 2.12). When comparing the periods 1979-1991 and 1992-2019, the statistics show the reanalyses have the same differences in the non-summer months, such that there are consistent improvements in all the statistics during the second time period.

The clear improvement of ERA5 in particular is highlighted in Figure 2.12, and ERA5 outperforms both ERA-Interim and ERA5-Land, especially after 1992. Highlighting ERA5, the greatest improvement in the correlation, variance ratio and bias is in winter, with an increase of 0.132 and decrease of 1.10 and 6.65 cm, respectively, over the previous period. The greatest improvement in the RMSE is in spring, with a decrease of 8.61 cm, from 16.92 cm to 8.31 cm.

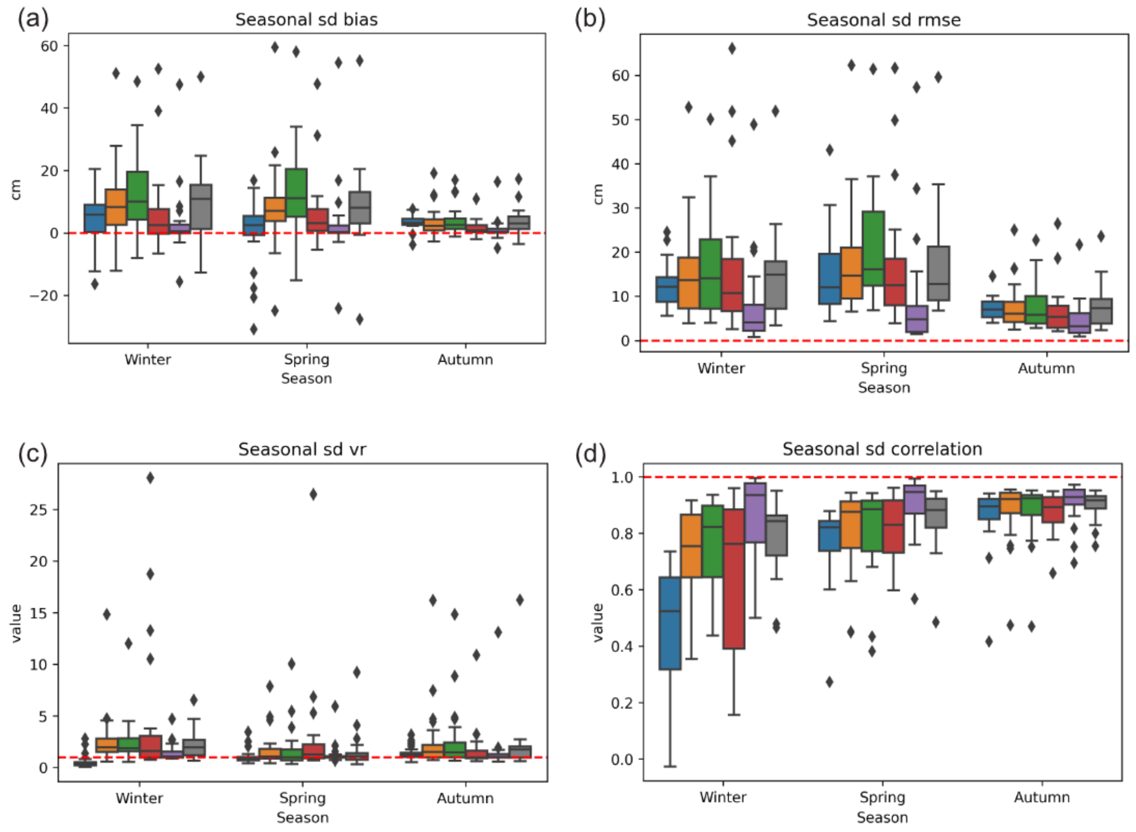

Figure 2.12. Seasonal values of the ERA-Interim 1979-1991 (blue), ERA5 1979-1991 (orange), ERA5-Land 1979-1991 (green), ERA-Interim 1992-2019 (red), ERA5 1992-2019 (purple) and ERA5-Land 1992-2019 (grey) bias (a), RMSE (b), variance ratio (c) and correlation (d) statistics for SD. The red dashed line indicates the optimum value for each statistic; the whiskers extend to a maximum of 1.5 x IQR.

Figure 2.13 shows the yearly SD of ERA5 against the values from three different meteorological stations: 23884, 30493 and 30504. The difference before and after 1992 is clear. With the exception of 1983 and 1984, ERA5 assimilates only once or twice per year throughout the 1980s, then at least 110 times from 1992, increasing up to around 200 assimilations per year through the 2010s.

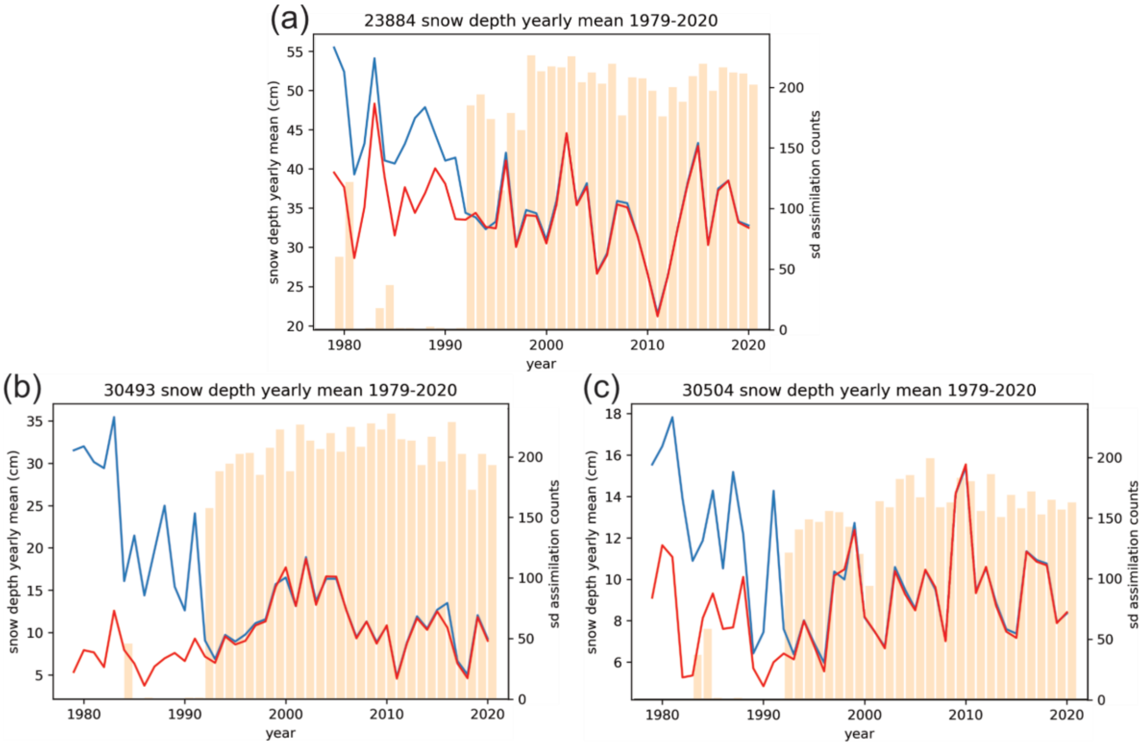

Figure 2.13. ERA5 (blue) and meteorological station (red) SD values per year, 1979-2020, for stations 23884 (a), 30493 (b) and 30504 (c), with their respective snow depth assimilation counts.

Similarly, Figure 2.14 shows three stations, 24371, 24763 and 29789, where the data from meteorological stations are almost never assimilated at all. The three stations are located in different areas of Siberia (Figure 2.1), highlighting the regional variability in the ERA5 SD as there is no consistency between them. Throughout the 1990s ERA5 vastly overestimates the values at station 24371 (Figure 2.14a), whereas from the early 2010s onwards the reanalysis data become very close to the station readings. Figure 2.14b shows that ERA5 performs well at station 24763 in the 1980s, 1990s and later 2010s, although underestimates SD during the 2000s. In contrast, ERA5 consistently significantly overestimates the values from station 29789 (Figure 2.14c). Station 24371 is in Verkhoyansk region with mountains rising 1000 m on three sides, and hills rising 300 m on the other, whereas 29789, in SW Siberia, is halfway down a steep valley, surrounded by mountains rising 500 m. Station 24763 is the anomaly here, located in E Yakutsk with flat, swampy surroundings.

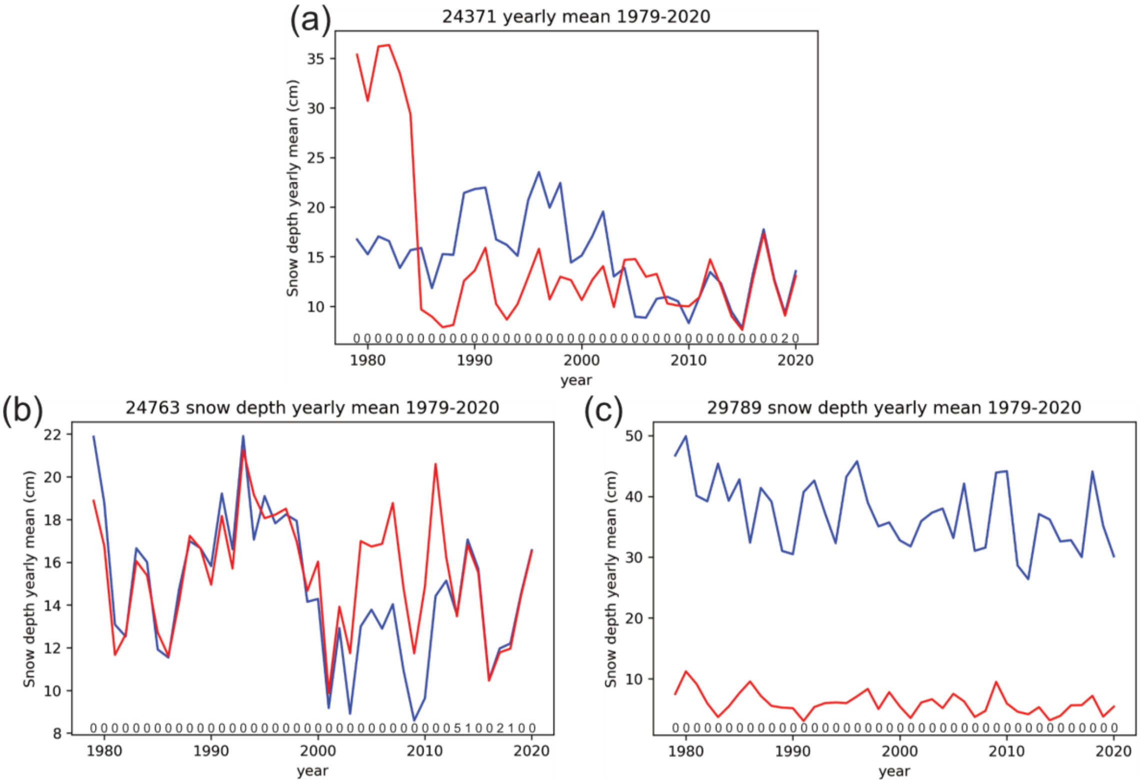

Figure 2.14. ERA5 (blue) and meteorological station (red) SD values per year, 1979-2020, for stations 24371 (a), 24763 (b) and 29789 (c) with the number of assimilations per year.

The ECMWF's yearly statistics on the ERA5 usage of *in-situ* snow depth observations show that the co-ordinates of some of the studied meteorological stations are also altered in the ERA5 assimilation model over time (H Hersbach, 2022, personal communication, 14 July). In general, this means an improvement in the precision of the meteorological station location, leading to an increased number of yearly assimilations. However, there are two stations where a change in the station co-ordinates does not benefit the SD reanalysis values. At 24266 (Verkhoyansk region), the change in co-ordinates in 2014 yields an improvement in the station location, however the number of assimilations drops to 0 and never recovers. In 2009, the co-ordinates of station 24967 (E Yakutsk) change from (60.17N, 130.20E) to (60.47N, 130.00E), implying that the station has moved from the outskirts of a town to a very remote area in the surrounding large hills. The current station location is disputed amongst sources (e.g. Klein Tank et al., 2002, Lobanov and Kirillina, 2019, Gladstone, 2023), although satellite imagery would suggest that the station location has not been changed. However, ERA5 does not assimilate 24967 before 2009 and the number of assimilations increases post-2009 to around 200 per year. 24967 is one of the few stations where the assimilation count makes little difference in reanalysis accuracy compared to the meteorological station values: ERA5 actually underestimates the recorded SD value peaks in both 2008 and 2012, and in general produces values close to those from the meteorological station pre- and post-2009.

In the first time period there are no marked spatial differences in the quality of all three reanalyses, whereas in the second period the SD is best represented in NW Siberia and consistently least well represented in SW Siberia, mainly due to the performance of ERA5 and ERA5-Land at station 29789. In both time periods there are large inter-regional differences in all the SD statistical variables, the largest differences of all the studied climate variables. For example, the largest bias difference is between NW Siberia and SW Siberia (10.88 cm) in the early time period and these two regions have a variance ratio difference of 6.09 in the later period. The largest difference between the correlations occurs in the first time period between W Yakutsk and Verkhoyansk region (0.346) and the largest RMSE difference occurs in the second time period between SW Siberia and Verkhoyansk region (11.38 cm). Overall, the reanalyses represent SD better at more northerly latitudes. Post-1992 there is a considerable advantage to using ERA5 over both ERA-Interim and ERA5-Land, however pre-1992 ERA-Interim and ERA5 perform similarly.

TP

TP is calculated as the sum of the hourly/6-hourly precipitation and is the variable that the reanalyses reproduce least well out of those examined in this study, as shown in Table 2.6.

Table 2.6. Validation statistics for daily TP.

Reanalysis	Bias (mm)	RMSE (mm)	vr	ρ
ERA-Interim	0.26	2.93	0.82	0.534
ERA5	0.30	2.97	0.96	0.549
ERA5-Land	0.30	2.97	0.96	0.552

The reanalyses tend to marginally overestimate TP and there is little difference between them, with almost no difference at all between ERA5 and ERA5-Land. On a daily timescale there are no significant differences between the performances of the reanalyses in the seven study regions. As TP observed at the meteorological stations increases, the deviation from the $y=x$ line increases (Figure 2.15); ERA-Interim underestimates more than the other two reanalysis datasets as precipitation increases.

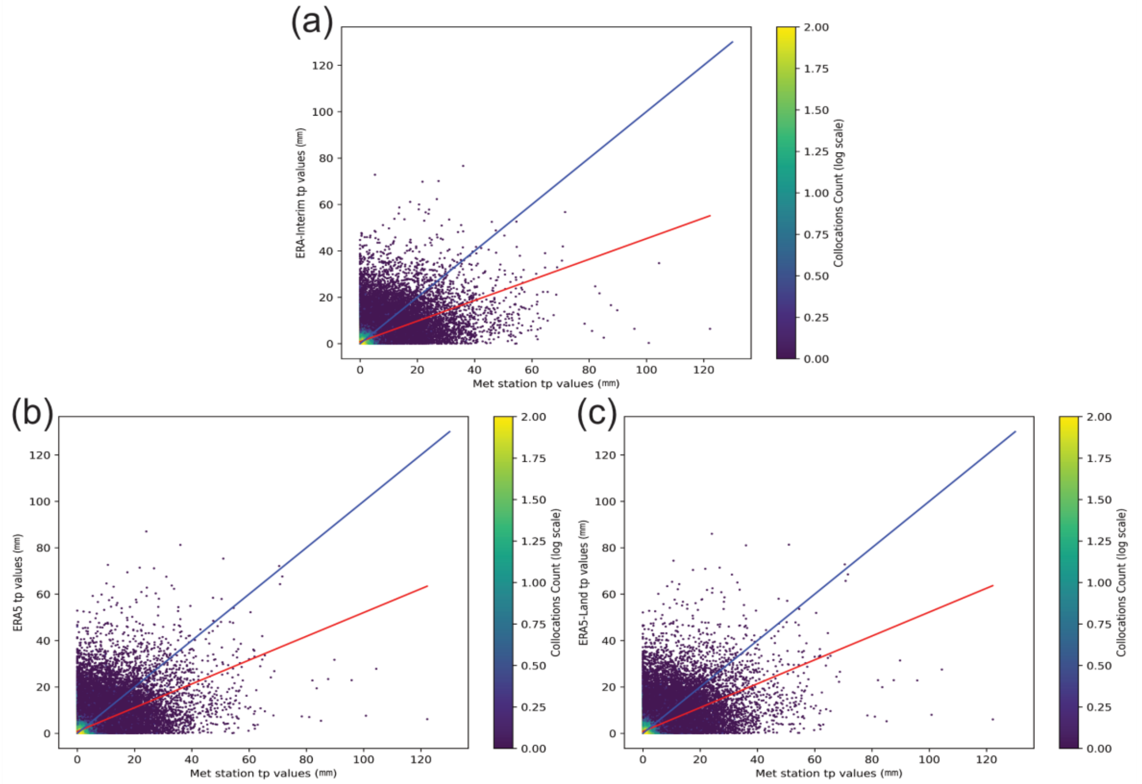

Figure 2.15. Daily TP values for ERA-Interim (a), ERA5 (b) and ERA5-Land (c) with respect to the corresponding values from each station. The solid blue line indicates perfect agreement, and the line of best fit is in red. The pixel colour scale indicates the number of collocations of each pixel on a logarithmic scale.

Unlike the temperature and snow depth variables, TP performs best in winter (Figure 2.16) as the majority of the extreme precipitation events, when the reanalyses perform worst, occur in summer. They are likely often associated with convective precipitation, which occurs on spatial scales too small for the reanalyses to represent accurately. The winter months have the lowest bias and RMSE (0.05 mm and 0.78 mm), and the second-lowest variance ratio (0.96) and correlation (0.554). On the contrary, summer has the greatest bias and the RMSE, 0.43 mm and 4.90 mm, respectively, whereas the variance ratio is furthest from 1.00 in spring (1.23).

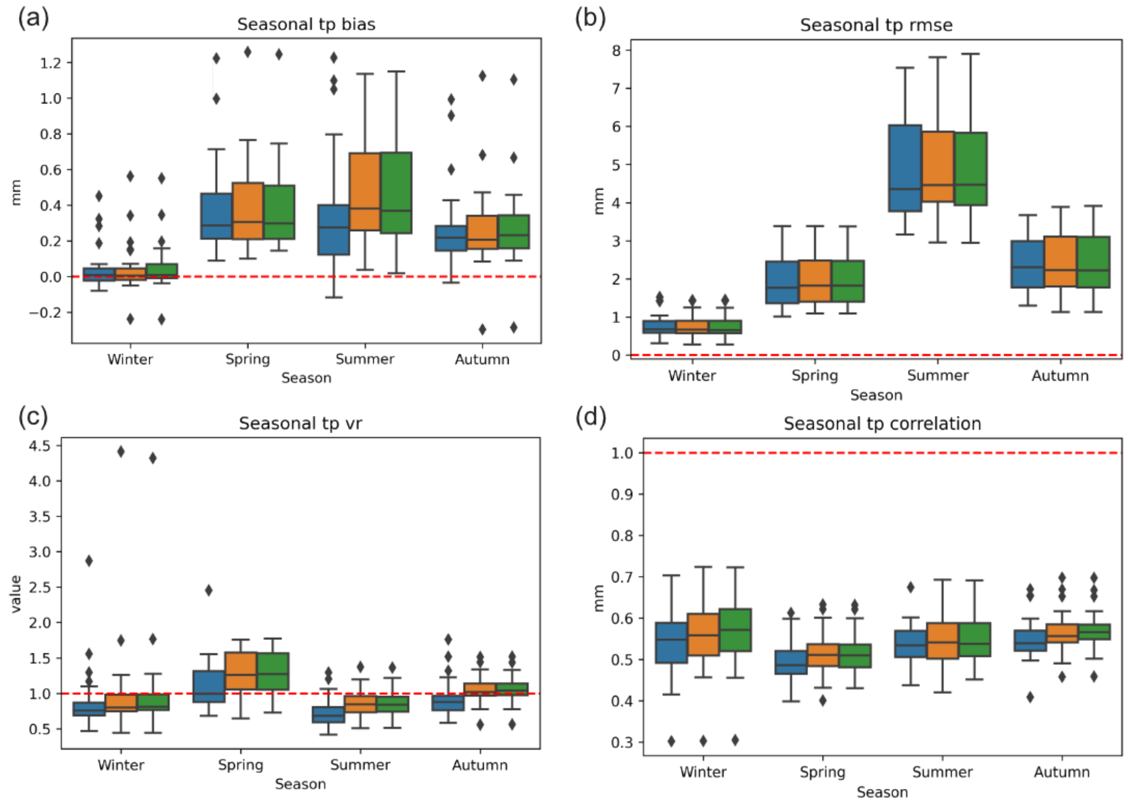

Figure 2.16. Seasonal values of the ERA-Interim (blue), ERA5 (orange) and ERA5-Land (green) bias (a), RMSE (b), variance ratio (c) and correlation (d) statistics for TP. The red dashed line indicates the optimum value for each statistic; the whiskers extend to a maximum of 1.5 x IQR.

Of the seven study areas, SW Siberia is the region where the reanalyses perform least well in winter and autumn, with the largest average biases of 0.31 and 0.66 mm, respectively, and the lowest correlations of 0.457 and 0.523, respectively. The area experiences an increased number of thunderstorms due to its geographical location close to the Altai Mountain range (Kocheeva et al., 2018, Gorbatenko et al., 2019). In autumn, NW Siberia is the region with the highest average correlation values (0.644) and lowest biases (0.108 mm), but there are no other significant seasonal spatial trends.

When considering TP, the difference between ERA5 and ERA5-Land is negligible, and the improvement of ERA5 (or ERA5-Land) over ERA-Interim is also minimal.

WSP

WSP is the only variable studied where there is a noticeable difference between the performance of ERA5 and ERA5-Land. The validation statistics for WSP are given in Table 2.7. Both ERA-Interim and ERA5 have a positive bias and a variance ratio greater than 1.00, whereas ERA5-Land has a negative bias and a variance ratio less than 1.00. ERA5-Land has the lowest RMSE and greatest ρ value, whereas ERA-Interim has the highest RMSE and lowest ρ value, although the difference between the maximum and minimum values are small.

Table 2.7. Validation statistics for daily WSP.

Reanalysis	Bias (ms^{-1})	RMSE (ms^{-1})	*vr*	ρ
ERA-Interim	0.72	1.31	1.19	0.525
ERA5	0.46	1.09	1.02	0.561
ERA5-Land	-0.05	0.94	0.54	0.577

Figure 2.17 shows the performance of the three reanalyses against observations from the meteorological stations. There is a significant difference with how the reanalysis datasets perform with wind speeds above and below 5.0 ms^{-1}. At lower wind speeds all three reanalyses tend to overestimate, most notably ERA-Interim, however they all greatly underestimate the highest recorded wind speeds. ERA5 shows a noticeable improvement over ERA-Interim with reduced variability. ERA5-Land performs better than both ERA-Interim and ERA5 at lower speeds, however it is the weakest of the three at higher speeds, vastly underestimating the extreme highs. For instance, for speeds above 10.0 ms^{-1}, the ERA5-Land bias is -6.48 ms^{-1}, compared to -4.22 ms^{-1} and -4.49 ms^{-1} for ERA-Interim and ERA5, respectively.

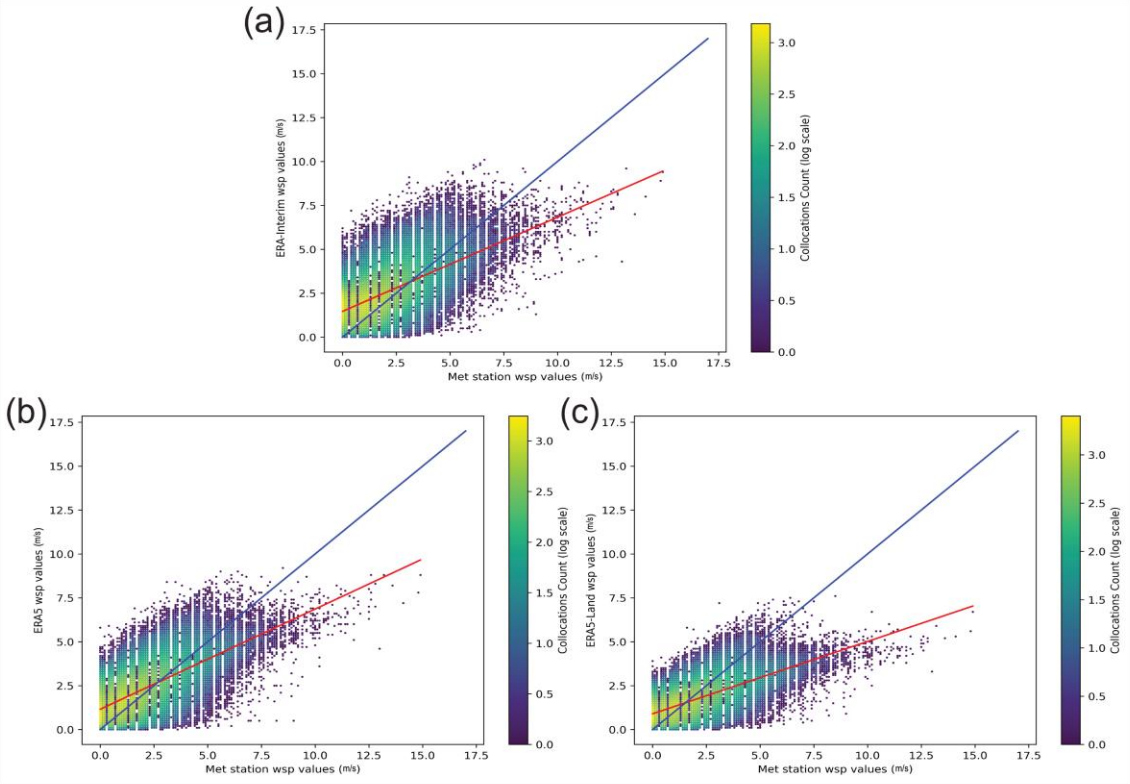

Figure 2.17. Daily WSP values for ERA-Interim (a), ERA5 (b) and ERA5-Land (c) with respect to the corresponding values from each station. The solid blue line indicates perfect agreement, and the line of best fit is in red. The pixel colour scale indicates the number of collocations of each pixel on a logarithmic scale.

Of the six studied variables, WSP has the greatest range in the statistical values between stations. The average correlation between the three reanalyses and the station values at station 36103 is 0.387, whereas at station 23986 it is 0.803. The variance ratio can be as high as 2.74 (station 29789) or as low as 0.34 (station 31102). This highlights that local factors can affect WSP readings more than any other studied variable.

On a regional scale, SW Siberia stands out as the area where the reanalyses reproduce WSP least well, especially in winter and autumn. WSP is the variable where the difference in regional correlation values is largest – the average correlation is greatest in NW Siberia (0.747), and lowest in SW Siberia (0.451). The average biases and RMSE values are relatively low – within 0.85 ms^{-1} of each other.

Figure 2.18 shows that, across all stations, the performance of the reanalyses in reproducing WSP is not affected by the season. The same broad trends are exhibited across all four seasons in all the statistics, with ERA-Interim having the most variance. ERA5-Land has the lowest bias and RMSE in winter, spring and autumn, and the highest correlations in the latter two seasons. The variance ratios are furthest from 1.00 (too much wind speed variability) in summer.

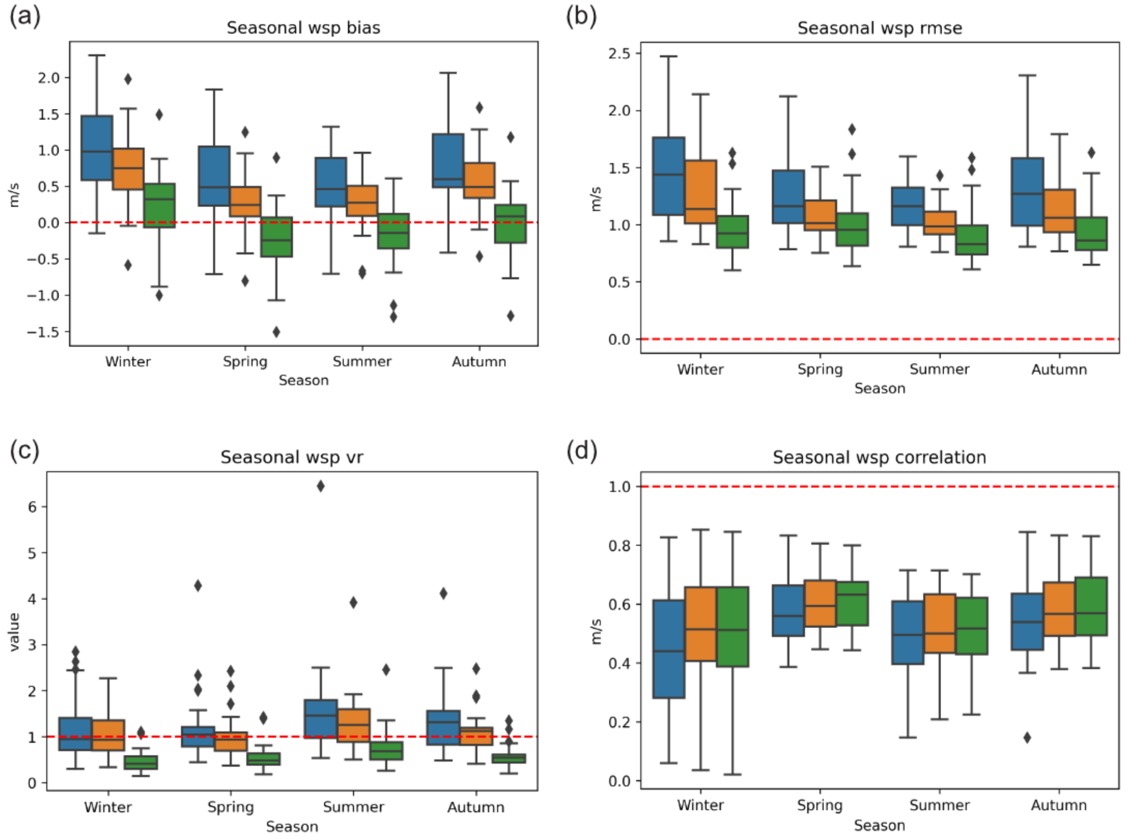

Figure 2.18. Seasonal values of the ERA-Interim (blue), ERA5 (orange) and ERA5-Land (green) bias (a), RMSE (b), variance ratio (c) and correlation (d) statistics for WSP. The red dashed line indicates the optimum value for each statistic; the whiskers extend to a maximum of 1.5 x IQR.

When considering the whole picture, ERA5 and ERA5-Land are an improvement over ERA-Interim. ERA5-Land performs the best at lower wind speeds, however ERA5 should be used for extreme high speeds, which are likely to be of most interest.

Analysis of data back to 1959

For ERA5 and ERA5-Land, the T2M, MX2T, MN2T, SD and TP validations were extended back to 1959, whereas the validations for WSP only start from 1966 due to the availability of data from the meteorological stations. Reanalyses have tended to struggle before 1979 due to reduced sounding data from instruments onboard polar orbiting satellites, fewer data from commercial aircraft and the lack of drifting buoys (Andersson, 2007, Minnett et al., 2019). Note that missing meteorological station data also becomes more of an issue prior to 1979, so only the key results and general trends are summarised here.

T2M, MX2T and MN2T are homogeneous back to 1959 in that the validation statistics exhibit the same seasonal variability, and the average bias and RMSE are within 0.5 °C for both ERA5 and ERA5-Land across all three variables.

With TP there is little difference on a daily basis from 1979, and the seasonal trends exhibit the same patterns as the earlier period. The differences in the biases and RMSEs are negligible. Although there are small changes in the validation statistics for WSP prior to 1979, they are not consistent across the two reanalysis datasets, leading to the conclusion that the accuracy of the reanalysis WSP is relatively homogeneous through time.

SD is the only variable for which the statistics are not temporally homogeneous. As discussed before, there are significant differences between the periods 1979-1991 and 1992-2019 (Table 2.5), however there is also a noticeable distinction between 1959-1978 and 1979-1991. The statistics for the first period are in Table 2.8.

Table 2.8. Validation statistics for the daily SD for the period 1959-1978.

Reanalysis	Bias (cm)	RMSE (cm)	*vr*	ρ
ERA5	7.68	15.87	2.49	0.856
ERA5-Land	7.91	16.33	2.44	0.838

Post 1979, the average correlation across the two reanalyses improves by 0.058, the mean daily RMSE decreases by 2.55 cm and the average bias is reduced by 1.57 cm. The seasonal trends remain consistent, which again reaffirms the first discontinuity noted by Urraca and Gobron (2023).

Discussion

ERA-Interim, ERA5 and ERA5-Land can all be considered as excellent representations of T2M, MX2T and MN2T across Siberia and the Russian Far East. ERA5 and ERA5-Land are homogeneous from 1959, with correlations over 0.98 and only small biases and RMSEs. There is only a marginal improvement with using ERA5 over ERA-Interim, and there is no additional benefit to using ERA5-Land over ERA5. The performance of the reanalyses at reproducing temperature is weakest in winter as the temperatures approach and reach their minima, although compared to the other studied variables the seasonal difference is minimal.

The results of our evaluation are consistent with previous validations of ERA-Interim and ERA5 against *in-situ* observations in comparable regions. As expected, when considering T2M, the reanalyses perform strongly with little variation across studies. The ERA5 T2M validation statistics here perform better than in Turkey (Yilmaz, 2023), and the Greenland Ice Sheet (Delhasse et al., 2020), and similar to results from the Yamal Peninsula (Matveeva and Sidorchuk, 2020), the Canadian Prairies (Betts et al., 2019), and the Arctic Gateway (Graham et al., 2019).

When considering TP, there is little difference between ERA5 and ERA5-Land, however both show some improvement over ERA-Interim. Nonetheless, all three reanalyses struggle with reproducing extreme precipitation events during the summer months, likely due to their inability to simulate the temporal and spatial distribution of convective precipitation. TP is relatively homogeneous through time in ERA5 and ERA5-Land.

Validations of TP in ERA-Interim and ERA5 have been conducted in various other studies, including in the Yamal Peninsula (Matveeva and Sidorchuk, 2020), and in South Siberia (Riazanova et al., 2016, Voropay et al., 2021). While there is a large amount of variability in the validation statistics between all the studies, depending on the research location, our results are consistent in that the correlations are significantly lower than temperature variables (only greater than 0.5), the reanalyses perform worst during occurrences of extreme high precipitation in the summer, and the spatial variability in their quality is relatively small.

The reanalysis validation statistics highlight the marked local variability of wind speed. There is a benefit to using either ERA5 or ERA5-Land over ERA-Interim, with ERA5-Land performing better at lower wind speeds and ERA5 performing better at the extreme high speeds. WSP shows the lowest seasonal variation of the studied variables amongst the validation statistics, although the station-to-station variability is the highest of all the variables. When considering WSP, the performance of ERA-Interim and ERA5 is again consistent with previous studies. The WSP statistics in this study are improved over the Greenland Ice Sheet area validation (Delhasse et al., 2020), and similar to results in the Black and Azov Seas (Grankina et al., 2019, Amarouche et al., 2021) and the Arctic (Graham et al., 2019, Dyakonov et al., 2020).

SD is the variable where most caution should be taken. ERA5 only consistently begins to assimilate the meteorological station data from 1992; before that the reanalysis vastly overestimates SD. Furthermore, ERA5 never assimilates data from some of the meteorological stations examined, and in these areas the reanalysis continues to overestimate SD. ERA5-Land takes its boundary conditions from ERA5, so the ERA5-Land SD values are further away from the observed values at meteorological stations. ERA-Interim appears to perform better before 1992, however this is likely due to anomalous values at several stations post-2000, where there appears to be a consistent maximum upper limit of 140 cm. The reanalyses perform weakest in winter and spring when dealing with extreme values.

Only two other studies have conducted validations of SD in reanalyses across Russia, the findings of the present study are consistent with results for ERA-Interim over Siberia (Klehmet et al., 2013), and the post-1992 results for ERA5 from the Yamal Peninsula (Matveeva and Sidorchuk, 2020). Urraca and Gobron (2023) identified potential discontinuities in the snow depth in 1977-1980, 1991-1992 and 2003-2004, with a negative trend between 1980 and 1991. This study reaffirms their findings that, unsurprisingly, the assimilations into ERA5, first in 1979 then 1992, significantly improved the snow depth values from the reanalysis. However, our study shows the third discontinuity to be in 2004-2005, as opposed to 2003-2004 although, as with the original findings, this discontinuity is relatively minor and likely associated with the start of the assimilation of a satellite snow cover product into ERA5. Graphs from our study showing the temporal evolution of the bias in ERA5 and ERA5-Land SD, equivalent to Fig. 4 from Urraca and Gobron (2023), can be found in the supporting material (Figures D2.1a and D2.1b; p. 68).

The validation could be refined if more meteorological stations were available. Individual stations may not always represent the region as a whole as they can be affected by local climate variables and regional topography. The coarse resolution of the reanalyses may also affect the results as they may be unable to reproduce localised weather activity or topographical influences, and interpolation cannot correct for this. Furthermore, when considering the line of best fit on each plot, the fit around the outliers may not always be well represented due to high-density values carrying more weight.

Conclusion

In this study we assessed the performance of ERA Interim, ERA5 and ERA5-Land in Siberia and the Russian Far East. We believe this is the first work comparing these three ECMWF reanalyses across a range of climate variables in this region. The results of this validation have shown that for the studied climate variables there is a small benefit to using ERA5 over ERA-Interim in Siberia and the Russian Far East, most notably as regards snow depth. The improved spatial and temporal resolutions as well as the increased data availability mean that ERA5 should be the reanalysis dataset of choice for the core climate variables moving forward. Despite a further increase in spatial resolution, we found no consistent, significant benefit to using ERA5-Land over ERA5. Thus, we conclude that ERA5 is the most appropriate current ECMWF reanalysis to examine climate change in Siberia.

Appendix A: List of stations used in the validation

Table A2.1. List of meteorological stations used in the validation in this report with their World Meteorological Organization (WMO) number, latitude and longitude and the years for which data are available.

Area	WMO No.	Station name	N latitude (°N)	E longitude (°E)	Data availability
1	23678	Verkhneimbatsk	63.15	87.95	1950-2020
1	23884	Bor	61.60	90.02	1950-2020
1	23986	Severo-Yeniseysk	60.37	93.02	1950-2020
2	24329	Selagoncy	66.25	114.28	1950-2020
2	24538	Chuchukan	64.23	116.92	1955-2020
2	24639	Nyurba	63.28	118.33	1950-2020
2	24641	Vilyuysk	63.77	121.62	1950-2020
2	24726	Mirny	62.53	113.87	1959-2020
2	24738	Suntar	62.15	117.65	1950-2020
3	24763	Lippelyakh	62.82	134.43	1966-2020
3	24768	Curapca	62.03	132.60	1950-2020
3	24966	Ust-Maya	60.38	134.45	1950-2020
3	24967	Tegyultya	60.17	130.20	1950-2020
3	31062	Yugorenok	59.77	137.72	1950-2020
4	30493	Nagorniy	55.97	124.88	1950-2020
4	30692	Skovorodino	54.00	123.97	1950-2020
4	31102	Kankunskiy	57.65	125.97	1950-2020
4	31137	Toko	56.28	131.13	1962-2020
4	31253	Bomnak	54.72	128.93	1950-2020
5	29698	Nizhneudinsk	54.88	99.03	1950-2020
5	29789	Verkhnyaya Gutara	54.22	96.97	1950-2020
5	30504	Tulun	54.60	100.63	1950-2020
5	36103	Toora-Khem	52.47	96.12	1950-2020
6	24266	Verkhoyansk	67.55	133.38	1950-2020
6	24371	Ust-Charky	66.80	136.68	1966-2020
7	25206	Srednekolymsk	67.45	153.72	1950-2020
7	25325	Ust-Oloy	66.55	159.42	1950-2012
7	25400	Zyryanka	65.73	150.90	1950-2020
7	25503	Korkodon	64.75	153.97	1950-2019

Appendix B: Ecoregions of the study areas

Figure B2.1. Ecoregions of Siberia, as per Soja et al. (2004b).

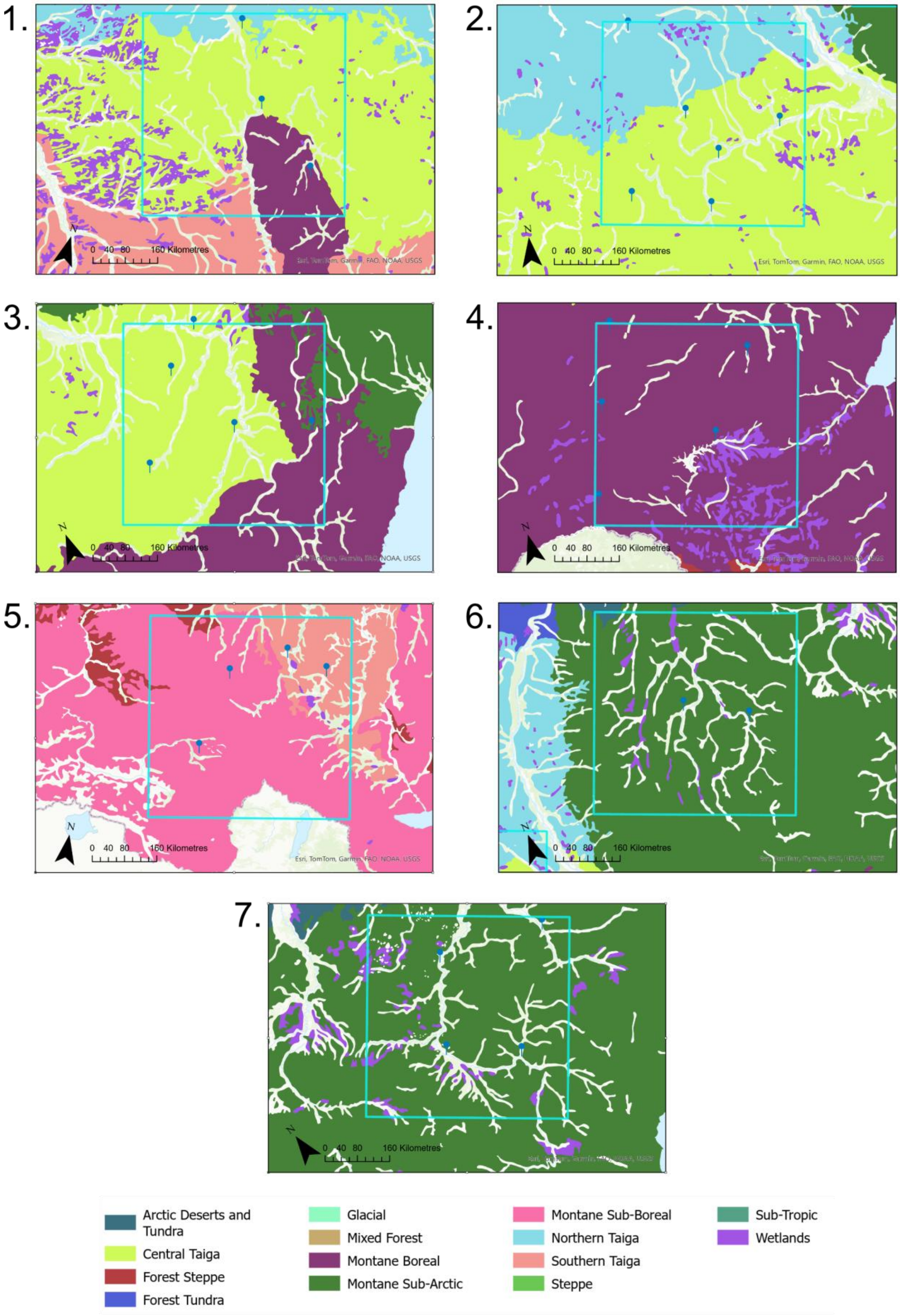

Figure B2.2. Ecoregions, as per Soja et al. (2004b), of each individual study area with pins representing the usable meteorological stations within them.

Appendix C: Variable conversions

Raw reanalysis data were converted to draw direct comparisons with meteorological station data and the conversion formulae are given below.

Temperature: $°\mathrm{C} = °\mathrm{K} - 273.15$

Total precipitation: $mm = \frac{m}{1000}$

Wind speed: $ms^{-1} = \sqrt{u^2 + v^2}$

Snow depth:

$$cm = \left(\frac{snow\ depth * 1000}{snow\ density}\right) * 100$$

Appendix D: Supplementary information for Chapter 2

Table D2.1. The number of SD assimilations at each station per year into ERA5. ‘-’ represents the absence of assimilations in a given year.

Station	**1979**	**1980**	**1981**	**1982**	**1983**	**1984**	**1985**	**1986**	**1987**	**1988**	**1989**	**1990**	**1991**	**1992**	**1993**	**1994**	**1995**	**1996**
23678	64	80	-	5	9	16	2	3	3	1	-	-	-	153	160	122	93	142
23884	59	120	-	1	17	36	1	1	-	2	1	-	1	182	191	171	113	176
23986	-	-	-	1	9	42	1	1	1	-	-	-	-	74	137	145	-	-
24329	101	155	-	3	1	4	1	1	1	2	1	3	-	157	156	148	155	181
24538	-	-	-	1	48	115	1	5	1	3	1	2	3	-	3	-	-	-
24639	1	-	-	3	43	85	3	2	3	1	3	-	1	172	204	193	186	188
24641	93	73	-	-	2	4	1	1	-	-	1	1	1	-	173	198	206	198
24726	-	-	-	1	-	-	-	-	-	-	-	-	-	-	-	-	-	-
24738	104	161	-	-	5	3	-	1	4	-	1	4	-	126	191	118	1	1
24763	-	-	-	-	-	-	-	-	-	-	-	-	-	-	-	-	-	-
24768	-	-	-	5	42	95	-	3	1	1	-	2	1	157	198	199	203	194
24966	79	49	-	1	1	4	5	1	1	1	1	1	-	159	192	181	190	186
24967	-	-	-	-	52	105	-	-	-	1	2	-	-	-	-	-	-	-
31062	-	-	1	-	47	94	-	2	-	-	1	1	-	-	-	-	-	-
30493	-	-	-	-	-	45	-	1	-	-	-	1	1	155	185	191	199	200
30692	93	157	-	-	8	20	-	1	-	-	2	3	-	125	87	50	122	110
31102	-	-	-	-	-	-	-	-	-	-	-	-	-	-	-	-	-	-
31137	103	62	-	1	2	4	-	2	1	-	2	2	1	217	294	313	320	319
31253	-	-	-	2	6	4	1	1	1	-	1	6	3	39	135	112	129	113
29698	87	149	-	-	17	38	-	-	-	-	1	2	-	122	142	154	151	165
29789	-	-	-	-	-	-	-	-	-	-	-	-	-	-	-	-	-	-
30504	-	-	-	-	36	57	1	-	1	-	-	-	-	119	138	146	144	153
36103	-	-	-	1	9	41	1	3	7	-	2	-	-	74	130	95	-	-
24266	110	166	-	-	1	2	-	1	2	4	3	-	2	164	183	192	202	182
24371	-	-	-	-	-	-	-	-	-	-	-	-	-	-	-	-	-	-
25206	-	-	-	-	46	103	2	1	-	4	1	-	1	1	-	-	-	-
25325	-	-	-	1	-	-	1	2	-	1	-	1	-	171	200	197	208	143
25400	86	146	-	-	1	2	-	2	2	-	1	2	1	188	192	192	200	202
25503	-	-	-	1	49	109	1	1	-	-	1	1	-	-	-	-	-	-

Station	1997	1998	1999	2000	2001	2002	2003	2004	2005	2006	2007	2008	2009	2010	2011	2012	2013	2014
23678	127	162	190	203	204	221	186	204	200	207	166	198	207	183	171	199	182	210
23884	162	223	210	214	213	222	201	209	200	216	174	205	204	194	173	197	185	206
23986	-	-	-	-	-	-	-	-	-	-	-	-	165	229	199	208	204	227
24329	182	226	208	202	192	218	192	215	199	211	189	221	188	213	194	203	189	200
24538	-	-	-	-	-	-	-	-	-	-	-	-	-	-	-	61	179	182
24639	183	216	213	194	207	216	191	221	206	201	185	218	183	200	190	215	174	201
24641	193	230	224	213	208	218	209	216	203	193	184	214	191	200	193	217	189	213
24726	-	1	1	-	-	-	-	-	-	-	-	-	-	-	-	87	183	205
24738	-	1	87	214	201	204	199	217	196	201	184	216	185	196	190	207	186	201
24763	-	-	-	-	-	-	-	-	-	-	-	-	-	-	-	-	5	1
24768	202	220	218	194	189	209	103	93	196	200	179	188	194	194	194	194	169	192
24966	175	214	200	183	173	208	188	198	185	198	181	209	202	187	194	118	-	-
24967	-	-	-	-	-	-	-	-	-	-	-	-	163	180	186	208	169	181
31062	-	-	-	-	-	-	-	-	-	-	-	-	-	-	-	-	1	-
30493	182	204	219	185	223	210	203	216	201	221	205	224	219	232	211	210	190	213
30692	103	124	178	161	169	178	155	158	143	176	164	158	149	113	-	15	120	90
31102	-	-	-	-	-	-	-	-	-	-	-	-	-	-	-	61	207	221
31137	313	293	279	290	223	213	208	213	175	224	180	162	215	226	224	199	192	219
31253	102	2	2	-	-	1	1	-	-	-	-	1	-	-	-	75	160	179
29698	155	164	166	164	154	176	161	172	163	178	154	158	171	161	150	172	144	153
29789	-	-	-	-	-	-	-	-	-	-	-	-	-	-	-	-	-	-
30504	152	140	118	92	161	156	179	182	164	196	156	160	180	177	153	183	148	166
36103	-	-	-	-	-	-	-	-	-	-	-	-	-	-	-	56	144	154
24266	184	192	209	191	219	224	203	213	202	206	181	199	210	206	196	130	-	4
24371	-	-	-	-	-	-	-	-	-	-	-	-	-	-	-	-	-	-
25206	-	-	-	-	-	-	-	-	-	-	-	-	174	218	198	146	-	-
25325	214	132	123	183	187	171	141	185	192	155	89	-	1	197	29	3	-	-
25400	220	212	211	195	228	221	217	229	207	213	181	209	213	211	214	139	-	-
25503	-	-	-	-	-	-	-	-	-	-	-	-	163	204	225	129	-	-

Station	2015	2016	2017	2018	2019	2020
23678	217	197	229	207	207	299
23884	216	194	213	209	208	199
23986	231	221	222	219	226	206
24329	199	219	231	222	241	228
24538	206	214	222	203	215	198
24639	208	205	205	174	192	186
24641	210	208	219	203	209	213
24726	208	224	236	197	216	199
24738	197	215	196	187	205	181
24763	-	-	2	1	-	-
24768	202	204	201	208	204	204
24966	-	-	-	-	-	1
24967	193	204	209	206	207	197
31062	-	-	-	-	-	-
30493	193	225	199	170	199	190
30692	-	-	-	-	-	-
31102	228	254	251	237	240	232
31137	213	220	209	218	219	213
31253	192	200	172	164	187	188
29698	146	167	152	163	147	150
29789	-	-	-	-	-	-
30504	155	169	150	162	154	160
36103	170	168	163	163	144	166
24266	-	-	-	20	2	-
24371	-	-	-	-	2	-
25206	-	-	-	-	-	-
25325	-	-	-	-	-	-
25400	-	-	-	-	-	-
25503	-	-	-	-	-	1

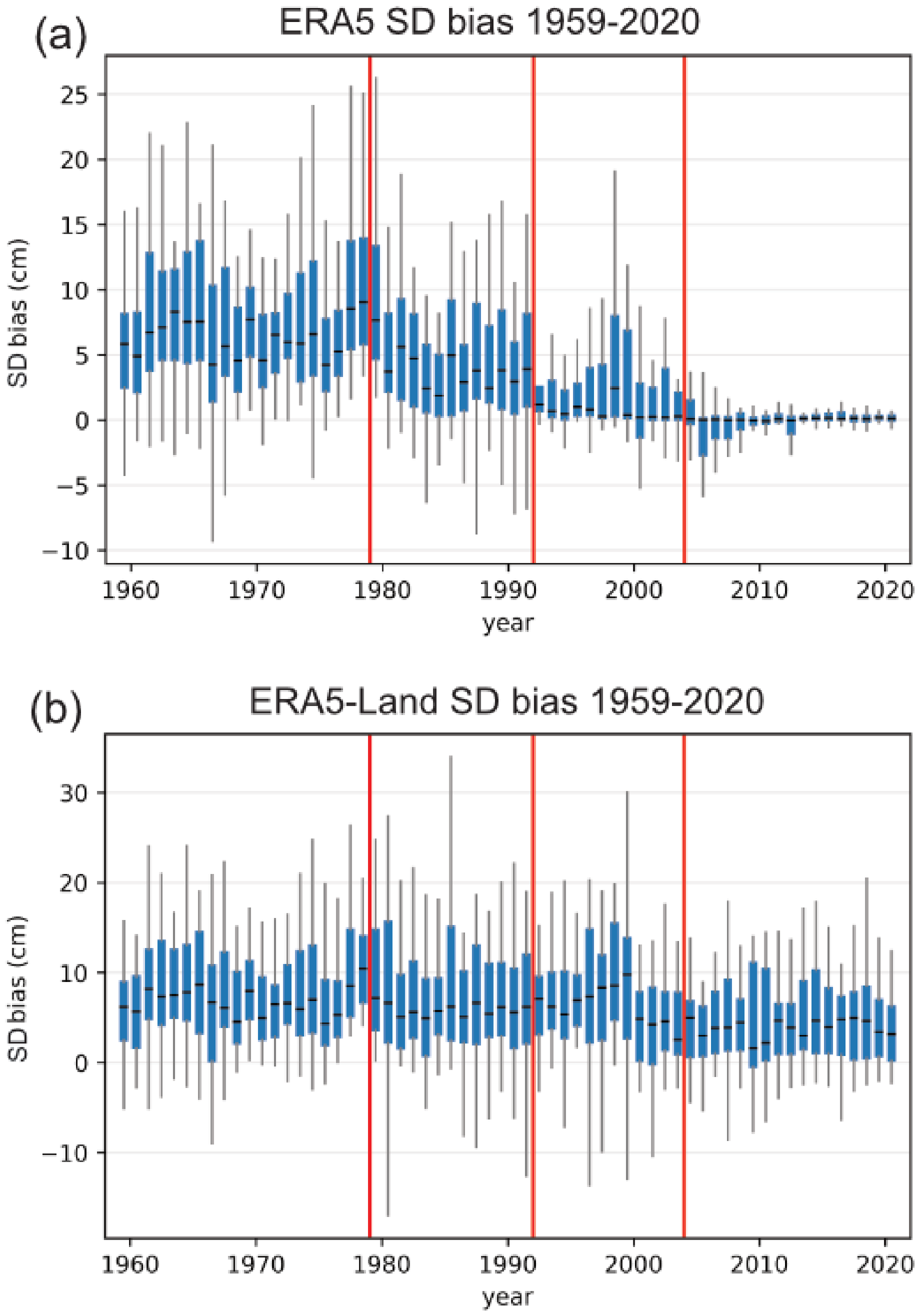

Figure D2.1. Values of the SD bias for all stations, 1959-2020, for ERA5 (a) and ERA5-Land (b). The vertical red lines highlight the discontinuities at 1978-1979, 1991-1992, and 2003-2004 identified by Urraca and Gobron (2023).

Chapter 3

Analysis of burned area products in the Arctic-boreal region

Burned black spruce (*Picea mariana*) stands from the 2021 Yankovich Road Fire, Fairbanks, Alaska, USA. *Photo credit: Joshua Rady.*

This chapter is published as: Clelland, A. A., Marshall, G. J., Baxter, R., Potter, S., Talucci, A. C., Rady, J. M., Genet, H., Rogers, B. M. and Natali, S. M. (2024) Annual and Seasonal Patterns of Burned Area Products in Arctic-Boreal North America and Russia for 2001-2020. *Remote Sensing*. 16(17), 3306.

The author contributions were as follows: A.A.C., S.P. and B.M.R. conceived the study. A.A.C., G.J.M., S.P., A.C.T., J.M.R. and B.M.R. developed the methodology. A.A.C. conducted the research. A.A.C. analysed the data and wrote the manuscript, with contributions from all authors.

Abstract

Boreal and Arctic regions have warmed up to four times quicker than the rest of the planet since the 1970s. As a result, boreal and tundra ecosystems are experiencing more frequent and higher intensity extreme weather events and disturbances, such as wildfires. Yet limitations in ground and satellite data across the Arctic and boreal have challenged efforts to track these disturbances at regional scales. In order to effectively monitor the progression and extent of wildfires in the Arctic-boreal zone, it is essential to determine whether burned area (BA) products are accurate representations of BA. Here, we use 12 different datasets together with MODIS active fire data to determine the total yearly BA and seasonal patterns of fires in Arctic-boreal North America and Russia for the years 2001-2020. We found relatively little variability between the datasets in North America, both in terms of total BA and seasonality, with an average BA of 2.55 ± 1.24 (sd) Mha/year for our analysis period, the majority (*ca.* 41 %) of which occurs in July. Whereas in Russia, there are large disparities between the products – GFED5 produces over four times more BA than GFED4s in southern Siberia. These disparities occur due to the different methodologies used; dNBR (difference Normalized Burn Ratio) of short-term composites from Landsat images used alongside hotspot data were the most consistently successful in representing BA. We stress caution using GABAM in these regions, especially for the years 2001-2013, as Landsat 7 ETM+ scan lines are mistaken as burnt patches, increasing errors of commission. On the other hand, we highlight using regional products where possible, such as ABoVE-FED or ABBA in North America, and the Talucci et al. (2022) fire perimeter product in Russia, due to their detection of smaller fires which are often missed by global products.

Introduction

Located at high latitudes across North America, Fennoscandia and Eurasia, the boreal forest, also known as the taiga, is the world's largest land biome, containing about 30 % of the total forested area (Gauthier et al., 2015). The boreal forest is one of the world's largest biogeoclimatic areas, with an assortment of climates, topographies, fauna and flora, making it one of the most important ecosystems on the planet (Ruckstuhl et al., 2008, Brandt et al., 2013). In North America, Fennoscandia and Eurasia, the boreal forest is generally bounded by regions of Arctic tundra to the north and steppe and other temperate ecosystems to the south (Scheffer et al., 2012).

The treeless tundra landscape encompasses a range of dominant vegetation types including polar desert, tussock and shrub tundra, and wetlands (Elmendorf et al., 2012). In many areas there may be permafrost present, either continuous, discontinuous, or sporadic, depending on climate, landscape position, vegetation, and disturbance history, among other factors (Heijmans et al., 2022). The steppe comprises mostly shrublands and grasslands (Chytrý et al., 2019). Both tundra and steppe vegetation result from prevailing limiting climatic conditions: low temperature in the tundra and water-energy balance relations in the steppe (Chen et al., 2019, Miles et al., 2019).

The Arctic has warmed 2-4 times faster than the rest of the planet since the 1970s (Chylek et al., 2022, Rantanen et al., 2022), a phenomenon termed 'arctic amplification'. Consequently, boreal and tundra ecosystems are experiencing more frequent and higher intensity extreme weather events and disturbances, particularly wildfires (Callaghan et al., 2021, Descals et al., 2022, Scholten et al., 2022). Burned area from wildfires and the associated greenhouse gas emissions have also increased during this time period (Turetsky et al., 2011, Hanes et al., 2019). The huge extent of the Arctic-boreal zone means that any changes to the ecosystem, including those caused by increased emissions from methane, carbon dioxide and aerosols, plus changes to land surface albedo, will have a significant impact upon the magnitude of future global climate change (Randerson et al., 2006, Olsson, 2009, Oris et al., 2014, Potter et al., 2020, Phillips et al., 2022).

Fire has long been considered an integral part of the ecological process of boreal forests and remains the main disturbance today (Rowe and Scotter, 1973, Payette, 1992, Stocks et al., 2002, Baltzer et al., 2021). Fire allows for large-scale germination and regeneration of component species, which may lead to significant, potentially long-term, changes in forest biodiversity over time (Lavoie and Sirois, 1998, Shive et al., 2018). Further, post-fire recovery of the taiga has been shown to be affected by both flora type and fire severity (Johnstone et al., 2016, Sun et al., 2021, Alfaro-Sánchez et al., 2024). Recently intensifying fire regimes have been shown to have serious negative impacts through forest regeneration failure (Baltzer et al., 2021), and, at both regional and global scales, through the loss of native fauna, permafrost thaw, harm to human health and damage to infrastructure (Cascio, 2018, Kayes and Mallik, 2020, Li et al., 2021). Although the majority of wildfires globally are caused by human activities (Balch et al., 2017, Pausas and Keeley, 2021), at more northerly latitudes with a low human population density, the majority of burned area in tundra and in boreal forests is caused naturally by lightning strikes (Veraverbeke et al., 2017, Kharyutkina et al., 2022, Xu et al., 2022).

Despite being mostly devoid of forested areas, wildfires still occur in regions of tundra and steppe; including overwintering fires, which also occur in taiga (McCarty et al., 2020, Erdős et al., 2022). Overwintering fires are those which ignite then smoulder under the layer of peat and snow through the winter months, before re-emerging early the following spring (Irannezhad et al., 2020).

Different land cover types give rise to different fire regimes when wildfires occur. For example, the large number of spruce and jack pine trees in North America promotes high intensity crown fires, whereas fires in Siberia are more often low-moderate intensity surface fires, due to greater coverage of larch trees, whose needles have a high moisture content, and Scots pines, which shed their lower branches and have thick bark, as well as more extensive shrublands and grasslands (de Groot et al., 2013, Kharuk et al., 2021).

Wildfires in North America generally lead to high immediate tree mortality rates, with a considerable amount of debris falling to the ground, increasing the amount of fuel available to burn in future years (Angers et al., 2011). Surface fires in Siberia often cause extensive tree mortality that occurs over a series of years after the fire, with the changing climate, compounded by the timing of masting events in relation to time since fire, leading to delays in the regeneration of tree stands post-fire (Conard and Ivanova, 1997, Sun et al., 2021). Grass and shrubs often appear a few months after an area has been burned (Shvetsov et al., 2019, Shvetsov et al., 2023). Whether this is an initial stage of succession in a gradual return to forest dominance once again, or whether grasses and shrubs continue to prevail as a result of recruitment failure of tree species, is a key consideration as the climate warms and becomes drier (Sun et al., 2021).

Given the varied nature and significant impacts of wildfires across different ecosystems, satellite images are used to effectively detect and monitor global fire activity (Zhang et al., 2011a). Satellite images help determine the changing nature of our planet by identifying natural hazards such as landslides and floods, as well as forest fires (e.g. Ulbricht and Heckendorff, 1998, Cheng et al., 2004, Skakun et al., 2014). Images from three main groups of sensors, those onboard Landsat satellites, the Advanced Very-High Resolution Radiometer (AVHRR), and the Moderate Resolution Imaging Spectroradiometer (MODIS), have been used, alongside others such as SPOT and Sentinel-2, in the development of burned area (BA) products.

Products depicting BA from fires are generally developed from a combination of satellite imagery and active fire, or ‘hotspot’, data, and derived land cover or vegetation maps. The hotspots are thermal anomalies, which can be caused by wildfires, smoke, agricultural fires, gas flares or volcanoes (Tang and Li, 2014). Each BA dataset is developed using differing algorithms at different spatial resolutions, which accounts for variations in the amount and location of BA, and scale and extent of the final product. The algorithms use various imagery input sources and consider different spectral indices. All, however, have to cope with the presence of clouds, which can complicate the process by obscuring the land for days, if not weeks, at a time and can be easily confused with smoke from fires (Dao et al., 2016, Roteta et al., 2021). Full information on production of each of the BA datasets is given in the Methodology section.

Given the large number of sensors and resulting BA products, with different spatial and temporal resolutions, assessing BA products is critical for understanding changing fire regimes in northern ecosystems. While comparisons of BA products have been conducted on regional scales across different biomes; none have done so for the Arctic-boreal region. A list of previous relevant literature is given in Table 3.1, with a more complete review provided in the Discussion.

Table 3.1. A list of previous relevant literature with associated study areas, products used, plus years of interest.

Title	Reference	Study area(s)	Products used	Year(s) of interest
Burned area mapping in Different Data Products for the Southwest of the Brazilian Amazon	Dutra et al. (2023)	Southwestern Brazilian Amazon	MCD64A1 (C6) GABAM GWIS MAPBIOMAS	2019
Performance of Three MODIS Fire Products (MCD45A1, MCD64A1, MCD14ML), and ESA Fire_CCI in a Mountainous Area of Northwest Yunnan, China, Characterized by Frequent Small Fires	Fornacca et al. (2017)	Northwest Yunnan, China	MCD45A1 (C5.1) MCD64A1 (C6) FireCCI41 MODIS active fires	2006 and 2009
Spatial and temporal intercomparison of four global burned area products	Humber et al. (2019)	Global	MCD45A1 (C5) MCD64A1 (C6) FireCCI41 Copernicus Burnt Area MODIS active fires	2005 to 2011
Intercomparison of Burned Area Products and Its Implication for Carbon Emission Estimations in the Amazon	Pessôa et al. (2020)	Brazilian Amazon	MCD64A1 (C6) FireCCI50 GABAM TREES	2015

A comparison of remotely-sensed and inventory datasets for burned area in Mediterranean Europe	Turco et al. (2019)	Mediterranean Europe	MCD64A1 (C6) FireCCI51 GFED4 GFED4s EFFIS	2001 to 2011
About Validation-Comparison of Burned Area Products	Valencia et al. (2020)	Northern Hemisphere Africa and South America	MCD45A1 (C5) MCD64A1 (C5) MCD64A1 (C6) FireCCI41 FireCCI50	2007 and 2008
How Well Does the 'Small Fire Boost' Methodology Used within the GFED4.1s Fire Emissions Database Represent the Timing, Location and Magnitude of Agricultural Burning?	Zhang et al. (2018)	Eastern China and Northwest India	MCD64A1 (C6) GFED4 GFED4s MODIS active fires VIIRS active fires	2015 to 2016 (Eastern China) 2016 (Northwest India)

Here we use 12 different BA datasets and MODIS active fire data to determine the total yearly BA and seasonal patterns of fires in Arctic-boreal North America, central/northern Siberia and southern Siberia for the years 2001-2020. Based on this analysis, we also consider the advantages and limitations of each dataset.

Methodology

Study areas

Our study is focused upon three broad regions, one in North America and two in Russia, and is partly constrained by the data products we compare. In North America, the analysis was conducted over the entire boreal and tundra biomes in Alaska and Canada as defined by Dinerstein et al. (2017). Whereas in Russia eight terrestrial ecoregions within the boreal and tundra biomes in the Siberian and Far Eastern Federal Districts were used, *sensu* Talucci et al. (2022). Hereafter these regions are referred to as North America and central/northern Siberia, respectively. The eight ecoregions comprising central/northern Siberia are the Bering tundra, Cherskii-Kolyma Mountain tundra, Chukchi Peninsula tundra, East Siberian taiga, Northeast Siberian coastal tundra, Northeast Siberian taiga, Taimyr-Central Siberian tundra and Trans-Baikal Bald Mountain tundra (see Talucci et al. (2022) and their Figure 1). This area spans *ca.* 7.75 million km^2 from *ca.* 50-78° N and 79° E-169° W; whereas the North America area spans *ca.* 8.86 million km^2 from *ca.* 46-83.5° N and 172.5° E-52.5° W.

A second region was defined in Russia to investigate the performance of the global BA datasets in southern Siberia, which has a somewhat distinct fire regime when compared to central/northern Siberia (Soja et al., 2004b, Rogers et al., 2015). This latter region's northern boundary is the Southern Eurasia border with Northwest and Northeast Eurasia as defined by Rogers et al. (2015) and Rogers et al. (2017) but, where necessary, the southern boundary of the central/northern Siberia region is used to avoid overlap. Its western boundary is the border of the Urals Federal District, and the southern boundary follows Russia's geographic borders with Kazakhstan, China, Mongolia and the Democratic People's Republic of Korea to the eastern boundary at the Pacific Ocean. This region, spanning *ca.* 2.70 million km^2 from *ca.* 43-60° N and 57-138° E, is shown alongside the other two study regions in Figure 3.1.

Figure 3.1. Map of study regions – North America (red), central/northern Siberia (blue), and southern Siberia (purple). The internal borders of each ecoregion in North America and central/northern Siberia are visible.

Black spruce (*Picea mariana*) and jack pine (*Pinus banksiana*) are the two most dominant tree species that burn across North America (Brassard and Chen, 2006, Rogers et al., 2015). The former is located across both Alaska and Canada, whereas the latter exists only in boreal Canada. Water bodies and permanent wetlands are prominent across the region, especially in areas of Arctic tundra, comprising approximately 24 % of the total area (Friedl and Sulla-Menashe, 2022). Other major tree species across North America include various poplars (*Populus spp.*), balsam fir (*Abies balsamea* – Canada only), quaking or trembling aspen (*Populus tremuloides*) and white spruce (*Picea glauca*) (Hart and Chen, 2006).

In contrast to North America, larch (*Larix spp.*) is the dominant tree species in central/northern Siberia, with three species of pine (Siberian dwarf (*Pinus pumila*), Siberian (*Pinus sibirica*) and Scots (*Pinus sylvestris*)), plus birch (*Betula spp.*) constituting most of the remainder (Kharuk et al., 2021). The majority of fires (*ca.* 82 %) occur in larch and Scots pine forests (Rogers et al., 2015). Larch tree cover spreads from the Yenisey river (the region's western border at ~90° E) through the central part of Siberia to the far north-east of the country to *ca.* 165° E. Siberian dwarf is the most common species of pine and is most prevalent in the eastern half of the region. Birch trees are found interspersed between areas of larch at mid and low latitudes. Scots pine is located at lower latitudes across the whole region, whereas there are two clusters of Siberian pines, in the south and south-west sections of the region, respectively. As with North America, there is an absence of trees in the tundra at the northern part of central/northern Siberia, although a large percentage of the region (*ca.* 40 %) is classified as open shrublands according to a global land cover product (Friedl and Sulla-Menashe, 2022).

Southern Siberia is the study region with the highest proportion of grasslands, known as steppe (19 % of the total area), and mixed forests (29 %) (Friedl and Sulla-Menashe, 2022). Here there is no single dominant tree species, although there are several distinct regions of mixed forests. Birch, Scots pine, Siberian pine and larch can be found throughout the whole region, with significant groups of Eurasian aspen (*Populus tremula*) in the west, and fir (*Abies spp.*) in the centre (Kharuk et al., 2021). Vast areas of steppe are located between the forests throughout the entire southern Siberia region.

Datasets

Twelve BA products of varying spatial and temporal resolutions, types and extents were included in the analysis, along with MODIS active fires. A list of the products used can be found in Table 3.2, followed by summaries of the methodologies of each dataset. One method which appears frequently is the differenced Normalised Burn Ratio (dNBR), which is the change between the pre- and post-fire Normalised Burn Ratio (NBR). NBR is calculated using the Near Infrared (NIR) and Short-Wave Infrared (SWIR) bands from satellite images using Equation 3.1.

$$NBR = \frac{NIR - SWIR}{NIR + SWIR} \tag{3.1}$$

Table 3.2. Information about the BA datasets used in this study.

Long name	Short name	Reference(s)	Years	Temporal resolution	Spatial resolution	Product type	Extent	Main production methods
ESA Fire Climate Change Initiative: MODIS Fire_cci Burned Area Pixel product, Version 5.1	FireCCI51	Lizundia-Loiola et al. (2020) https://doi.org/10.5285/58f00d8814064b79a0c49662ad3af537	2001-2022	Monthly	250 m 0.25°	Pixel Grid	Global	MODIS imagery: min. NIR value around fire found. Hotspot seeds generated and grown.
Collection 6 MCD64A1 MODIS Burned Area Monthly Global 500m	MCD64A1	Giglio et al. (2018) https://doi.org/10.5067/MODIS/MCD64A1.061	2001-present	Monthly	500 m	Pixel	Global	MODIS imagery: max. VI values around fire found. Probabilistic thresholds determined to classify fires and surrounding cells.
30 m Resolution Global Annual Burned Area Maps	GABAM	Long et al. (2019) https://doi.org/10.7910/DVN/3CTMKP	1985-2021	Annual	30 m	Pixel	Global	Landsat imagery: 6 image bands and 8 spectral indices used. Random forest model, thresholds and iterative procedures used to grow fires.
Global Fire Emissions Database, Version 4.1 with small fires	GFED4s	Giglio et al. (2013) van der Werf et al. (2017) https://doi.org/10.3334/ORNLDAAC/1293	1997-2016	Monthly	0.25°	Grid	Global	Derived from MCD64A1 (C5.1) and combined with MODIS active fire data. dNBR used.
Global Fire Emissions Database, Version 5	GFED5	Chen et al. (2023) https://doi.org/10.5281/zenodo.7668424	1997-2020	Monthly	1° (1997-2000) 0.25° (2001-2020)	Grid	Global	Derived from MCD64A1 (C6) and combined with MODIS active fire data. Corrective scalars used to make adjustments.

ESA Fire Climate Change Initiative: AVHRR-LTDR Burned Area Pixel product, version 1.1	FireCCILT11	Otón et al. (2021) https://dx.doi.org/10.5285/b1bd715112ca43ab948226d11d72b85e	1982-2018 (excluding 1994)	Monthly	0.05° 0.25°	Pixel Grid	Global	AVHRR imagery. Random forest models and thresholds used alongside the LTDR burned index.
Monitoring Trends in Burn Severity	MTBS	Eidenshink et al. (2007) https://mtbs.gov/direct-download	1984-present	Annual	30 m	Polygon	United States of America	Landsat imagery: dNBR calculated and perimeters delineated.
Canadian National Fire Database National Burned Area Composite	NBAC	Hall et al. (2020) Skakun et al. (2022) https://cwfis.cfs.nrcan.gc.ca/datamart/download/nbac	1986-present	Annual	30 m	Polygon	Canada	Landsat imagery: NDVI and dNBR used alongside MODIS active fire data.
NASA Arctic–Boreal Vulnerability Experiment Fire Emissions Database	ABoVE-FED	Potter et al. (2023) https://doi.org/10.3334/ORNLDAAC/2063	2001-2020	Annual	500 m	Pixel	Alaska and Canada	Landsat imagery: dNBR used alongside MODIS active fire data.
Surface Reflectance Burned Area product	SRBA	Bartalev et al. (2012)	2006-2020	Annual	250 m	Pixel	Russian Federation	MODIS imagery: dNBR used with thresholds and MODIS active fire data.
Fire perimeter product	Talucci et al.	Talucci et al. (2022) https://arcticdata.io/catalog/view/doi%3A10.18739%2FA2GB1XJ4M	2001-2020	Annual	30 m	Polygon	Siberia	Landsat imagery: dNBR used alongside MODIS active fire data.
Arctic Boreal Burned Area Dataset	ABBA	Loboda et al. (2024) https://doi.org/10.3334/ORNLDAAC/2328	2002-2022	Annual	500 m	Pixel	Boreal and tundra biomes	MODIS imagery: dNBR used alongside MODIS active fire data.
MODIS MOD14A1 (Terra) and MYD14A1 (Aqua) Active Fire Data Products Version 6.1	MODIS active fires	Giglio et al. (2016) https://doi.org/10.5067/MODIS/MOD14A1.061 https://doi.org/10.5067/MODIS/MYD14A1.061	2000-present (MOD14A1) 2002-present (MYD14A1)	Daily	1000 m	Pixel	Global	MODIS imagery: thresholds used and rejection tests conducted.

FireCCI51

FireCCI51 (Lizundia-Loiola et al., 2020), developed by the European Space Agency (ESA) as part of their Climate Change Initiative programme, replaces two previous products: FireCCI41 (2005-2011: Chuvieco et al., 2016) and FireCCI50 (2001-2016: Chuvieco et al., 2018). The product uses data from four different input sources to generate BA information. The Red and NIR bands were taken from the MODIS Terra MOD09GQ (Collection 6) product (Vermote et al., 2011) at 250 m spatial resolution, with additional pixel state data from the Terra MOD09GA product (1 km). The 1 km MODIS Global Monthly Fire Location Product, MCD14ML (collection 6) was used to extract active fire (hotspot) information. Finally, the 300 m Land Cover CCI v2.0.7 product (ESA, 2017) was used to generate a burnable mask for each year, which was created by removing urban and bare areas, water bodies and permanent snow and ice classes. Subsequently, monthly image composites were made from cloudless and cloud shadow-less images, based on the date of hotspot detection and the minimum NIR value. The minimum NIR was taken as the lowest value within a 10-day window pre- and post-fire, with up to 15 post-fire days included if less than four valid observations were obtained. Hotspot spatial clusters were then generated, with a radius of influence of 1875 m (1500 m buffer with 375 m to account for potential geolocation issues), and a temporal threshold of 4 days. These clusters formed the basis of the seed phase, where only pixels with a high probability of being burned were selected. A growing phase was then carried out on these pixels under certain threshold conditions. Finally patch filtering was conducted to reduce commission errors caused by excessive growing and remove noise before the final product was created. FireCCI51 reports a commission error (false positives included) of 54.4 % and an omission error (false negatives included) of 67.1 % for the years 2003-2014.

The FireCCI51 product is available at two spatial resolutions projected over the WGS84 reference ellipsoid: pixel (250 m spatial resolution) and grid (0.25°), with monthly global BA data from 2001 to 2022. The grid product is formed by summing the number of burned 250 m pixels within each 0.25° grid. For this analysis we chose to use the pixel product, as the day of burn and a confidence score are also given for each pixel in separate bands. We initially considered all pixels with a 50 % or greater confidence of being burned, however, after preliminary analysis, this was subsequently increased to greater than or equal to 80 % (Figure C3.1; p.116) to reduce the likelihood of commission errors. The value of 80 % was chosen to align with the upper confidence bound of the MODIS active fires.

MCD64A1

The Collection 6 (C6) MCD64A1 product (Giglio et al., 2018) is the third 500 m BA product released by NASA, following the Collection 5.1 (C5) MCD45A1 and MCD64A1 products. MCD64A1 takes advantage of the C6 suite of MODIS products, including bands 1, 5 and 7 from the Terra/Aqua 500 m atmospherically corrected Level 2G daily surface reflectance products (MOD09GHK/MYD09GHK, respectively - Vermote et al., 2002), 1 km Terra/Aqua level-3 daily active fire products replicated to 500 m resolution (MOD14A1/MYD14A1 - Justice et al., 2002a), and the 500 m Level-3 annual land cover product MCD12Q1 (Friedl et al., 2010). First, the surface reflectance time series values were extracted such that the observations were cloud-free, fire-free, over land and had physically valid reflectance. If multiple values for each day were available, then the observation sensed at the smallest view zenith angle was chosen. Grid cells having too few valid observations to fill the pre- and post-burn windows were labelled as unclassified and so ignored. Subsequently, active fire composite imagery was produced based on the maximum separability of pre- and post-fire burn-sensitive vegetation index (VI) values over sliding 8-day pre- and post-fire windows. Several burned and unburned grid cells were then selected to be used as part of the model training process to estimate probabilistic thresholds suitable for classifying individual 500 m grid cells as either burned or unburned. The probabilities for each cell of being burned prior to or after a fire event were estimated, given the observed change in VI, before being classified subject to the previously determined thresholds and labelled. MCD64A1 reports a commission error of 24 % and an omission error of 37 %.

The C6 MCD64A1 monthly BA product is available globally from 2001 to present at a 500 m resolution on the MODIS sinusoidal projection, with the approximate day of burn given for each pixel. A second “Uncertainty” band was added which indicates the uncertainty of the burn date (± number of days), however this was not used in this analysis.

GABAM

The Global Annual Burned Area Maps product (GABAM - Long et al., 2019) used 6 bands (Blue, Green, Red, NIR and two SWIR bands) across all available Landsat 8 Surface Reflectance Tier 1 and Tier 2 collections as its core data source. Pixels masked by clouds, cloud shadows, water, snow, ice, or filled/dropped pixels were excluded, leaving only clear land pixels. Land cover information was extracted from the MODIS MCD12C1 product (Friedl and Sulla-Menashe, 2015), from which 7 land cover categories were ultimately considered. The BA density of the GFED4 product (Giglio et al., 2013) was used to create five equal-frequency fire intervals with quantile classification. Training and validation sites were subsequently chosen by stratified random sampling with a 3:2 ratio. Alongside the surface reflectance of the 6 bands, 8 spectral indices (2 NBR indices, Burned Area Index, Mid-Infrared Burn Index, Normalized Difference Vegetation Index (NDVI), Global Environmental Monitoring Index, Soil-Adjusted Vegetation Index and Normalized Difference Moisture Index) were also derived to perform the global BA mapping. A random forest (RF) algorithm was used to train a decision forest classifier based on the aforementioned input features. The outputs of the RF algorithm were used alongside NDVI and dNBR thresholds developed from imagery of the current and previous year to select seeds to be used as the starting point for growing each fire. Finally, an iterative procedure around each seed pixel was used to grow each fire based on the burned probabilities of the eight neighbouring pixels being greater than or equal to 0.5 to give the final BA product. GABAM reports a commission error of 13.2 % and an omission error of 30.1 %.

Note the methodology for the GABAM publication is given specifically for the year 2015. The collection of Landsat 8 images was used as its principle data source, however Landsat 8 was only launched in February 2013, whereas the GABAM product covers the entire 1985-2021 period on an annual temporal resolution. Landsat 5 and Landsat 7 images were used prior to 2013 to ensure a consistent 30 m BA product, however there is no mention of this in the paper, nor if the authors corrected for the Landsat 7 Scan Line Corrector failure in May 2003.

GFED4s

The Global Fire Emissions Database version 4.1 with small fires (GFED4s) is an extension of the original GFED4 product (Giglio et al., 2013), with the additional "s" signifying "small fires". Both GFED4 and GFED4s also give information about carbon emissions from fires alongside BA (van der Werf et al., 2017). The methodology to identify small (sub 500 m) fires was first given in Randerson et al. (2012). GFED4s begins in 1997 and ends in 2016, therefore two different methodologies were used depending on whether MODIS data were available (August 2000 onwards) or not. During the MODIS era, the 500 m MCD64A1 Collection 5.1 product, aggregated to a 0.25° grid, was used as a baseline. This product was then combined with 1 km MODIS Terra/Aqua thermal anomaly data and 500 m surface reflectance observations to estimate additional BA associated with small fires in each grid cell. The MODIS fire location product MCD14ML was additionally used to improve geolocation accuracies, and only detections with small or moderate scan angles were retained to reduce uncertainties in the geolocation. dNBR was then estimated for those active fire detections for which all four overlapping pixels were also classed as burned. Note that the Aqua satellite only came online in January 2003, so for the period August 2000-December 2002 a climatological ratio was used to estimate the small fires alongside data from Terra. In the pre-MODIS era (January 1997-July 2000) active fire data were extracted from either the Visible and Infrared Scanner (VIRS) and the Along Track Scanning Radiometers (ATSR) to estimate BA. VIRS only came online in January 1998 so for the first year only ATSR data were used. A relationship was developed between aggregated active fires in the pre-MODIS era and the BA during the MODIS era using linear regression models, before the aggregated BA was distributed to individual 0.25° grid cells. The final GFED4s BA product is global with a monthly temporal resolution and 0.25° spatial resolution.

GFED5

GFED5 (Chen et al., 2023) takes advantage of the availability of high spatial resolution satellite data from Landsat (30 m) and Sentinel-2 (20 m), as well as the updated Collection 6 MODIS suite, including the MCD64A1 BA product, 500 m MCD12Q1 land cover product (Sulla-Menashe and Friedl, 2018) and 250 m Terra and Aqua combined Vegetation Continuous Fields product MOD44B (DiMiceli et al., 2015). As with GFED4s, the Terra/Aqua MODIS active fire products were used from 2001, with ATSR/VIRS data again utilised in the pre-MODIS (1997-2000) era. MCD64A1 C6 was used as the core BA input during the MODIS era, with nine Landsat or Sentinel-2 datasets used for calibration and an additional eight for validation. To account for commission errors of unburned “islands” within MCD64A1 pixels, BA was multiplied by a correction scalar. Similarly, omission errors caused by the absence of small fires or incompletely mapped burned areas within MCD64A1 were accounted for by multiplying a second corrective scalar with the surface area of MODIS active fire detections outside the perimeter of the 500 m MCD64A1 pixels. These scalars were derived from the fine-resolution images and the MODIS BA and active fire data. Note that the BA for croplands, tropical peatlands and deforestations regions were calculated separately before being summed together with the normal land cover BA. The final GFED5 global BA product for 2001-2020 was produced at a 0.25° spatial resolution and monthly temporal resolution.

The methodology for the pre-MODIS era is similar to that of GFED4s, although the data are produced at 1°, as opposed to 0.25°, due to poor spatial variability of BA derived from the ATSR and VIRS active fires.

FireCCILT11

This product was derived by the ESA from the Land Long Term Data Record (LTDR), which provides a continuous dataset of AVHRR images that have been corrected both geometrically and radiometrically (Otón et al., 2021). The imagery was collected by the AVHRR 2/3 sensors aboard NOAA-7, 9, 11, 14, 16, 18 and 19 satellites before being stored at a reduced 4 km resolution. The LTDR resamples these data to 0.05° (approximately 5.5 km) and the Surface Reflectance Product of this dataset was used. Note that although the final product is provided from 1982 to 2018, the year 1994 was removed due to an absence of several dates in the LTDR dataset; 2019 and 2020 were also excluded as a result of poor quality LTDR data. Land cover data from the Copernicus Climate Change Service (Copernicus, 2019) and the ESA Climate Change Initiative (ESA, 2017) were used to create a burnable mask for each year from 1992, the same process as with FireCCI51. For the pre-1992 period, the land cover for the year 1992 was used. Monthly imagery compositing was employed to mitigate problems from daily image acquisitions and cloud-free images were removed. An LTDR burned index (LBI) was developed based on the input channels and derived bands. The bands considered were Red, NIR, medium infrared reflectance, brightness temperature for channels 3, 4 and 5, view and solar zenith angles, relative azimuth and a quality assessment layer. Two different random forest models, one global model and a second specifically for the boreal region, were developed to detect BA and trained using FireCCI51 for the years 2001-2018. The boreal model was developed as a result of poor estimations in boreal regions of the global model. The global model considered composites using the LBI 5-months pre-fire and 6-months post-fire, whereas the window for the boreal model was reduced to 3 months before and 4 months after fire occurrence. Detection thresholds were used to create binary burned/unburned pixels before an estimation of the total BA in each burned pixel was performed for both models. The final BA product was achieved by combining the global and boreal models into one unified product.

Both FireCCILT11 and FireCCI51 are produced by the ESA and as such share several formatting similarities. As with FireCCI51, FireCCILT11 is available as both a pixel (0.05°) and grid (0.25°) product, and the pixel dataset offers an uncertainty band. We again initially considered all pixels with a confidence of greater than or equal to 50 %, however this was subsequently decreased to 30 % or greater due to poor performance of the BA product (Figure C3.2; p. 116). The 30 % confidence value was chosen to align with the lower confidence bound of the MODIS active fires. For this analysis we used the pixel product as the approximate day of burn is provided for each pixel.

MTBS

The first region-specific and fire polygon-based product considered is Monitoring Trends in Burn Severity (MTBS - Eidenshink et al., 2007), covering the United States of America at a 30 m spatial resolution and generated annually from 1984 to present. Imagery from the Landsat 4, 5, 7 and 8 satellites was used as the core input, and Landsat 9 images will be considered from 2023. The NBR of pre- and post-fire images was calculated using the NIR and SWIR bands and dNBR was computed. The dNBR images were then used to determine the severity of each fire and to delineate the fire perimeters. This last step relied on the interpretation of several analysts using their past experience of fire behaviour and effects. The final perimeter product also includes the start date for each polygon.

NBAC

The National Burned Area Composite (NBAC - Hall et al., 2020) is compiled using three different BA products. The first is from the Canadian National Fire Database (CNFDB), where fire polygons are mapped annually by several fire management agencies. However, due to inter-annual variation caused by a lack of a unified mapping system, the NBAC considers these polygons only as potential sources which may or may not be used in the final product.

The second product is the Multi-Acquisition Fire Mapping System (MAFiMS), using atmospherically corrected Landsat 5, 7 and 8 pre- (1 year) and post-burn imagery. Pixels masked by cloud or covered by water were excluded, as were agricultural activities. The Red and NIR bands were used to calculate NDVI, which was compared before and after fire occurrence to define unburned regions. dNBR was then determined for each image to produce a threshold which identified regions of high vegetation change, where some pixels will likely have been burned. This high change layer was then converted to polygons, buffered at 1500 m, and filtered using MODIS hotspot data to create units which fully contain individual fire events. Active fire data were further used to determine the dates in which each event occurred to ensure they took place only in the year of interest. Finally, for quality control, each polygon was visually inspected and adjusted if necessary.

The third data source used to determine NBAC is the Hotspot and NDVI Differencing Synergy (HANDS) algorithm (Fraser et al., 2000), which provides polygons for large (> 250 ha) fires not reported either by the agencies or through using MAFiMS. The HANDS algorithm used 1 km SPOT VEGETATION imagery, which was replaced by Prova-V imagery resampled to 250 m in 2013. The algorithm used a normalised NIR-SWIR index based on pre- and post-burn imagery alongside active fire and land cover data. Burned pixels were then mapped based on given thresholds and were converted to polygons to be incorporated into NBAC. As coarse satellite images tend to overestimate the total BA (Fraser et al., 2004), a Theil-Sen regression (Fernandes and Leblanc, 2005) was used alongside area-based calibration models and spatial and temporal filters to generate statistically unbiased estimates of the BA from HANDS polygons.

The methodology described above was taken from Hall et al. (2020), referring to fires for the period 2004-2016. This was later extended in Skakun et al. (2022) to cover the years 1986-2020 and is summarised here. CNFDB polygons for the early period were obtained from the Canadian Wildland Fire Information System (Natural Resources Canada, 2022) using various methods including manual sketch mapping and aerial GPS, which are often far less accurate than Landsat derived polygons (Kolden and Weisberg, 2007). MAFiMS was extended in recent years using the same methodology but also incorporated Sentinel-2 satellite imagery. MAFiMS was extended back using a combination of AVHRR and MODIS active fire detections and Landsat collection 1 archive imagery. Finally, polygons from the HANDS algorithm could be developed back to the start of SPOT VEGETATION satellite data in 1995. A fourth product, the National Terrestrial Ecosystem Monitoring System Composite to Change (Hermosilla et al., 2016) was also integrated to better represent some fire events that were missed by MAFiMS.

The complete NBAC polygon product is continually updated annually at a 30 m spatial resolution across Canada. The ignition date of each fire polygon occurrence is also given. Note for this analysis the MTBS product for boreal/tundra Alaska is used alongside NBAC for boreal/tundra Canada to create a combined MTBS/NBAC polygon product.

ABoVE-FED

The Fire Emissions Database (FED) from NASA's Arctic Boreal Vulnerability Experiment (ABoVE) program contains BA information for the entirety of Alaska and Canada from 2001 to 2019 at a 500 m spatial resolution and annual timescale (Potter et al., 2023). Atmospherically corrected cloud-free Landsat 5, 7 and 8 30 m images were extracted and 1-year pre- and post-fire NBR values were calculated at field-based burned and unburned control sites to create a dNBR threshold. A 30 m resolution unburnable land cover mask for each year was created using the Joint Research Center's yearly water history product (Pekel et al., 2016) and the 2010 land cover product of the North American Land Change Monitoring System (Latifovic et al., 2012). A 30 m binary burned/unburned Landsat product was generated using the dNBR threshold and vegetation mask. The product was then upscaled to the MODIS 500 m resolution and projection, assigning the value of the percentage of burnable area within each 500 m pixel as the associated burn fraction when > 50% of the 30 m vegetated pixel were burned within it. This process took place when at least 85 % of the Landsat data were available, accounting for 81 % of the total burned pixels. For the remaining 19 %, the pixel was classified using a similar process derived from MODIS Terra (MOD09GA) and Aqua (MYD09GA) imagery. To account for fire detection issues arising from using imagery 1-year pre- and post-fire, a seasonal MODIS product was also developed with a 30-day pre- and post-fire window, masking out pixels with 10 or fewer valid observations in each window. The day of burn for each pixel was taken from MODIS active fire data where possible, with an interpolation approach or the MODIS seasonal BA product used where no active fire data were associated with a given polygon. ABoVE-FED reports a balanced commission/omission error of 6.6 % when using Landsat data and 14.2 % using MODIS data.

SRBA

The Surface Reflectance Burned Area product (SRBA - Bartalev et al., 2012) is derived from two MODIS products: MOD09 daily surface reflectance data and MOD14 active fires. Pre-processing was carried out at the MODIS 500 m spatial resolution before being resampled to 250 m. Pixels with a high view or solar zenith angle were first masked out, and then pixels contaminated by clouds were detected using threshold values from the Normalized Difference Snow Index, using the Blue and SWIR bands from the MOD09 product, and also masked out. NIR was analysed along the cloud-shadow line to correctly identify areas covered by cloud shadow, which were then removed. A moving monthly time window was used to filter out residual noise. dNBR was calculated based on daily composites from uncontaminated pixels, comparing the NBR in pre- and post-fire seasons. Note that although Bartalev et al. (2012) call this variable the Normalised Short-Wave Vegetation Index, the formula used is identical to NBR. Potentially burned pixels were identified using a dNBR threshold, and spatial filtering was used to remove pixels affected by non-fire disturbance factors. Finally, pixels were grouped together into polygons for each day by comparing fire events with MODIS active fire data.

SRBA is produced at a daily temporal resolution covering the entirety of the Russian Federation from 2006 to present. We were provided with access to SRBA data for longitudes from 60-180° E for the years 2006-2020. The data were given to us with an annual temporal resolution, so the day of burn for each pixel was not provided.

Talucci et al. fire perimeter product

The Talucci et al. (2022) fire perimeter product covers eight boreal and tundra ecosystems in Russia, as outlined in the Study areas subchapter. 30 m Landsat 5, 7 and 8 Surface Reflectance Tier 1 images during the growing season months (May to October) were chosen to ensure a high spatial resolution. Pixels covered by snow and clouds were masked, before annual composite images were generated using the best pixel approach (Hermosilla et al., 2015) to allow for missing data from snow- and cloud-cover, and the Landsat 7 scan line error. dNBR was calculated using one-year pre- and post-fire composites before each image was binary classified as either burned or unburned. MODIS active fire data were used to create polygons, before the fire perimeters were delineated, around the corresponding Landsat pixels and exported as shapefiles. The polygons were buffered at 1 km resolution to combine adjacent polygons before removing any holes and applying the reverse buffer. A smoothing and simplification function was then applied to reduce the pixelated appearance and the number of vertices of each polygon. MODIS active fires were again used to estimate the polygon start and end date and to eliminate perimeters with a 0 % confidence rating. Small fires (< 200 ha) were removed to match the criteria in the Canadian large fire database (Stocks et al., 2002) but low-confidence fires were retained as Siberian fires often burn at a lower intensity.

The final product was produced at a 30 m resolution from 2001 to 2020. When considering the seasonality of fires in our analysis we used the MinDay value (the given start date for each polygon). The difference between MinDay and AvgDay (the mean date in between the start and end dates) is shown in Figure C3.3 (p. 117).

ABBA

The Arctic Boreal Burned Area (ABBA - Loboda et al., 2024) dataset is provided at a 500 m resolution covering the boreal and tundra biomes on an annual timescale for the years 2002-2022 and is designed to capture fires occurring later in the season. Several MODIS products were used as inputs, including the C6 MCD14ML active fires (Giglio et al., 2016), C6 MOD09A1 Surface Reflectance (Vermote, 2015), C5 MOD44W land-water mask (Carroll et al., 2009) and the C5 MOD44B Vegetation Continuous Fields Collection (Hansen et al., 2003). 8-day surface reflectance composites from MOD09A1 were collected in the year of the fire alongside that of the previous year. Poor-quality pixels were masked out and dNBR grids were produced best on an 8-day pre- and post-fire window. Thresholds were then developed based upon vegetation indices to separate the dNBR grids into binary 'potentially burned' and 'unburned' categories, before being compared with the active fire data to eliminate any changes due to non-fire reasons. The resultant 8-day burn masks were used to create the final BA product.

MODIS Active Fires

Although MODIS active fires are used in this analysis, they should not be regarded as a substitute for a BA dataset, as the relationships between active fires and burned areas are not spatially or temporally constant (Giglio et al., 2006, Hantson et al., 2013). However, the active fire data can help bound BA estimates and are particularly useful for diagnosing seasonality. Here we use MOD in this summary to refer to both Terra (MOD) and Aqua (MYD) as the detection algorithm remains the same for both satellites. Note that we chose to use active fire data from MODIS rather than VIIRS – not to be confused with VIRS – as MODIS data are provided for the whole time period, whereas VIIRS was only launched in October 2011.

Several bands of different wavelengths from MOD021KM Swath Radiance and MOD03 Swath Geolocation data from the satellites were extracted, aggregated to a 1 km spatial resolution, checked and used as inputs into the algorithm. Coastal pixels were detected and removed from consideration and images obscured by clouds were also removed. Daytime fire pixels were tentatively identified using thresholds derived from the input data: however, the final identification for nighttime fire pixels was conducted at this stage. Further rejection tests were carried out for water and daytime land pixels based on more thresholds, and include sun glint rejection, desert boundary rejection, land-pixel coastal rejection, forest clearing rejection and water-pixel coastal rejection. Finally, each pixel which passed these tests was assigned a confidence rating. In our analysis we considered pixels with both a nominal (30-80 %) and high (> 80 %) confidence to include the low intensity fires in southern Siberia. Note there was a discontinuity in July 2002 when Aqua came online, substantially increasing the total BA. There were also major science data outages for both Terra (15 June-3 July 2001) due to a MODIS Characterization Support Team outage and Aqua (16 August-2 September 2020), caused by a Formatter-Multiplexer Unit/Solid State Recorder error.

Analysis techniques

Yearly BA

The total BA for each year during the MODIS era (2001-2020) was computed using the sum reducer (ee.Reducer.sum - Google, 2024b) in Google Earth Engine (GEE - Gorelick et al., 2017). The datasets were either uploaded as assets into GEE or imported directly from the Earth Engine Data Catalog. Each pixel-based product was uploaded as a collection of GeoTIFF images and therefore processed as an ee.ImageCollection, whereas each polygon-based product became an ee.FeatureCollection as the datasets were uploaded as shapefiles.

For those datasets where the whole pixel is designated as burned (FireCCI51, MCD64A1, GABAM, SRBA, ABBA, MODIS active fires), the burned pixels were given the value 1, with unburned pixels assigned 0. The sum reducer then summed all the pixels of value 1 in a given region, which was then multiplied by the area of the pixel to give the total BA in square metres (m^2), before being converted to Megahectares (Mha).

A similar technique was applied to those datasets which provide the burned fraction of each pixel (FireCCILT11, GFED4s, ABoVE-FED). Here the original value of each pixel was maintained before applying the sum reducer, multiplied by the area of the pixel and converted to Mha in each region.

The total BA in GFED5 was computed using a variation of this process: in the dataset each pixel was given the value of the BA in square kilometres (km^2), so the sum reducer was applied before being converted to Mha.

As the polygon-containing datasets (MTBS, NBAC, Talucci et al.) were uploaded as shapefiles to GEE, they were necessarily processed differently to the pixel-based products. The area of each polygon in m^2 was computed using the geometry.area function in GEE which was mapped over the whole region, before the total area was summed over each polygon using the sum reducer and subsequently converted to Mha.

This study used two methods to counteract the possibility of repeated fire events taking place in a single year. For pixel datasets where the approximate day of burn was provided (FireCCI51, MCD64A1, FireCCILT11 and ABoVE-FED), we assumed that each pixel could only be burned once in a given year, based upon the fire return intervals in the Arctic-boreal region (de Groot et al., 2013, Burrell et al., 2022). Alternatively, for GFED4s, GFED5 and MODIS active fires we conducted our analysis monthly to ensure that repeat events could occur on the same grid cells or pixels within a given year, and all would be accounted for. Polygon products and pixel datasets with an annual temporal resolution were not affected by repeat fire events.

Monthly fire percentage

The monthly proportion of each year's total fires (e.g. in 2004 around 45 % of the fires in North America occurred in July) was also computed in GEE using the unweighted frequency histogram reducer (ee.Reducer.frequencyHistogram.unweighted - Google, 2024a). This could only be computed where either the temporal resolution of the dataset was monthly or the Julian Day value was provided (Table 3.2).

For the pixel datasets with a daily temporal resolution (FireCCI51, MCD64A1, ABoVE-FED, FireCCILT11, MODIS active fires) along with Talucci et al., the first day in the year of fire occurrence detection, often referred to as the Julian day, was given as a number between 1 and 365 (366 for leap years). The unweighted frequency histogram reducer was then used to find the total number of pixels with the same Julian day, and subsequently the total daily BA, before grouping by month. The proportion of each month's fires was then calculated as a percentage relative to the whole year. The MTBS and NBAC data were processed similarly, although these had already been grouped by month, bypassing the first step.

For GFED4s, GFED5 and MODIS active fire data, the total BA was computed monthly, then divided by the yearly total to find the relative percentage.

When referring to seasonal patterns, we split the seasons as follows: winter (December, January, February), spring (March, April, May), summer (June, July, August) and autumn (September, October, November).

Results

North America

The BA for each dataset per year from 2001-2020 is given in Table C3.1 and depicted in Figure C3.4 (pp. 118-119). However, the analysis for North America focusses upon the years 2002-2016 in order to include all the datasets. The total BA for each dataset during the analysis period is given in Figure 3.2a, with the related box and whisker plots in Figure 3.2b. The largest fire year in North America during this period was 2004, with an average BA of 4.88 ± 0.89 (standard deviation (sd)) Mha across the products, with a mean BA across the datasets of 2.55 ± 1.24 Mha/year. On average, more area is burned in the second half of the time period, 2.81 ± 1.34 Mha/year for 2010-2016, than the first, 2.32 ± 1.19 Mha/year for 2002-2009, demonstrating an increasing tendency. 2004 was also the largest fire year over the entire 20-year period.

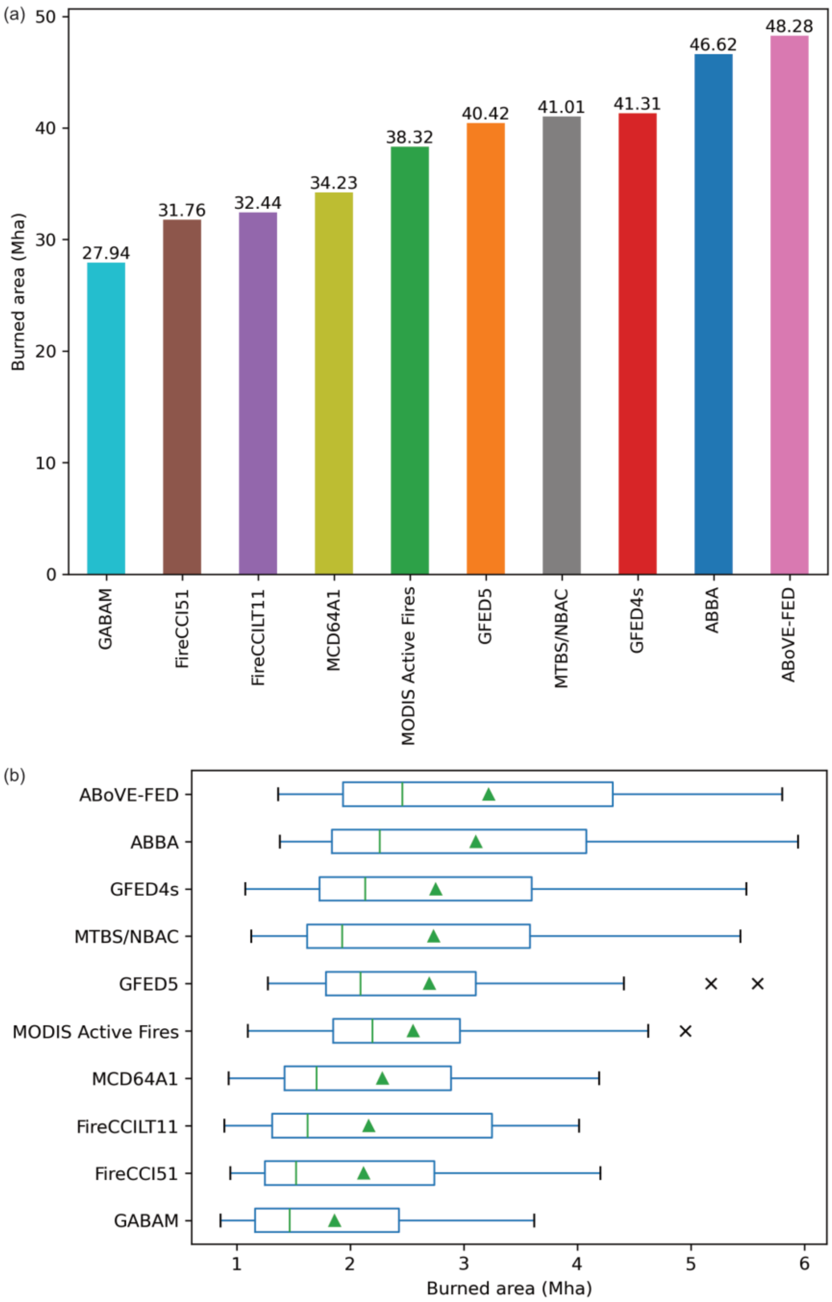

Figure 3.2. Total BA (a) and box and whisker plot (b) for each dataset for the analysis period (2002-2016) in North America. The whiskers extend to 1.5 x Interquartile Range (IQR). The mean of each dataset is given as the green triangle.

MODIS active fires are perhaps expected to produce the most amount of BA as the MODIS sensors detect all thermal anomalies, which can be related to non-wildfire activities such as cropland fires, partial burns or even increased haziness across satellite images (Liu et al., 2019, Yao et al., 2022). However, in North America this is not the case. MODIS active fires detect significantly less BA in Alaska and produce the greatest amount of BA in only 8 of the 20 years in Canada. Here most fires are high intensity, rapidly spreading crown fires, and as such MODIS sensors can miss burned pixels. MODIS active fires have also been known to struggle in this region due to fires occurring on cloudy days going undetected, underestimating the total number of fires by at least 18 % (Hawbaker et al., 2008).

Note that the datasets cannot be split into any statistically significant groups based upon average annual BA from 2002-2016 (Figure 3.2b and Table C3.2; p. 120), as described in Appendix B. GABAM is the product which shows the least amount of BA between 2002 and 2016, with a total BA of 27.9 Mha. Datasets with a high spatial resolution, such as GABAM, will often produce less BA than those with lower spatial resolutions, as they will more precisely identify the edges of fires and unburned "islands" within them. However, the combined MTBS/NBAC polygon product, also at 30 m resolution, contains 46.8 % more BA (Figure C3.5; p. 121), meaning that differences in total BA are also related to the different product methodologies. The two pixel datasets developed specifically for North America, ABBA and ABoVE-FED, show the highest amount of BA, 46.6 and 48.3 Mha, respectively.

In North America, six of the eight datasets where the day of burn was provided agree on the seasonal patterns of boreal fires for the period 2001-2016 (Figure 3.3), exhibiting a single peak in July with a three-month increase from April to July and a three-month decrease from July to October. All the datasets agree that the peak occurs in July, with *ca.* 41 % of all BA occurring during this month. With the exception of FireCCI51 and FireCCILT11, the datasets concur that June is the second biggest fire month, when an average of 33 % of the yearly BA occurs, followed by August with *ca.* 15 %. Among these datasets there is more variation in June (10.5 %) than August (4.4 %) due to the difference in methodology between the pixel and polygon-based datasets. The MTBS/NBAC combined datasets show a tendency towards earlier occurrence in June followed by a steeper drop in August as the Julian Day value is taken as the first day of fire occurrence in each polygon, whereas the pixel datasets track the constant progression of the fire on a pixel-by-pixel basis, with later Julian Day values as each fire spreads.

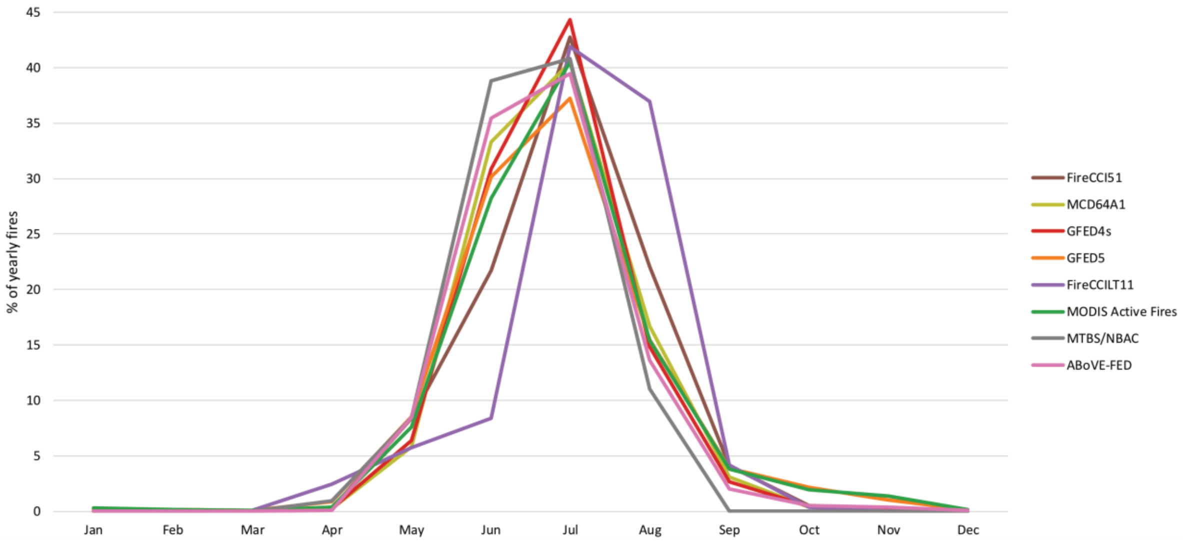

Figure 3.3. Seasonality of North American fires, 2001-2016.

For FireCCI51, the proportions of June/August fires are decreased/increased, respectively, with an almost identical percentage, *ca.* 22 %, of BA occurring in both early and late summer. The FireCCILT11 dataset agrees that most BA in this region is produced in July (42 %). However, the seasonal pattern otherwise differs significantly from the other datasets. FireCCILT11 shows that BA constantly increases by 2.5-3 % per month from March to June, before jumping to the July peak, a small drop to August (37 %), followed by a second, steeper drop down to 4 % in September, suggesting that BA is produced toward the end of summer rather than the start.

Central/northern Siberia

The analysis for central/northern Siberia spans 2006-2016 to include all datasets; however the results for the entire 2001-2020 period are given in Table C3.3 and shown in Figure C3.6 (pp. 122-123). The total BA for each dataset during the shorter analysis period is given in Figure 3.4a, with the related box and whisker plots in Figure 3.4b. Despite this study region having a smaller area than the North America region, an average of 4.04 ± 1.49 (sd) Mha/year burned in central/northern Siberia between 2006 and 2016, 58 % higher than North America. The largest fire year during this period was 2014, with a mean BA across the datasets of 5.92 ± 2.17 Mha: however, over the full 20-year period it only ranks as the fifth largest after 2003 (14.29 ± 5.31 Mha), 2020 (9.61 ± 4.00 Mha), 2019 (7.98 ± 3.19 Mha), and 2002 (7.44 ± 3.66 Mha). There is a large increase in the mean BA per year in the second half of the analysis period (2012-2016) compared to the first half (2006-2011), with fires increasing from 3.21 ± 1.29 Mha/year to

5.03 ± 1.10 Mha/year, and 4.39 ± 3.95 Mha/year to 5.64 ± 1.92 Mha/year for the 2001-2010 and 2011-2020 time periods, respectively.

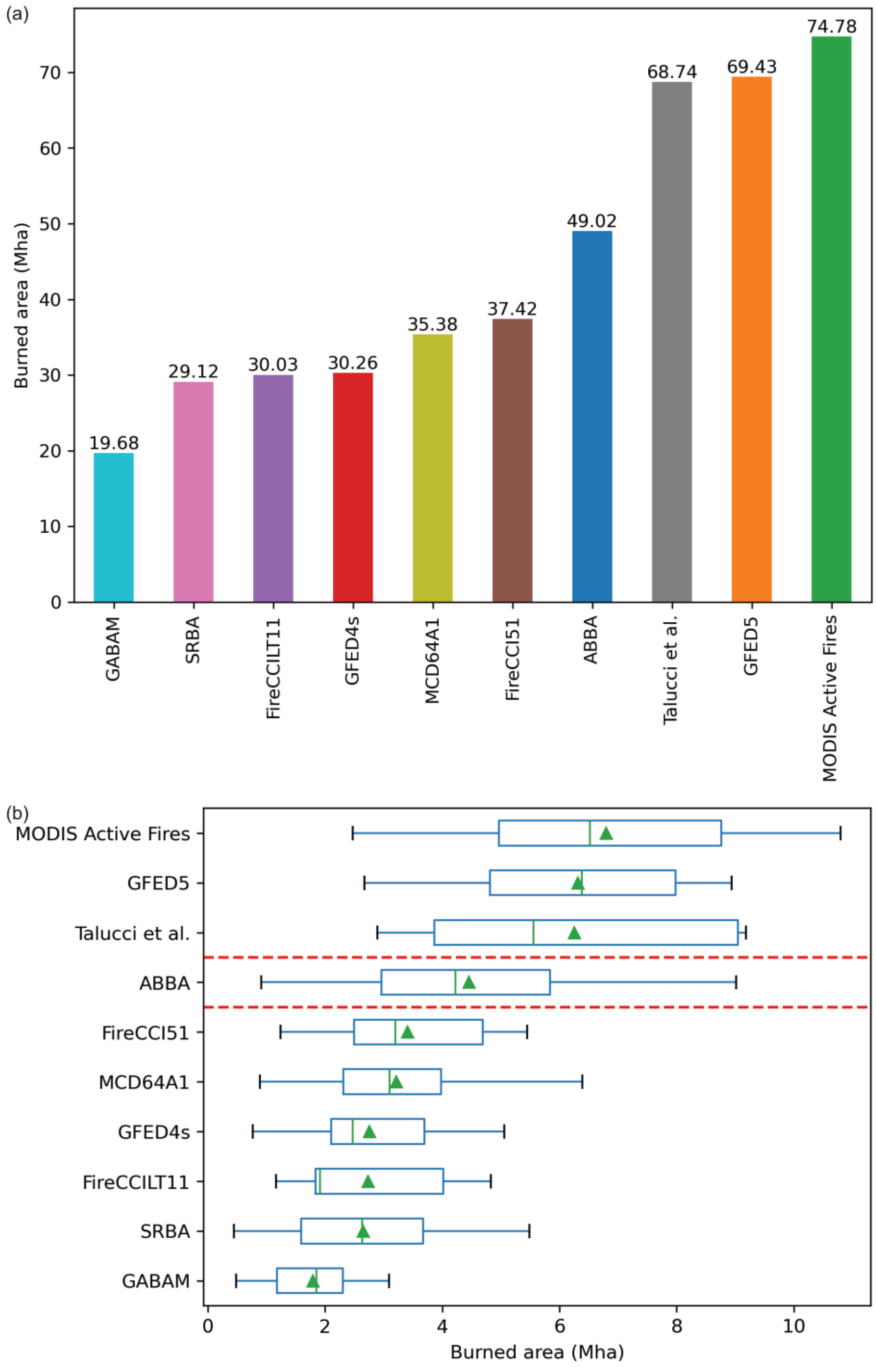

Figure 3.4. Total BA (a) and box and whisker plot (b) for each dataset for the analysis period (2006-2016) in central/northern Siberia. The whiskers extend to 1.5 x IQR. The mean of each dataset is given as the green triangle.

In central/northern Siberia there is considerably more disagreement between the datasets compared to North America (Figure C3.7; p. 123) and, unlike in North America, we cannot rely upon official statistics from government agencies, which have consistently been grossly underestimated (Conard and Ivanova, 1997, Flannigan et al., 2009, Nefedova, 2021). One primary reason for this is that boreal forest areas in the Siberian and Far Eastern Federal Districts, comprising 21.6 % of the total forest area in Russia, are classed as “remote unused forests” and are excluded from official statistics (Shvidenko et al., 2011, Shvidenko and Schepaschenko, 2013, Romanov et al., 2022).

We split the datasets into three distinct groups based on the computed BA statistical significance values (Figure 3.4b and Table C3.4; p. 124), as described in Appendix B. Once again GABAM is the dataset with the lowest amount of average annual BA; 1.79 ± 0.77 Mha/year from 2006 to 2016, whereas MODIS active fires shows the most amount of average BA in this period; 6.80 ± 2.58 Mha/year. The group with the most amount of BA (Talucci et al., GFED5 and MODIS active fires) has over 3.5 times more average annual BA than GABAM. However, large differences can occur between individual datasets each year. For example, in 2007 Talucci et al. has 12.5 times more BA than SRBA (5.56 Mha vs 0.44 Mha), and in 2012 ABBA has 11.8 times more BA than GFED4s (9.01 Mha vs 0.77 Mha).

Additionally, we also found significant issues with GABAM during the years 2001-2013. Pixels are often incorrectly identified as burned in the form of additional “stripes” and/or “boxes” (Figure 3.5a), or scan lines appear as missing patches through burned areas (Figure 3.5b). The stripes are a result of Landsat 7 ETM+ scan lines being mistaken as burnt patches, increasing commission errors (Chan et al., 2023). The Landsat 7 ETM+ Scan Line Corrector (SLC) failed permanently on May 31, 2003, causing all subsequent images to miss *ca.* 22 % of the normal scene area (Storey et al., 2005). However, we found that boxes can occur if the GABAM processing algorithm fails at the point of overlap between two or more Landsat 7 ETM+ images. While we found that these issues can occur all over the world, they are most prevalent in Siberia.

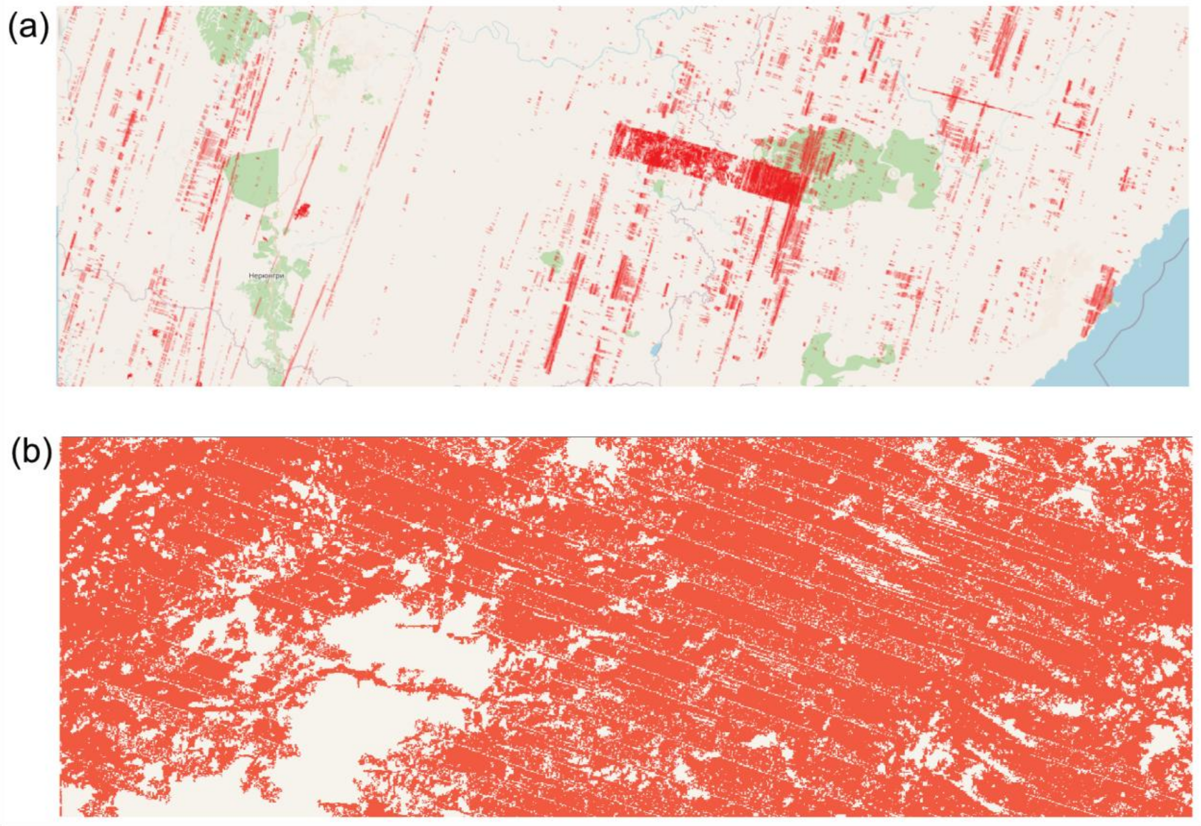

Figure 3.5. The “stripe” and “box” effects in GABAM shown in 2001 (a) and scan lines appearing as missing patches through burned areas in 2003 (b) in the central/northern Siberia region.

When considering the seasonal patterns over the 2001-2016 period, as shown in Figure 3.6, the datasets show further disagreement in central/northern Siberia compared to North America. GFED4s, GFED5 and MODIS active fires show a constant increase to an initial peak (*ca.* 16 %) in May, followed by a drop to 12.5 % in June, a second, larger peak ranging from 28 to 38 % in July, a steady decrease through August to *ca.* 5.5 % in September before dropping below 1.5 % in October.

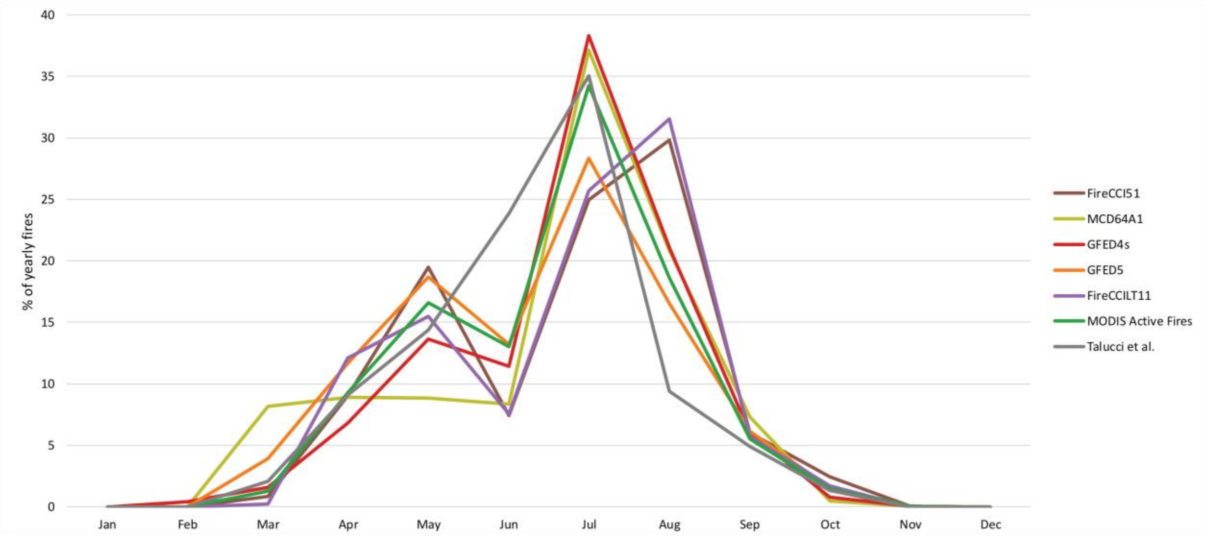

Figure 3.6. Seasonality of central/northern Siberian fires, 2001-2016.

FireCCI51 and FireCCILT11 display consistent seasonal tendencies with each other but, as in North America, show an inflated proportion of late summer BA compared to early summer. These products again have an initial small peak in May (*ca.* 17.5 %), however the main summer peak comes in August (*ca.* 30.7 %), rather than July (*ca.* 25.4 %), before dropping sharply to 5.8 % in September and decreasing to the end of the year.

MCD64A1 is anomalous for the pixel-based products in that it does not recognise an initial spring peak, with BA spread evenly between March and June; approximately 8.5 % of the yearly BA happens in each of the four months. This is then followed by a jump to the July peak at 37.1 %, before dropping through 20.8 % in August to 7.3 % in September and a negligible amount for the rest of the year.

The seasonality of the Talucci et al. polygon product can be compared to that of the MTBS/NBAC polygon product in North America, as it shows a tendency towards earlier fire occurrence as it does not take into account the spread of the fire between pixels, rather giving the date of the initial fire for the whole polygon. This can be somewhat improved by using the AvgDay value, which accounts for an increased proportion of late summer BA. However, both products show a single peak at approximately 35.4 % in July following a constantly increasing number of fires over the previous four months and preceding a rapid two-month drop.

Southern Siberia

For southern Siberia the analysis is limited to the six global BA datasets (FireCCI51, MCD64A1, GABAM, GFED4s, GFED5, FireCCILT11) and MODIS active fires for the years 2001-2016. The results for the whole 2001-2020 period are shown in Table C3.5 and visualised in Figure C3.8 (pp. 125-126). The total BA for each dataset during the analysis period is given in Figure 3.7a, with the related box and whisker plots in Figure 3.7b. Despite the total area covering only 35 % of the central/northern Siberia region and 30 % of the North America region, southern Siberia sees a mean BA of 11.2 ± 4.46 (sd) Mha/year from 2001-2016. 2003 and 2008 were the largest fire years with 18.88 ± 10.61 and 22.88 ± 10.28 Mha BA on average across the datasets, respectively. However, unlike in North America and central/northern Siberia, southern Siberia has seen a decreasing tendency in the amount of BA per year, falling from 11.9 ± 5.56 Mha/year in 2001-2008 to 8.5 ± 3.25 Mha/year in the second half of the analysis period.

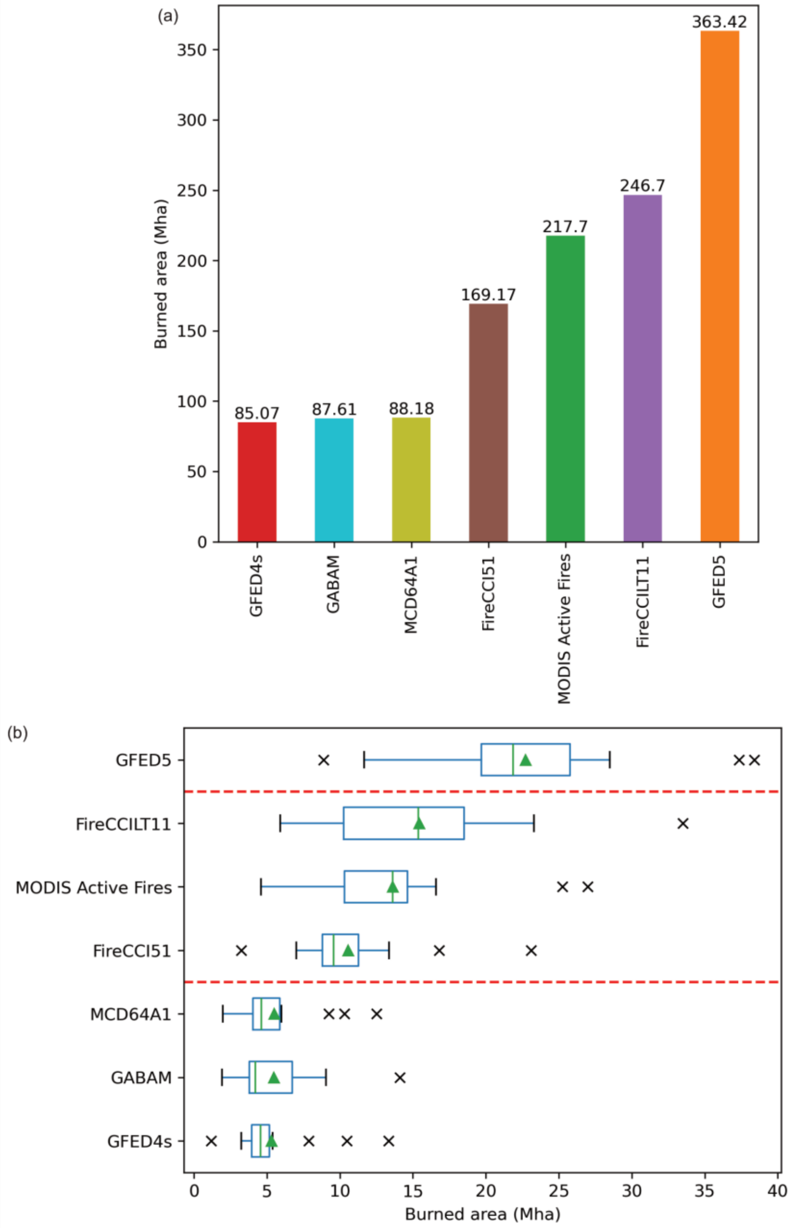

Figure 3.7. Total BA (a) and box and whisker plot (b) for each dataset for the analysis period (2001-2016) in southern Siberia. The whiskers extend to 1.5 x IQR. The mean of each dataset is given as the green triangle.

Furthermore, there are large disparities between the datasets, even greater than in central/northern Siberia, with GFED5 showing over four times more BA than GABAM and GFED4s (Figure C3.9; p. 126). These differences are further exacerbated during the smaller fire years; for instance, in 2002, 2004 and 2012 the BA in GFED5 is 530 %, 758 % and 837 % higher than GABAM, and 558 %, 452 % and 518 % higher than GFED4s, respectively. However, the largest difference between any dataset is in 2001, where GFED5 has over 10 times more BA than MCD64A1 (28.5 Mha vs 2.82 Mha).

In southern Siberia the datasets can be split into three groups based on the statistical significance (Figure 3.7b and Table C3.6; p. 127), as described in Appendix B. This time GFED4s produces the least amount of BA, 5.32 ± 2.94 Mha/year, whereas GFED5, with an average annual BA of 22.71 ± 7.91 Mha/year, produces more BA than all the others at a statistically significant level.

Four of the six datasets where the Julian Day was provided (FireCCI51, GFED4s, GFED5 and MODIS active fires) agree on the seasonality of fires in southern Siberia (Figure 3.8). There is a sharp increase in the amount of BA from March to April, with a similar amount of BA produced in April and May (*ca.* 35 % each), before a sharp decrease to June. Unlike in North America and central/northern Siberia, a far smaller proportion of BA occurs during the summer months, with *ca.* 6.2 % happening during June, July and August combined. There is then a second, smaller peak (*ca.* 11.7 %) in October. As in the other study regions, FireCCI51 shows a tendency towards later-occurring BA, however this is not as notable here. The dataset shows an increase from April to May, has the lowest amount of BA produced between June and September, before the largest peak in October (14.1 %). On the contrary, GFED5 shows that BA happens earlier in the season, showing a drop from 38.9 % in April to 33.5 % in May and the smallest peak in October (10.3 %).

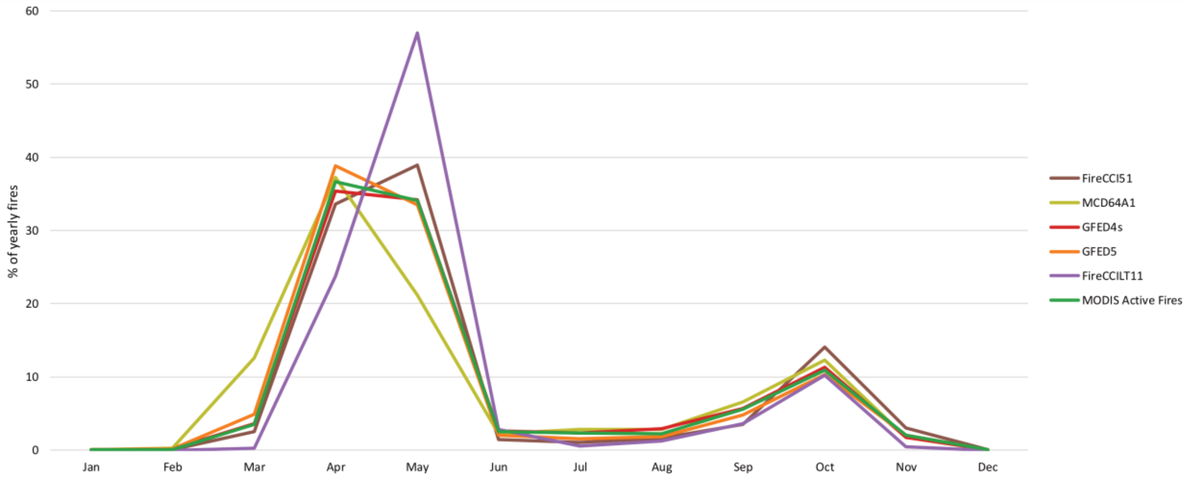

Figure 3.8. Seasonality of southern Siberian fires, 2001-2016.

MCD64A1 follows a more pronounced early-season BA occurrence tendency than the aforementioned datasets. Rather than a sudden increase/decrease between March and April/May and June, respectively, there is a single peak in April, with a greater proportion of

BA produced in March (12.6 %) and much less in May (21.2 %). The summer and autumn BA occurrence patterns are similar to those of the other products although, as in spring, autumn BA in MCD64A1 happens slightly earlier, with September having *ca.* 2 % more BA; however, this difference is relatively minor. Conversely, the seasonality of FireCCILT11 shows a heavily weighted tendency towards later spring BA. Here just 23.8 % of pixels are burned in April, with a substantial 57.0 % of pixels burning in May, before a large drop to 2.8 % in June and following similar tendencies to the other products to the end of the year.

Discussion

Seasonal patterns

Both North America and central/northern Siberia have broadly similar seasonal fire patterns, despite being composed of different tree types with distinct fire regimes. Both regions have their largest peak in July. However, while this is the only peak in North America, there is a second smaller, early-season peak in May in central/northern Siberia. This is likely due to the imperfect delineation between the two Siberia study regions, so the southern parts of central/northern Siberia are catching some of the spring fire regime from southern Siberia. The seasonality of fires in southern Siberia differs significantly from those in the more northerly study regions. The majority (*ca.* 70 %) of the BA here happens during April and May, with relatively few fires occurring during the summer months, before a second smaller peak (*ca.* 11 %) in October. Most precipitation in southern Siberia occurs during July and August (Sun et al., 2021), which accounts for why there are fewer fires in the summer months here. The grass and shrubs, which grow quickly during this regenerative period, produce the ground-level fuel for repeat, low-moderate intensity fires in the 20-year period.

Advantages and limitations of different methodologies

Compared to Siberia, the BA products show relatively good consistency in North America. This is partly since the official MTBS and NBAC databases are considered good representations of the total BA and can be used for validation, and partly because it is comparatively easier to detect BA from crown fires using remote sensing imagery due to the drastic change in pre- and post-fire canopy vegetation. In this regard, dNBR calculated from high resolution images from satellites such as Landsat can more precisely and successfully determine the extent of fires in North America, as with the MTBS and NBAC polygons and ABoVE-FED.

The products face significant challenges in determining the BA in both Siberian study regions, as the majority of fires are surface fires of low to moderate intensity (Rogers et al., 2015, Kharuk et al., 2021). The canopy can obscure these fires from satellite imagery, and the lower energy output means that they are more difficult to detect using thermal sensors (de Groot et al., 2013). In southern Siberia, the vast majority of the yearly fires occur during spring; these fires are often smaller in size but greater in quantity (Randerson et al., 2012). The steppe then regenerates quickly during the rainy summer months with grass and shrubs growing between the burnt tree stands (Shvetsov et al., 2023). As such, it is substantially more difficult for products using image composites at a low temporal resolution, such as annual, to determine where the fires took place, and this leads to large inconsistencies and variations between the datasets. The clearest example of these differences occurs in 2012: GFED4s has 0.77 Mha BA in central/northern Siberia and 3.49 Mha in southern Siberia, whereas GFED5 has 8.94 Mha and 21.58 Mha, respectively. Short-term composites of dNBR, such as with ABBA, again produce the most consistently strong results in Siberia, however without reliable official data we cannot determine with any certainty the most accurate product.

Products with a greater omission error than commission error, such as FireCCI51, MCD64A1 and GABAM, will underestimate the total BA, and this has been shown in our analysis. For pixels to be declared burnt using the GABAM algorithm, the stringent threshold tests, using the surface reflectance of 6 bands alongside 8 spectral indices, mean the total BA is likely to be a conservative estimate. ABoVE-FED was designed to roughly split omission and commission equally, so the amount of overestimated and underestimated BA is designed to be similar, thus producing a balanced total.

When considering which BA product to use, we suggest those with high spatial (≤ 250 m) and temporal (monthly) resolutions, and those which are made using short-term dNBR composites and include threshold tests. If applicable, products with roughly equal commission and omission errors and those which are designed for one particular region are also preferable. If there is concern over using a less reliable product, consider using another as validation.

Advantages and limitations of each BA product

Even though FireCCI51 was masked to only show fires of 80 % and greater confidence, it still performs well in the boreal regions, produces significantly more BA than MCD64A1 in southern Siberia and is more reliable than FireCCILT11. Its availability as both a global, relatively high spatial resolution, pixel and gridded product allows for greater flexibility than other, single-type products. FireCCI51 is used in training both GABAM and FireCCILT11, demonstrating that it is considered versatile and reliable. MCD64A1 is also deemed a reliable product as it is used as the baseline dataset for GFED4s (Collection 5) and GFED5 (Collection 6). However, both versions have known limitations in boreal regions: C5 MCD64A1 underestimates in boreal Russia as fires detected by the MODIS hotspot algorithm are often too small to class the entire pixel as burned (Roy et al., 2008). Due to the masking of small lakes at high latitudes in North America, the BA in this region is significantly underestimated in C6 (Giglio et al., 2018, Moreno-Ruiz et al., 2023), which is why GFED5 has less BA in North America than GFED4s.

Despite the higher spatial resolution, the errors due to Landsat 7 scan line failings in GABAM for the years 2001-2013, which are not accounted for in the dataset methodology (Long et al., 2019), are significant and users should be aware of its limitations in the study regions considered here for these years. The years 2014-2020 can be considered more reliable due to the introduction of Landsat 8 data from 2014 onwards, which supersedes data from Landsat 7.

It also appears that FireCCILT11 has significant limitations in representing Arctic-boreal fire regimes, with the relatively low confidence level (30 %) and spatial resolution (*ca.* 5.5 km) negatively affecting the output. This is most evident with the fire seasonality, where FireCCILT11 significantly differs from all the other datasets in North America and southern Siberia. FireCCILT11 is also the only product which uses AVHRR data. AVHRR sensors have been in operation since 1981, and as such are fairly limited and have been known to degrade over time, producing more unreliable imagery with reduced quality compared to images from more modern satellites (Nagol et al., 2009, Beck et al., 2011, Dech et al., 2021).

GFED5 shows a considerable improvement over GFED4s, and it performs well in both North America and central/northern Siberia, making it a reliable gridded product. However, when a dataset produces more BA than all the others at a statistically significant level, as with GFED5 in southern Siberia (Table C3.6; p. 127), caution should be taken.

Region-specific products are, in theory, optimised for the local fire and vegetation characteristics. In North America ABoVE-FED balances the omission and commission errors, and, by using the burnable fraction of a 500 m pixel derived from 30 m Landsat images, produces more accurate results than the comparable MCD64A1. ABBA performs similarly to ABoVE-FED, although ABoVE-FED provides data on the estimated day of burn for each pixel, whereas ABBA does not. The BA products in North America are compared to the official statistics from the 30 m MTBS and NBAC products, which are considered as reference BA.

In central/northern Siberia, however, we do not have a similar baseline from which we can compare the performance of all the products because of the absence of reliable official statistics. The Talucci et al. (2022) dataset is an excellent representation of fire perimeters in central/northern Siberia at a high spatial resolution. However, the product does not always take into account unburned patches within the polygons, so it may overestimate the total BA. In this region ABBA detects substantially more BA than most products, including the Russia-specific SRBA product, but less than GFED5, which, like Talucci et al. (2022), may overestimate BA. SRBA produces less BA than both the global FireCCI51 and MCD64A1 datasets in central/northern Siberia, suggesting that the total BA is likely to be underestimated.

Active fire data, from MODIS or otherwise, are used in different ways to create BA products, but should not be taken as a definitive account of BA as they tend to overestimate small fires, but underestimate larger fires (Roy et al., 2008, Zhang et al., 2011b). In our study, with fires of low (less than 30 %) confidence masked out, this is most notable in Alaska where the MODIS active fires vastly underestimate the total BA, especially in the large fire year of 2004, as also shown in Loboda et al. (2011). The MODIS hotspot data are best used to determine which BA products perform well when considering the seasonality, as the first thermal anomaly for each pixel is determined twice per day (once for each pass of the Terra and Aqua satellites), thus modelling the spread of fire well. Active fire products from VIIRS have been shown to perform better than those from MODIS (Schroeder et al., 2014, Oliva and Schroeder, 2015), however we did not include these due to the relatively short time series available.

Study limitations

This study took measures, as described in the methodology, where necessary to ensure that any re-occurrences of fire events within a single year were dealt with. Another limitation is that the Julian Day values for the polygon products are not directly comparable to the Julian Day values for the pixel products. The pixel products show the dynamic nature of each fire as different values are given for each pixel within the same fire event, based upon how the fire spreads. For the polygon products the Julian Day value is assigned for the entire polygon, meaning that the seasonality of the fires will be biased towards early season fires, as shown especially with the Talucci et al. fire perimeter product.

Comparisons with previous literature

For the whole of Alaska and Canada, Potter et al. (2023) stated that, compared to ABoVE-FED, MCD64A1 produces 23 % less BA (2001-2019) and GFED4s 18 % less (2001-2016). We found that for our North America region the reductions are very similar, at 29 % and 14 %, respectively. Similarly, Chen et al. (2023) claimed that globally GFED5 has 93 % more BA than MCD64A1 and 61 % more than GFED4s. In our study for the three regions combined, GFED5 has 180 % more BA than MCD64A1 (2001-2020) and 187 % more than GFED4s (2001-2016). Some global BA products can struggle in boreal regions due to the absence of a consistent fire regime; the influence of the dominant tree species shapes the regime for each region, which is not always taken into account (de Groot et al., 2013, Rogers et al., 2015). Note that both FireCCI51 and FireCCILT11 also report global comparison statistics (Lizundia-Loiola et al., 2020, Otón et al., 2021): however, these are not directly comparable with our results as we used higher confidence values.

As shown in Table 3.1, MCD64A1 is analysed with other products across several other studies, with either active fire data or high-resolution imagery used as validation. Zhang et al. (2018) looks at how GFED4, GFED4s and MCD64A1 (C6) compare with both MODIS active fire data and higher-resolution imagery from VIIRS, Landsat and Sentinel-2 in East China (2015-2016) and North-West India (2016 only) to determine which dataset best represents agricultural burning in these regions. Fires in China, specifically the mountainous area of Northwest Yunnan, are also the focus in Fornacca et al. (2017), which looks at MCD45A1 (C5.1), MCD64A1 (C6) and FireCCI41 alongside MODIS active fire data and Landsat reference imagery for two sample years (2006 and 2009) to determine which dataset performs best in representing small fires in this area of steep terrain. MCD64A1 (C6), GFED4 and GFED4s are also compared in Mediterranean Europe, this time with FireCCI51 and local data from the European Forest Fire Information System for the years 2001-2011 (Turco et al., 2019). 44 areas across Northern Hemisphere Africa and South America were used to validate the output from MCD45A1 (C5), MCD64A1 (C5 and C6) and FireCCI (4.1 and 5.0) for the years 2007-2008 in Valencia et al. (2020). Staying in South America, parts of the Brazilian Amazon biome have also been studied in Pessôa et al. (2020) and Dutra et al. (2023). The former considers the global MCD64A1 (C6), FireCCI50 and GABAM products against region-specific data from the Tropical Ecosystems and Environmental Sciences lab for fires during the summer and autumn months of 2015, whereas the latter compares MCD64A1 (C6) and GABAM against the Global Wildfire Information System (Boschetti et al., 2020) and the regional MapBiomas Fogo product (Alencar et al., 2022) for fires in 2019.

Humber et al. (2019) is the only study to use a similar methodology to the present work. However, the paper considers the total BA globally, split into several ecoregions as defined by Giglio et al. (2006) and van der Werf et al. (2006), for the years 2005-2011. MCD45A1 (C5), MCD64A1 (C6) and FireCCI41 are compared with MODIS active fires and also the Copernicus Burnt Area product. It is difficult to directly compare our results to those from previous works due to the use of different versions of datasets (e.g. FireCCI51 in this work vs FireCCI41 in Humber et al. (2019)) and the products perform differently in boreal forests compared to other regions.

Conclusion

To conclude, we conducted what we believe to be the first comprehensive analysis of 12 BA products alongside MODIS active fire data across North America, central/northern Siberia and southern Siberia. We found that there is relatively little variability between the datasets in North America both in terms of total BA and seasonality, whereas in both central/northern and southern Siberia there are large disparities between the products. These disparities occur due to the different methodologies used to determine BA, with dNBR of short-term composites from Landsat images used alongside hotspot data seemingly the most consistently successful. Differences between pixel, gridded and polygon products should be considered when choosing a BA dataset. We suggest that FireCCI51 and MCD64A1 are relatively reliable and consistent global pixel products, and GFED5 can be considered a reliable global gridded product. On the other hand, we stress caution using GABAM, especially for the years 2001-2013 in these regions. We also highlight ABoVE-FED and ABBA for use specifically in North America, and Talucci et al. in central/northern Siberia due to their detection of smaller fires which are often missed by global products. Future work could consider extending the analysis into the 2020s and including newly-developed datasets, such as FireCCIS311 (Lizundia-Loiola et al., 2022), which uses Sentinel-3 images alongside VIIRS active fire data. Furthermore, projections of future fire occurrence could be made under different climate change scenarios to determine the potential risks of fire to indigenous communities and the impact it could have in the wider Arctic-boreal zone.

Appendix A: Percentage difference

The percentage difference of the total BA between two datasets, as given in Figures C3.5, C3.7 and C3.9, is calculated using Equation A3.1.

$$\% \, diff = \frac{i - j}{j} * 100 \qquad (A3.1)$$

where *i* is the dataset on the *x*-axis, and *j* is the dataset on the *y*-axis.

Appendix B: Statistical significance

To test for statistical significance between datasets in order to sort them into different groups for analysis, Welch's t-test is used as homogeneous variance cannot be assumed. The test is conducted using the scipy.stats.ttest_ind function in Python, specifying equal_var=False, to find the associated *p*-value. Statistically significant results are those with *p*-values less than 0.05. The outputs from this test for each region are given in Tables C3.2, C3.4 and C3.6.

To conduct these tests by hand, the test statistic *t* is calculated using Equation B3.2, and the degrees of freedom value *df* is calculated using Equation B3.3.

$$t = \frac{\bar{x}_i - \bar{x}_j}{\sqrt{\frac{s_i^2}{n_i} + \frac{s_j^2}{n_j}}} \tag{B3.2}$$

$$df = \frac{\left(\frac{s_i^2}{n_i} + \frac{s_j^2}{n_j}\right)^2}{\frac{\left(\frac{s_i^2}{n_i}\right)^2}{n_i - 1} + \frac{\left(\frac{s_j^2}{n_j}\right)^2}{n_j - 1}} \tag{B3.3}$$

where $\bar{x}$ is the mean, *s* is the standard deviation, and *n* is the sample size for each pair of datasets i, j to be compared. *df* is rounded down to the nearest integer and the *p*-value is then found using statistical tables.

Appendix C: Supplementary material for Chapter 3

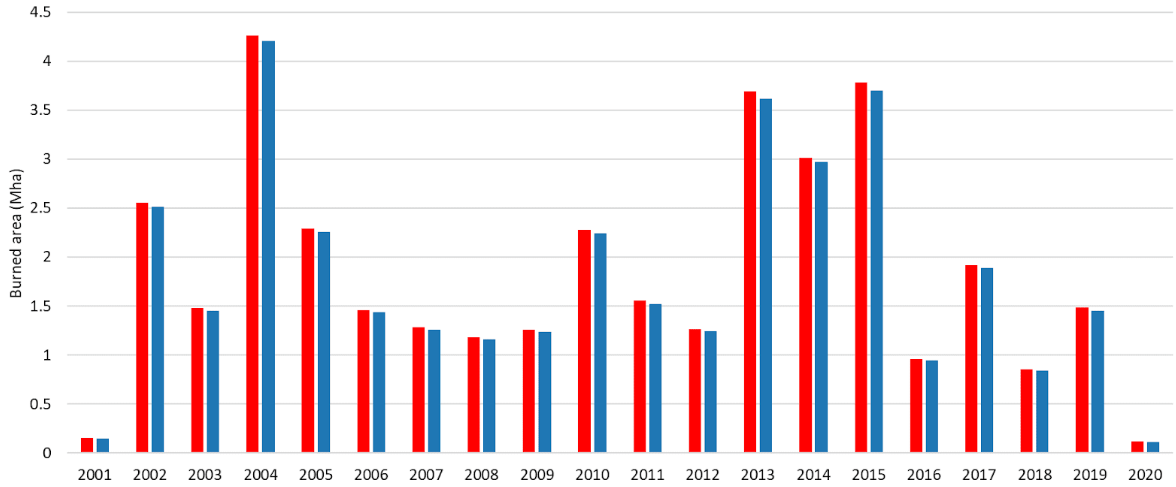

Figure C3.1. Total burned area from FireCCI51 at 50 % (red) and 80 % (blue) confidence in North America for the years 2001-2020.

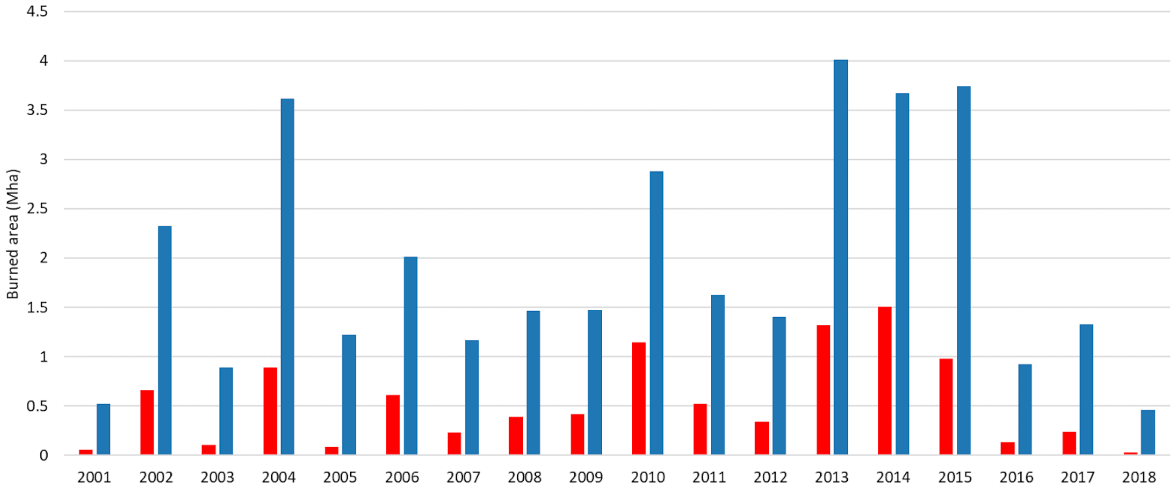

Figure C3.2. Total burned area from FireCCILT11 at 50 % (red) and 30 % (blue) confidence in North America for the years 2001-2018.

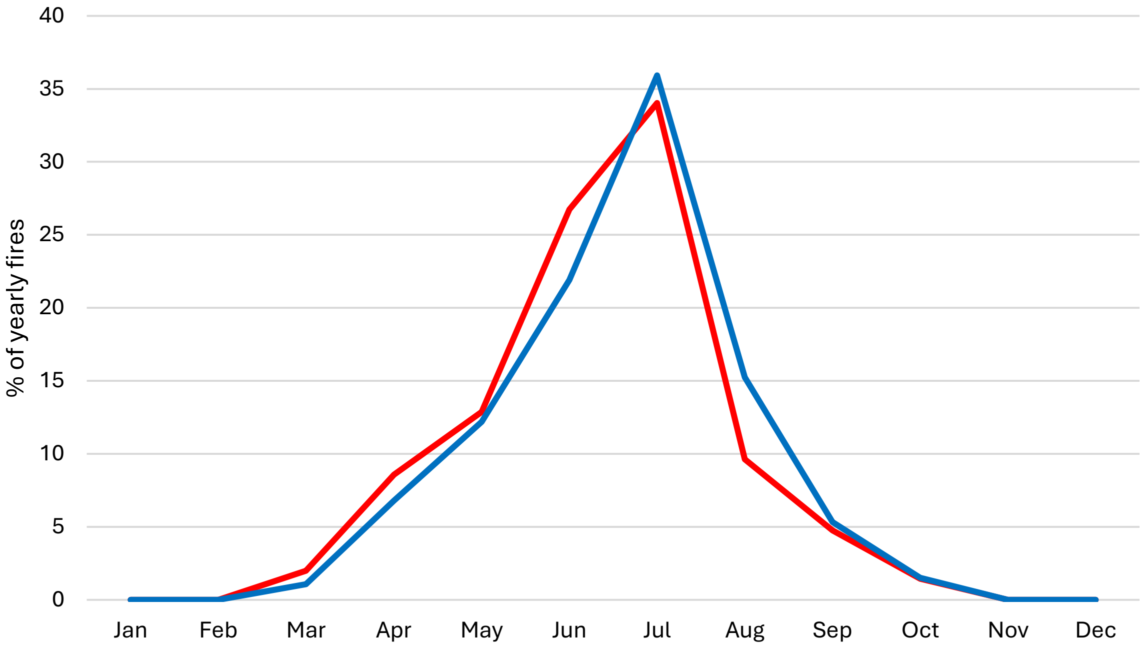

Figure C3.3. Talucci et al. MinDay (red) and AvgDay (blue) average seasonality in central/northern Siberia for the years 2001-2020.

Table C3.1. Yearly burned area (Mha) for North America for 2001-2020. N/A denotes an absence of data. The averages (avg) for each year (y) and dataset (d) are given, as are the relative standard deviations (SD). Avg (d) and SD (d) are calculated for the analysis period (2002-2016) only.

	FireCCI51	MCD64A1	GABAM	MTBS/NBAC	GFED4s	GFED5	ABoVE-FED	FireCCILT11	MODIS AF	ABBA	Avg (y)	SD (y)
2001	0.15	0.28	0.48	0.47	0.45	0.61	0.41	0.52	0.14	N/A	0.39	0.16
2002	2.51	2.91	2.45	3.36	3.42	2.71	4.12	2.33	2.13	3.48	2.94	0.63
2003	1.45	1.69	1.20	1.58	1.76	1.92	2.46	0.89	2.49	2.21	1.77	0.52
2004	4.20	4.19	3.62	5.44	5.49	5.59	5.81	3.62	4.95	5.85	4.88	0.89
2005	2.26	2.81	1.92	3.56	3.21	3.04	3.82	1.22	1.95	3.86	2.76	0.90
2006	1.44	1.70	1.37	1.75	1.84	1.89	2.25	2.01	1.96	2.07	1.83	0.27
2007	1.26	1.40	1.17	1.72	1.59	1.58	1.94	1.17	1.75	1.87	1.54	0.28
2008	1.16	1.32	1.00	1.40	1.51	1.46	1.77	1.46	1.37	1.65	1.41	0.22
2009	1.24	1.08	1.16	1.13	1.71	1.69	1.94	1.47	1.10	1.74	1.43	0.32
2010	2.24	2.24	2.08	2.84	2.75	2.54	3.44	2.88	2.53	3.27	2.68	0.45
2011	1.52	1.54	1.47	1.93	1.81	2.09	2.27	1.62	2.19	2.26	1.87	0.32
2012	1.25	1.44	0.89	1.66	2.13	1.88	1.87	1.41	2.21	1.80	1.65	0.41
2013	3.62	4.05	3.05	4.49	4.53	4.41	5.33	4.02	4.39	4.92	4.28	0.64
2014	2.97	2.86	2.41	3.60	3.78	3.18	4.50	3.67	3.40	4.30	3.47	0.64
2015	3.70	4.05	3.30	5.28	4.72	5.18	5.40	3.74	4.63	5.94	4.59	0.87
2016	0.94	0.93	0.86	1.28	1.08	1.27	1.37	0.93	1.26	1.38	1.13	0.20
2017	1.89	1.90	1.42	2.36	N/A	2.37	2.47	1.33	2.59	2.55	2.10	0.48
2018	0.84	0.95	0.78	1.21	N/A	1.30	1.36	0.46	1.42	1.30	1.07	0.33
2019	1.45	1.61	1.30	2.62	N/A	2.42	2.28	N/A	2.02	2.53	2.03	0.52
2020	0.12	0.12	0.11	0.12	N/A	0.38	0.13	N/A	0.33	0.20	0.19	0.11
Avg (d)	2.12	2.28	1.86	2.73	2.75	2.69	3.22	2.16	2.55	3.11	2.55	0.44
SD (d)	1.06	1.13	0.92	1.47	1.37	1.36	1.51	1.13	1.23	1.55	1.24	X

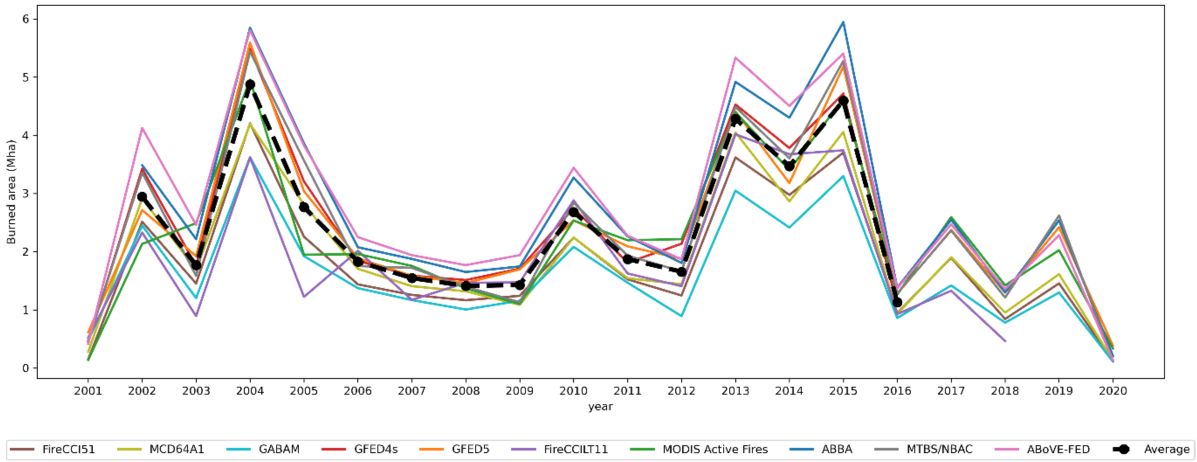

Figure C3.4. Total BA (Mha) of each dataset for the North America region, 2001-2020. The average of the datasets is given for the analysis period (2002-2016) only.

Table C3.2: *P*-values between each pair of datasets for the years 2002-2016 in North America, calculated using Welch's *t*-test, as described in Appendix B. Statistically significant values at the 5 % level are highlighted in yellow.

FireCCI51	X									
MCD64A1	0.685	X								
GABAM	0.488	0.274	X							
MTBS/NBAC	0.200	0.353	0.063	X						
GFED4s	0.166	0.311	0.046	0.970	X					
GFED5	0.207	0.373	0.061	0.940	0.907	X				
ABoVE-FED	0.029	0.065	0.007	0.381	0.384	0.327	X			
FireCCILT11	0.911	0.774	0.430	0.242	0.207	0.253	0.039	X		
MODIS Active Fires	0.307	0.532	0.092	0.719	0.678	0.769	0.197	0.370	X	
ABBA	0.052	0.108	0.014	0.504	0.513	0.445	0.844	0.067	0.289	X
	FireCCI51	MCD64A1	GABAM	MTBS/NBAC	GFED4s	GFED5	ABoVE-FED	FireCCILT11	MODIS Active Fires	ABBA

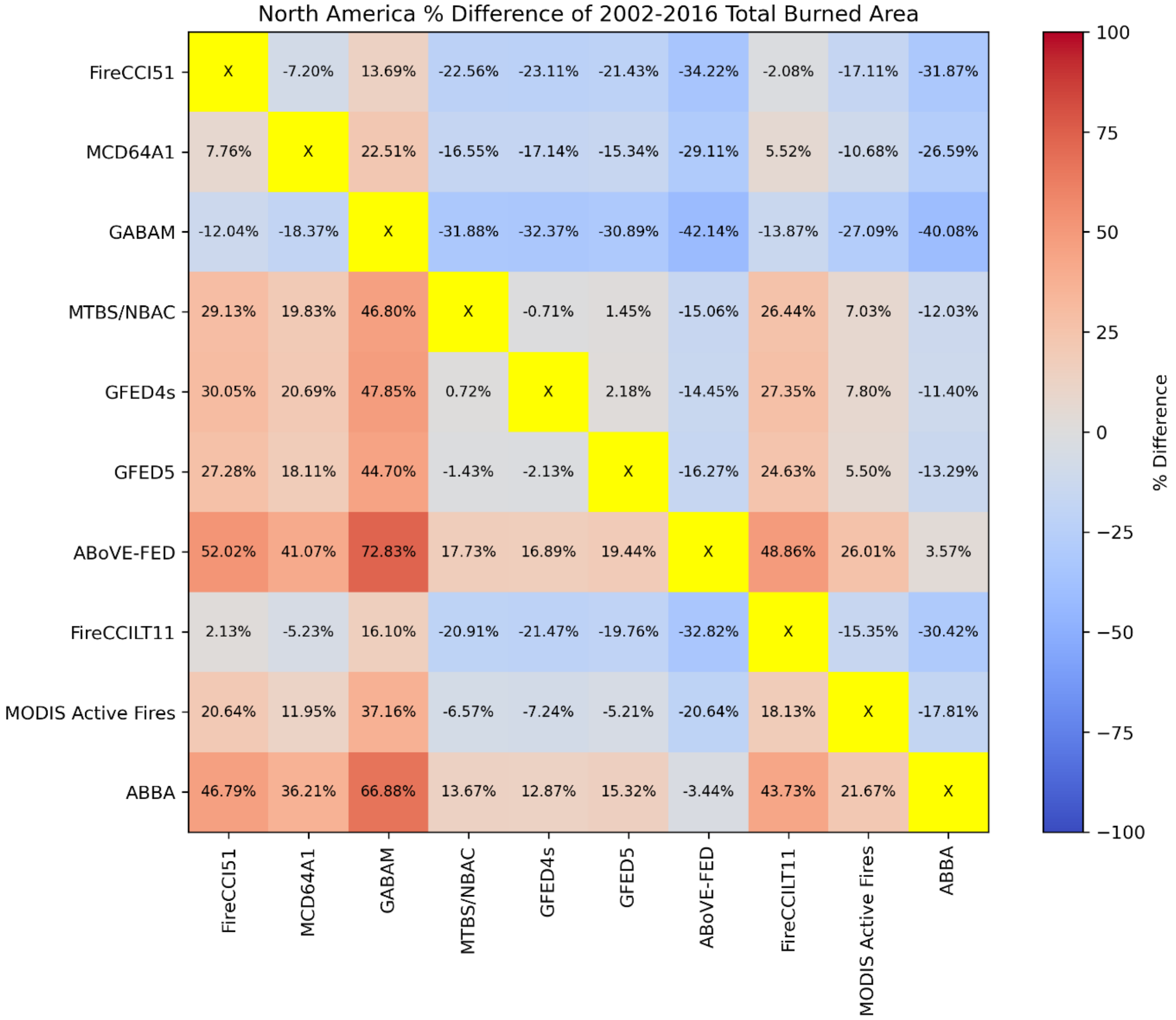

	FireCCI51	MCD64A1	GABAM	MTBS/NBAC	GFED4s	GFED5	ABoVE-FED	FireCCILT11	MODIS Active Fires	ABBA
FireCCI51	X	-7.20%	13.69%	-22.56%	-23.11%	-21.43%	-34.22%	-2.08%	-17.11%	-31.87%
MCD64A1	7.76%	X	22.51%	-16.55%	-17.14%	-15.34%	-29.11%	5.52%	-10.68%	-26.59%
GABAM	-12.04%	-18.37%	X	-31.88%	-32.37%	-30.89%	-42.14%	-13.87%	-27.09%	-40.08%
MTBS/NBAC	29.13%	19.83%	46.80%	X	-0.71%	1.45%	-15.06%	26.44%	7.03%	-12.03%
GFED4s	30.05%	20.69%	47.85%	0.72%	X	2.18%	-14.45%	27.35%	7.80%	-11.40%
GFED5	27.28%	18.11%	44.70%	-1.43%	-2.13%	X	-16.27%	24.63%	5.50%	-13.29%
ABoVE-FED	52.02%	41.07%	72.83%	17.73%	16.89%	19.44%	X	48.86%	26.01%	3.57%
FireCCILT11	2.13%	-5.23%	16.10%	-20.91%	-21.47%	-19.76%	-32.82%	X	-15.35%	-30.42%
MODIS Active Fires	20.64%	11.95%	37.16%	-6.57%	-7.24%	-5.21%	-20.64%	18.13%	X	-17.81%
ABBA	46.79%	36.21%	66.88%	13.67%	12.87%	15.32%	-3.44%	43.73%	21.67%	X

Figure C3.5. Matrix of the total BA percentage difference between datasets in North America, 2002-2016. The percentage differences are calculated as the burned area from the dataset on the *x*-axis relative to the corresponding dataset on the *y*-axis (Equation A3.1).

Table C3.3. Yearly burned area (Mha) for central/northern Siberia for 2001-2020. N/A denotes an absence of data. The averages (avg) for each year (y) and dataset (d) are given, as are the standard deviations (SD). Avg (d) and SD (d) are calculated for the analysis period (2006-2016) only.

	FireCCI51	MCD64A1	GABAM	Talucci et al.	SRBA	GFED4s	GFED5	FireCCILT11	MODIS AF	ABBA	Avg (y)	SD (y)
2001	3.27	3.09	7.15	5.00	N/A	3.55	6.90	1.62	4.17	N/A	4.34	1.91
2002	5.36	4.92	3.63	14.38	N/A	5.22	9.25	4.36	8.52	11.31	7.44	3.66
2003	11.87	8.78	10.89	22.10	N/A	9.79	18.40	8.57	19.84	18.34	14.29	5.31
2004	0.53	0.61	3.22	0.81	N/A	0.40	1.50	0.25	1.36	0.55	1.02	0.93
2005	1.82	1.59	0.66	2.15	N/A	1.51	4.02	1.45	3.79	2.03	2.11	1.10
2006	2.45	2.16	1.22	3.77	1.53	2.44	4.77	1.85	5.41	2.74	2.83	1.39
2007	1.24	0.89	0.48	5.56	0.44	0.86	2.67	1.16	2.47	0.91	1.67	1.56
2008	4.68	3.30	2.33	3.97	3.45	5.06	7.68	4.83	8.45	6.48	5.02	1.97
2009	2.00	1.81	1.10	2.89	1.66	1.76	4.85	1.83	4.33	2.45	2.47	1.22
2010	2.54	2.46	1.14	3.67	1.12	2.46	4.73	1.33	4.52	3.19	2.72	1.31
2011	3.27	3.73	1.58	9.18	2.64	2.71	7.93	1.90	8.09	4.22	4.53	2.80
2012	5.45	4.79	2.01	7.70	5.49	0.77	8.94	4.83	10.80	9.01	5.98	3.17
2013	3.20	3.10	2.27	4.77	2.78	3.06	6.38	3.39	6.52	5.17	4.06	1.53
2014	5.07	6.39	3.09	9.16	3.89	4.35	8.02	4.65	9.08	5.48	5.92	2.17
2015	2.82	2.53	1.85	9.07	2.08	2.47	4.91	1.91	5.56	3.17	3.64	2.28
2016	4.70	4.23	2.59	9.02	4.04	4.33	8.54	2.35	9.57	6.20	5.56	2.64
2017	2.93	3.02	2.11	4.51	2.85	N/A	5.22	2.35	6.05	3.59	3.63	1.35
2018	5.04	4.51	3.48	7.13	4.69	N/A	7.22	2.78	8.45	6.41	5.52	1.89
2019	6.37	5.87	3.39	11.54	5.55	N/A	10.57	N/A	12.20	8.38	7.98	3.19
2020	7.51	5.98	5.17	15.15	5.96	N/A	13.78	N/A	13.24	10.10	9.61	4.00
Avg (d)	3.40	3.22	1.79	6.25	2.65	2.75	6.31	2.73	6.80	4.46	4.04	1.80
SD (d)	1.38	1.53	0.77	2.58	1.48	1.39	2.04	1.43	2.58	2.29	1.49	X

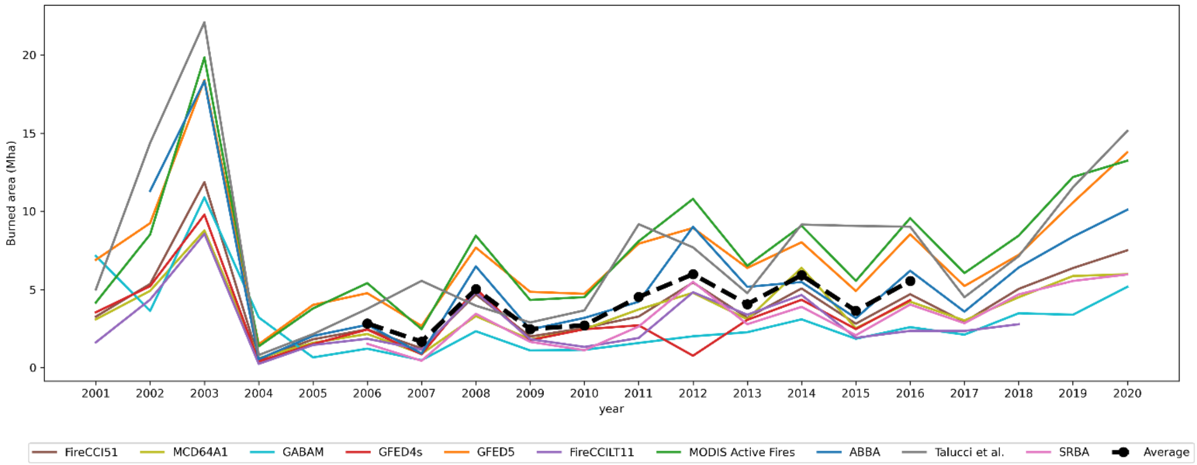

Figure C3.6. Total BA (Mha) of each dataset for the central/northern Siberia region, 2001-2020. The average of the datasets is given for the analysis period (2006-2016) only.

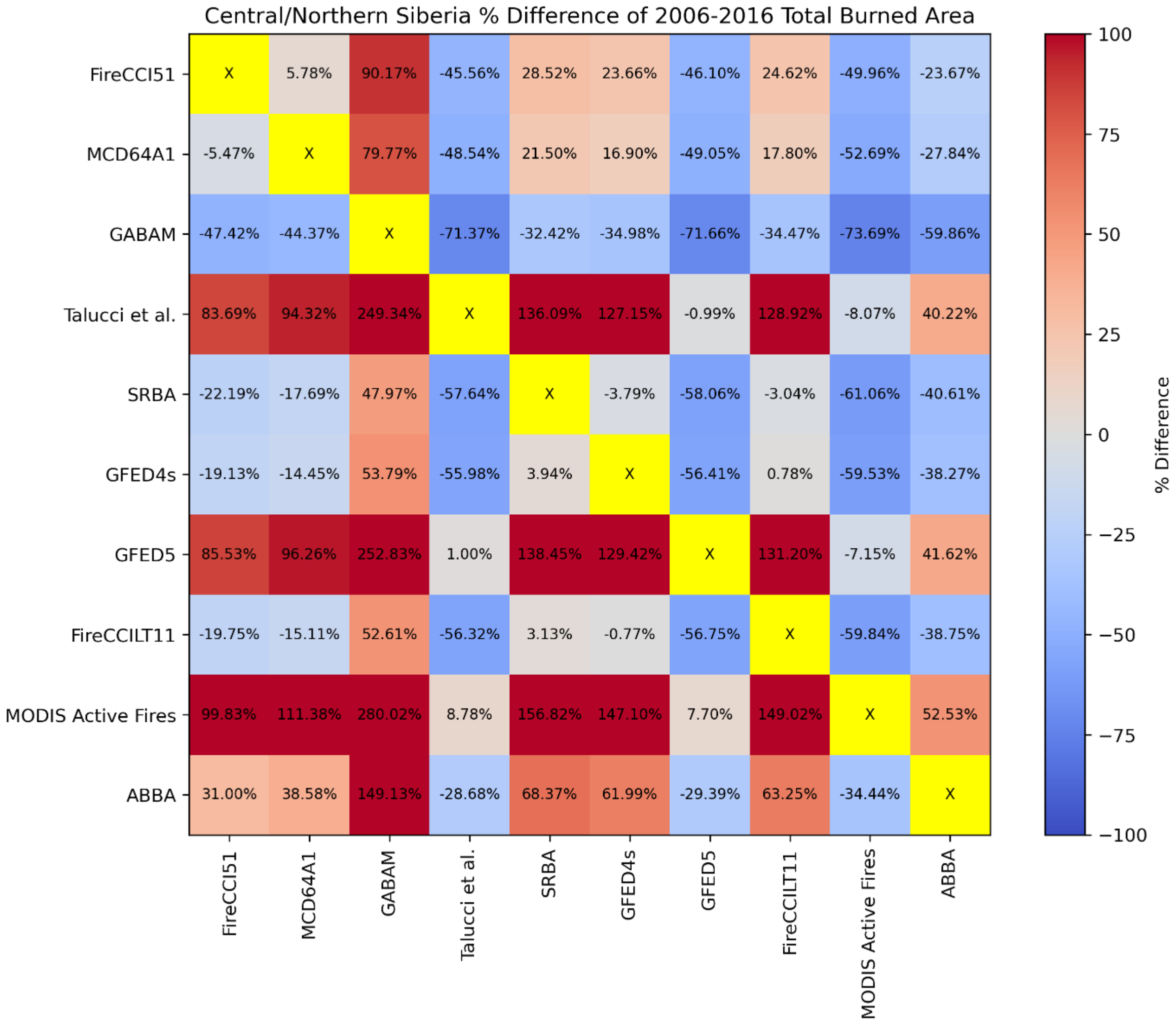
Central/Northern Siberia % Difference of 2006-2016 Total Burned Area

	FireCCI51	MCD64A1	GABAM	Talucci et al.	SRBA	GFED4s	GFED5	FireCCILT11	MODIS Active Fires	ABBA
FireCCI51	X	5.78%	90.17%	-45.56%	28.52%	23.66%	-46.10%	24.62%	-49.96%	-23.67%
MCD64A1	-5.47%	X	79.77%	-48.54%	21.50%	16.90%	-49.05%	17.80%	-52.69%	-27.84%
GABAM	-47.42%	-44.37%	X	-71.37%	-32.42%	-34.98%	-71.66%	-34.47%	-73.69%	-59.86%
Talucci et al.	83.69%	94.32%	249.34%	X	136.09%	127.15%	-0.99%	128.92%	-8.07%	40.22%
SRBA	-22.19%	-17.69%	47.97%	-57.64%	X	-3.79%	-58.06%	-3.04%	-61.06%	-40.61%
GFED4s	-19.13%	-14.45%	53.79%	-55.98%	3.94%	X	-56.41%	0.78%	-59.53%	-38.27%
GFED5	85.53%	96.26%	252.83%	1.00%	138.45%	129.42%	X	131.20%	-7.15%	41.62%
FireCCILT11	-19.75%	-15.11%	52.61%	-56.32%	3.13%	-0.77%	-56.75%	X	-59.84%	-38.75%
MODIS Active Fires	99.83%	111.38%	280.02%	8.78%	156.82%	147.10%	7.70%	149.02%	X	52.53%
ABBA	31.00%	38.58%	149.13%	-28.68%	68.37%	61.99%	-29.39%	63.25%	-34.44%	X

Figure C3.7. Matrix of the total BA percentage difference between datasets in central/northern Siberia, 2006-2016. The percentage differences are calculated as the burned area from the dataset on the *x*-axis relative to the corresponding dataset on the *y*-axis (Equation A3.1).

Table C3.4: *P*-values between each pair of datasets for the years 2006-2016 in Central/northern Siberia, calculated using Welch's *t*-test, as described in Appendix B. Statistically significant values at the 5 % level are highlighted in yellow.

FireCCI51	X									
MCD64A1	0.768	X								
GABAM	0.004	0.015	X							
Talucci et al.	0.006	0.004	0.000	X						
SRBA	0.231	0.386	0.109	0.001	X					
GFED4s	0.283	0.464	0.062	0.001	0.867	X				
GFED5	0.001	0.001	0.000	0.950	0.000	0.000	X			
FireCCILT11	0.275	0.451	0.073	0.001	0.895	0.972	0.000	X		
MODIS Active Fires	0.002	0.001	0.000	0.624	0.000	0.000	0.630	0.000	X	
ABBA	0.208	0.153	0.003	0.101	0.042	0.050	0.058	0.049	0.036	X
	FireCCI51	MCD64A1	GABAM	Talucci et al.	SRBA	GFED4s	GFED5	FireCCILT11	MODIS Active Fires	ABBA

Table C3.5. Yearly burned area (Mha) for southern Siberia for the years 2001-2020. N/A denotes an absence of data. The averages (avg) for each year (y) and dataset (d) are given, as are the standard deviations (SD). Avg (d) and SD (d) are calculated for the analysis period (2001-2016) only.

	FireCCI51	MCD64A1	GABAM	GFED4s	GFED5	FireCCILT11	MODIS AF	Avg (y)	SD (y)
2001	9.06	2.82	7.33	4.76	28.48	13.56	4.60	10.09	8.85
2002	8.13	4.17	4.16	3.98	26.18	15.76	10.40	10.40	8.18
2003	16.79	10.31	8.34	10.47	37.35	21.90	26.97	18.88	10.61
2004	9.61	5.83	2.99	4.64	25.62	5.91	14.25	9.84	7.89
2005	9.54	4.31	4.15	3.92	20.56	11.84	13.57	9.70	6.20
2006	13.36	5.43	5.30	7.86	25.32	23.30	16.59	13.88	8.25
2007	9.02	4.49	3.85	4.38	19.61	10.58	13.24	9.31	5.78
2008	23.11	12.50	14.09	13.34	38.39	33.49	25.25	22.88	10.28
2009	10.63	4.72	4.23	4.54	22.14	18.17	14.40	11.26	7.23
2010	9.45	3.65	3.64	4.16	19.73	19.52	12.35	10.36	7.13
2011	9.78	6.00	5.68	4.61	21.30	14.95	13.63	10.85	6.11
2012	11.68	5.42	2.30	3.49	21.58	16.10	14.62	10.74	7.24
2013	3.24	1.99	1.93	1.18	8.87	6.84	5.17	4.17	2.88
2014	11.15	9.25	9.06	5.38	22.75	17.89	14.68	12.88	5.95
2015	7.60	4.26	6.55	5.10	13.89	9.29	10.10	8.11	3.30
2016	7.02	3.01	4.02	3.24	11.66	7.60	7.87	6.35	3.13
2017	4.40	2.34	3.45	N/A	11.69	7.48	7.15	6.08	3.41
2018	8.81	4.49	6.44	N/A	13.21	7.89	8.45	8.22	2.91
2019	6.46	3.67	5.65	N/A	12.82	N/A	8.13	7.35	3.45
2020	6.91	2.53	2.66	N/A	12.18	N/A	7.34	6.33	3.98
Avg (d)	10.57	5.51	5.48	5.32	22.71	15.42	13.61	11.23	6.54
SD (d)	4.43	2.85	3.08	2.94	7.91	7.14	5.98	4.46	X

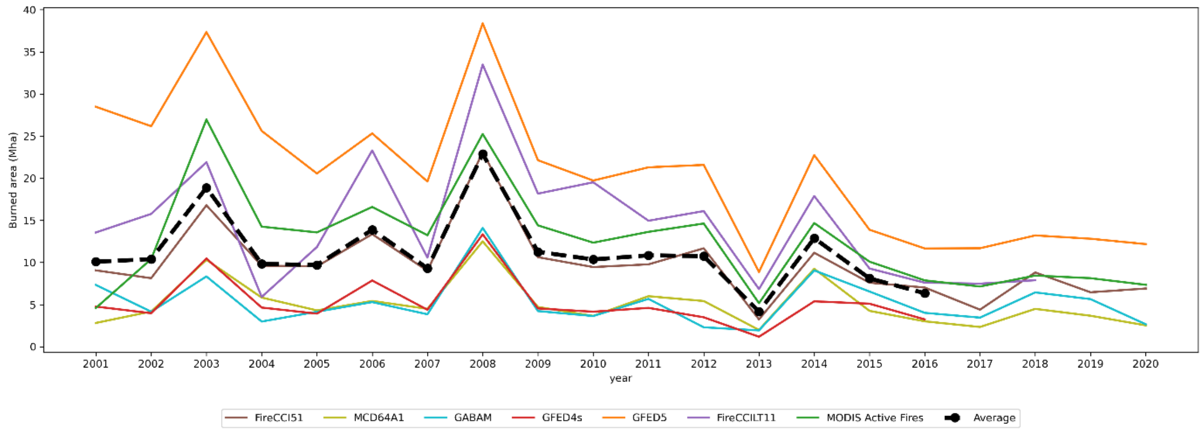

Figure C3.8. Total BA (Mha) of each dataset for the southern Siberia region, 2001-2020. The average of the datasets is given for the analysis period (2001-2016) only.

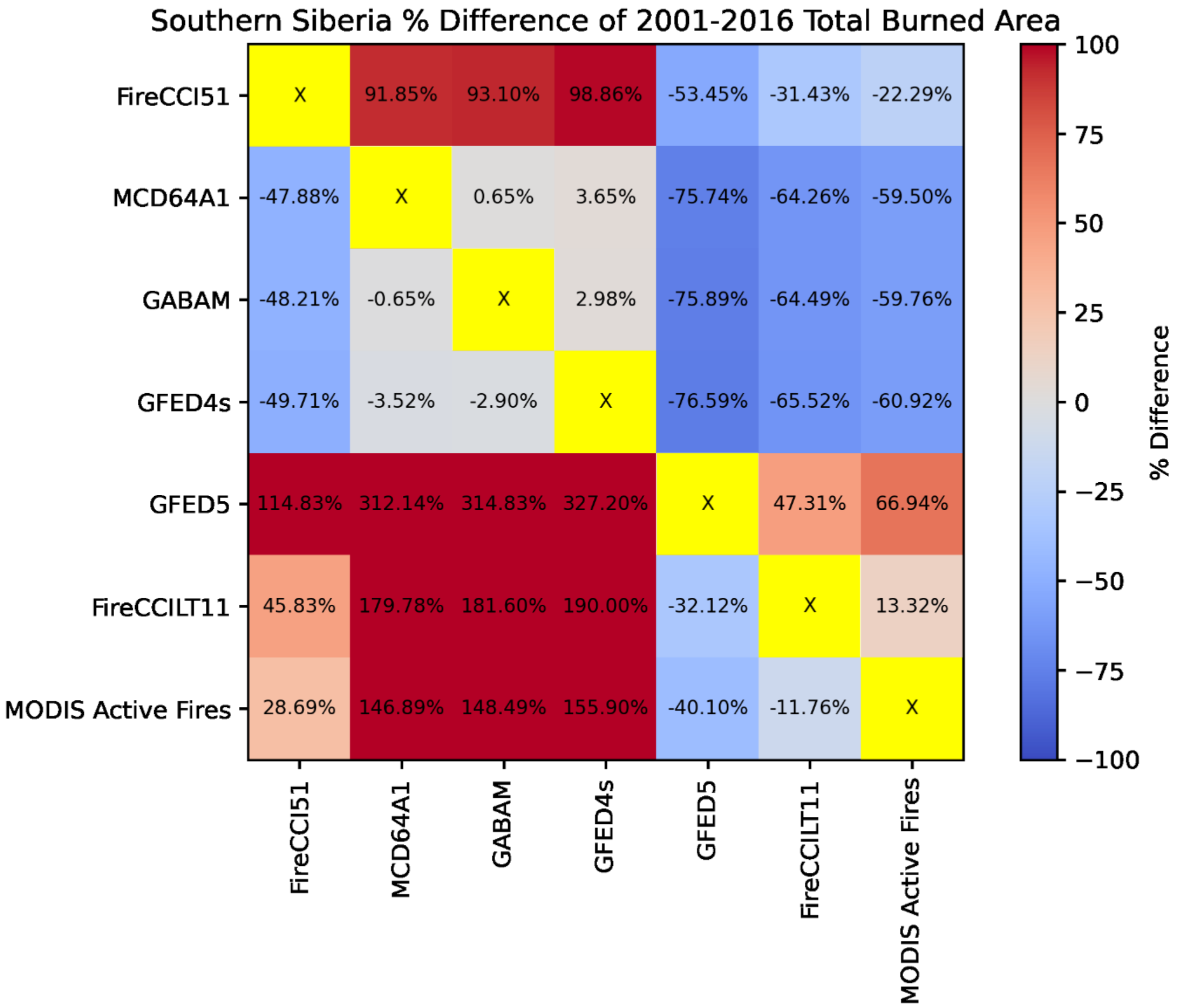

	FireCCI51	MCD64A1	GABAM	GFED4s	GFED5	FireCCILT11	MODIS Active Fires
FireCCI51	X	91.85%	93.10%	98.86%	-53.45%	-31.43%	-22.29%
MCD64A1	-47.88%	X	0.65%	3.65%	-75.74%	-64.26%	-59.50%
GABAM	-48.21%	-0.65%	X	2.98%	-75.89%	-64.49%	-59.76%
GFED4s	-49.71%	-3.52%	-2.90%	X	-76.59%	-65.52%	-60.92%
GFED5	114.83%	312.14%	314.83%	327.20%	X	47.31%	66.94%
FireCCILT11	45.83%	179.78%	181.60%	190.00%	-32.12%	X	13.32%
MODIS Active Fires	28.69%	146.89%	148.49%	155.90%	-40.10%	-11.76%	X

Figure C3.9. Matrix of the total BA percentage difference between datasets in southern Siberia, 2001-2016. The percentage differences are calculated as the burned area from the dataset on the *x*-axis relative to the corresponding dataset on the *y*-axis (Equation A3.1).

Table C3.6: *P*-values between each pair of datasets for the years 2001-2016 in Southern Siberia, calculated using Welch's *t*-test, as described in Appendix B. Statistically significant values at the 5 % level are highlighted in yellow.

FireCCI51	X						
MCD64A1	0.001	X					
GABAM	0.001	0.973	X				
GFED4s	0.001	0.851	0.883	X			
GFED5	0.000	0.000	0.000	0.000	X		
FireCCILT11	0.030	0.000	0.000	0.000	0.010	X	
MODIS Active Fires	0.114	0.000	0.000	0.000	0.001	0.442	X
	FireCCI51	MCD64A1	GABAM	GFED4s	GFED5	FireCCILT11	MODIS Active Fires

Appendix D: Additional technical information for Chapter 3

Introductions to the three main satellite image acquisition methods used in the creation of burned area products, Landsat, AVHRR, and MODIS, are provided here.

The Landsat image acquisition program – a joint National Aeronautics and Space Administration (NASA)/United States Geological Survey (USGS) initiative – is the longest running venture, with the first satellite, Landsat 1, launched in July 1972, and the most recent, Landsat 9, in September 2021 (Wulder et al., 2022). Landsat imagery is provided at a relatively high spatial resolution; the Multispectral Scanner (4 spectral bands) onboard Landsat satellites 1-5 had a resolution of 79 m, often resampled to 60 m, whereas the Thematic Mapper onboard Landsat 4-5 (7 bands), Enhanced Thematic Mapper Plus (ETM+) on Landsat 7 (8 bands), and the Operational Land Imager and Thermal Infrared Sensor on Landsat 8-9 (both 11 bands) all have resolutions of 30 m (Chander et al., 2009). However, the temporal resolution (or orbit repeat period) is relatively low at 16 days to image the entire Earth.

The Advanced Very High Resolution Radiometer (AVHRR) sensor measures the reflectance of the Earth in five spectral bands (Holben, 1986). The initial mission goal was to monitor clouds, estimate snow cover extent and sea surface temperature. However, it became apparent that it was also useful for monitoring global vegetation (Cihlar et al., 1994, Simpson et al., 1998). AVHRR instruments have been carried by the National Oceanic and Atmospheric Administration (NOAA) series of polar orbiting platforms since 1978, and European MetOp satellites since 2006 (Cracknell, 1997, Marsouin et al., 2015). The AVHRR sensor produces images with the lowest spatial resolution of the three groups of sensors, at 1.1 km, although at a high temporal resolution – twice daily (Riffler et al., 2015).

There have been two MODerate resolution Imaging Spectroradiometer (MODIS) sensors in orbit; the first has been onboard the NASA Terra satellite since December 1999, and the second on the NASA Aqua satellite, launched in May 2002. The MODIS sensors capture data in more spectral bands (36) than the other sensors, to take measurements of both the earth and climate, although the spatial resolutions vary, with 2 bands at 250 m, 5 at 500 m and 29 at 1 km (Justice et al., 2002b). The sensors also produce images frequently; the entire Earth is imaged by each satellite twice daily. Although still in orbit, the MODIS sensors have been superseded by the

Visible Infrared Imaging Radiometer Suite (VIIRS), which was launched in October 2011 (Schroeder et al., 2014).

All three sensors are onboard satellites in sun-synchronous polar orbits, increasing the temporal resolution at high-latitude areas. For AVHRR and MODIS, this means an extra one to two passes over polar areas per day. However, the high spatial resolution of Landsat limits its ability to cover wide areas frequently and, as such, the revisit time at high latitudes remains relatively long: between seven and nine days.

Chapter 4

Machine learning projections of future wildfire occurrence in the Arctic-boreal zone

The June 2024 McDonald Fire south of Fairbanks, Alaska, USA. *Photo credit: Joshua Rady.*

An adapted version of this chapter is currently in preparation for submission to *Nature Communications Earth and Environment* as: Clelland, A. A., Potter, S., Marshall, G. J., Baxter, R., Hosking, J. S., Talucci, A. C., Yang, Y., Rady, J. M., Genet, H. and Rogers, B. M. Escalating wildfire extremes across boreal forests under climate change.

The author contributions were as follows: A.A.C., G.J.M., R.B., J.S.H. and B.M.R. conceived the study. A.A.C., S.P., G.J.M., J.S.H., Y.Y., H.G. and B.M.R. developed the methodology. A.A.C. conducted the research. A.A.C. analysed the output and wrote the first draft of the manuscript, with contributions from all authors.

Abstract

Wildfire activity in the Arctic-boreal zone (ABZ) is expected to continue to intensify under climate change, yet spatial and temporal projections of burned area (BA) remain highly uncertain. Here we present monthly projections of fire occurrence across the ABZ from 2025 to 2100 using XGBoost machine learning models trained on historical fire, climate, topographic and land cover data. The models achieved high predictive performance (AUC = 0.71-0.93) and accurately reproduced observed spatial patterns of fire occurrence. We applied the models to bias-corrected climate projections from two CMIP6 models (ACCESS-CM2 and MRI-ESM2-0) under three shared socioeconomic pathways (SSP1-2.6, SSP2-4.5, SSP3-7.0). Mean annual BA is projected to increase across all six model-SSP combinations, with the highest increase under ACCESS-CM2 SSP3-7.0, reaching 14.63 Mha yr^{-1} in 2076-2100 – a 65 % rise over the 2001-2023 observed average. While BA patterns vary by scenario and model, North American boreal ecoregions are consistently projected to experience the most extreme increases, especially under SSP3-7.0, with an average increase of 116 % to 5.16 Mha $year^{-1}$ and regional rises of up to 270 % towards the end of the century. Fire season duration is also expected to increase by up to two months, with earlier starts and later finishes across all regions. Eurasia maintains a bimodal burn distribution while North America sees a marked rise in early-season fires, particularly under the MRI-ESM2-0 SSP1-2.6 combination. Extreme fire years – defined as years exceeding the 95th percentile of historic BA – become more frequent, especially under higher-emission scenarios, from 1-in-20-year events up to 1-in-3. Monotonic increases in BA, statistically significant at the 0.1 % level, are detected across both boreal and tundra biomes using the Mann-Kendall trend test. Our findings suggest that climate-driven increases in fire activity will fundamentally alter disturbance regimes across the ABZ, with serious implications for carbon dynamics, ecosystem resilience, and policy planning in high-latitude regions.

Introduction

High-latitude ecosystems, including boreal forest and Arctic tundra, collectively referred to here as the Arctic-boreal zone (ABZ), are undergoing an increase in fire activity driven by climate change (Scholten et al., 2024). While these systems have historically experienced long fire return intervals, longer fire seasons, higher temperatures, shifting precipitation patterns and more ignitions from lightning strikes are contributing to increases in fire frequency, severity and burned area, which impact vegetation dynamics and ecosystem resilience (McCarty et al., 2021, Scholten et al., 2021, Li et al., 2024, Zhang et al., 2024b). As fire regimes intensify, they threaten biodiversity, permafrost stability, and the long-term carbon balance of these regions, with cascading effects on global climate systems (Jafarov et al., 2013, Duncan et al., 2020, Potter et al., 2023).

Fire plays a fundamental role in shaping high-latitude ecosystems, influencing vegetation composition, nutrient cycling, and landscape succession (Hobbie et al., 2002, Frost et al., 2020). In boreal forests, periodic burning clears accumulated aboveground and near-surface organic matter, promotes regeneration of fire-adapted species, and maintains ecosystem diversity (Rogers et al., 2020, Baltzer et al., 2021). However, as fire activity intensifies, these natural cycles can be disrupted, leading to shifts in dominant vegetation types and altering habitat structures (Sun et al., 2021). Fire also affects carbon dynamics by releasing large amounts of stored carbon from vegetation and soil, particularly in peatlands and permafrost regions (Walker et al., 2019, Lin et al., 2021, Veraverbeke et al., 2021, Miner et al., 2022). These emissions contribute to climate warming, creating feedback loops that further accelerate fire frequency and ecosystem change (Huang et al., 2024).

Beyond ecological impacts, increasing fire activity poses growing challenges for communities, infrastructure, and regional economies. In remote settlements within the ABZ, resource industries, and transportation networks are particularly vulnerable to wildfire damage, while smoke exposure presents serious health risks (McCarty et al., 2021, Schmidt et al., 2024). Indigenous communities, who have deep cultural and subsistence connections to the land, face disruptions to traditional practices and heightened threats to food security (Golden et al., 2015, Groisman et al., 2017). As fire regimes shift, the need for proactive fire management, policy adaptation, and risk reduction strategies becomes increasingly urgent (Birge et al., 2020).

Fire regimes in high-latitude ecosystems are highly sensitive to climate change, as temperature, precipitation, and atmospheric moisture directly influence fire ignition, spread, and intensity (Jones et al., 2022, Lund et al., 2023). Rising temperatures accelerate fuel drying, while changes in precipitation patterns can lead to longer periods of fire-prone conditions. Increased lightning activity, a key ignition source in boreal forests, is also expected to rise with warming (Veraverbeke et al., 2017). These climatic shifts interact with vegetation changes, altering fuel availability and flammability. As a result, fire return intervals are shortening, and extreme fire events are becoming more frequent, reshaping landscapes and challenging ecosystem resilience (Burrell et al., 2022, Descals et al., 2022).

Future climate projections, using models from the Coupled Model Intercomparison Project Phase 6 (CMIP6 - Eyring et al., 2016) ensemble, indicate significant warming across the ABZ, with the magnitude of change varying under different Shared Socioeconomic Pathways (SSPs - O'Neill et al., 2016, Riahi et al., 2017). According to the latest estimates from the Intergovernmental Panel on Climate Change, under lower-emission scenarios, such as SSP1-2.6 or SSP2-4.5, warming to the end of the century remains more moderate, at 1.3-2.4°C, but under the high-emission pathways SSP3-7.0 and SSP5-8.5 temperatures could rise dramatically; up to 5.7°C (IPCC, 2023). This warming is expected to accelerate permafrost thaw, alter precipitation regimes, and extend the duration of fire-prone conditions (Hu et al., 2022, Quilcaille et al., 2023). The spatial distribution of warming will also vary, with some regions experiencing more rapid temperature increases than others.

Lightning ignitions account for 77 ± 8 % of total ignitions in boreal forests (Janssen et al., 2023) and, in North America, this can increase up to 87 % (Veraverbeke et al., 2017). Under higher-emission climate change scenarios, the risk of fire from lightning ignitions will be amplified due to enhanced fuel flammability, and the climatic conditions will be more conducive to large, intense wildfires (Curasi et al., 2024, Zhang et al., 2024a).

As fire activity intensifies in the ABZ, there is a growing need for reliable future projections to anticipate its ecological and socio-economic impacts. Projections based on robust models can support policy decisions, land-use planning, and targeted fire mitigation strategies (Sohl et al., 2016, Gao et al., 2021). By anticipating future fire regimes under different climate scenarios, researchers and decision-makers can develop adaptive management approaches to reduce risks and build resilience in fire-prone landscapes.

Fire models range from interpretable parametric models to more flexible machine learning (ML) frameworks. The different approaches reflect a trade-off between interpretability, uncertainty quantification and predictive flexibility, with the optimal choice depending on whether the priority is process-based understanding, inferring the probability of fire or maximising predictive skill.

Generalised linear models have been widely used to relate fire occurrence or burned area to climate and anthropogenic drivers, providing transparent parameter estimates and clear hypothesis testing about driver-response relationships (Kwak et al., 2012, Haas et al., 2026). However, their reliance on pre-specified functional forms has limitations in capturing the complex interactions between climate, vegetation, and fire dynamics, particularly under changing environmental conditions (Alexander and Cruz, 2013, Hantson et al., 2016, Hanan et al., 2022). They can struggle to account for large-scale spatial and temporal variability, which can reduce their predictive accuracy, especially when applied to future climate scenarios (Flatley and Fulé, 2016, Williams and Abatzoglou, 2016).

Maximum entropy approaches, adapted from species-distribution modelling, relax strict parametric assumptions and estimate environmental suitability for fire occurrence from presence-only data, allowing more flexible response shapes but often focussing on probability of occurrence rather than continuous burned area (Moritz et al., 2012, Barbosa et al., 2025). Bayesian extensions provide a formal framework for incorporating prior knowledge and propagating uncertainty, which is particularly valuable when observational records are short or noisy, although at increased computational and structural complexity (Kelley et al., 2019, Kelley et al., 2021).

More recently, hybrid approaches have combined statistical or process-based components with ML methods, such as tree ensembles or neural networks, seeking to retain physical interpretability while capturing nonlinear climate-fire interactions (Guo et al., 2025, Lampe et al., 2026). ML offers a promising alternative by leveraging large datasets to identify hidden patterns and nonlinear relationships in fire occurrence. By integrating a broad range of environmental variables, ML models can improve fire projections, adapt to changing conditions, and provide more accurate, data-driven insights for fire risk assessment and management (Abid, 2021, Arif et al., 2021, Coughlan et al., 2021).

Recent studies, which have applied ML models to project wildfire activity under future climate scenarios, vary widely in geographic focus, time horizon, and methodological complexity (Sung et al., 2022, Shao et al., 2023, Herrmann et al., 2023, Zhao et al., 2025). Some rely on a single climate model, using a limited number of environmental predictors, while others integrate multiple drivers and model ensembles.

Our approach is, we believe, the first study to provide future fire projections for the entire Arctic-boreal zone under a range of SSP scenarios on a monthly timescale. Monthly projections enable the detection of seasonal trends, shifts in fire season duration, and short-term variability that decadal averages may obscure. The present study aims to elucidate the drivers of future changes in fire patterns in the ABZ, and to determine the extent of burned area under the different climate change scenarios.

As detailed in the Methodology, we trained an XGBoost ML model using 21 topographic, climate and fire danger variables to make monthly projections of fire occurrence for the years 2025-2100 using two models from the CMIP6 ensemble and three SSP scenarios. We then present our results from testing the model, alongside the key findings from analysis of the future projections. Potential reasons for differences between the CMIP6 models and SSP scenarios are discussed, before concluding remarks are made.

Methodology

Study region

Our ABZ study area comprises the boreal and tundra biomes, as defined by Dinerstein et al. (2017). Within this area there are 58 ecoregions – 26 in the boreal biome and 32 in the tundra, across North America, Fennoscandia and Eurasia (Table A4.1, Figure A4.1; pp. 169-171). We grouped these ecoregions into broader regions, including North America boreal, Eurasia boreal, and tundra (all). We used a 4 km spatial resolution for analysis, representing a compromise between high-resolution topographic and land cover variables and coarse climate and fire weather indices.

To effectively capture the markedly different fire regime of southern Siberia (Rogers et al., 2015, Clelland et al., 2024b) compared to northern Siberia and Arctic-boreal North America in our models, we defined a separate subregion within the ABZ, which includes the mainland "Mixed Forest", "Southern Taiga", "Montane Boreal", and "Montane Sub-Boreal" ecoregions from Soja et al. (2004a), bounded to the west by the Ural Mountains. We chose these ecoregions over those defined by Dinerstein et al. (2017) as they were developed specifically for Eurasia and show better latitudinal definition. Both distinct regions are illustrated in Figure 4.1. Hereafter, the two areas shall be referred to as "Northern" and "South Siberia".

Figure 4.1. Map of our study region, with the “Northern” area in blue, and “South Siberia” area in red.

Model inputs

The inputs for the training, testing and validation of the models across the historical (2001-2023) and future (2025-2100) time periods are summarised in Table 4.1. The models were initially trained using data from 2001 to 2020, with the years 2008, 2015 and 2020 withheld for validation. Testing was performed on the more recent 2021 to 2023 period, before being incorporated into the final models. All datasets were processed in Google Earth Engine (GEE - Gorelick et al., 2017) and stored as GeoTIFF files in Google Cloud Storage buckets. Where necessary, the data were resampled using nearest neighbour to the 4 km spatial resolution of the domain, aggregated to a monthly temporal resolution, and reprojected to the equal-area EPSG:6931 (NSIDC EASE Grid-2.0 North) coordinate system.

Table 4.1. List of model inputs. “-” denotes an absence of data.

Source	Variables	Units	Spatial resolution	Temporal resolution	Time span of product	Model time period
Copernicus DEM GLO-30 Airbus (2022)	Elevation	m	30 m	-	-	Historic and future
	Aspect$^{\#}$	°				
	Slope$^{\#}$	°				
	Latitude	°				
	Longitude (sine)*	-				
	Month	-				
DVM-DOS-TEM Land Cover Map Briones et al. (2025)	Land cover	-	1 km	-	-	Historic and future
ERA5-Land Muñoz-Sabater et al. (2021)	Relative humidity (*rh*)$^{+}$	%	0.1° (~9 km)	Hourly	1950-present	Historic
	Total precipitation (*tp*)	m				
	Surface downwelling shortwave/longwave radiation (*rsds*/*rlds*)	J/m^2				
	Wind speed (*wsp*)$^{+}$	m/s				
	Minimum/mean/maximum 2-metre air temperature (*mn2t*/*t2m*/*mx2t*)	K				
Copernicus Emergency Management System (CEMS) Fire Danger Indices Vitolo et al. (2020)	Fine Fuel Moisture Code (FFMC)	-	0.25° (~28 km)	Daily	1940-present	Historic
	Duff Moisture Code (DMC)	-				
	Drought Code (DC)	-				
	Buildup Index (BUI)	-				
	Initial Spread Index (ISI)	-				
	Fire Weather Index (FWI)	-				

FireCCI v5.1 Lizundia-Loiola et al. (2020)	Burned area	-	250 m	Monthly	2001-2020[^]	Historic
MCD64A1 Giglio et al. (2018)	Burned area	-	463 m	Monthly	2001-present	Historic
NEX-GDDP-CMIP6 Thrasher et al. (2021) Thrasher et al. (2022)	Relative humidity (*hurs*) Precipitation (*pr*) Surface downwelling shortwave/longwave radiation (*rsds*/*rlds*) Wind speed (*sfcWind*) Minimum/mean/maximum 2-metre air temperature (*tasmin*/*tas*/*tasmax*)	% $kg/m^2/s$ W/m^2 m/s K	0.25° (~28 km)	Daily	1950-2014 2015-2100	Future
NEX-GDDP-FWI Park et al. (2023)	Fine Fuel Moisture Code (FFMC) Duff Moisture Code (DMC) Drought Code (DC) Buildup Index (BUI) Initial Spread Index (ISI) Fire Weather Index (FWI)	- - - - - -	0.25° (~28 km)	Daily	1950-2014 2015-2100	Future

[#] Aspect and slope were derived from elevation using Google Earth Engine.

* The sine of the longitude was calculated to avoid the discontinuity at 0/360°.

[+] Relative humidity was derived from the 2 m dewpoint and mean air temperatures, and wind speed was calculated from the 10-metre u- and v-wind components.

^ FireCCI v5.1 has subsequently been extended to 2022.

Our model inputs contain a range of topographical, climate and fire danger sources. Elevation was taken from the Copernicus DEM GLO-30 map (Airbus, 2022). Aspect, slope, latitude and longitude were derived using GEE. To avoid the longitudinal discontinuity at 0°/360°, we used the sine of longitude values.

A newly developed circumpolar Arctic-boreal land cover map (Briones et al., 2025) was incorporated to assess the influence of land cover type on wildfire activity. The original land cover classes were consolidated into ten broader classes to improve model discernibility (Table B4.1; p. 172). Boreal ecoregions contain a greater proportion of forests compared to tundra ecoregions, whereas the latter comprises mostly shrub tundra and barrens.

ERA5-Land historic climate reanalysis data (Muñoz-Sabater et al., 2021) were used during the model training, validation and testing due to their high spatial (~9 km) and temporal (hourly) resolutions. Previous work has shown ERA5-Land to be a good approximation for the 2-metre air temperature, wind speed and total precipitation across Russia (Clelland et al., 2024a). Note that in Chapter 2 it was found that there is no significant advantage to using ERA5-Land over ERA5 (Hersbach et al., 2020). However, the availability of ERA5 within GEE is limited compared to ERA5-Land, with a shorter time series (1979-2020 vs 1950-present) and fewer variables (9 vs 150). Additionally, the coarser resolution of ERA5 (~27 km) meant that the data would be less accurate compared to ERA5-Land after downsampling to the final 4 km resolution.

Total precipitation (*tp*), surface downwelling shortwave/longwave radiation (*rsds*/*rlds*), and minimum/mean/maximum 2-metre air temperature (*mn2t*/*t2m*/*mx2t*) were all taken directly from ERA5-Land, and wind speed (*wsp*) was calculated using the 10-metre *u*- and *v*- wind components. Relative humidity (*rh*) was derived using Equation 4.1, where *exp* is the exponential function, *d2m* and *t2m* are the mean 2-metre dewpoint and air temperatures, respectively, in °C, taken from ERA5-Land, and *a* (17.625) and *b* (243.04) are constants used in the Magnus formula (Magnus, 1844), which approximates the saturation vapour pressure over liquid water as a function of temperature.

$$rh = \frac{exp\left(\frac{a * d2m}{b + d2m}\right)}{exp\left(\frac{a * t2m}{b + t2m}\right)} * 100 \tag{4.1}$$

Fire danger indices were obtained from the Copernicus Emergency Management System (CEMS - Vitolo et al., 2020), derived from ERA5 reanalysis data (Hersbach et al., 2020) and available in GEE. The computed indices were from the Canadian Fire Weather Index system (van Wagner, 1987) and contain three proxies of soil moisture (Fine Fuel Moisture Code (FFMC), Duff Moisture Code (DMC), and Drought Code (DC)) and three fire behaviour indices (Build Up Index (BUI), Initial Spread Index (ISI), and Fire Weather Index (FWI)). They collectively provide an indication of both immediate and longer-term weather conditions. The indices can be summarised as follows, and Figure 4.2 shows how they interact with the climate variables and each other.

- FFMC measures the moisture content of fine surface fuels (e.g. needles, twigs, grasses), influencing fire ignition and surface fire spread.
- DMC measures the moisture content of loosely compacted organic soil layers (5-10 cm depth), affecting medium-term (10-12 days) fire sustainability and moderate fuel consumption.
- DC measures the deep organic fuel moisture (10-20 cm depth), indicating long-term (50 day) dryness and potential for deep-burning fires.
- BUI measures the amount of fuel available for combustion, combining DMC and DC to indicate total fuel moisture content.
- ISI measures the expected fire spread rate based on FFMC and wind speed.
- FWI is the overall fire intensity, combining fuel availability (BUI) and fire spread potential (ISI).

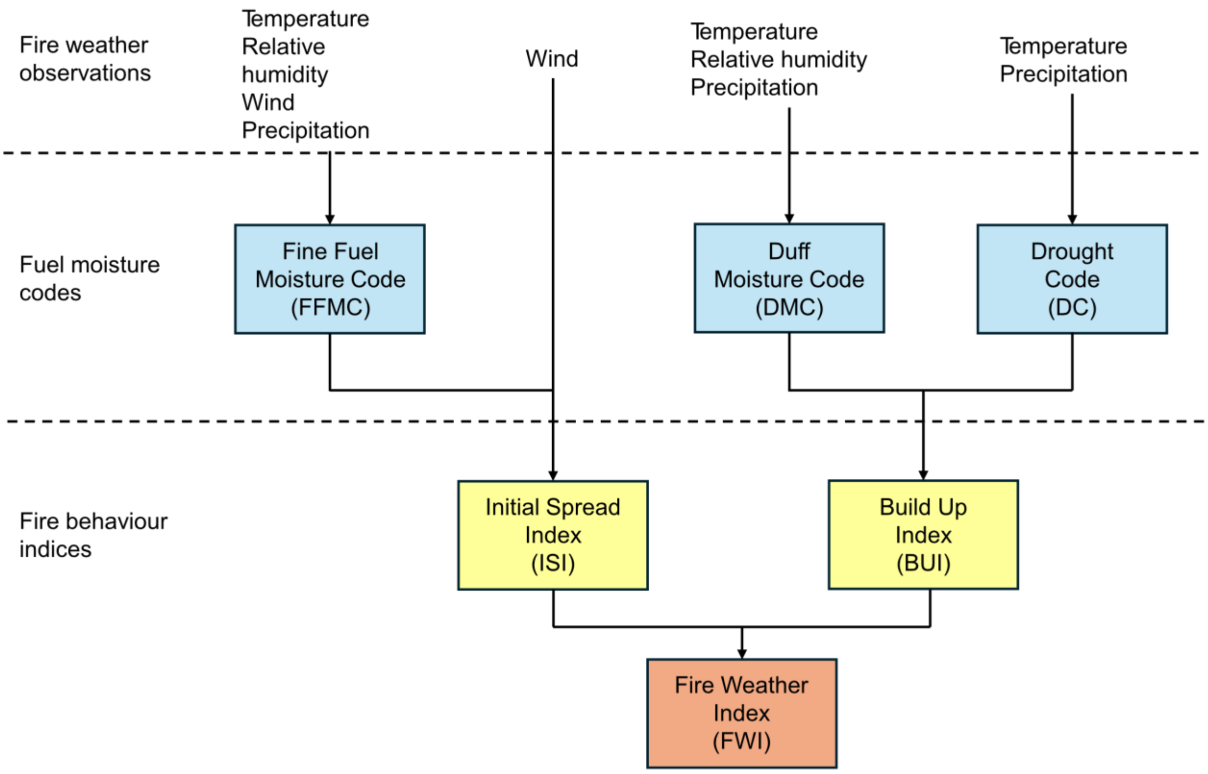

Figure 4.2. The Canadian Fire Weather Index system.

For model training and validation, we used the FireCCI v5.1 burned area product (Lizundia-Loiola et al., 2020) with a minimum confidence threshold of 80 %. This value was chosen to align with the high confidence class of MODIS active fires to reduce the likelihood of commission errors, after initially considering a threshold of 50 %. For testing (2021-2023), we used the MCD64A1 product (Giglio et al., 2018). FireCCI was preferred for training due to its improved performance in detecting small fires in Russia compared to MCD64A1 (Clelland et al., 2024b), although its limited temporal range (2001-2020) constrained the model training period.

Future climate data were obtained from the NASA Earth Exchange Global Daily Downscaled Projections project (NEX-GDDP-CMIP6 - Thrasher et al., 2021, 2022), which provides downscaled global climate projections at 0.25° resolution, derived from the original 2.5° resolution. Corresponding fire danger indices were sourced from NEX-GDDP-FWI (Park et al., 2023), which uses the same methodology as CEMS to derive the Canadian Fire Weather variables.

To derive future projections we used two models from the CMIP6 ensemble – ACCESS-CM2 (Bi et al., 2020) and MRI-ESM2-0 (Yukimoto et al., 2019) – under three Shared Socioeconomic Pathway (SSP) scenarios (O'Neill et al., 2016, Meinshausen et al., 2020) – SSP1-2.6 (low emissions pathway), SSP2-4.5 (medium emissions pathway) and SSP3-7.0 (high emissions pathway) – for the years 2025-2100. The two Earth system models were selected for their capacity to reproduce historical weather data across the study region, and the projected changes in air temperature and precipitation. The historical accuracy of the models was evaluated against ERA5 climate data by quantifying RMSE by month by ecoregion (Genet et al., in prep). SSP5-8.5 was not used as it is considered increasingly unlikely given policy changes over the last decade (Hausfather and Peters, 2020, Meinshausen et al., 2022, Scafetta, 2024).

To ensure consistency, the same variables were used for both model training and making the future projections, with unit conversions applied where necessary. *rsds* and *rlds* from ERA5-Land were converted from J/m^2 to W/m^2, and the future precipitation variable (*pr*) was converted from the mean of the daily precipitation rate (kg m^{-2} s^{-1}) to the total monthly precipitation in metres.

An initial assessment showed that significant biases existed between CMIP6 projections and ERA5-Land and CEMS training data and impacted model results. Therefore, we applied bias corrections using the delta method, which has been shown to perform well for monthly climate variables in the ABZ (Hill et al., 2015, Walsh et al., 2018), to ensure comparability. For each month during the overlapping period (2001-2023), we calculated the mean difference between CMIP6 and observed values for each ecoregion and applied this correction to the future climate and fire danger parameters. A visual example of this process, applied to wind speed in the Mid-Canada Boreal Plains forests ecoregion, is shown in Figure 4.3.

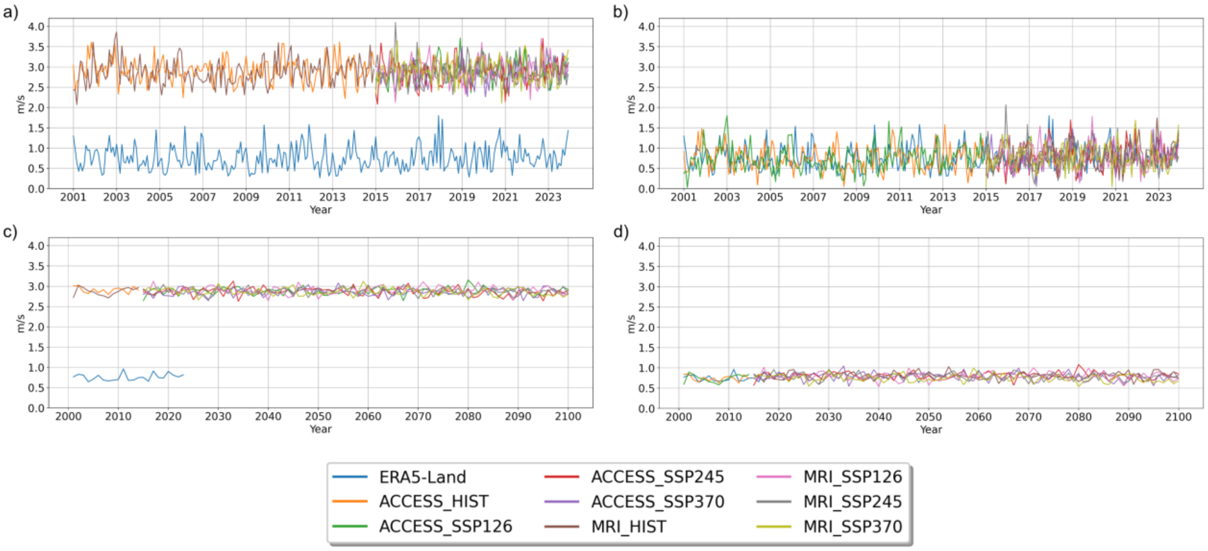

Figure 4.3. Bias correction for the wind speed (ms^{-1}) in the Mid-Canada Boreal Plains forests ecoregion. The original monthly raw and corrected data for 2001-2023 are given in a) and b), respectively, with the mean annual raw and corrected data for 2001-2100 in c) and d).

Topographic variables and land cover remained unchanged between the historic and future time periods. Missing data were assigned the value -9999, which was converted to NaN when read into the model. Since we focus on the impact of climate variables on burned area and due to the high percentage of lightning strike ignitions in the ABZ, anthropogenic variables are beyond the scope of this study and therefore excluded.

XGBoost model

In this study we considered a Gradient Boosted Decision Trees (GBDT - Natekin and Knoll, 2013) model using the XGBoost Python package (Chen and Guestrin, 2016) and a Random Forest (RF - Breiman, 2001) model using the scikit-learn Python package (Pedregosa et al., 2011). We opted for the XGBoost model due to its superior computational efficiency, options for parameter modification, overfitting control and handling of class imbalances (Langford et al., 2018, Sahin, 2020).

GBDT models follow a boosted framework where decision trees are sequentially built to correct the residual errors of the combined prediction of the previous trees (Figure D4.1; p. 187). Unlike an RF model, which trains trees independently, XGBoost optimises model performance by iteratively refining weak learners, leading to improved prediction accuracy. XGBoost incorporates regularisation techniques to prevent overfitting and uses a sparsityaware algorithm to efficiently handle large datasets. Given its capacity to capture subtle interactions between climate, topography and fire occurrence, the XGBoost model provides more refined predictions, particularly in areas with complex fire dynamics.

In this work, a regression model is preferable to a classification model as wildfire occurrence and burned area are inherently probabilistic and continuous, and predicting probabilities provides more information than binary class labels alone. Using the "binary logistic" regression objective in XGBoost constrains the predictions to probabilities and limits the effect of extreme values relative to squared-error losses, which improves robustness to imbalanced and noisy burned area data.

Our training dataset is severely imbalanced; previously burned pixels account for just 0.044 % of all training data across both study regions. An XGBoost model contains measures, as described in this section, to help the algorithm place greater emphasis on the minority class during training. Other ML models, such as Convolutional Neural Networks (CNNs - LeCun and Bengio, 1995), can struggle with severely imbalanced training datasets, and are often characterised by limited transparency and interpretability (Buda et al., 2018, Zhang et al., 2019, Zhang et al., 2021).

To test how our model responded to the severely imbalanced dataset, we began by using a 50:50 ratio of previously burned to unburned pixels for model training. We then subsequently incrementally increased the number of unburned pixels whilst maintaining the same number of burned pixels, so the ratios became 40:60, 30:70, 20:80, 10:90, 1:99, and finally 1:999. The maximum tree depth was initially set to the default value of 6, which we found did not result in overfitting. We kept the predictive probability threshold at 50 % for the duration of the model testing. We decided on the 1:999 ratio to include as much training data as possible and as higher proportions of burned pixels led to substantial overestimations of burned area (BA): increases by a factor of 300-700 for the 50:50 and 40:60 ratios, depending on area. Note that in the South Siberia model the final ratio was approximately 1:930 as we used all the pixels available for training.

The models were evaluated using the area under curve (AUC) of the receiver operating characteristic (ROC), and confusion matrices. The ROC curve plots the True Positive Rate (TPR) against the False Positive Rate (FPR) at each possible threshold. A perfect (overfitted) model would have a score of 1.0. The AUC represents the likelihood that, when given a randomly selected positive and negative example, the model will assign a higher rank to the positive instance than the negative one and is calculated by taking the area under the ROC curve. The TPR and FPR are calculated as in Equations 4.2a and 4.2b, respectively, where TP, TN, FP and FN are True Positive, True Negative, False Positive and False Negative instances.

$$TPR = \frac{TP}{TP + FN} \ (4.2a); \ FPR = \frac{FP}{FP + TN} \ (4.2b)$$

These first tests included running both RF and XGBoost models at each ratio of burned to unburned pixels, although we quickly decided on the XGBoost model due to its superior performance at predicting True Positives and reducing False Negatives, and ability to tweak more model parameters. Our choice of model is supported by the findings of Di Giuseppe et al. (2025), who state that the XGBoost model is superior to both RF and CNN models when predicting fire activity, and only the XGBoost model was used going forward.

Since a model can easily achieve over 99 % accuracy by predicting zero everywhere, the accuracy metric was not considered. As we considered the overall omission and commission errors, the confusion matrix was chosen over precision, recall, F1-score and Intersection over Union.

Having found the optimal ratio of burned to unburned pixels for training the model, we implemented a weighted logistic loss function to penalise the model for predicting False Negative values. Failing to predict an observed fire (a False Negative) is more consequential than issuing a false alarm as the training dataset is severely imbalanced in favour of unburned pixels. The negative log-likelihood loss function $\mathcal{L}$ is calculated using Equation 4.3, where y_i is the true label (0 or 1), the predicted probability p_i is computed as in Equation 4.4, $y_{pred,i}$ is the raw prediction score before applying the sigmoid function, and exp is the exponential function.

$$\mathcal{L} = -\sum_i (y_i \log p_i + (1 - y_i) \log(1 - p_i)) \tag{4.3}$$

$$p_i = \frac{1}{1 + exp\,(-y_{pred,i})} \tag{4.4}$$

The gradient and Hessian (first and second derivates) were calculated using Equations 4.5 and 4.6, respectively. Here, we used a weight of 10 to penalise False Negative values by a factor of 10, which modifies the gradient and Hessian for positive cases. This value represents a moderate but effective adjustment that counteracts class imbalance without causing instability or excessive overprediction of fire. Preliminary sensitivity testing indicated that values of this order improved the number of True Positives and significantly reduced False Negatives while maintaining overall model stability.

$$\frac{\partial \mathcal{L}}{\partial y_{pred,i}} = p_i - y_i \tag{4.5}$$

$$\frac{\partial^2 \mathcal{L}}{\partial y_{pred,i}^2} = p_i(1 - p_i) \tag{4.6}$$

To find the optimal combination of parameters for each model, we ran a scikit-learn exhaustive grid-search cross-validation model (GridSearchCV) to test multiple parameters for the learning rate, max depth and number of estimators. This model involved a 3-fold cross-validation across all processors, finding the optimal combination of parameters according to the AUC score. The optimal number of boosting rounds was 11,500 for South Siberia and 13,000 for the Northern region, both with a learning rate of 0.01 and max depth of 6 (Table C4.1; p. 173). Higher values of the max depth quickly led to overfitting.

We then introduced the class weight parameter, which controls the balance between positive and negative weights, set at a value of 100, to balance the loss function and reduce the shown bias of overpredicting the majority (unburned) class. The value of 100 was chosen after using a similar process when selecting the optimal proportion of burned to unburned pixels for model training. We started with a value of 999 (the ratio of burned to unburned pixels), reducing the value in turn, and found that by using 100 we balanced the omission and commission errors.

This combination of parameters was tested initially on the validation and testing datasets, as well as on the bias corrected 2015-2023 downscaled CMIP6 model data for all SSP scenarios and compared with actual data from FireCCI v5.1 and MCD64A1. We found that the Northern model tended to overestimate the BA at central latitudes in both North America and Eurasia, whereas the South Siberia model predicted BA in the correct areas but with lower burn probabilities. Furthermore, our Northern model did not capture the severity of the 2023 fire season in Canada. To address this, we included additional training data from North America only for the years 2021-2023, using the MCD64A1 fire data. MCD64A1 is a reliable product in North America, similar to FireCCI v5.1, but misses substantial amounts of BA in Russia (Clelland et al., 2024b). Thus, the final model parameters and values were given as in Table 4.2.

Table 4.2. Parameters and values used in model training for making the future projections.

Parameter	Northern region	South Siberia region
No. of burned pixels	72,074 (maximum available)	45,788 (maximum available)
No. of unburned pixels	72,001,926 (1:999 ratio)	42,575,572 (maximum available)
No. of boosting rounds	13,000	11,500
Learning rate	0.01	0.01
Max. depth	6	6
Class weight factor	100	500
False Negative weight	10	10

Post-processing of the model outputs and conducting the analysis

Between November and March, several isolated coastal pixels in the high Arctic exhibited irregular, non-zero values in the model outputs. This was due to erroneous, anomalously high values in the fire weather dataset. For instance, DC values in coastal areas of northern Greenland attain a maximum of 27,461, where the median value across the entire domain and time series is 198. To address this, these pixels were assigned the value of zero to align with the surrounding areas.

We assessed feature importances using the built-in get_score function in XGBoost, which quantifies how much each variable improved prediction performance when used in a split during model training. In addition, we considered SHapley Additive exPlanations (SHAP) values using the shap Python package (Lundberg and Lee, 2017), which indicate how the models' predictions of BA vary based on the input variables. Positive SHAP values indicate an increase in the projected burned area, while negative SHAP values suggest a decrease.

For the analysis, outputs from both models were combined to examine changes across ecoregions. Unless stated otherwise, we considered changes over three time periods – near-future (2025-2050), middle-future (2051-2075) and far-future (2076-2100) – for both CMIP6 models (ACCESS-CM2 and MRI-ESM2-0) and three SSP scenarios (SSP1-2.6, SSP2-4.5 and SSP3-7.0). Only pixels with a predicted burn probability of 50 % or greater were included in the analysis.

To determine the appropriate statistical methods for the analysis, the BA output was checked for normality using the Shapiro-Wilk test (Shapiro and Wilk, 1965) through the shapiro function from the scipy.stats Python package (Virtanen et al., 2020). All ecoregions with fire occurrence across both models and all SSP scenarios returned non-normal distributions; therefore, non-parametric tests were employed throughout the analysis.

A trend analysis of the output BA was conducted using the non-parametric Mann-Kendall test (Mann, 1945, Kendall, 1975), implemented via the pyMannKendall Python package (Hussain and Mahmud, 2019). This test was performed for the full projection period (2025-2100) and the three 25-year periods.

To examine the variability of BA over time, we considered the interquartile range (IQR), defined as the difference between the 75th and 25th percentiles. IQRs were calculated for each 25-year period and for overlapping 30-year moving windows: 2025-2054, 2030-2059, …, 2070-2099. We also used the IQR to present the changing seasonality of BA across each 30-year moving window period through boxplots. Extreme fire years were defined as those exceeding the 95th percentile during the historical baseline period (2001-2023). The fire return interval (FRI), expressed in years, was calculated as the total ecoregion area divided by the mean annual BA.

Results

The average AUC scores for both models across the validation and testing periods are presented in Table 4.3. Both models perform well overall, with AUC scores exceeding 0.85 for the Northern model and 0.72 for the South Siberia model. It is likely that our South Siberia model identifies areas that may have burned not captured by the input burned area (BA) products, contributing to the relatively lower AUC scores, where validation-period AUC scores ranged from 0.78 to 0.86, compared to 0.91-0.93 in the Northern model. The lower AUC scores for the 2021-2023 period are expected due to the use of MCD64A1 data instead of FireCCI51, as the MCD64A1 product has been shown to underestimate BA across Russia (Clelland et al., 2024b). In addition, fires in South Siberia often occur in grassland and steppe ecosystems, where rapid vegetation regrowth can make fire detection more challenging.

Table 4.3. Average AUC scores for both models across the validation (2008, 2015 and 2020) and testing (2021-2023) periods.

	2008	2015	2020	2021	2022	2023
Northern	0.91	0.93	0.92	0.88	0.89	0.85
South Siberia	0.85	0.78	0.86	0.72	0.83	0.72

According to FireCCI51 and MCD64A1 data, an average of 8.88 Mha burned per year across the ABZ for the historic 2001-2023 period. Running our models over the same historical period, we projected a mean annual BA of 8.95 Mha. This slight increase is due to the models presenting a high probability of burn for pixels surrounding those which actually burned. The 2023 fire season in Canada, the largest fire season in this region in the 21st Century (Jain et al., 2024, Wang et al., 2024), was the only time our models predicted less BA than observed. Figure 4.4a shows how our model output, aggregated to 2.5° grid cells, compares to observed MCD64A1 data for the June 2023 fires in eastern Canada. However, Figure 4.4b, showing predicted fire locations overlaid with actual BA, indicates that the model captures the spatial extent of the 2023 fires, albeit with many predictions falling below the 50 % threshold. As our analysis only includes pixels with a predicted burn probability of 50 % or greater, this suggests we are likely to see a tendency to underestimate BA in eastern Canada.

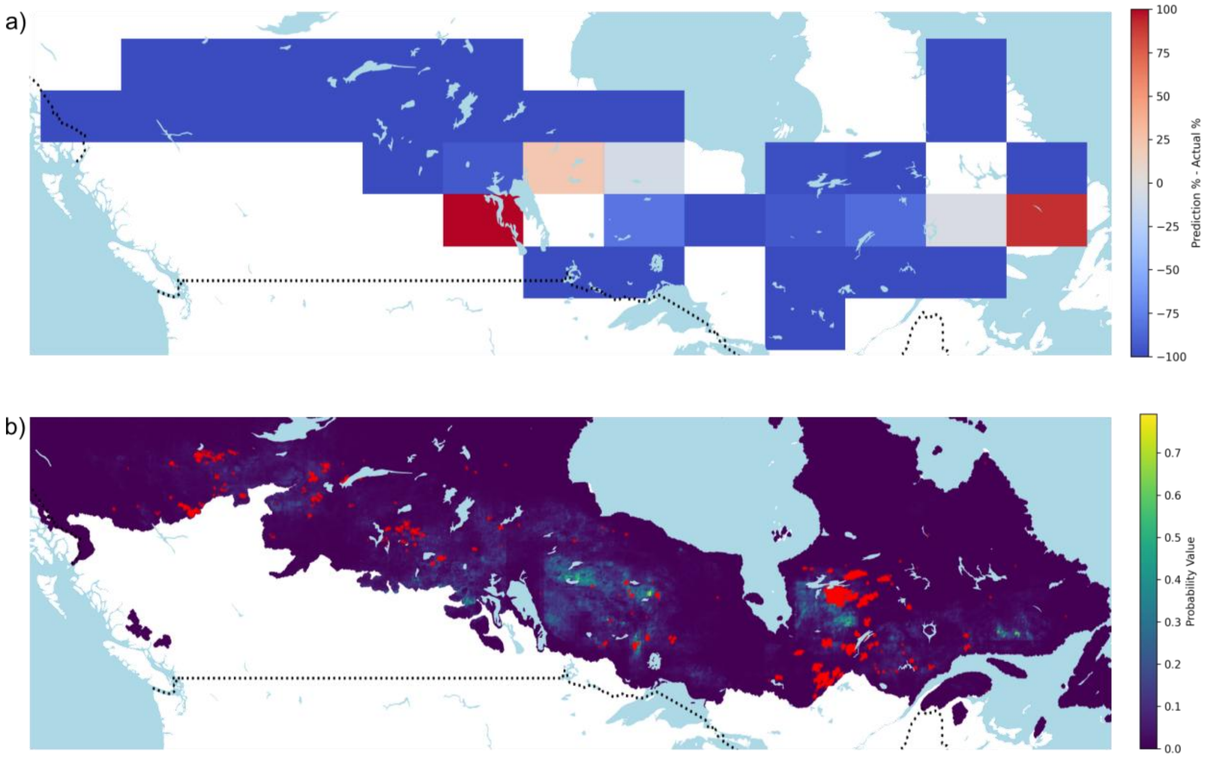

Figure 4.4. Model predictions for June 2023 in Canada, aggregated to 2.5° grid cells of fire occurrence, compared to actual data (a). Blue cells indicate our model underestimates the observed data, whereas red cells indicate our model overestimates the observed data at the 50 % probability level. The raw model predictions at the pixel level are given with the observed fires overlaid in red (b) for the same month.

The relative importances of input features during model training, as determined by XGBoost, are shown in Figure C4.1 (p. 173), whereas the impact of each input variable on output BA is shown in the SHAP value summary plots for the Northern and South Siberia models in Figure 4.5.

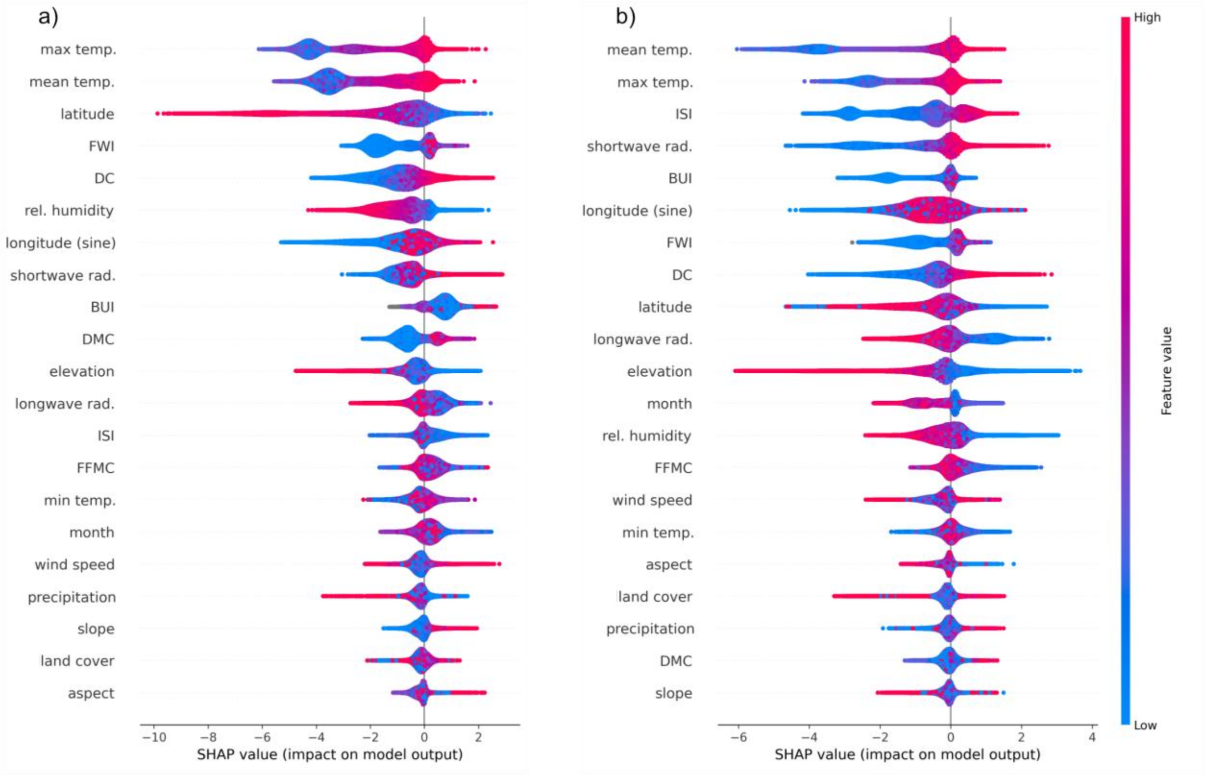

Figure 4.5. Summary plots of Shapley additive explanations (SHAP) values for the Northern a) and South Siberia b) models. Higher, positive, SHAP values suggest that the input variable has a stronger influence on increasing the amount of the burned area projected by the models, whereas lower, negative, SHAP values indicate that the variable has a stronger influence on decreasing the amount of projected burned area. Features are sorted from most to least important based on their average absolute SHAP value. The colour scale represents the input value of each variable across its range, with blue indicating low values and red indicating high values.

Considering the impact of each variable on output BA, the maximum and mean 2-metre air temperatures (*mx2t* and *t2m*) were the most influential for both the Northern and South Siberia models (Figure 4.5). As *mx2t* and *t2m* increase, their impact on BA also increases, an observation that also applies to the next most important variables in South Siberia: Initial Spread Index (ISI) and surface solar radiation. In our Northern model, latitude is the third most influential variable, which shows an inversely proportional effect: as latitude increases northwards the BA decreases. Across both models, slope, land cover type, aspect and total precipitation were among the variables with the weakest influence on the overall BA. Precipitation has a longer-term effect by influencing the fire danger indices, rather than an immediate impact during the month of burn.

Combining the output from both models, Table 4.4 gives our predicted mean annual BA for the whole region through the three 25-year future time periods and for each CMIP6 model and SSP scenario, compared to the historic period.

Table 4.4. Mean annual burned area (Mha) across the entire Arctic-boreal zone for each SSP scenario, model and time period.

Scenario	Model	Time period			
		2001-2023	2025-2050	2051-2075	2076-2100
Historical	Observed	8.88	-	-	-
	Our model	8.95	-	-	-
SSP1-2.6	ACCESS-CM2	-	9.71	9.35	9.06
	MRI-ESM2-0	-	9.13	9.31	11.00
SSP2-4.5	ACCESS-CM2	-	10.30	10.49	11.58
	MRI-ESM2-0	-	9.59	8.79	8.21
SSP3-7.0	ACCESS-CM2	-	10.01	10.32	14.63
	MRI-ESM2-0	-	13.50	11.56	11.81

The models project an increase in the mean annual BA for five of the six climate model-scenario combinations across all three future time periods compared to the historic average, however the magnitude and pattern of these increases differs. Under MRI-ESM2-0 SSP1-2.6 and ACCESS-CM2 SSP2-4.5 and SSP3-7.0, we see that mean annual BA continually increases through time. The increase is relatively modest from the near- to middle-future periods, followed by a substantial rise toward the end of the century, to 11.00, 11.58 and 14.63 Mha, respectively; the latter being a 64.75 % increase over the observed historic annual mean.

For the ACCESS-CM2 SSP1-2.6 and MRI-ESM2-0 SSP3-7.0 combinations, the models project mean annual BA will be greater than the historic average across all future time periods, however the pattern is not continually increasing. The near-future will see the largest increase in mean annual BA, followed by a decrease in both cases to the middle-future. While the latter grouping then increases again to the far-future (11.81 Mha), under ACCESS-CM2 SSP1-2.6 conditions the far-future will see an increase in mean annual BA of just 1.28 % compared to the historic period (9.06 Mha).

The MRI-ESM2-0 SSP2-4.5 combination is anomalous compared to other scenarios. Although it shows an increase in mean annual BA for the first 25-year period, the subsequent 50 years show decreases, with the middle-future having slightly less annual BA than the 2001-2023 period (8.79 Mha – a 1.76 % decrease), and the far-future having 8.25 % less (8.21 Mha). This is most likely due to our model producing lower probabilities of burn within this permutation (average non-zero burn probability 52 % compared to 58 % across other combinations); thus, the overall BA is decreased as a greater proportion is below the 50 % analysis threshold.

Whereas Table 4.4 gives the mean annual BA for the entire ABZ, Figure 4.6 shows the percentage change in BA for each ecoregion through the future periods and SSP scenarios compared to the historical baseline. Note that some ecoregions experience apparent extreme increases or decreases, especially around high-latitude Arctic areas, due to the very small (< 0.1 Mha) BA values in both the historic and future periods.

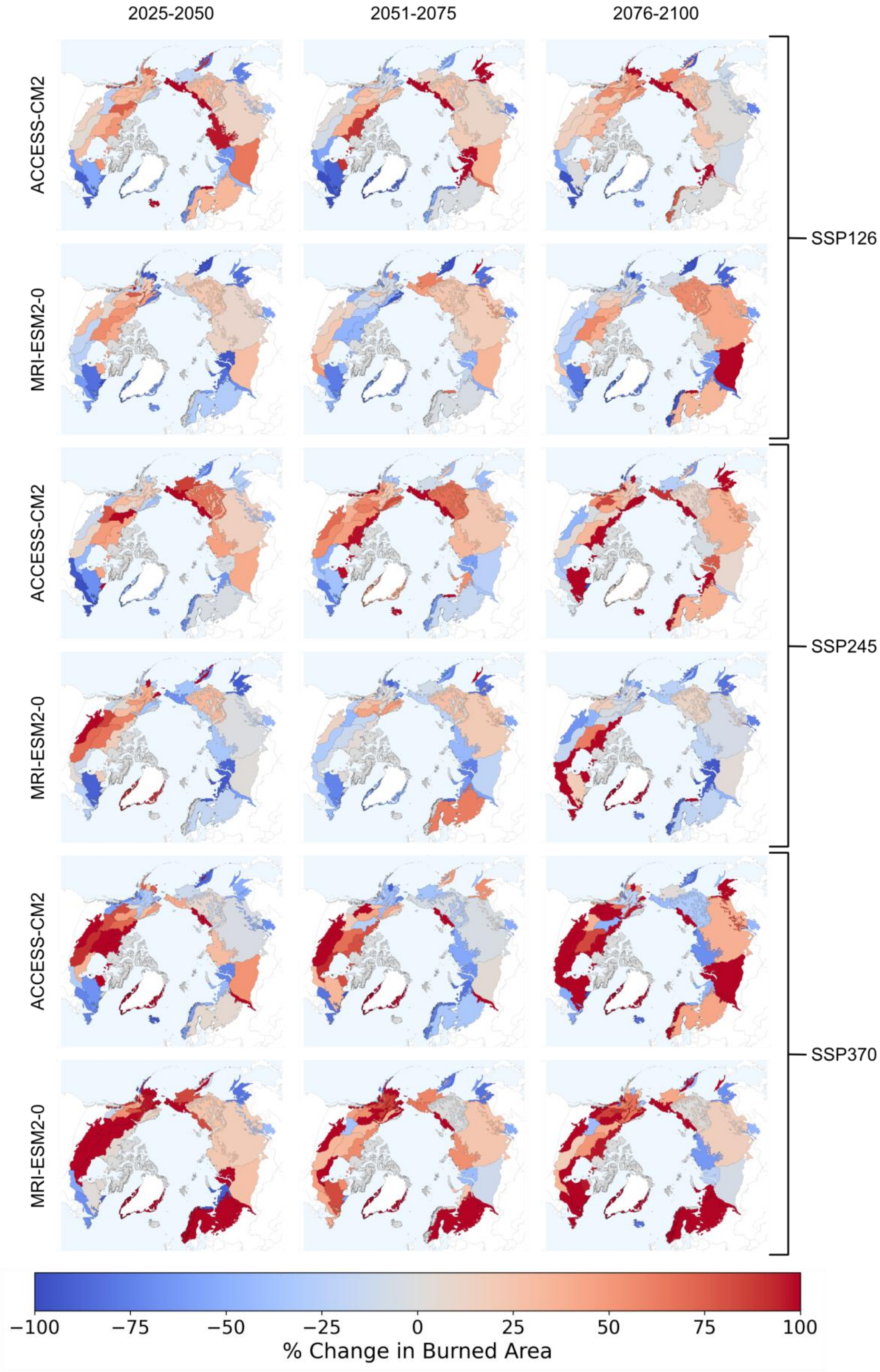

Figure 4.6. Percentage change in mean annual burned area for each ecoregion compared to the observed 2001-2023 historic baseline.

For future BA projections derived from ACCESS-CM2, we observe an increase in the amount of mean annual BA across the majority of ecoregions as time progresses and also with strengthening SSP. This is most pronounced in the far-future period for SSP3-7.0, where most North American ecoregions experience a high percentage (83-270 %) increase; an average of 116 % to 5.16 Mha per year across the whole region. The largest ecoregion by area, the East Siberian taiga, also shows its greatest increase (38 %) under this scenario, with a mean of 5.43 Mha per year.

MRI-ESM2-0 projections exhibit more fluctuations and fewer extreme changes compared to ACCESS-CM2, likely due to differences associated with the future temperature and precipitation data (Figures C4.2 to C4.4; pp. 174-176). For instance, under SSP1-2.6, *t2m* and total precipitation are projected to increase from the near- to middle-future periods, but then decrease in the far-future period. This is most notable for the West Siberian taiga ecoregion, which is the only boreal ecoregion where the mean annual BA is expected to at least double in the far-future period under this scenario, with an average of 1.38 Mha burned per year, due to a significant decrease in the amount of precipitation within the ecoregion.

Compared to the observed historical mean, for many scenarios parts of eastern Canada show a decrease in the mean annual BA for both CMIP6 models, as the large fire year of 2023 increases the historic mean BA across the region from 0.35 to 0.51 Mha (a 46% increase). However, compared to the modelled historic mean (0.41 Mha), the region will see annual mean increases for sixteen of the eighteen scenario-model-time period combinations – the exceptions being the SSP1-2.6 scenario in the middle-future period and SSP2-4.5 scenario in the near-future period, both for ACCESS-CM2. Extreme fire years, such as 2023, will occur in this area in the future, especially towards the end of the century.

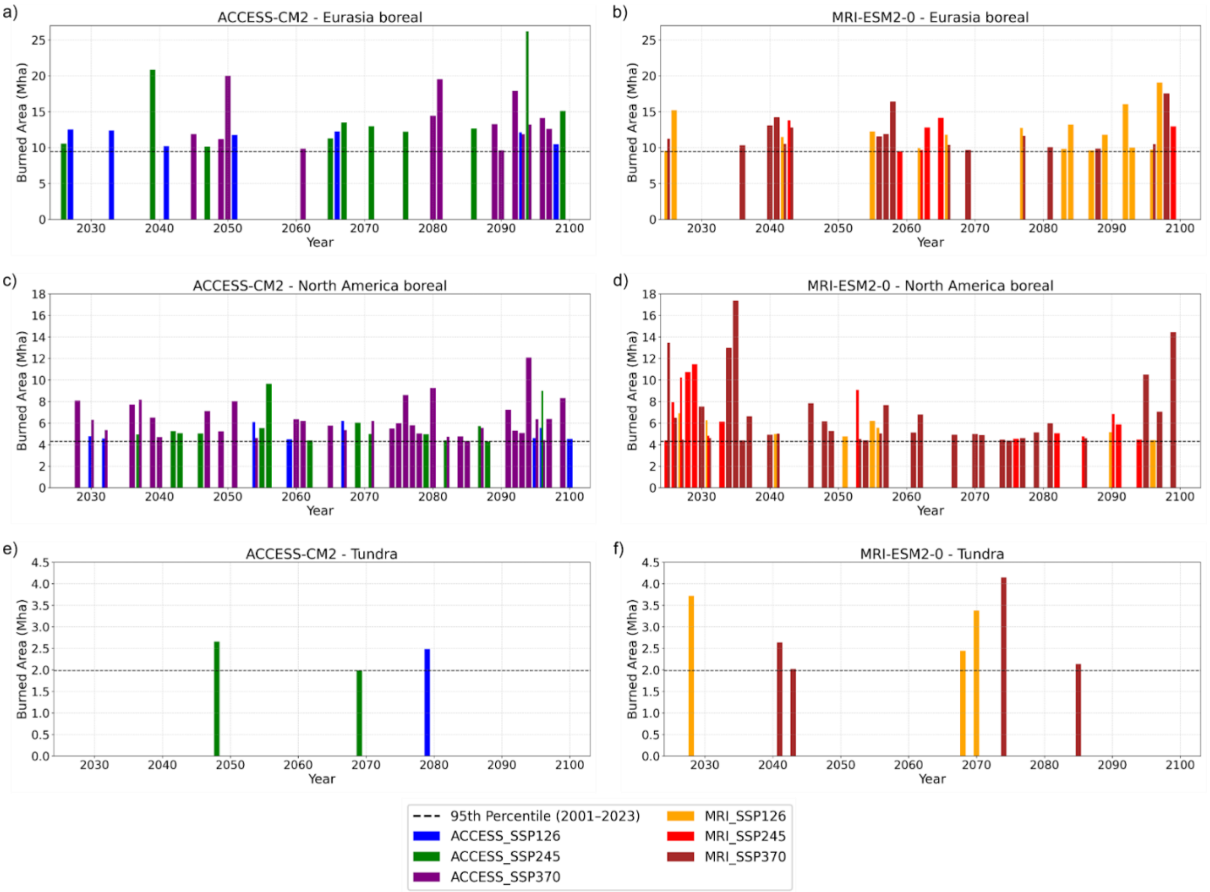

Figure 4.7. Extreme fire years in Eurasia boreal (a, b), North America boreal (c, d) and tundra (e, f) ecoregions for ACCESS-CM2 and MRI-ESM2-0, respectively. An extreme year is one which exceeds the 95th percentile (dashed black line) from the historic (2001-2023) data within each region. Full bar plots for each region, CMIP6 model and SSP scenario are shown in Figures C4.5, C4.6 and C4.7, respectively.

Occurrences of extreme fire years from our model outputs, defined as any year with BA above the 95th percentile from the historic (2001-2023) period within each region are shown in Figure 4.7. North American boreal ecoregions are expected to see the largest increase in the number of extreme fire years, especially under the SSP3-7.0 scenario – up to one in every three years will be extreme in this case. Here, similar to patterns of the mean annual BA (Figure 4.6), the frequency of extreme fire years increases with time for ACCESS-CM2 and sees a middle-future dip with MRI-ESM2-0. The same tendencies are shown within the Eurasian boreal ecoregions, although there are fewer extreme fire years here – ranging from one every twelve years to one in five, depending on scenario.

For each region we conducted a Mann-Kendall test to see if any statistically significant monotonic trends exist. Across the Eurasian boreal, North American boreal, and tundra regions the trend for the entire 2025-2100 period is statistically significant increasing for each CMIP6 model and SSP scenario (Table C4.2; p. 180). The area with the highest mean increase was the Eurasian boreal under the ACCESS-CM2 SSP3-7.0 grouping, at 0.089 Mha per year. We also considered the variability in BA through time (Table C4.3; p. 181) using the IQR for each 25-year period. There are no consistent tendencies of the BA variability through time, scenario or region. The variability peaks in the Eurasian boreal region under the ACCESS-CM2 SSP3-7.0 combination, increasing from 2.63 Mha in the near-future to 7.47 Mha in the far-future.

Fire seasonality in the North American boreal region differs depending on the model used. Under the three SSP scenarios from the ACCESS-CM2 model, fires will continue to exhibit a single peak in July (~ 60 %) with less burned area in August compared to historic observations. However, under MRI-ESM2-0 scenarios, the peak will be split across June and July (~ 40 % each), with a seasonal shift of fires to begin earlier in the year towards the end of the century (Figure 4.8). For four of the six model-scenario combinations, we continue to see a bimodal seasonal distribution of fires in the Eurasian boreal, with South Siberia having an initial spring peak, and more northerly latitudes having a second, summer peak (Figure C4.8, p. 182) The spring peak occurs a month later than compared to the historic period, although the proportion of earlier fires will increase through time. Under SSP1-2.6 and SSP2-4.5 from the MRI-ESM2-0 model, the spring peak is less well-represented, with a more even split between spring and summer, likely due to South Siberia pixels having a lower probability of burn below the 50% analysis threshold, as seen with the overall burned area. Tundra ecoregions are projected to exhibit a single July peak (~ 60 %) across both models and all scenarios, with the length of the fire season increasing by a month for the ACCESS-CM2 SSP scenarios through time (Figure C4.9, p. 183). The observed historic peak is split more evenly between July and August which is missed by our models due to the lower burn probabilities.

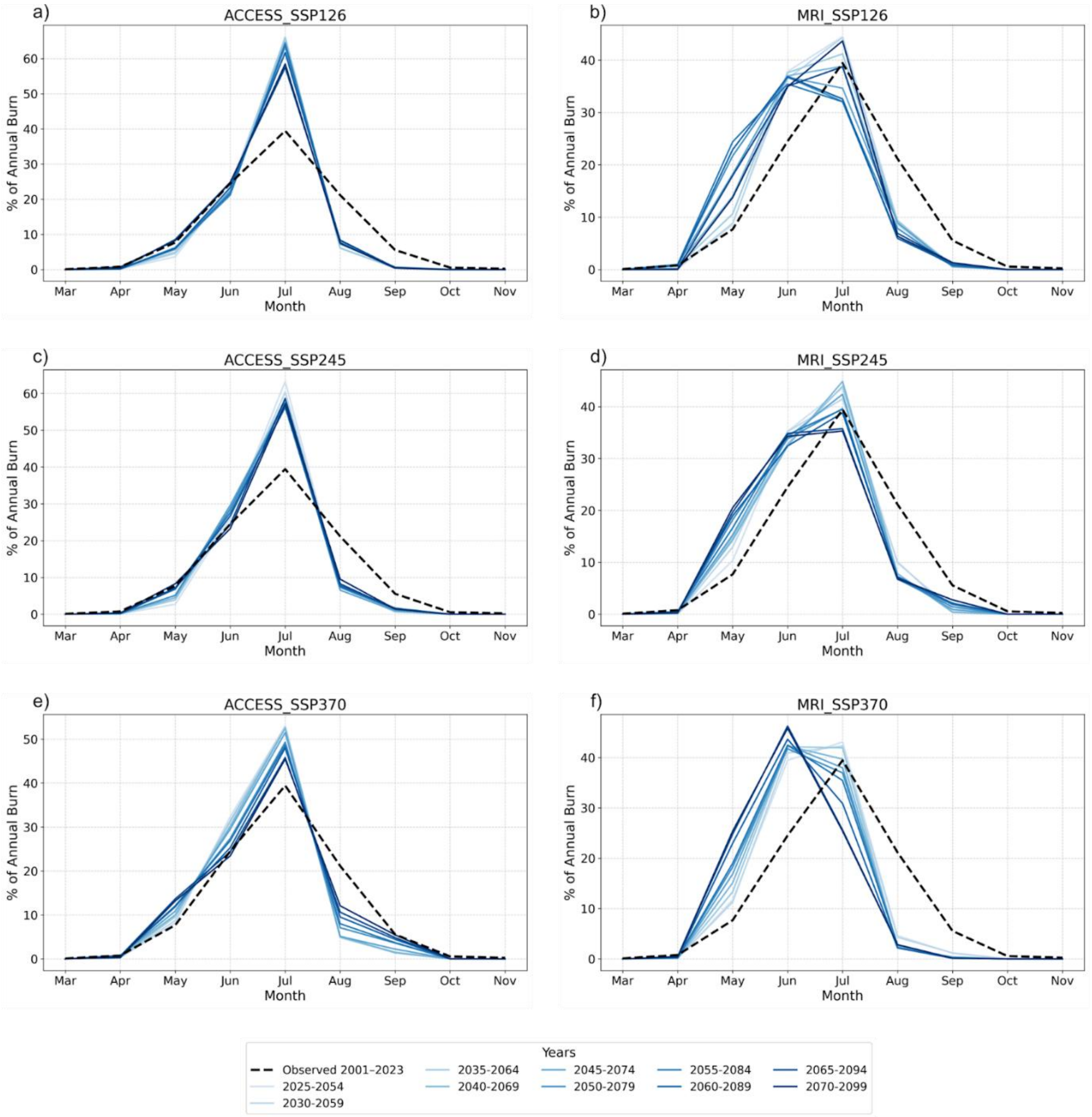

Figure 4.8. Seasonality of burned area for 30-year moving windows in the North America boreal ecoregions under SSP1-2.6 (a, b), SSP2-4.5 (c, d) and SSP3-7.0 for ACCESS-CM2 and MRI-ESM2-0, respectively. Only the months March to November are shown, and the lines become darker as time progresses. The dashed black line shows the observed 2001-2023 mean.

The fire return interval (FRI) was calculated for each ecoregion and 25-year future time period, and is given in Figure C4.10, with the change from the observed 2001-2023 period in Figure C4.11 (pp. 184-185). The changes in FRI through time and scenario are relatively minimal, with few ecoregions experiencing a significant change from the historic baseline. A large increase in FRI is seen in the Okhotsk-Manchurian taiga ecoregion, located in Russia’s Far East, across each of the MRI-ESM2-0 scenarios and time periods, suggesting that we underestimate BA in this model. The largest number of FRI decreases occur under the SSP3-7.0 scenario of both models, across North America and western Eurasia, suggesting a higher frequency of fire activity in these regions in the future. Increases are seen in eastern Canada in the near- and middle-future periods due to the 2023 fire season substantially increasing the observed historic baseline mean, however compared to the modelled historical mean no change in FRI is observed for sixteen of the eighteen scenario/time period combinations.

Discussion

Our models project substantial increases in BA across the ABZ through the 21st Century, with the magnitude and spatial extent of change highly dependent on scenario and model choice. These findings underscore the growing influence of fire on high-latitude landscapes in a warming climate and rising concerns about ecosystem resilience, carbon loss, and feedbacks to the climate system. Despite some variability between the two CMIP6 models used (ACCESS-CM2 and MRI-ESM2-0), consistent patterns of increasing BA in key fire-prone regions provide robust evidence of widespread intensification in fire regimes.

Temperature and fire weather indices reflect the underlying energy and moisture dynamics governing fire risk. These predictors generally capture the effects of fuel availability, dryness, and atmospheric conditions related to fire ignition and the extent of total burned area. For both our Northern and South Siberia ML models, the most influential predictors were the mean and maximum 2-metre air temperatures (*t2m* and *mx2t*). Their positive association with BA is consistent with empirical evidence linking elevated temperatures to fuel drying, increased evapotranspiration, and enhanced flammability (Pausas and Keeley, 2021). Southern Siberia fires are more often flash, "runaway" fires (Kharuk et al., 2021), which suggests why the initial spread index (ISI), surface solar radiation and build up index (BUI) emerged as key drivers here. By contrast, in the Northern model, latitude was ranked third in importance, showing a strong inverse relationship with BA, reflecting decreasing vegetation biomass and fire-prone conditions at higher latitudes. The Fire Weather Index (FWI) and Drought Code (DC) variables were also influential in the Northern model, implying that longer term build up and lag, which are accounted for in these indices, are important in forested areas. For instance, decreases in FWI and DC in central and western Canada between the early- and middle-future periods in the ACCESS-CM2 SSP3-7.0 combination were likely responsible for the decrease in mean annual BA between these periods. Temperature and fire weather indices reflect underlying energy and moisture dynamics governing fire risk. These predictors generally capture the effects of fuel availability, dryness, and atmospheric conditions related to fire ignition and the extent of total burned area.

Variables such as slope, aspect, and land cover had a limited role. Monthly total precipitation also exerted little direct influence in the model, likely because it is already incorporated, both in current and lagged form, into the fire danger fuel moisture codes (DC, DMC and FFMC).

As a result, standalone precipitation did not provide substantial additional predictive value, despite its known role in influencing fire behaviour, including ignition likelihood and suppression potential (Peterson et al., 2010).

Despite some variability between the two CMIP6 models used, consistent patterns of increasing BA in key fire-prone regions provide robust evidence of widespread intensification in fire regimes. North American boreal forests are projected to experience the greatest increases in BA, with mean annual values rising by an average of 116 % (from 2.39 to 5.16 Mha per year), and as much as 270 % in some ecoregions, under the ACCESS-CM2 SSP3-7.0 combination in the far-future period (2076-2100). This result is consistent with the findings of Wotton et al. (2010), who suggested that fires across Canada could increase by 75-140 % by the end of the century. In contrast, parts of Eurasia show more moderate increases or even decreases in some scenarios, particularly using MRI-ESM2-0, chiefly due to more modest temperature changes in that climate model, which also affects the key fire danger variables.

The record of high quality circumpolar burned area is fairly short, and our historical baseline includes the record-breaking 2023 fire season in Canada. This year alone increased the observed historic annual BA by 46%. As a result, our model shows decreases in mean annual BA in eleven of the eighteen scenario/time period combinations by comparison. However, compared to the modelled historical mean BA (0.41 Mha) and the observed mean for 2001-2022 (0.35 Mha), our model projects increases in this region for sixteen of the eighteen combinations, most notably under the SSP3-7.0 scenario in the latter half of the century. This suggests that large fire seasons, such as in 2023, could occur more regularly under high-emission scenarios and underscores the importance of accounting for interannual variability and the choice of baseline period when evaluating relative change.

The MRI-ESM2-0 model produced more fluctuations in both annual and extreme fire year projections than ACCESS-CM2, reflecting differing trajectories of projected temperature and precipitation variables in each model (Figure C4.2; p. 174). For instance, under MRI-ESM2-0 SSP1-2.6, both temperature and precipitation increase into the middle-future period (2051-2075) but decline thereafter (Figures C4.3 and C4.4; pp. 175-176), driving complex fire responses in ecoregions like the West Siberian taiga.

Extreme fire years, defined as annual BA above the 95th percentile of the 2001 to 2023 occurrences, are projected to become substantially more frequent, especially in North American boreal regions under high-emission scenarios, where previous 1-in-20-year events could become 1-in-3-year events. This pattern is mirrored, though less sharply, in Eurasian boreal forests, and is consistent with expectations from fire-climate theory and observational studies (Flannigan et al., 2009). The increasing occurrence of such years raises concerns about long-term ecosystem resilience, vegetation recovery, emissions of greenhouse gases and aerosols, and society's ability to respond and adapt to these changes. In tundra regions, extreme fire years remain infrequent but are projected to occur more often than in the historical period, suggesting potential encroachment of fire regimes into previously fire-resistant landscapes.

Despite the increase in frequency of extreme fire years, increases in total BA across boreal ecoregions remain modest. When excluding extreme years, the models do not project mean annual BA to be consistently higher in the future periods than in the historic period (Figures C4.5 and C4.6; pp. 177-178) and, as a result, the increases in total BA are moderate. This is not the case in tundra ecoregions, where the mean from non-extreme years is consistently higher in the future than the past (Figure C4.7; p. 179).

The shift in fire seasonality, marked by longer duration fire seasons, starting earlier and often ending later, across all regions, may further reduce recovery time between fire events and complicate suppression efforts (Flannigan et al., 2013, Tangney et al., 2022). This is especially evident under ACCESS-CM2 SSP3-7.0, where fire seasons extend by up to two months: nonetheless, spring ignitions also increase by up to 20 % in North America under MRI-ESM2-0 scenarios in the second half of the century.

Comparisons with other studies

Our results align with findings from recent studies using ML models to forecast future fire activity under climate change scenarios. For instance, Zhao et al. (2025) applied an XGBoost model to assess the role of threshold effects ("tipping points") in driving changes in BA across mid- to high-latitude ecosystems (from 30° N) over three broad time periods (2030-2050, 2051-2070 and 2071-2100). Their study included only nine climate, fire danger and anthropogenic variables at a coarser spatial resolution (0.25°) for pixels which had previously burned during the training period, although they considered all four SSP scenarios for six CMIP6 models.

They projected that most areas would experience a 41-58 % increase in BA by the end of the century relative to the 2001-2022 period, depending on climate scenario. However, they also identified that 7.6 % of the study area could see a substantial decline in BA (over 20 km^2 per grid cell). Our projections are more modest (36-52 %), likely due to methodological differences: we include every pixel within the study region, rather than only those previously burned, and we focus on higher latitude areas (from 43° N). Similarly, Stephens et al. (2025) found that, between 1983 and 2020, burned area across the circumpolar boreal increased by 53%, with large regional variability, including one ecoregion with a decreasing trend.

Shao et al. (2023) also used an XGBoost model to project future BA across China, incorporating a broad set of climate, topographic, vegetation, and social variables, and achieving model performance comparable to ours: AUC scores of 0.85 for testing and 0.82 for validation. Similarly, Herrmann et al. (2023) applied an ensemble of ML models to forecast fire in Brazil's Rio Grande do Sul state under two SSPs and found increasing fire risk, though they relied on a single CMIP6 model and twenty-year time steps.

Furthermore, our results support the conclusions from Abatzoglou et al. (2025) and Tian et al. (2025), which focus specifically on the impact of future changes in FWI values. The former study suggests that anomalously high FWI values will have the greatest impact in temperate forested ecosystems, including Siberia and Canada, whereas the latter study indicates that the length of the Eurasian fire season will increase as a result of higher FWI values.

Across these studies, increased fire activity under high-emission scenarios is observed, with fires projected to occur more frequently at lower latitudes. However, the present work contains a more comprehensive spatial and temporal coverage, a broader set of climate and fire danger variables, and a model architecture tuned to Arctic-boreal fire regimes. Most notably, we produce monthly projections, enabling seasonal analysis and improved management relevance, whereas previous studies have focussed only on changes over 20- or 30-year periods.

Study limitations

There are several limitations to the present study. Land cover in boreal ecosystems is dynamic and will continue to evolve both through the century and after fire occurrence. For instance, the tree line is changing in response to climate warming (Rees et al., 2020), as is shrubification in the tundra (Mekonnen et al., 2021). Our models cannot take into account how any changes in future land cover will affect BA, nor how projected changes in BA may in turn alter future land cover. Lightning strikes are the most common source of wildfire ignition in the ABZ (Veraverbeke et al., 2017); however we are unable to consider their impact due to the absence of a complete dataset encompassing the entire study area and both the training and projecting periods.

Similarly, the static latitude, longitude, and month parameters likely improve model performance by capturing spatial and seasonal patterns not fully explained by the gridded environmental predictors, particularly regional idiosyncrasies or seasonal indicators. However, because they do not change over time, relying on them may constrain the model's ability to respond dynamically to future changes in climate or vegetation, potentially limiting the generalisability of projections under novel conditions. Ideally, a model would learn these patterns from physical drivers alone, rather than relying on proxies.

Our training dataset only includes 23 years of BA due to MODIS satellite data becoming available from 2001. While earlier satellite imagery from AVHRR and Landsat is available globally from the 1970s, there are concerns regarding the consistency and reliability of global BA products derived from them (Clelland et al., 2024b). Although regional, Landsat-derived products are available for North America, we lack a reliable global, or at least Arctic-boreal, product which we could use to extend the training dataset further back in time.

The climate and fire danger data are provided at coarse native resolution (0.25° for CMIP6, 0.1° for ERA5-Land), and were downsampled rather than statistically or dynamically downscaled to the 4 km resolution of the model. Furthermore, the topographic and land cover data were upsampled from 30 m and 1 km, respectively, potentially omitting important spatial detail, such as fine-resolution vegetation heterogeneity and localised features like wetlands, forest edges, or human infrastructure that can influence fire ignition and spread (Moreira et al., 2011, San-Miguel et al., 2020). Temporal resolution is another constraint; we used monthly data for model training and testing, whereas fire spread is best captured at daily or sub-daily scales. However, without access to accurate daily lightning ignition data and a modelling framework that explicitly simulates two-dimensional fire spread, developing a reliable daily model remains highly challenging.

Conducting the analysis using burned pixels of 50 % or greater probability ensures that we effectively capture high-confidence patterns across time and scenario. However, this approach excludes a large proportion of low-confidence fires, particularly in remote, high-latitude areas or in regions where fires are historically rare, such as eastern Canada in 2023. This is likely the reason why we see fewer extreme fire years in tundra ecoregions than elsewhere and why seasonal patterns occasionally differ from the historic observed period.

Future directions

Future research could explore the use of long short-term memory neural network models, which would allow recursive forecasting by using predicted BA as input for subsequent time steps, or probabilistic models, which can quantify uncertainty in future projections and provide confidence intervals around predicted outcomes. Our model outputs could also be integrated into terrestrial biosphere models that simulate permafrost carbon dynamics, as well as infrastructure models that account for the effects of permafrost thaw, to assess how increasing fire activity and future climate change may accelerate permafrost degradation and impact infrastructure and communities in the ABZ. Furthermore, predicted changes in BA could be used alongside permafrost projections and urban expansion scenarios to model future land cover changes in the region.

Conclusion

Using XGBoost machine learning models trained on twenty-one climate, fire danger and topographic parameters, we made monthly projections of fire occurrence across the Arctic-boreal zone at a 4 km spatial resolution from 2025 to 2100 under three different SSP scenarios using two models from the CMIP6 ensemble (ACCESS-CM2 and MRI-ESM2-0). Our results show that burned area is expected to increase throughout the century, especially under high-emission scenarios, showing a statistically significant upward trend under all examined future scenarios, although the magnitude of the increase differs between ecoregions. Under ACCESS-CM2 conditions, burned area increases steadily with both SSP scenario severity and time, whereas with MRI-ESM2-0 projections burned area will see its peak in the middle-future (2051-2075) period. Fire seasons are projected to lengthen, both starting earlier and ending later, in all ecoregions as time progresses, with the Eurasian boreal maintaining a bimodal distribution indicative of large spring fires at more southern latitudes and summer fires further north. Of particular concern is the projected increase in the frequency of extreme fire years – defined as those exceeding the 95th percentile of observed burned area from 2001-2023 – especially under the SSP3-7.0 scenario. These findings underscore the urgency of emissions mitigation efforts in high-latitude ecosystems: as climate change continues to reshape fire regimes, adaptive planning informed by spatially explicit, data-driven models such as ours will be essential to minimising ecological and societal impacts.

Appendix A: Ecoregions

Table A4.1. List of ecoregions, their region and size (Mha) used in this study. For the regions: NA = North America, EU = Eurasia. Regions 1 to 26 are in the boreal biome, regions 27 to 58 are in the tundra biome.

#	Full name	Region	Mha
1	Alaska Peninsula montane taiga	NA	4.86
2	Central Canadian Shield forests	NA	27.07
3	Cook Inlet taiga	NA	2.79
4	Copper Plateau taiga	NA	1.72
5	Eastern Canadian forests	NA	46.41
6	Eastern Canadian Shield taiga	NA	75.46
7	Interior Alaska-Yukon lowland taiga	NA	42.35
8	Mid-Canada Boreal Plains forests	NA	56.72
9	Midwest Canadian Shield forests	NA	75.38
10	Muskwa-Slave Lake taiga	NA	29.73
11	Northern Canadian Shield taiga	NA	62.92
12	Southern Hudson Bay taiga	NA	37.17
13	Watson Highlands taiga	NA	23.77
14	Northern Cordillera forests	NA	16.85
15	Northwest Territories taiga	NA	33.22
16	East Siberian taiga	EU	390.01
17	Iceland boreal birch forests and alpine tundra	EU	9.15
18	Kamchatka-Kurile meadows and sparse forests	EU	14.64
19	Kamchatka taiga	EU	1.52
20	Northeast Siberian taiga	EU	112.59
21	Okhotsk-Manchurian taiga	EU	40.20
22	Sakhalin Island taiga	EU	6.87
23	Trans-Baikal conifer forests	EU	20.05
24	West Siberian taiga	EU	167.05
25	Scandinavian and Russian taiga	EU	215.71
26	Urals montane forest and taiga	EU	17.46
27	Ahklun and Kilbuck Upland Tundra	NA	5.05
28	Aleutian Islands tundra	NA	1.64
29	Beringia lowland tundra	NA	15.26
30	Brooks-British Range tundra	NA	15.95
31	Kalaallit Nunaat High Arctic tundra	NA	14.80
32	Pacific Coastal Mountain icefields and tundra	NA	10.61
33	Novosibirsk Islands Arctic desert	EU	3.69
34	Wrangel Island Arctic desert	EU	0.75
35	Alaska-St. Elias Range tundra	NA	16.43
36	Arctic coastal tundra	NA	4.97

37	Arctic foothills tundra	NA	12.94
38	Beringia upland tundra	NA	4.69
39	Canadian Low Arctic tundra	NA	83.54
40	Davis Highlands tundra	NA	9.78
41	Canadian High Arctic tundra	NA	64.45
42	Interior Yukon-Alaska alpine tundra	NA	15.26
43	Canadian Middle Arctic Tundra	NA	97.89
44	Ogilvie-MacKenzie alpine tundra	NA	30.10
45	Torngat Mountain tundra	NA	3.26
46	Kalaallit Nunaat Arctic steppe	NA	32.67
47	Russian Arctic desert	EU	16.15
48	Russian Bering tundra	EU	47.43
49	Cherskii-Kolyma mountain tundra	EU	55.68
50	Chukchi Peninsula tundra	EU	29.84
51	Kola Peninsula tundra	EU	5.88
52	Northeast Siberian coastal tundra	EU	22.26
53	Northwest Russian-Novaya Zemlya tundra	EU	28.43
54	Scandinavian Montane Birch forest and grasslands	EU	24.33
55	Taimyr-Central Siberian tundra	EU	95.48
56	Trans-Baikal Bald Mountain tundra	EU	21.76
57	Yamal-Gydan tundra	EU	41.21
58	Kamchatka tundra	EU	11.93

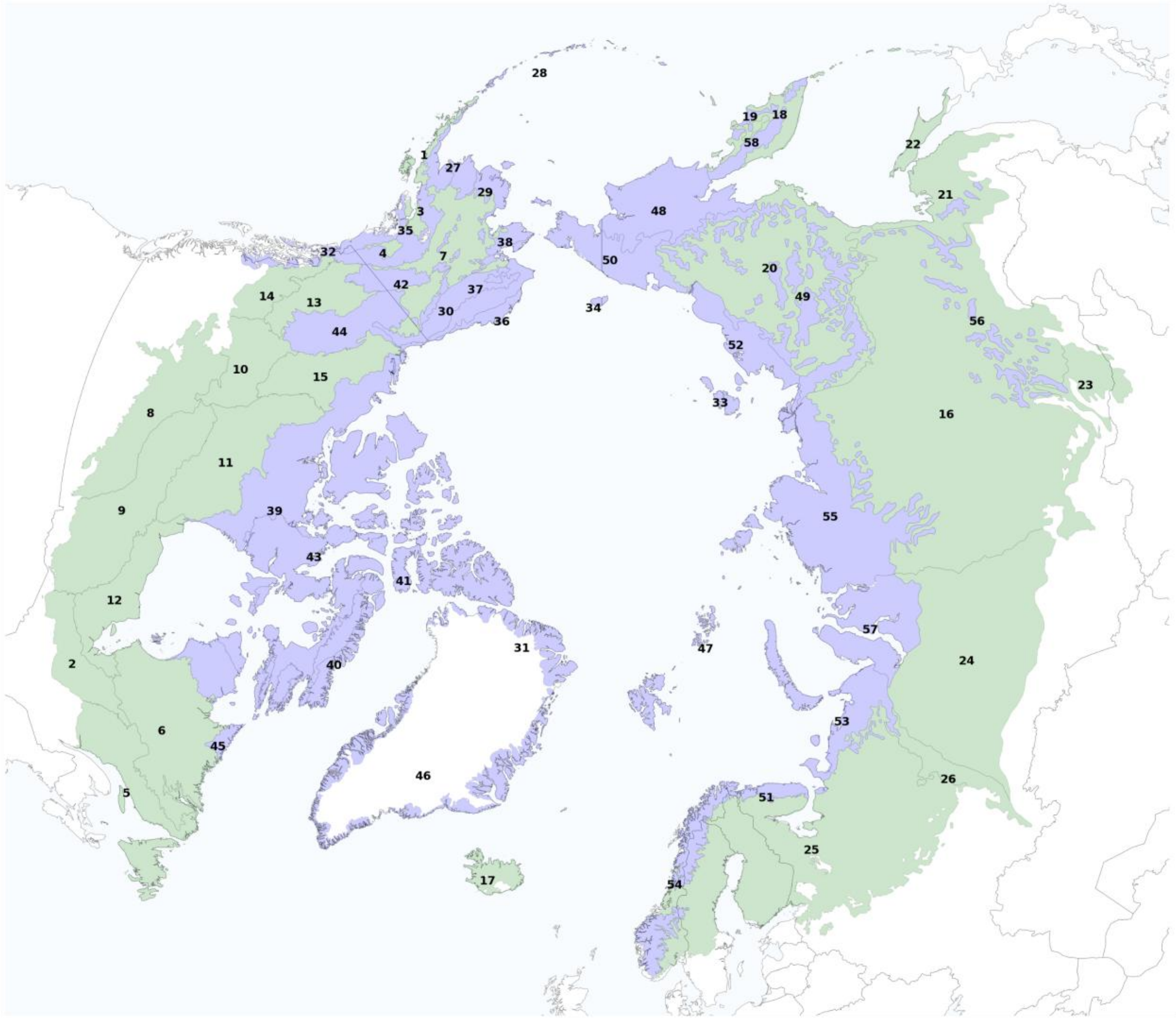

Figure A4.1. Ecoregions used in this study, numbered as per Table A4.1. Tundra ecoregions are shaded blue, boreal ecoregions are shaded green.

Appendix B: Land cover classes

Table B4.1. Grouping of land cover classes.

Original Value	Original Class Name	New Class Name	New Value
0	Unclassified	Unclassified	100
6	Poplar forest	Deciduous forests	110
7	Oak forest	Deciduous forests	110
10	Pine forest	Coniferous forests	120
11	Fir forest	Coniferous forests	120
12	Aspen forest	Deciduous forests	110
13	Hemlock forest	Coniferous forests	120
14	Spruce forest	Coniferous forests	120
15	White Spruce forest	Coniferous forests	120
16	Black Spruce forest	Coniferous forests	120
17	Mixed forest	Mixed forest	130
18	Larch forest	Deciduous forests	110
19	Birch forest	Deciduous forests	110
20	Scots Pine forest	Coniferous forests	120
21	Jack Pine forest	Coniferous forests	120
22	Cedar forest	Coniferous forests	120
23	Maple	Deciduous forests	110
24	Siberian Pine	Coniferous forests	120
25	Linden	Deciduous forests	110
26	Cedar Elfin Wood	Coniferous forests	120
30	Alpine shrubland	Shrublands	140
31	Riparian shrubland	Shrublands	140
32	Other shrublands	Shrublands	140
33	Herbaceous	Herbaceous	150
35	Sparsely Vegetated	Barrens	160
50	Bog	Wetlands	170
51	Fen	Wetlands	170
52	Marsh	Wetlands	170
60	Erect-shrub tundra	Shrub tundra	180
61	Prostrate-shrub tundra	Shrub tundra	180
62	Shrub tundra	Shrub tundra	180
63	Graminoid tundra	Shrub tundra	180
64	Wet-sedge tundra	Shrub tundra	180
65	Barren tundra	Barrens	160
70	Developed	Other	190
98	Snow/Ice	Barrens	160
99	Other	Other	190

Appendix C: Supporting material for Chapter 4

Table C4.1. Grid search parameters used for tuning the XGBoost models. Parameters in bold were selected for final model implementation.

Parameter Type	Values
Learning rate	0.001, 0.005, **0.01**, 0.05, 0.1
Max depth	4, **6**, 8, 10
Number of estimators (initial)	100, 500, 1000, 5000, 10000, **15000**, 20000 (Northern model) 100, 500, 1000, 5000, **10000**, 15000, 20000 (South Siberia model)
Number of estimators (final)	12000, **13000**, 14000, 15000, 16000, 17000 (Northern model) 10000, 10500, 11000, **11500**, 12000, 12500 (South Siberia model)

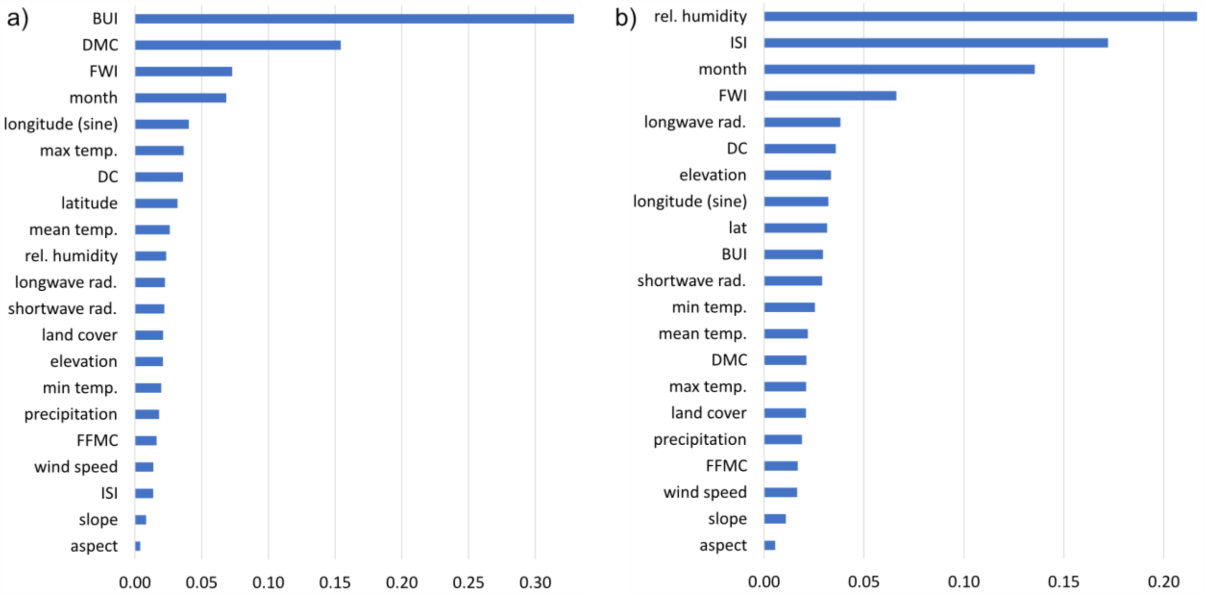

Figure C4.1. XGBoost feature importances for the Northern a) and South Siberia b) model training. Features are sorted from most to least important.

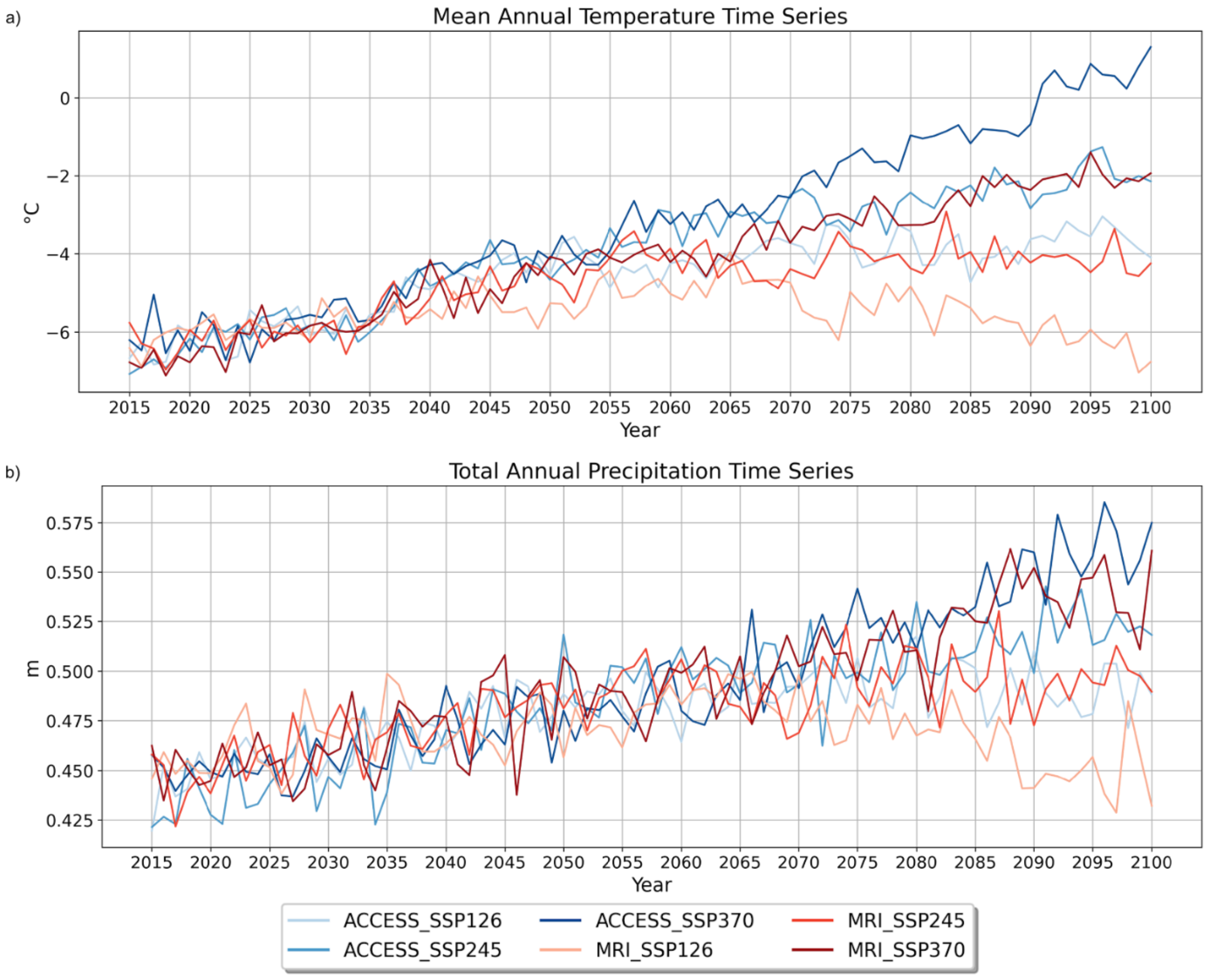

Figure C4.2. Mean annual temperature (a) and total annual precipitation (b) for the future ACCESS-CM2 and MRI-ESM2-0 permutations across the Arctic-boreal zone, 2015-2100.

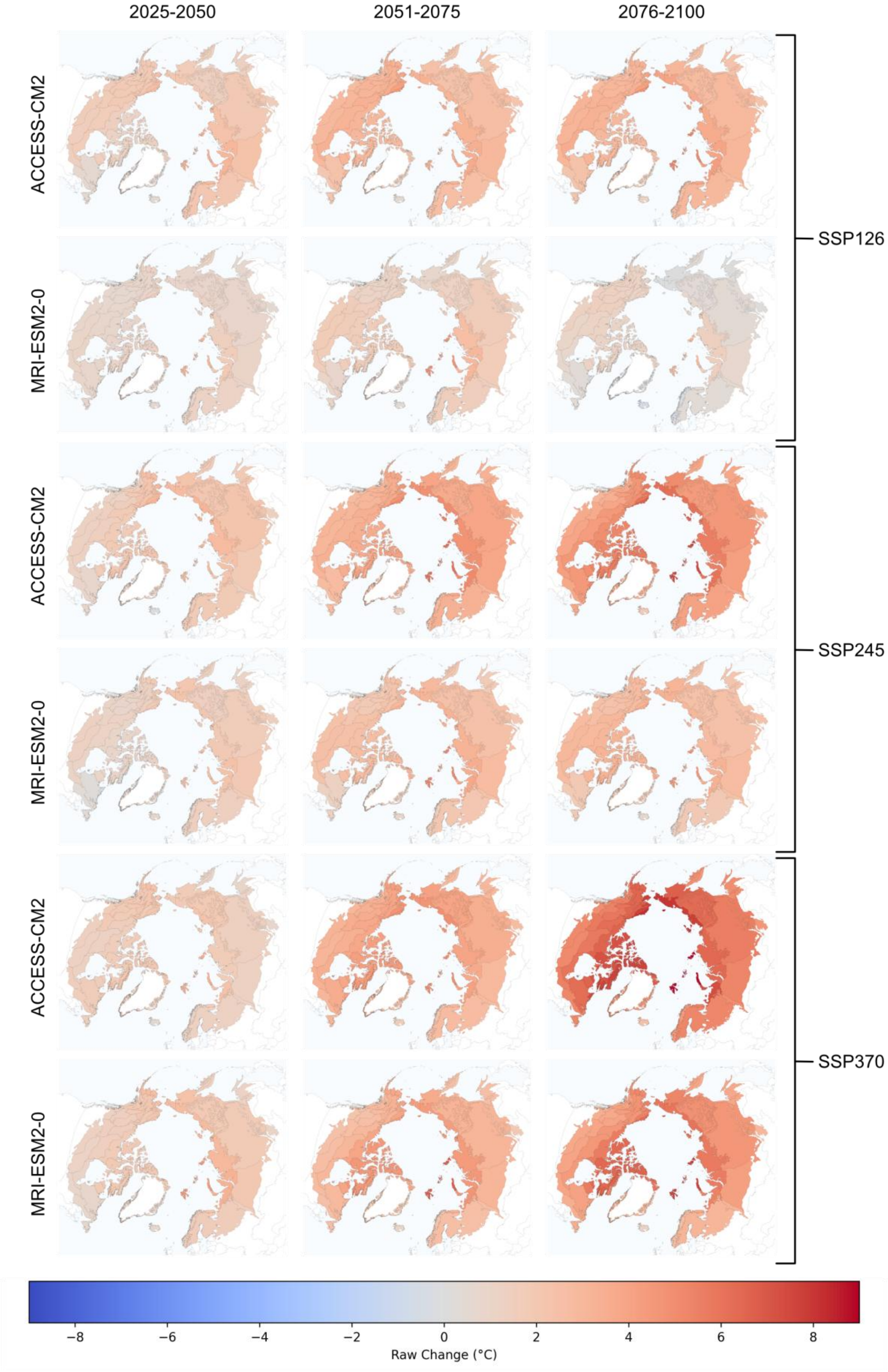

Figure C4.3. Raw change in mean 2-metre air temperature (°C) for each ecoregion compared to the observed 2001-2023 historic baseline.

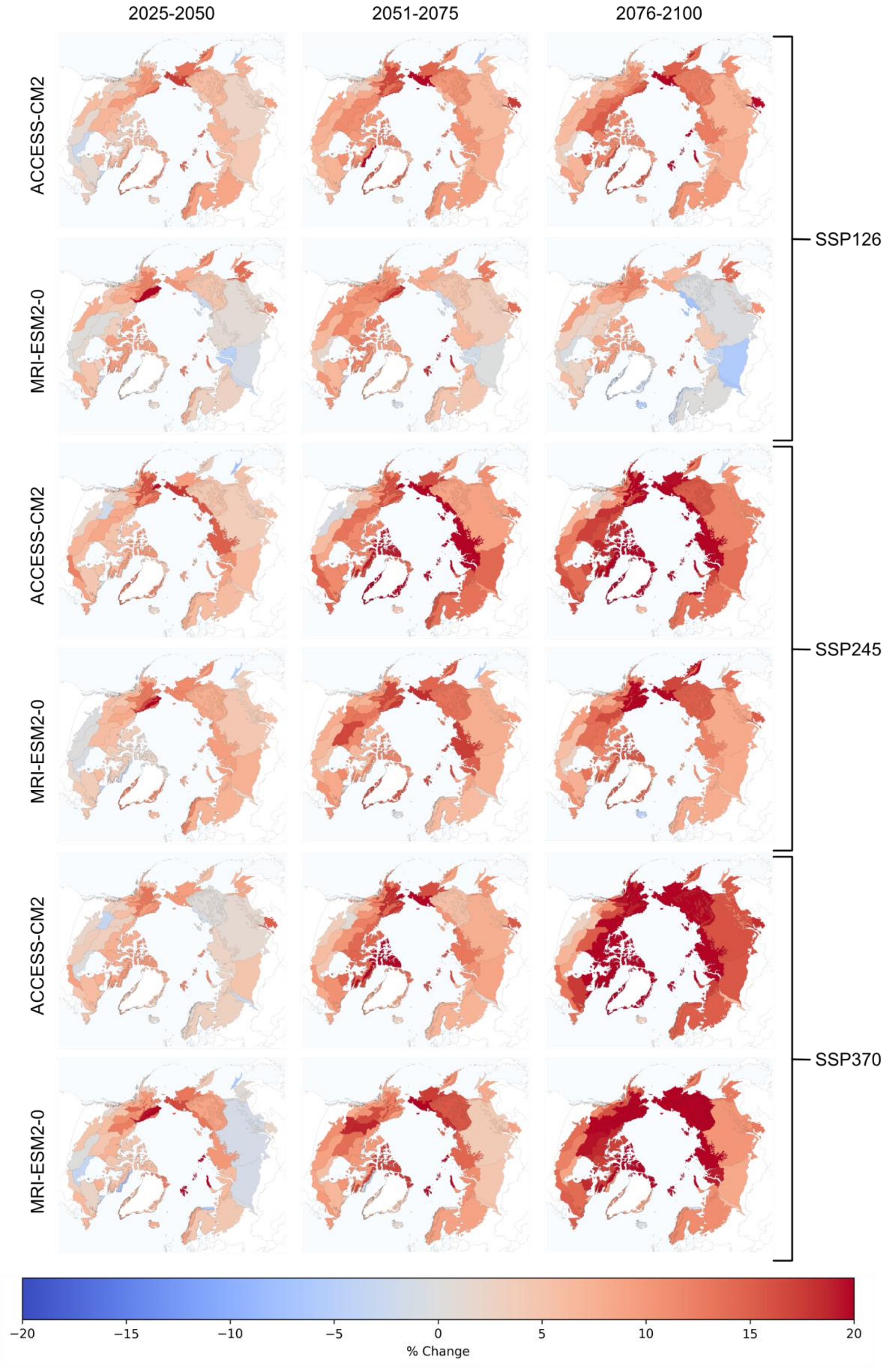

Figure C4.4. Percentage change in total precipitation for each ecoregion compared to the observed 2001-2023 historic baseline.

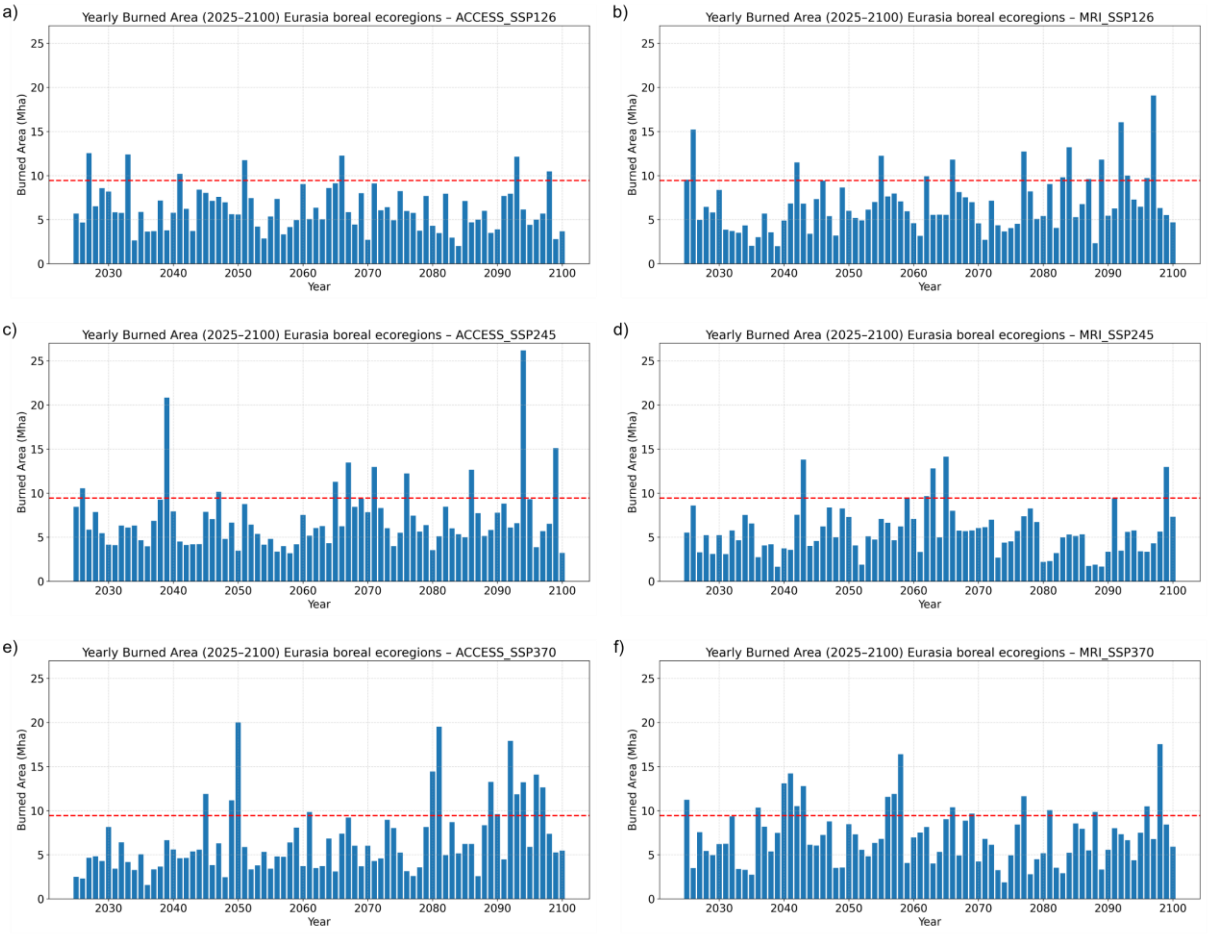

Figure C4.5. Bar plots of the yearly burned area (Mha) for Eurasia boreal ecoregions under SSP1-2.6 (a, b), SSP2-4.5 (c, d) and SSP3-7.0 for ACCESS-CM2 and MRI-ESM2-0, respectively. The red dashed line represents the 95th percentile value from the historic (2001-2023) period.

Figure C4.6. Bar plots of the yearly burned area (Mha) for North America boreal ecoregions under SSP1-2.6 (a, b), SSP2-4.5 (c, d) and SSP3-7.0 for ACCESS-CM2 and MRI-ESM2-0, respectively. The red dashed line represents the 95th percentile value from the historic (2001-2023) period.

Figure C4.7. Bar plots of the yearly burned area (Mha) for tundra ecoregions under SSP1-2.6 (a, b), SSP2-4.5 (c, d) and SSP3-7.0 for ACCESS-CM2 and MRI-ESM2-0, respectively. The red dashed line represents the 95th percentile value from the historic (2001-2023) period.

Table C4.2. Mann-Kendall trend test for each region and scenario for the entire 2025-2100 period, with associated *p*-value, Kendall Tau score and Theil-Sen estimator (slope). EU = Eurasia, NA = North America.

Scenario	Model	Region	*p*-value	Tau	Slope	H	Trend
SSP1-2.6	ACCESS-CM2	EU boreal	5.05×10^{-6}	0.307	0.056	True	Increasing
		NA boreal	8.58×10^{-9}	0.388	0.028	True	Increasing
		Tundra	4.30×10^{-10}	0.421	0.007	True	Increasing
	MRI-ESM2-0	EU boreal	1.28×10^{-11}	0.456	0.082	True	Increasing
		NA boreal	9.95×10^{-7}	0.330	0.021	True	Increasing
		Tundra	8.29×10^{-8}	0.361	0.005	True	Increasing
SSP2-4.5	ACCESS-CM2	EU boreal	1.15×10^{-9}	0.410	0.077	True	Increasing
		NA boreal	4.85×10^{-8}	0.368	0.031	True	Increasing
		Tundra	4.34×10^{-9}	0.396	0.007	True	Increasing
	MRI-ESM2-0	EU boreal	9.47×10^{-8}	0.360	0.057	True	Increasing
		NA boreal	6.90×10^{-6}	0.303	0.019	True	Increasing
		Tundra	3.01×10^{-8}	0.373	0.006	True	Increasing
SSP3-7.0	ACCESS-CM2	EU boreal	4.44×10^{-15}	0.528	0.089	True	Increasing
		NA boreal	1.23×10^{-11}	0.457	0.055	True	Increasing
		Tundra	1.55×10^{-15}	0.537	0.008	True	Increasing
	MRI-ESM2-0	EU boreal	6.35×10^{-8}	0.364	0.073	True	Increasing
		NA boreal	1.11×10^{-5}	0.296	0.030	True	Increasing
		Tundra	1.10×10^{-8}	0.385	0.010	True	Increasing

Table C4.3. Interquartile range (75th-25th percentile – Mha) for each region and scenario for the near- (2025-2050), middle- (2051-2075) and far- (2076-2100) periods. EU = Eurasia, NA = North America.

Scenario	Model	Region	2025-2050	2051-2075	2076-2100
SSP1-2.6	ACCESS-CM2	EU boreal	2.35	3.30	3.36
		NA boreal	1.38	1.08	1.70
		Tundra	0.42	0.41	0.41
	MRI-ESM2-0	EU boreal	3.60	2.94	4.40
		NA boreal	1.67	1.29	1.91
		Tundra	0.39	0.66	0.53
SSP2-4.5	ACCESS-CM2	EU boreal	3.57	3.99	3.11
		NA boreal	1.47	2.24	1.78
		Tundra	0.68	0.55	0.37
	MRI-ESM2-0	EU boreal	3.31	2.40	2.41
		NA boreal	2.69	0.94	2.69
		Tundra	0.44	0.62	0.41
SSP3-7.0	ACCESS-CM2	EU boreal	2.64	3.11	7.47
		NA boreal	3.25	2.48	3.05
		Tundra	0.29	0.39	0.91
	MRI-ESM2-0	EU boreal	4.14	3.96	3.25
		NA boreal	3.02	3.34	2.52
		Tundra	0.70	0.74	0.49

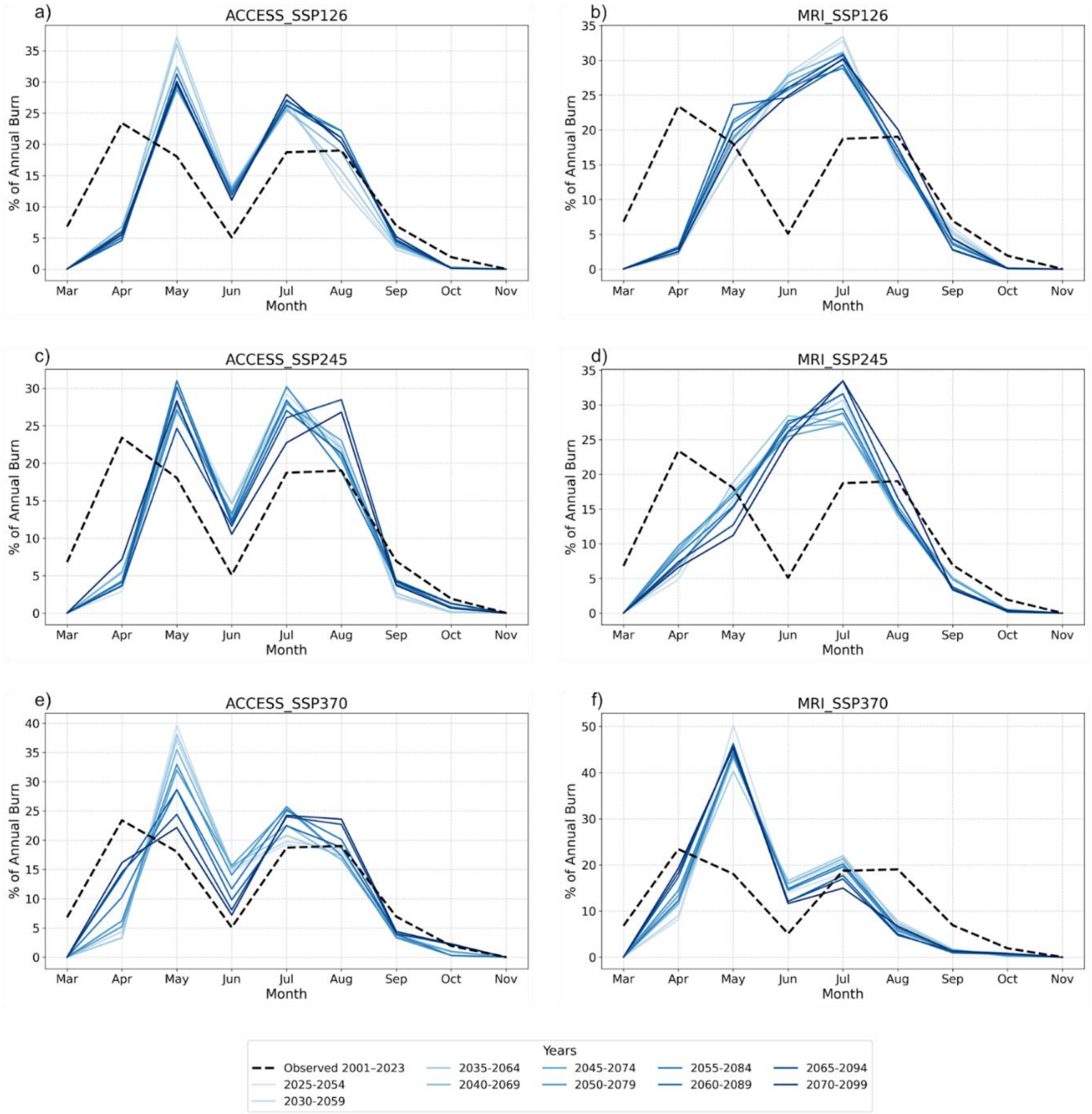

Figure C4.8. Seasonality of burned area for 30-year moving windows in the Eurasia boreal ecoregions under SSP1-2.6 (a, b), SSP2-4.5 (c, d) and SSP3-7.0 for ACCESS-CM2 and MRI-ESM2-0, respectively. Only the months March to November are shown, and the lines become darker as time progresses. The dashed black line shows the observed 2001-2023 mean.

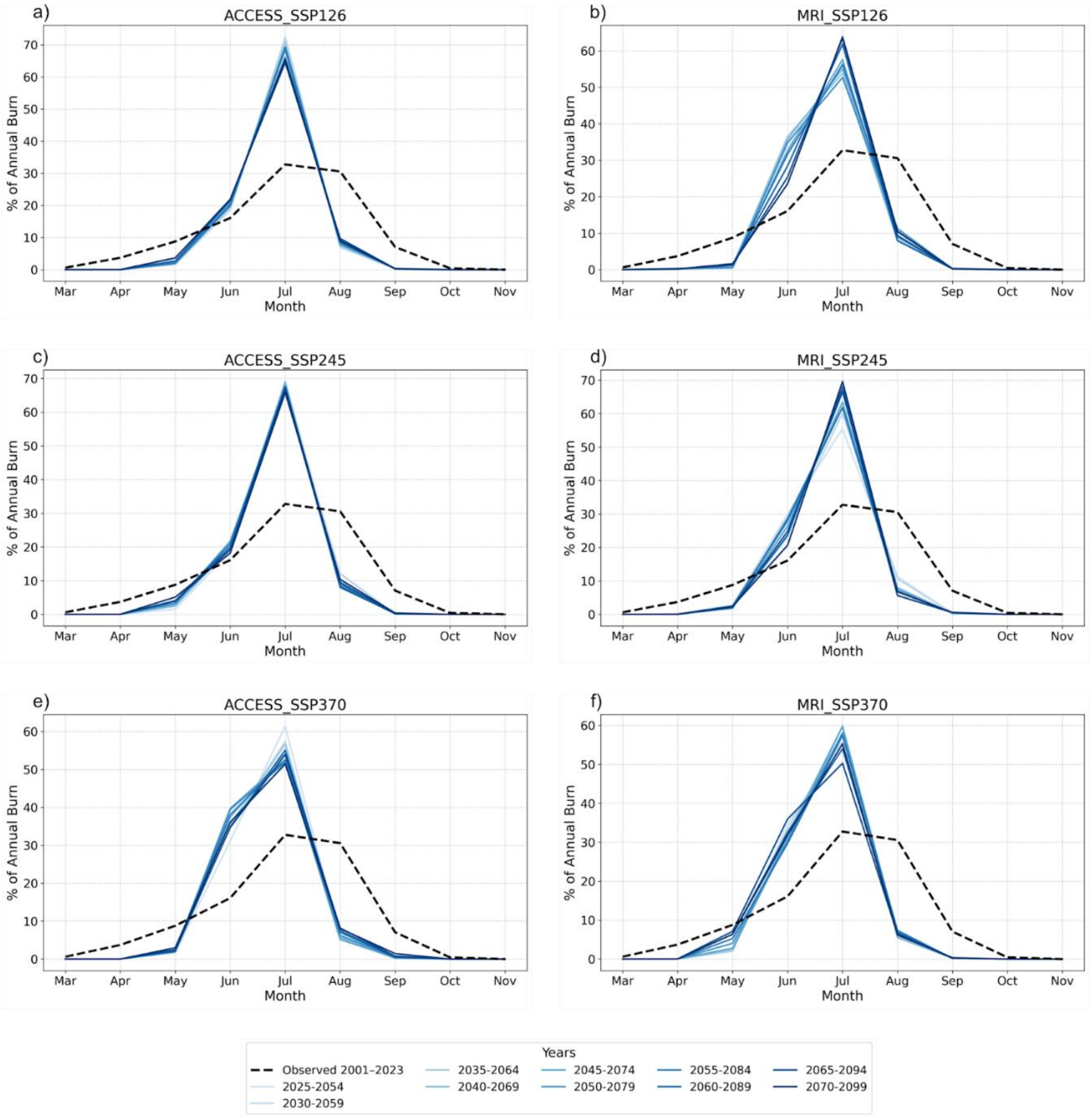

Figure C4.9. Seasonality of burned area for 30-year moving windows in the tundra ecoregions under SSP1-2.6 (a, b), SSP2-4.5 (c, d) and SSP3-7.0 for ACCESS-CM2 and MRI-ESM2-0, respectively. Only the months March to November are shown, and the lines become darker as time progresses. The dashed black line shows the observed 2001-2023 mean.

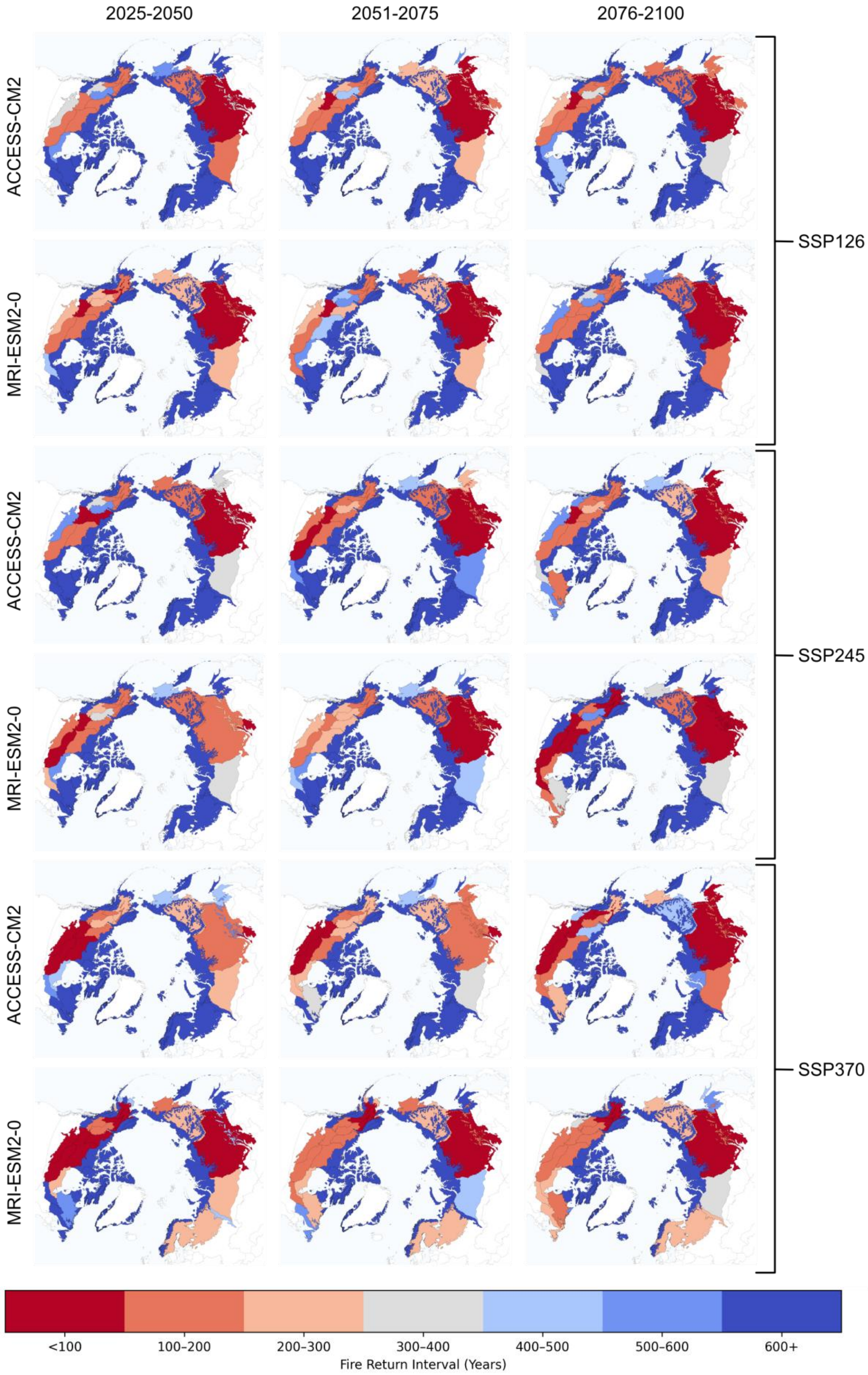

Figure C4.10. Fire return interval (FRI) for each ecoregion, grouped into 100-year categories.

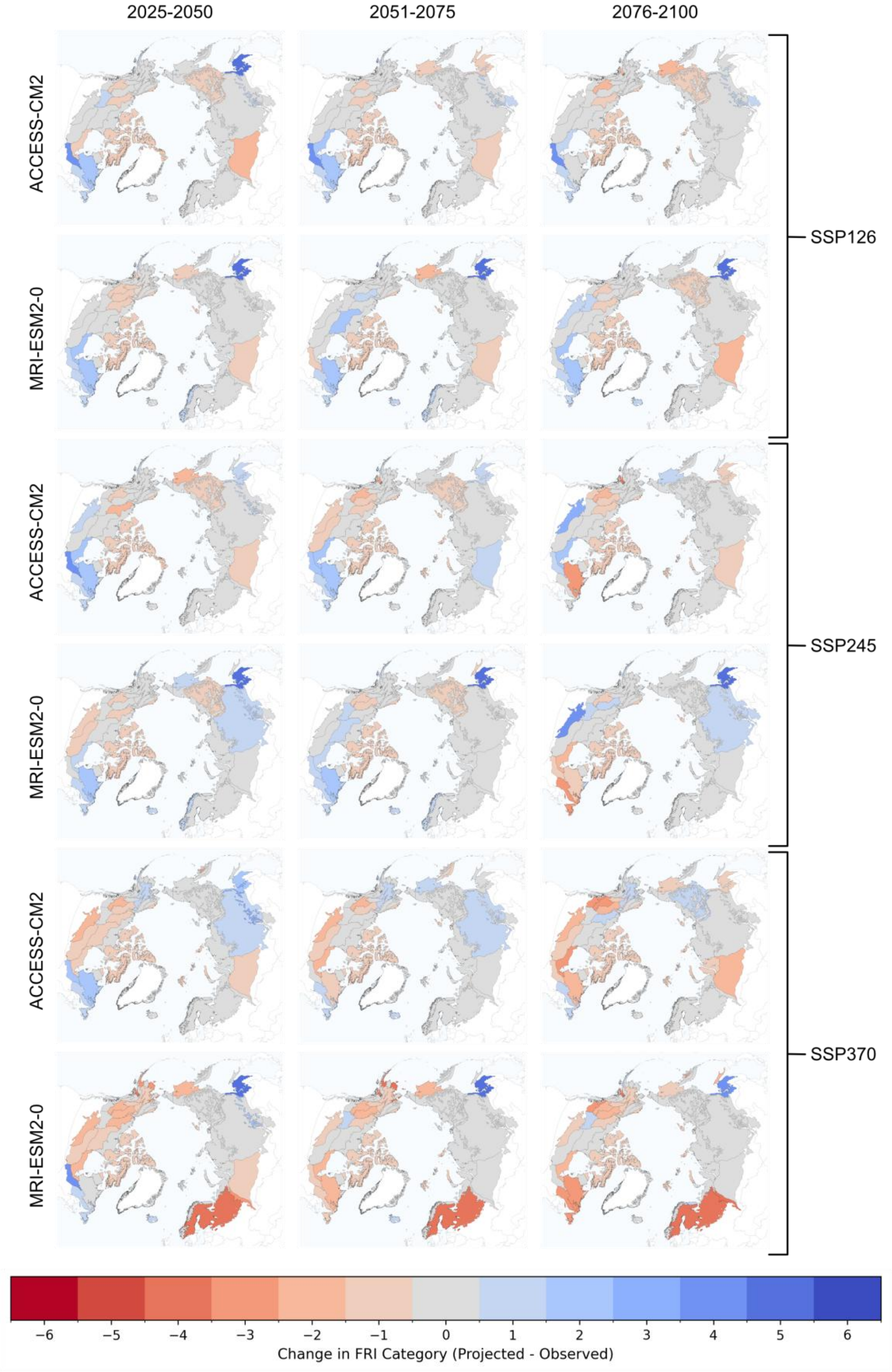

Figure C4.11. Change in fire return interval (FRI) 100-year category, as given in Figure C4.11, compared to the observed historical (2001-2023) period. Red indicates the FRI is decreasing and blue indicates the FRI is increasing.

Appendix D: Additional technical information for Chapter 4

Although not suitable for this study, Random Forest (RF) and Convolutional Neural Networks (CNN) models have previously been used to make projections of future wildfire occurrence in other regions (e.g. Langford et al., 2018, Mohajane et al., 2021, Zhang et al., 2021, Rubí et al., 2023).

The RF model is an ensemble learning method that constructs multiple decision trees during training and averages their predictions to improve accuracy and reduce overfitting. Each tree is trained on a bootstrapped subset of the data, where the model creates a new training set for each tree by randomly picking data points from the original dataset with replacement. Random feature selection then occurs at each split, ensuring model robustness and decorrelation between individual trees. RF is particularly useful for understanding variable importance, as it provides metrics that indicate which input features contribute most to predictions. Its ability to handle missing data, high-dimensional inputs, and interactions between variables makes it an important tool for fire modelling.

A CNN is a type of deep learning model particularly well-suited for processing spatially structured data, such as images or gridded geospatial inputs. CNNs consist of multiple layers, including convolutional layers that apply learnable filters to input data, capturing local spatial patterns and features such as edges, textures, or shapes. These filters slide across the input to produce feature maps, which are then passed through non-linear activation functions and are often downsampled using pooling layers to reduce dimensionality and enhance generalisation. As the network deepens, it learns increasingly abstract representations of the input, allowing for the detection of complex spatial relationships. CNNs are especially powerful in tasks where spatial context and patterns are critical, making them useful for fire modelling applications that incorporate satellite imagery, land cover maps, or gridded climate data. A visualisation of the CNN model structure alongside XGBoost and RF models is shown in Figure D4.1.

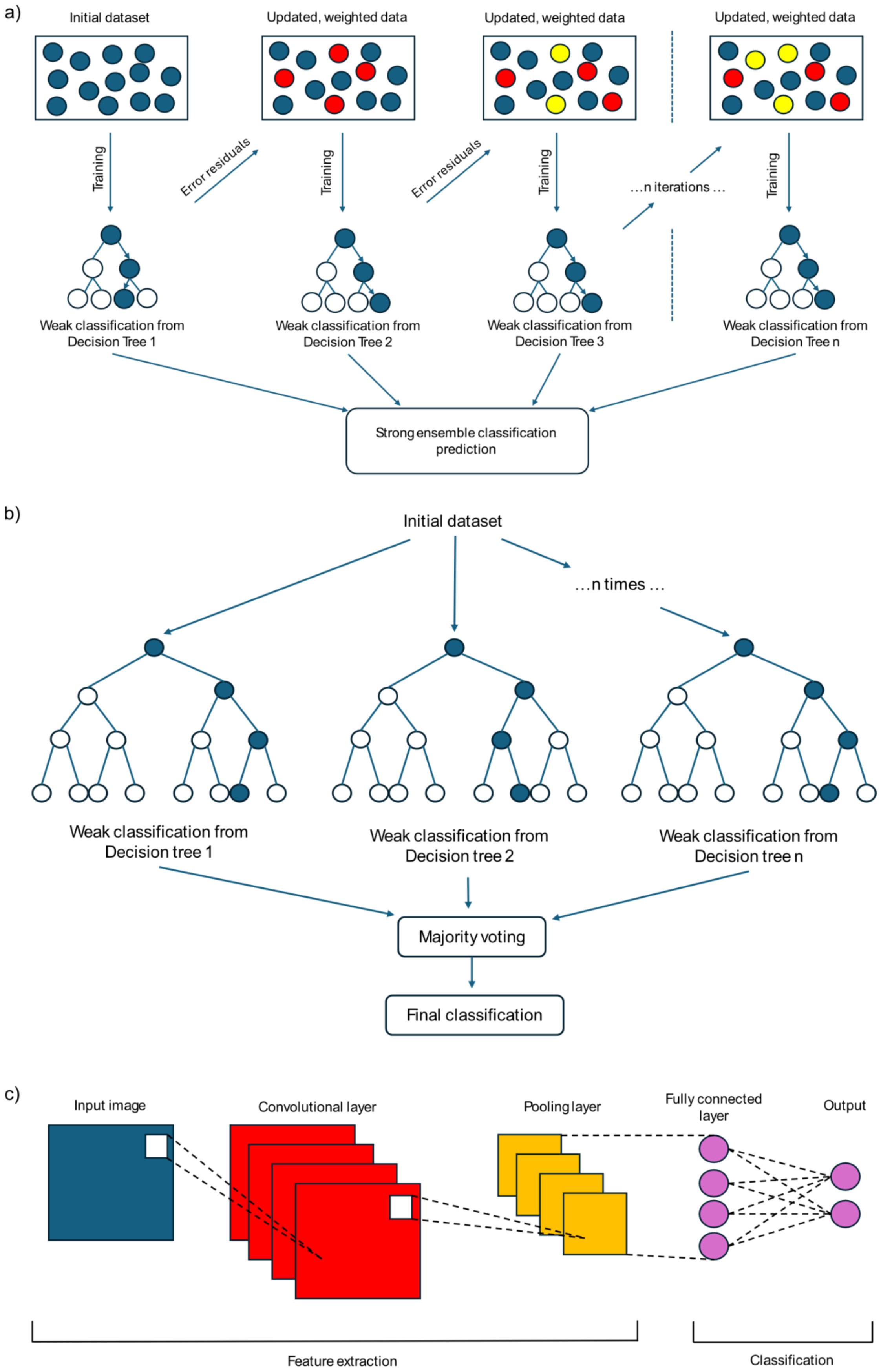

Figure D4.1. Visualisation of the structure of gradient boosted trees (a), random forest (b) and convolutional neural network (c) models.

Chapter 5

General discussion

Shrub tundra by the Pechora River in Naryan-Mar, Russia.

Thesis summary and implications

The work undertaken in this thesis set out to investigate the relationship between climate change and fire activity across boreal forests, using a combination of reanalysis datasets, satellite-derived observations, and machine learning projections. Collectively, the findings confirm that climate change is exerting a strong and intensifying influence on boreal fire regimes, driven by rising temperatures, lengthened fire seasons, and increased flammability of fuel due to climate change. These pressures are contributing to a widespread shift towards more fire-prone conditions, with implications for ecosystem dynamics, carbon cycling, and climate feedbacks, as outlined in Chapter 1.

A key insight emerging from the present work is the substantial regional heterogeneity in both historical and projected fire activity. Variability in vegetation composition, landscape characteristics, and local climate conditions results in spatially distinct patterns of change. While some regions exhibit clear signals of increasing fire risk and burned area, others display delayed or nonlinear responses due to interactions among fuel availability, moisture regimes, and vegetation feedbacks. This underscores the vital importance of region-specific adaptation and fire management strategies, particularly in areas that cross national or administrative borders where coordinated responses are essential.

The three chapters of this thesis have provided synergistic approaches to understanding boreal climate-fire dynamics. Chapter 2 assessed the reliability of six climate variables linked to fire activity in reanalysis datasets across Siberia, forming a foundation for robust fire risk assessment. Chapter 3 evaluated satellite imagery-derived burned area products across North America and Russia, identifying their strengths and limitations for monitoring fire activity. Together, these empirical insights support the machine learning projections made in Chapter 4, which forecast future wildfire occurrences under different climate scenarios. As a whole, this thesis demonstrates the value of integrating observational, diagnostic, and predictive tools in understanding and anticipating changes in fire regimes.

By adopting a more general evaluation framework in Chapters 2 and 3 biases and inter-product inconsistencies are identified independently of any specific modelling architecture. This helps to ensure that the subsequent machine learning modelling rests on solid data foundations and avoids tailoring evaluation criteria too narrowly to a single prediction objective. Furthermore, a general approach facilitates comparison with the wider literature and enhances the relevance of the thesis beyond fire modelling alone. The compromise is that such an approach may not directly quantify the aspects of data quality most critical for model performance, such as threshold behaviour, representation of extreme values or class imbalances, which become more evident in a fire-specific, model-targeted evaluation. A dedicated evaluation aligned explicitly with the objectives in Chapter 4 could provide sharper insights into predictive skill, feature importance and decision-relevant error characteristics, but risks conflating data weaknesses with model deficiencies and may reduce the broader applicability of the findings. Importantly, driver assessment also provides a benchmark against which machine learning-derived variable importance can be interpreted: where importance rankings diverge from established physical expectations or from the driver-evaluation findings this may show collinearity effects or model reliance on compensating errors rather than genuine process representation. The two approaches combined offer complementary strengths: the general evaluation establishes credibility and robustness, while the fire-specific assessment sharpens relevance and practical model optimisation.

The results set out within the thesis provide credible evidence that many areas of the Arctic-boreal zone are approaching, or may already have crossed, critical thresholds in fire activity. Projections indicate that without substantial mitigation, further warming is likely to intensify fire danger and increase the frequency of extreme fire seasons. The implications are far-reaching: increased fire activity in high-latitude regions threatens permafrost stability, accelerates the decomposition of deep carbon-rich soils, and releases large volumes of greenhouse gases and aerosols. These processes contribute to a reinforcing cycle of climate-fire feedbacks that amplify both regional and global warming.

In parallel, changes in fire frequency and severity are reshaping boreal forest structure and composition. Enhanced disturbance regimes may favour early-successional (e.g., birch and Scots pine) or fire-adapted (e.g., black spruce and jack pine) species, driving transitions towards more open or deciduous-dominated landscapes with reduced ecological resilience. Such shifts have consequences for biodiversity, hydrology, and carbon storage, and are particularly evident in the long-range projections presented in Chapter 4.

The performance metrics discussed in this work are applicable across a range of applications. For instance, long-term stability and sensitivity to trends are critical for making future projections, as consistency across extended satellite records and accurate representations of interannual variability may matter more than perfect spatial precision in individual years, unlike in hazard forecasting, which places greater emphasis on spatial precision and the accurate prediction of high-risk locations on shorter timescales. In contrast, fire management applications prioritise accurate seasonality which directly informs preparedness and resource allocation.

Beyond ecological impacts, the findings of this thesis carry implications for international climate policy. Increasing boreal fire emissions complicate carbon accounting and may undermine national greenhouse gas inventories, particularly for Canada and Russia with expansive boreal territories. These depend primarily on accurate estimations of absolute burned area and total extent, since systematic biases directly propagate into flux calculations. Integrating projected fire regime shifts into national adaptation plans will be critical for effective climate mitigation and resilience planning. More broadly, the thesis supports the need to better incorporate fire science into global environmental governance and climate strategies.

Contributions to scientific knowledge

This thesis makes several contributions to the field of climate-fire research. The validation of reanalysis data in Chapter 2 adds to recent efforts to validate the reliability of reanalysis products against *in situ* observations (Shestakova et al., 2024, Titkova and Ananicheva, 2024, Wilczak et al., 2024), but is the first to do so both across a range of climate variables and reanalysis datasets, and across the data-sparse Arctic-boreal region in Siberia. The publication was also the first to highlight that errors with snow depth values in ERA-Interim still exist, despite previous efforts to correct them (NCAR, 2023).

By comparing twelve burned area products and MODIS active fire data over a 20-year period in Chapter 3, this work became the first publication to conduct an analysis of burned area products on this scale. Furthermore, this was the first study to analyse total burned area across the entire Arctic-boreal zone, and the first to detect issues with GABAM during the Landsat 7 era. The work complements a handful of recent studies which compare burned area products across smaller regions (e.g., Turco et al., 2019, Valencia et al., 2020, Khairoun et al., 2024), however only one (Humber et al., 2019) uses a similar methodology to the present study.

Chapter 4 demonstrates the utility of harmonising multiple data streams – reanalysis, remote sensing, and climate models – to assess fire dynamics across scales. Additionally, it shows how traditional fire danger indices can be effectively used to track climate sensitivity in fire regimes, especially when spatially disaggregated and linked to specific climate drivers. Previous studies have used machine learning to make broad, decadal projections across SSP scenarios (Sung et al., 2022, Herrmann et al., 2023, Shao et al., 2023, Zhao et al., 2025), however this is the first work to make monthly projections of fire occurrence to the end of the century, and the first to produce high spatial resolution forecasts on a biome-wide scale. By making monthly projections, this adds to research efforts by identifying critical windows of fire risk within the fire season, supporting the development of more targeted adaptation and mitigation strategies.

Using machine learning methods to project future burned area introduces a dynamic, data-driven framework that complements traditional, process-based fire models. XGBoost enables the capture of complex, non-linear interactions between climate predictors and fire response, while also offering interpretable insights into variable importance. At the same time, the findings within this thesis emphasise the importance of careful model evaluation and transparency in interpreting machine learning outputs, particularly when forecasting into climates not yet observed.

The work contained within this thesis has already begun to be recognised internationally. Chapter 2, first published in April 2024, has been cited 45 times at the time of writing, including in *Nature Geoscience*, by researchers on all six inhabited continents. The burned area product analysis paper (Chapter 3) was published in September 2024 and has been cited on 11 occasions so far, including by a study in *Nature Communications Earth and Environment*. This paper was also recognised by *Remote Sensing*, the journal of publication, as the most notable article in the "General" category for September to November 2024. These early indicators of impact highlight the global relevance of this research for advancing understanding of reanalysis and burned area datasets and improving the tools used to monitor and project fire activity in boreal forests and other fire-prone ecosystems worldwide.

Limitations

While the thesis offers significant new insights, several limitations must be acknowledged. Datasets remain imperfect, whether from station observations and climate reanalyses (Chapter 2), or fire occurrence and burned area products (Chapter 3), particularly in earlier decades and, for the latter, in areas with high cloud cover. For instance, meteorological station records may contain measurement errors due to instrument calibration issues, site relocations or data gaps that introduce artificial biases or inflated variability. However, the comparison with reanalysis products revealed systematic discrepancies in a small number of stations, indicating that some observational biases were identifiable through cross-validation. Stations that closely matched the reanalyses provide greater confidence that large systematic biases are unlikely in those records, although residual uncertainties remain. When station data are used to evaluate or calibrate reanalysis products, these uncertainties can lead to over- or underestimations of the reanalyses which, in turn, affects the quality of training data in the machine learning models. Underestimated temperature data, for example, imply that fires have occurred under cooler conditions than was actually the case, whereas previously overestimated temperature records would suggest that fires occur only under unrealistically warm conditions, potentially exaggerating model sensitivity to heat extremes.

Meanwhile, fire danger indices, while useful proxies, do not capture all aspects of fire behaviour or ignition sources, and their relationship to actual fire outcomes can vary by context (Camia et al., 1999, Sirca et al., 2018, Di Giuseppe, 2023). This is especially prominent in the monthly Northern model (Chapter 4), where the Fine Fuel Moisture Code and Initial Spread Index, which rely on climate parameters with high temporal variability, such as wind speed, are less influential than combined or longer-term indices, like the Drought Code and Fire Weather Index.

For a tree-based model, such as XGBoost, the implications of different performance metrics extend beyond aggregate skill scores. A consistent, systematic bias in an input variable may be less problematic than unbiased but noisy data, because gradient-boosted trees partition feature space based on relative thresholds and monotonic changes rather than absolute values; consistent shifts can often be accommodated through split adjustments, whereas noise reduces the signal-to-noise ratio and weakens the learning ability of the model. Variable suitability may also be regime-dependent: certain drivers may be physically irrelevant or misleading beyond specific thresholds; for example, snow depth during snow-free periods, where numerical variability conveys no meaningful fire-related signal. In such cases masking, thresholding, or feature engineering may improve robustness.

Furthermore, more fire-specific variables, such as binary snow cover or duration of snow-free days as opposed to raw snow depth, may better align with ignition and fuel-availability mechanisms, improving interpretability and reducing the risk that the model exploits false relationships. These considerations highlight that metric evaluation should be coupled with process-informed input selection, as not all statistically informative variables are physically meaningful predictors of fire behaviour.

The machine learning projections rely on the assumption that past relationships between climate and fire are temporally invariant and thus can be extrapolated into future climates. This assumption becomes increasingly tenuous under extreme warming, especially if ecosystem thresholds are crossed or if future fire drivers (e.g., human activity, fuel build-up, lightning patterns) diverge from historical norms. Furthermore, CMIP6 climate model projections carry their own uncertainties, particularly in regional precipitation trends, which can strongly influence fire potential. While the thesis attempts to mitigate these limitations through bias correction, cross-validation, sensitivity analysis, and scenario-based exploration, residual uncertainties remain.

Future research directions

Several promising avenues for future research emerge from the present work. Integrating dynamic vegetation models or land cover change scenarios could improve projections of future fire activity by accounting for feedbacks between fire, vegetation, and climate. While some modelling frameworks, such as FireMIP (Fire Model Intercomparison Project - Hantson et al., 2016, Rabin et al., 2017), have begun to explore these interactions, few have done so at biome-wide scale (Forkel et al., 2019), and even fewer have incorporated machine learning outputs into dynamic ecosystem models. The output from the machine learning models in Chapter 4 will be integrated into DVM-DOS-TEM (Dynamic Vegetation Model-Dynamic Organic Soil-Terrestrial Ecosystem Model); a circumpolar model designed to forecast changes in permafrost and vegetation structure in boreal and tundra regions (Euskirchen et al., 2025). This represents a novel step toward two-way coupling between fire activity and permafrost dynamics. It would be valuable in future work to explore the reverse influence: how projected changes in permafrost conditions can, in turn, affect wildfire risk.

Additionally, greater incorporation of ignition sources, both natural and anthropogenic, would allow for more comprehensive fire risk assessments. Lightning remains the primary cause of fires in boreal forests, accounting for 77 ± 8 % of total ignitions (Janssen et al., 2023). However, lightning remains a highly variable and unpredictable phenomenon, and previous work has shown that modelling fires from non-random ignition locations can be less effective than from random locations under typical weather conditions (Bar Massada et al., 2011). Nevertheless, machine learning methods have begun to more accurately predict ignitions from lightning forecasts in other regions (Coughlan et al., 2021), and similar approaches could be adapted for high-latitude areas, using new datasets such as the BoLtFire database, which catalogues lightning-ignited fires across the boreal biome from 2012 to 2022, as reference (Engle et al., 2025).

Hybrid machine learning-burned area products could be developed from this work, potentially within the scope of an “Intercomparison Project” initiative. Burned area products differ in their detection algorithms, spatial resolutions and sensitivity to small fires, leading to structural uncertainty that spreads into both driver evaluation and training of machine learning models. An intercomparison, such as in Chapter 3, could quantify these differences, identifying strengths and weaknesses of the products in different regions, and providing the basis for statistically merging products into probabilistic or ensemble burned area estimates. These harmonised datasets would improve the robustness of machine learning training by reducing noise and better characterising observational uncertainty. Conversely, machine learning models trained across multiple products can help diagnose inconsistencies between datasets: spatial or climate regimes where predictive skill diverges may indicate observational artefacts rather than actual process-based differences. In this way, driver evaluation and burned area intercomparison would not only inform machine learning architecture and feature selection, but the model framework itself could act as a diagnostic tool to guide future burned area product development, prioritising improvements in driver datasets, and targeting regions where enhanced fire observation capacity would yield the greatest benefit. Together, these elements suggest an integrated approach in which data products, modelling and evaluation evolve iteratively rather than independently (Figure 5.1).

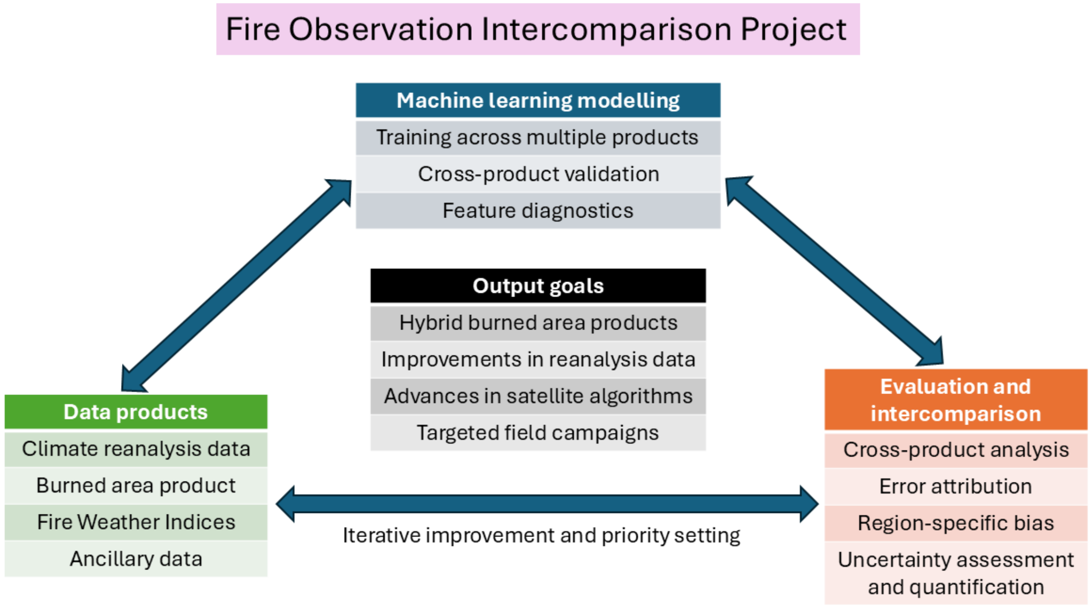
Fire Observation Intercomparison Project

Machine learning modelling
Training across multiple products
Cross-product validation
Feature diagnostics

Output goals
Hybrid burned area products
Improvements in reanalysis data
Advances in satellite algorithms
Targeted field campaigns

Data products
Climate reanalysis data
Burned area product
Fire Weather Indices
Ancillary data

Evaluation and intercomparison
Cross-product analysis
Error attribution
Region-specific bias
Uncertainty assessment and quantification

Iterative improvement and priority setting

Figure 5.1. Conceptual diagram showing how data products, machine learning modelling and evaluation frameworks interact.

More work is needed to downscale and bias-correct climate model output on a pixel level to ensure regional reliability in the projections. This requires not only high-resolution observational datasets for calibration, but also robust statistical or dynamical methods that preserve key extremes and seasonality in future climate variables. However, such efforts are often limited by the availability of consistent historical data across remote boreal regions. For instance, Arctic CORDEX (COordinated Regional climate Downscaling EXperiment) simulations have been downscaled from 2.5° CMIP6 ensemble data, but the spatial resolutions are still low at 0.22° or 0.44° (25 or 50 km - Koenigk et al., 2015). As a result, many fire modelling studies rely on coarse-scale projections, which may obscure important local variability and reduce confidence in impact assessments.

Separating changes in fire frequency, as opposed to predicting the magnitude of burned area, can be further explored, providing clearer insight into underlying mechanisms and model behaviour. For example, climate drivers such as temperature anomalies may primarily influence the probability of fire occurrence, whereas fuel continuity or suppression capacity may govern fire growth and hence magnitude. Evaluating whether a model captures shifts in frequency, size distribution, or both can therefore improve interpretability, reveal compensating errors, such as too many small fires vs too few large ones, and offer a more process-aligned basis for attributing change under future climate scenarios.

Collaboration with indigenous knowledge holders and local communities could provide critical insights into fire regimes, especially in remote boreal areas where scientific observations are sparse or discontinuous. Indigenous fire stewardship is based on long-term, site-specific observation and traditional ecological knowledge, which can offer refined insights into fire frequency, seasonality, vegetation responses, and the ecological role of fire across generations (Lake and Christianson, 2019, Hoffman et al., 2022). These perspectives can not only complement academic research, but also challenge prevailing assumptions, for instance what constitutes a "natural fire regime" (Krebs et al., 2010), by integrating cultural, historical and environmental knowledge. Future work should include co-designed methodologies that support mutual knowledge exchange and respect data sovereignty. Indigenous-led fire management can serve as both a scientific and social model for resilience as climate change intensifies.

In parallel, future fire models may also benefit from incorporating metrics of forest health (such as canopy dieback or drought stress), pest and pathogen outbreaks, and human vulnerability (such as community isolation or infrastructure exposure) to produce more holistic fire risk assessments (Dale et al., 2001, Ghorbanzadeh et al., 2019). Including these factors would allow models to account for compound disturbances and socio-ecological feedbacks, which are particularly important under climate change. Such developments would support not only more accurate projections of wildfire occurrence, but also better-informed decision-making around preparedness, mitigation and adaption planning in boreal regions.

Concluding remarks

Boreal forests are on the front lines of climate-driven ecological change, and fire is one of the clearest and most consequential signals of this transformation. This thesis provides evidence that fire activity in the boreal biome is intensifying, and that climate change is a central driver of these shifts. Through the integration of historical analyses, spatial fire patterning, and forward-looking machine learning projections, the work contributes to a growing understanding of how fire regimes may evolve in the coming decades. While considerable uncertainties remain, the path forward is clear: there is an urgent need for sustained monitoring, improved modelling, and targeted policy responses that reflect the changing fire realities of boreal ecosystems. By advancing our knowledge of climate-fire interactions and demonstrating new tools for future risk assessment, this thesis aims to support more informed and adaptive approaches to managing wildfire in a rapidly warming world.

Bibliography

ABATZOGLOU, J. T., KOLDEN, C. A., CULLEN, A. C., SADEGH, M., WILLIAMS, E. L., TURCO, M. & JONES, M. W. 2025. Climate change has increased the odds of extreme regional forest fire years globally. *Nature Communications,* 16**,** 6390.

ABID, F. 2021. A Survey of Machine Learning Algorithms Based Forest Fires Prediction and Detection Systems. *Fire Technology,* 57**,** 559-590.

AIRBUS 2022. Copernicus DEM Product Handbook v5.0. *In:* GMBH, A. D. A. S. (ed.).

ALENCAR, A. A. C., ARRUDA, V. L. S., DA SILVA, W. V., CONCIANI, D. E., COSTA, D. P., CRUSCO, N., DUVERGER, S. G., FERREIRA, N. C., FRANCA-ROCHA, W., HASENACK, H., MARTENEXEN, L. F. M., PIONTEKOWSKI, V. J., RIBEIRO, N. V., ROSA, E. R., ROSA, M. R., DOS SANTOS, S. M. B., SHIMBO, J. Z. & VÉLEZ-MARTIN, E. 2022. Long-Term Landsat-Based Monthly Burned Area Dataset for the Brazilian Biomes Using Deep Learning. *Remote Sensing,* 14**,** 2510.

ALEXANDER, M. E. & CRUZ, M. G. 2013. Limitations on the accuracy of model predictions of wildland fire behaviour: A state-of-the-knowledge overview. *The Forestry Chronicle,* 89**,** 372-383.

ALFARO-SÁNCHEZ, R., JOHNSTONE, J. F. & BALTZER, J. L. 2024. Low-severity fires in the boreal region: reproductive implications for black spruce stands in between stand-replacing fire events. *Annals of Botany*.

AMAROUCHE, K., AKPıNAR, A., SORAN, M. B., MYSLENKOV, S., MAJIDI, A. G., KANKAL, M. & ARKHIPKIN, V. 2021. Spatial calibration of an unstructured SWAN model forced with CFSR and ERA5 winds for the Black and Azov Seas. *Applied Ocean Research,* 117**,** 102962.

ANDERSSON, E. 2007. Data assimilation in the polar regions. *ECMWF Newsletter,* 112**,** 10-15.

ANGERS, V., GAUTHIER, S., DRAPEAU, P., JAYEN, K. & BERGERON, Y. 2011. Tree mortality and snag dynamics in North American boreal tree species after a wildfire: A long-term study. *International Journal of Wildland Fire,* 20**,** 751-763.

ARIF, M., ALGHAMDI, K. K., SAHEL, S. A., ALOSAIMI, S. O., ALSAHAFI, M. E., ALHARTHI, M. A. & ARIF, M. 2021. Role of Machine Learning Algorithms in Forest Fire Management: A Literature Review. *Journal of Robotics and Automation,* 5**,** 212-226.

ARMSTRONG MCKAY, D. I., STAAL, A., ABRAMS, J. F., WINKELMANN, R., SAKSCHEWSKI, B., LORIANI, S., FETZER, I., CORNELL, S. E., ROCKSTRÖM, J. & LENTON, T. M. 2022. Exceeding 1.5°C global warming could trigger multiple climate tipping points. *Science,* 377**,** eabn7950.

BALCH, J. K., BRADLEY, B. A., ABATZOGLOU, J. T., NAGY, R. C., FUSCO, E. J. & MAHOOD, A. L. 2017. Human-started wildfires expand the fire niche across the United States. *Proceedings of the National Academy of Sciences,* 114**,** 2946-2951.

BALTZER, J. L., DAY, N. J., WALKER, X. J., GREENE, D., MACK, M. C., ALEXANDER, H. D., ARSENEAULT, D., BARNES, J., BERGERON, Y., BOUCHER, Y., BOURGEAU-CHAVEZ, L., BROWN, C. D., CARRIÈRE, S., HOWARD, B. K., GAUTHIER, S., PARISIEN, M.-A., REID, K. A., ROGERS, B. M., ROLAND, C., SIROIS, L., STEHN, S., THOMPSON, D. K., TURETSKY, M. R., VERAVERBEKE, S., WHITMAN, E., YANG, J. & JOHNSTONE, J. F. 2021. Increasing fire and the decline of fire adapted black spruce in the boreal forest. *Proceedings of the National Academy of Sciences,* 118**,** e2024872118.

BAR MASSADA, A., SYPHARD, A. D., HAWBAKER, T. J., STEWART, S. I. & RADELOFF, V. C. 2011. Effects of ignition location models on the burn patterns of simulated wildfires. *Environmental Modelling & Software,* 26**,** 583-592.

BARBOSA, M. L. F., KELLEY, D. I., BURTON, C. A., FERREIRA, I. J. M., DA VEIGA, R. M., BRADLEY, A., MOLIN, P. G. & ANDERSON, L. O. 2025. FLAME 1.0: a novel approach for modelling burned area in the Brazilian biomes using the maximum entropy concept. *Geosci. Model Dev.,* 18**,** 3533-3557.

BARTALEV, S. A., EGOROV, V. I., EFREMOV, V. S., FLITMAN, E. V., LOUPIAN, E. A. & STYTSENKO, F. V. 2012. Assessment of burned forest areas over the Russian federation from MODIS and Landsat-TM/ETM+ imagery. *Global Forest Monitoring from Earth Observation.* CRC Press Boca Raton, FL.

BECK, H. E., MCVICAR, T. R., VAN DIJK, A. I. J. M., SCHELLEKENS, J., DE JEU, R. A. M. & BRUIJNZEEL, L. A. 2011. Global evaluation of four AVHRR–NDVI data sets: Intercomparison and assessment against Landsat imagery. *Remote Sensing of Environment,* 115**,** 2547-2563.

BERRISFORD, P. 2023. *RE: ERA-Interim snow depth errors.* Type to CLELLAND, A. A.

BETTS, A. K., CHAN, D. Z. & DESJARDINS, R. L. 2019. Near-Surface Biases in ERA5 Over the Canadian Prairies. *Frontiers in Environmental Science,* 7.

BI, D., DIX, M., MARSLAND, S., O'FARRELL, S., SULLIVAN, A., BODMAN, R., LAW, R., HARMAN, I., SRBINOVSKY, J., RASHID, H. A., DOBROHOTOFF, P., MACKALLAH, C., YAN, H., HIRST, A., SAVITA, A., BOEIRA DIAS, F., WOODHOUSE, M., FIEDLER, R. & HEERDEGEN, A. 2020. Configuration and spin-up of ACCESS-CM2, the new generation Australian Community Climate and Earth System Simulator Coupled Model. *Journal of Southern Hemisphere Earth Systems Science,* 70**,** 225-251.

BIRGE, H., SHULSKI, M., TRUMP, B. D., ERNAKOVICH, J., HEFLEY, T., HUNTINGTON, O., JARDINE, C., KLASA, K., LINES, L.-A. & LINKOV, I. 2020. An Information-Based Resilience Framework for the Changing Arctic. *Cybersecurity and Resilience in the Arctic.* IOS Press.

BOSCHETTI, L., SPARKS, A., ROY, D., GIGLIO, L. & SAN-MIGUEL-AYANZ, J. 2020. GWIS National and Sub-National Fire Activity Data from the NASA MODIS Collection 6 Burned Area Product in Support of Policy Making, Carbon Inventories and Natural Resource Management. *NASA Applied Sciences Grant USA.*

BRANDT, J. P., FLANNIGAN, M. D., MAYNARD, D. G., THOMPSON, I. D. & VOLNEY, W. J. A. 2013. An introduction to Canada’s boreal zone: ecosystem processes, health, sustainability, and environmental issues. *Environmental Reviews,* 21**,** 207-226.

BRASSARD, B. W. & CHEN, H. Y. H. 2006. Stand Structural Dynamics of North American Boreal Forests. *Critical Reviews in Plant Sciences,* 25**,** 115-137.

BREIMAN, L. 2001. Random Forests. *Machine Learning,* 45**,** 5-32.

BRIONES, V., GENET, H., JAFAROV, E. E., ROGERS, B. M., WATTS, J. D., VIRKKALA, A. M., BARTSCH, A., MAGLIO, B. C., RADY, J. & NATALI, S. M. 2025. Fusing Regional and Global Datasets to Develop a Composite Land Cover Product Across High Latitudes. *Earth Syst. Sci. Data Discuss.,* 2025**,** 1-24.

BROWN, J., FERRIANS JR, O. J., HEGINBOTTOM, J. A. & MELNIKOV, E. S. 1998. Digital circum-Arctic map of permafrost and ground-ice conditions. *International Permafrost Association Data and Information Working Group, Circumpolar Active-Layer Permafrost System (CAPS), CD-ROM version,* 1.

BUDA, M., MAKI, A. & MAZUROWSKI, M. A. 2018. A systematic study of the class imbalance problem in convolutional neural networks. *Neural Networks,* 106**,** 249-259.

BURRELL, A. L., SUN, Q., BAXTER, R., KUKAVSKAYA, E. A., ZHILA, S. V., SHESTAKOVA, T., ROGERS, B. M., KADUK, J. & BARRETT, K. 2022. Climate change, fire return intervals and the growing risk of permanent forest loss in boreal Eurasia. *Science of The Total Environment,* 831**,** 154885.

CALLAGHAN, T. V., SHADUYKO, O., KIRPOTIN, S. N. & GORDOV, E. P. 2021. Siberian environmental change: Synthesis of recent studies and opportunities for networking. *Ambio,* 50**,** 2104-2127.

CAMIA, A., BOVIO, G., AGUADO, I. & STACH, N. 1999. Meteorological fire danger indices and remote sensing. *In:* CHUVIECO, E. (ed.) *Remote Sensing of Large Wildfires: in the European Mediterranean Basin.* Berlin, Heidelberg: Springer Berlin Heidelberg.

CAO, B., GRUBER, S., ZHENG, D. & LI, X. 2020. The ERA5-Land soil temperature bias in permafrost regions. *The Cryosphere,* 14**,** 2581-2595.

CARDIL, A., RODRIGUES, M., TAPIA, M., BARBERO, R., RAMÍREZ, J., STOOF, C. R., SILVA, C. A., MOHAN, M. & DE-MIGUEL, S. 2023. Climate teleconnections modulate global burned area. *Nature Communications,* 14**,** 427.

CARROLL, M., DIMICELI, C., TOWNSHEND, J., SOHLBERG, R., HUBBARD, A. B. & WOOTEN, M. R. 2009. A new global raster water mask at 250 m resolution. *International Journal of Digital Earth,* 2.

CASCIO, W. E. 2018. Wildland fire smoke and human health. *Science of The Total Environment,* 624**,** 586-595.

CHAN, A. H. Y., GUIZAR-COUTIÑO, A., KALAMANDEEN, M. & COOMES, D. A. 2023. Reconstructing 34 Years of Fire History in the Wet, Subtropical Vegetation of Hong Kong Using Landsat. *Remote Sensing,* 15**,** 1489.

CHANDER, G., MARKHAM, B. L. & HELDER, D. L. 2009. Summary of current radiometric calibration coefficients for Landsat MSS, TM, ETM+, and EO-1 ALI sensors. *Remote Sensing of Environment,* 113**,** 893-903.

CHEN, J., SHAO, C., JIANG, S., QU, L., ZHAO, F. & DONG, G. 2019. Effects of changes in precipitation on energy and water balance in a Eurasian meadow steppe. *Ecological Processes,* 8**,** 17.

CHEN, T. & GUESTRIN, C. 2016. XGBoost: A Scalable Tree Boosting System. *Proceedings of the 22nd ACM SIGKDD International Conference on Knowledge Discovery and Data Mining.* San Francisco, California, USA: Association for Computing Machinery.

CHEN, Y., HALL, J., VAN WEES, D., ANDELA, N., HANTSON, S., GIGLIO, L., VAN DER WERF, G. R., MORTON, D. C. & RANDERSON, J. T. 2023. Multi-decadal trends and variability in burned area from the fifth version of the Global Fire Emissions Database (GFED5). *Earth Syst. Sci. Data,* 15**,** 5227-5259.

CHENG, K. S., WEI, C. & CHANG, S. C. 2004. Locating landslides using multi-temporal satellite images. *Advances in Space Research,* 33**,** 296-301.

CHUVIECO, E., LIZUNDIA-LOIOLA, J., PETTINARI, M. L., RAMO, R., PADILLA, M., TANSEY, K., MOUILLOT, F., LAURENT, P., STORM, T., HEIL, A. & PLUMMER, S. 2018. Generation and analysis of a new global burned area product based on MODIS 250 m reflectance bands and thermal anomalies. *Earth Syst. Sci. Data,* 10**,** 2015-2031.

CHUVIECO, E., YUE, C., HEIL, A., MOUILLOT, F., ALONSO-CANAS, I., PADILLA, M., PEREIRA, J. M., OOM, D. & TANSEY, K. 2016. A new global burned area product for climate assessment of fire impacts. *Global Ecology and Biogeography,* 25**,** 619-629.

CHYLEK, P., FOLLAND, C., KLETT, J. D., WANG, M., HENGARTNER, N., LESINS, G. & DUBEY, M. K. 2022. Annual Mean Arctic Amplification 1970–2020: Observed and Simulated by CMIP6 Climate Models. *Geophysical Research Letters,* 49**,** e2022GL099371.

CHYTRÝ, M., HORSÁK, M., DANIHELKA, J., ERMAKOV, N., GERMAN, D. A., HÁJEK, M., HÁJKOVÁ, P., KOČÍ, M., KUBEŠOVÁ, S., LUSTYK, P., NEKOLA, J. C., PAVELKOVÁ ŘIČÁNKOVÁ, V., PREISLEROVÁ, Z., RESL, P. & VALACHOVIČ, M. 2019. A modern analogue of the Pleistocene steppe-tundra ecosystem in southern Siberia. *Boreas,* 48**,** 36-56.

CIHLAR, J., MANAK, M. & D' IORIO, M. 1994. Evaluation of compositing algorithms for AVHRR data over land. *IEEE Transactions on Geoscience and Remote Sensing,* 32**,** 427-437.

CLELLAND, A. A., MARSHALL, G. J. & BAXTER, R. 2024a. Evaluating the performance of key ERA-Interim, ERA5 and ERA5-Land climate variables across Siberia. *International Journal of Climatology,* 44**,** 2318-2342.

CLELLAND, A. A., MARSHALL, G. J., BAXTER, R., POTTER, S., TALUCCI, A. C., RADY, J. M., GENET, H., ROGERS, B. M. & NATALI, S. M. 2024b. Annual and Seasonal Patterns of Burned Area Products in Arctic-Boreal North America and Russia for 2001–2020. *Remote Sensing,* 16**,** 3306.

CONARD, S. G. & IVANOVA, G. A. 1997. Wildfire in Russian Boreal Forests—Potential Impacts of Fire Regime Characteristics on Emissions and Global Carbon Balance Estimates. *Environmental Pollution,* 98**,** 305-313.

COPERNICUS 2019. Algorithm Theoretical Basis Document, Version 1.0. D1.5.2-v.1.0_ATBD_ICDR_LC_v2.1_PRODUCTS_v1.0.1. UCLouvain, Belgium.

COUGHLAN, R., DI GIUSEPPE, F., VITOLO, C., BARNARD, C., LOPEZ, P. & DRUSCH, M. 2021. Using machine learning to predict fire-ignition occurrences from lightning forecasts. *Meteorological Applications,* 28**,** e1973.

CRACKNELL, A. P. 1997. *Advanced very high resolution radiometer AVHRR*, Crc Press.

CURASI, S. R., MELTON, J. R., ARORA, V. K., HUMPHREYS, E. R. & WHALEY, C. H. 2024. Global climate change below 2 °C avoids large end century increases in burned area in Canada. *npj Climate and Atmospheric Science,* 7**,** 228.

DALE, V. H., JOYCE, L. A., MCNULTY, S., NEILSON, R. P., AYRES, M. P., FLANNIGAN, M. D., HANSON, P. L. J., IRLAND, L. C., LUGO, A. E., PETERSON, C. J., SIMBERLOFF, D., SWANSON, F. J., STOCKS, B. J. & WOTTON, B. M. 2001. Climate Change and Forest Disturbances: Climate change can affect forests by altering the frequency, intensity, duration, and timing of fire, drought, introduced species, insect and pathogen outbreaks, hurricanes, windstorms, ice storms, or landslides. *BioScience,* 51**,** 723-734.

DAO, M., KWAN, C., AYHAN, B. & TRAN, T. D. Burn scar detection using cloudy MODIS images via low-rank and sparsity-based models. 2016 IEEE Global Conference on Signal and Information Processing (GlobalSIP), 7-9 Dec. 2016 2016. 177-181.

DE GROOT, W. J., CANTIN, A. S., FLANNIGAN, M. D., SOJA, A. J., GOWMAN, L. M. & NEWBERY, A. 2013. A comparison of Canadian and Russian boreal forest fire regimes. *Forest Ecology and Management,* 294**,** 23-34.

DECH, S., HOLZWARTH, S., ASAM, S., ANDRESEN, T., BACHMANN, M., BOETTCHER, M., DIETZ, A., EISFELDER, C., FREY, C., GESELL, G., GESSNER, U., HIRNER, A., HOFMANN, M., KIRCHES, G., KLEIN, D., KLEIN, I., KRAUS, T., KRAUSE, D., PLANK, S., POPP, T., REINERMANN, S., REINERS, P., ROESSLER, S., RUPPERT, T., SCHERBACHENKO, A., VIGNESH, R., WOLFMUELLER, M., ZWENZNER, H. & KUENZER, C. 2021. Potential and Challenges of Harmonizing 40 Years of AVHRR Data: The TIMELINE Experience. *Remote Sensing,* 13**,** 3618.

DEE, D. P., UPPALA, S. M., SIMMONS, A. J., BERRISFORD, P., POLI, P., KOBAYASHI, S., ANDRAE, U., BALMASEDA, M. A., BALSAMO, G., BAUER, P., BECHTOLD, P., BELJAARS, A. C. M., VAN DE BERG, L., BIDLOT, J., BORMANN, N., DELSOL,

C., DRAGANI, R., FUENTES, M., GEER, A. J., HAIMBERGER, L., HEALY, S. B., HERSBACH, H., HÓLM, E. V., ISAKSEN, L., KÅLLBERG, P., KÖHLER, M., MATRICARDI, M., MCNALLY, A. P., MONGE-SANZ, B. M., MORCRETTE, J.-J., PARK, B.-K., PEUBEY, C., DE ROSNAY, P., TAVOLATO, C., THÉPAUT, J.-N. & VITART, F. 2011. The ERA-Interim reanalysis: configuration and performance of the data assimilation system. *Quarterly Journal of the Royal Meteorological Society,* 137**,** 553-597.

DELHASSE, A., KITTEL, C., AMORY, C., HOFER, S., VAN AS, D., S. FAUSTO, R. & FETTWEIS, X. 2020. Brief communication: Evaluation of the near-surface climate in ERA5 over the Greenland Ice Sheet. *The Cryosphere,* 14**,** 957-965.

DEMCHEV, D. M., KULAKOV, M. Y., MAKSHTAS, A. P., MAKHOTINA, I. A., FIL'CHUK, K. V. & FROLOV, I. E. 2020. Verification of ERA-Interim and ERA5 Reanalyses Data on Surface Air Temperature in the Arctic. *Russian Meteorology and Hydrology,* 45**,** 771-777.

DESCALS, A., GAVEAU, D. L. A., VERGER, A., SHEIL, D., NAITO, D. & PEÑUELAS, J. 2022. Unprecedented fire activity above the Arctic Circle linked to rising temperatures. *Science,* 378**,** 532-537.

DI GIUSEPPE, F. 2023. Accounting for fuel in fire danger forecasts: the fire occurrence probability index (FOPI). *Environmental Research Letters,* 18**,** 064029.

DI GIUSEPPE, F., MCNORTON, J., LOMBARDI, A. & WETTERHALL, F. 2025. Global data-driven prediction of fire activity. *Nature Communications,* 16**,** 2918.

DIMICELI, C., CARROLL, M., SOHLBERG, R., KIM, D., KELLY, M. & TOWNSHEND, J. 2015. MOD44B MODIS/Terra Vegetation Continuous Fields Yearly L3 Global 250m SIN Grid V006. *NASA EOSDIS Land Processes Distributed Active Archive Center.*

DINERSTEIN, E., OLSON, D. M., JOSHI, A., VYNNE, C., BURGESS, N. D., WIKRAMANAYAKE, E. D., HAHN, N., PALMINTERI, S., HEDAO, P., NOSS, R., HANSEN, M. C., LOCKE, H., ELLIS, E. C., JONES, B., BARBER, C. V., HAYES, R., KORMOS, C., MARTIN, V., CRIST, E., SECHREST, W., PRICE, L., BAILLIE, J. E. M., WEEDEN, D., SUCKLING, K., DAVIS, C., SIZER, N., MOORE, R., THAU, D., BIRCH, T., POTAPOV, P., TURUBANOVA, S., TYUKAVINA, A., DE SOUZA, N., PINTEA, L., BRITO, J. C., LLEWELLYN, O. A., MILLER, A. G., PATZELT, A., GHAZANFAR, S. A., TIMBERLAKE, J., KLÖSER, H., SHENNAN-FARPÓN, Y., KINDT, R., LILLESØ, J.-P. B., VAN BREUGEL, P., GRAUDAL, L., VOGE, M., AL-SHAMMARI, K. F. & SALEEM, M. 2017. An Ecoregion-Based Approach to Protecting Half the Terrestrial Realm. *BioScience,* 67**,** 534-545.

DONG, X., LUO, H., XU, C., YOU, C., SONG, X., JIN, J., LIN, R., ZHANG, H. & XUE, F. 2024. Historical Simulation and Future Projection of Arctic-Boreal Fire Carbon Emissions and Related Surface Climate by 17 CMIP6 ESMs. *Journal of Geophysical Research: Atmospheres,* 129**,** e2024JD041806.

DUNCAN, B. N., OTT, L. E., ABSHIRE, J. B., BRUCKER, L., CARROLL, M. L., CARTON, J., COMISO, J. C., DINNAT, E. P., FORBES, B. C., GONSAMO, A., GREGG, W. W., HALL, D. K., IALONGO, I., JANDT, R. R., KAHN, R. A., KARPECHKO, A. Y., KAWA, S. R., KATO, S., KUMPULA, T., KYRÖLÄ, E., LOBODA, T. V., MCDONALD, K. C., MONTESANO, P. M., NASSAR, R., NEIGH, C. S. R., PARKINSON, C. L., POULTER, B., PULLIAINEN, J., RAUTIAINEN, K., ROGERS, B. M., ROUSSEAUX, C. S., SOJA, A. J., STEINER, N., TAMMINEN, J., TAYLOR, P. C., TZORTZIOU, M. A., VIRTA, H., WANG, J. S., WATTS, J. D., WINKER, D. M. & WU, D. L. 2020. Space-Based Observations for Understanding Changes in the Arctic-Boreal Zone. *Reviews of Geophysics,* 58**,** e2019RG000652.

DUTRA, D. J., FEARNSIDE, P. M., YANAI, A. M., GRAÇA, P. M. L. D. A., DALAGNOL, R., PESSÔA, A. C. M., CABRAL, B. F., BURTON, C., JONES, C. & BETTS, R. A. 2023. Burned area mapping in Different Data Products for the Southwest of the Brazilian Amazon. *Rev. Bras. Cartogr,* 75**,** 1-16.

DUTRA, E., BALSAMO, G., VITERBO, P., MIRANDA, P. M. A., BELJAARS, A., SCHÄR, C. & ELDER, K. 2010. An Improved Snow Scheme for the ECMWF Land Surface Model: Description and Offline Validation. *Journal of Hydrometeorology,* 11**,** 899-916.

DYAKONOV, G. S., IBRAYEV, R. A. & SHISHKOVA, P. O. 2020. Assessment of ERA-Interim Reanalysis Data Qualityfor the Caspian Sea Area. *Russian Meteorology and Hydrology,* 45**,** 650-657.

EIDENSHINK, J., SCHWIND, B., BREWER, K., ZHU, Z.-L., QUAYLE, B. & HOWARD, S. 2007. A Project for Monitoring Trends in Burn Severity. *Fire Ecology,* 3**,** 3-21.

ELMENDORF, S. C., HENRY, G. H. R., HOLLISTER, R. D., BJÖRK, R. G., BJORKMAN, A. D., CALLAGHAN, T. V., COLLIER, L. S., COOPER, E. J., CORNELISSEN, J. H. C., DAY, T. A., FOSAA, A. M., GOULD, W. A., GRÉTARSDÓTTIR, J., HARTE, J., HERMANUTZ, L., HIK, D. S., HOFGAARD, A., JARRAD, F., JÓNSDÓTTIR, I. S., KEUPER, F., KLANDERUD, K., KLEIN, J. A., KOH, S., KUDO, G., LANG, S. I., LOEWEN, V., MAY, J. L., MERCADO, J., MICHELSEN, A., MOLAU, U., MYERS-SMITH, I. H., OBERBAUER, S. F., PIEPER, S., POST, E., RIXEN, C., ROBINSON, C. H., SCHMIDT, N. M., SHAVER, G. R., STENSTRÖM, A., TOLVANEN, A., TOTLAND, Ø., TROXLER, T., WAHREN, C.-H., WEBBER, P. J., WELKER, J. M. & WOOKEY, P. A. 2012. Global assessment of experimental climate warming on tundra vegetation: heterogeneity over space and time. *Ecology Letters,* 15**,** 164-175.

ENGLE, B., BRATOEV, I., CROWLEY, M. A., ZHU, Y. & SENF, C. 2025. Distribution and characteristics of lightning-ignited wildfires in boreal forests – the BoLtFire database. *Earth Syst. Sci. Data,* 17**,** 2249-2276.

ERDŐS, L., TÖRÖK, P., VELDMAN, J. W., BÁTORI, Z., BEDE-FAZEKAS, Á., MAGNES, M., KRÖEL-DULAY, G. & TÖLGYESI, C. 2022. How climate, topography, soils, herbivores, and fire control forest–grassland coexistence in the Eurasian forest-steppe. *Biological Reviews,* 97**,** 2195-2208.

ESA 2017. Land cover CCI product user guide version 2.

EUSKIRCHEN, E., GENET, H., MCGUIRE, A. D., CARMAN, T. B., RUTTER, R. A., MAGLIO, B., CLEIN, J., YUAN, F., YI, S. & ZHUANG, Q. 2025. DVMDOSTEM (v0.8.2). *In:* ZENODO (ed.).

EYRING, V., BONY, S., MEEHL, G. A., SENIOR, C. A., STEVENS, B., STOUFFER, R. J. & TAYLOR, K. E. 2016. Overview of the Coupled Model Intercomparison Project Phase 6 (CMIP6) experimental design and organization. *Geosci. Model Dev.,* 9**,** 1937-1958.

FERNANDES, R. & LEBLANC, S. G. 2005. Parametric (modified least squares) and non-parametric (Theil–Sen) linear regressions for predicting biophysical parameters in the presence of measurement errors. *Remote Sensing of Environment,* 95**,** 303-316.

FLANNIGAN, M., CANTIN, A. S., DE GROOT, W. J., WOTTON, M., NEWBERY, A. & GOWMAN, L. M. 2013. Global wildland fire season severity in the 21st century. *Forest Ecology and Management,* 294**,** 54-61.

FLANNIGAN, M. D., STOCKS, B., TURETSKY, M. & WOTTON, M. 2009. Impacts of climate change on fire activity and fire management in the circumboreal forest. *Global Change Biology,* 15**,** 549-560.

FLATLEY, W. T. & FULÉ, P. Z. 2016. Are historical fire regimes compatible with future climate? Implications for forest restoration. *Ecosphere,* 7**,** e01471.

FORKEL, M., ANDELA, N., HARRISON, S. P., LASSLOP, G., VAN MARLE, M., CHUVIECO, E., DORIGO, W., FORREST, M., HANTSON, S., HEIL, A., LI, F., MELTON, J., SITCH, S., YUE, C. & ARNETH, A. 2019. Emergent relationships with respect to burned area in global satellite observations and fire-enabled vegetation models. *Biogeosciences,* 16**,** 57-76.

FORNACCA, D., REN, G. & XIAO, W. 2017. Performance of Three MODIS Fire Products (MCD45A1, MCD64A1, MCD14ML), and ESA Fire_CCI in a Mountainous Area of Northwest Yunnan, China, Characterized by Frequent Small Fires. *Remote Sensing,* 9**,** 1131.

FRASER, R. H., HALL, R. J., LANDRY, R., LYNHAM, T., RAYMOND, D., LEE, B. & LI, Z. 2004. Validation and Calibration of Canada-Wide Coarse-Resolution Satellite Burned-Area Maps. *Photogrammetric Engineering & Remote Sensing,* 4**,** 451-460.

FRASER, R. H., LI, Z. & CIHLAR, J. 2000. Hotspot and NDVI Differencing Synergy (HANDS): A New Technique for Burned Area Mapping over Boreal Forest. *Remote Sensing of Environment,* 74**,** 362-376.

FREYCHET, N., TETT, S., WANG, J. & HEGERL, G. C. 2017. Summer heat waves over Eastern China: dynamical processes and trend attribution. *Environmental Research Letters,* 12**,** 024015.

FRIEDL, M. A. & SULLA-MENASHE, D. 2015. MODIS/Terra+Aqua Land Cover Type Yearly L3 Global 0.05Deg CMG V006. NASA EOSDIS Land Processes Distributed Active Archive Center.

FRIEDL, M. A. & SULLA-MENASHE, D. 2022. MODIS/Terra+Aqua Land Cover Type Yearly L3 Global 500m SIN Grid V061. *In:* CENTER, N. E. L. P. D. A. A. (ed.).

FRIEDL, M. A., SULLA-MENASHE, D., TAN, B., SCHNEIDER, A., RAMANKUTTY, N., SIBLEY, A. & HUANG, X. 2010. MODIS Collection 5 global land cover: Algorithm refinements and characterization of new datasets. *Remote Sensing of Environment,* 114**,** 168-182.

FROST, G. V., LOEHMAN, R. A., SAPERSTEIN, L. B., MACANDER, M. J., NELSON, P. R., PARADIS, D. P. & NATALI, S. M. 2020. Multi-decadal patterns of vegetation succession after tundra fire on the Yukon-Kuskokwim Delta, Alaska. *Environmental Research Letters,* 15**,** 025003.

GALE, M. G., CARY, G. J., VAN DIJK, A. I. J. M. & YEBRA, M. 2021. Forest fire fuel through the lens of remote sensing: Review of approaches, challenges and future directions in the remote sensing of biotic determinants of fire behaviour. *Remote Sensing of Environment,* 255**,** 112282.

GAO, P., TERANDO, A. J., KUPFER, J. A., VARNER, J. M., STAMBAUGH, M. C., LEI, T. L. & HIERS, J. K. 2021. Robust projections of future fire probability for the conterminous United States. *Science of The Total Environment,* 789**,** 147872.

GAUTHIER, S., BERNIER, P., KUULUVAINEN, T., SHVIDENKO, A. Z. & SCHEPASCHENKO, D. G. 2015. Boreal forest health and global change. *Science,* 349**,** 819-822.

GHORBANZADEH, O., BLASCHKE, T., GHOLAMNIA, K. & ARYAL, J. 2019. Forest Fire Susceptibility and Risk Mapping Using Social/Infrastructural Vulnerability and Environmental Variables. *Fire,* 2**,** 50.

GIGLIO, L., BOSCHETTI, L., ROY, D. P., HUMBER, M. L. & JUSTICE, C. O. 2018. The Collection 6 MODIS burned area mapping algorithm and product. *Remote Sensing of Environment,* 217**,** 72-85.

GIGLIO, L., RANDERSON, J. T. & VAN DER WERF, G. R. 2013. Analysis of daily, monthly, and annual burned area using the fourth-generation global fire emissions database (GFED4). *Journal of Geophysical Research: Biogeosciences,* 118**,** 317-328.

GIGLIO, L., SCHROEDER, W. & JUSTICE, C. O. 2016. The collection 6 MODIS active fire detection algorithm and fire products. *Remote Sensing of Environment,* 178**,** 31-41.

GIGLIO, L., VAN DER WERF, G. R., RANDERSON, J. T., COLLATZ, G. J. & KASIBHATLA, P. 2006. Global estimation of burned area using MODIS active fire observations. *Atmos. Chem. Phys.,* 6**,** 957-974.

GLADSTONE, P. 2023. *Synop Information for 24967 in Tegyul'tya|Tegjultje-Terde, SA, Russian Federation* [Online]. Available: https://weather.gladstonefamily.net/site/24967 [Accessed 07 August 2023 2023].

GOLDEN, D. M., AUDET, C. & SMITH, M. A. 2015. "Blue-ice": framing climate change and reframing climate change adaptation from the indigenous peoples' perspective in the northern boreal forest of Ontario, Canada. *Climate and Development,* 7**,** 401-413.

GOOGLE. 2024a. *ee.Reducer.frequencyHistogram* [Online]. Available: https://developers.google.com/earth-engine/apidocs/ee-reducer-frequencyhistogram [Accessed August 9 2024].

GOOGLE. 2024b. *ee.Reducer.sum* [Online]. Available: https://developers.google.com/earth-engine/apidocs/ee-reducer-sum [Accessed August 9 2024].

GORBATENKO, V., NECHEPURENKO, O. & ERSHOVA, T. 2019. Characteristics of atmosphere on days with thunderstorms in the Southeast of Western Siberia. *IOP Conference Series: Materials Science and Engineering,* 698**,** 044043.

GORELICK, N., HANCHER, M., DIXON, M., ILYUSHCHENKO, S., THAU, D. & MOORE, R. 2017. Google Earth Engine: Planetary-scale geospatial analysis for everyone. *Remote Sensing of Environment,* 202**,** 18-27.

GRAHAM, R. M., HUDSON, S. R. & MATURILLI, M. 2019. Improved Performance of ERA5 in Arctic Gateway Relative to Four Global Atmospheric Reanalyses. *Geophysical Research Letters,* 46**,** 6138-6147.

GRANKINA, T. B., IBRAYEV, R. A. & MOGILNIKOV, P. A. 2019. Verification of the ERA-Interim Reanalysis Data in the Azov-Black Sea Basin. *Physical Oceanography,* 26**,** 236-246.

GROISMAN, P. Y., SHUGART, H. H., KICKLIGHTER, D., HENEBRY, G., TCHEBAKOVA, N. M., MAKSYUTOV, S., MONIER, E., GUTMAN, G., GULEV, S., QI, J., PRISHCHEPOV, A. V., KUKAVSKAYA, E. A., PORFIRIEV, B., SHIKLOMANOV, A. I., LOBODA, T., SHIKLOMANOV, N., NGHIEM, S., BERGEN, K. M., ALBRECHTOVÁ, J., CHEN, J., SHAHGEDANOVA, M., SHVIDENKO, A. Z., SPERANSKAYA, N. A., SOJA, A., DE BEURS, K., BULYGINA, O. N., MCCARTY, J. L., ZHUANG, Q. & ZOLINA, O. 2017. Northern Eurasia Future Initiative (NEFI): facing the challenges and pathways of global change in the twenty-first century. *Progress in Earth and Planetary Science,* 4**,** 41.

GUO, Z., LI, W., CIAIS, P., SITCH, S., VAN DER WERF, G. R., BOWRING, S. P. K., BASTOS, A., MOUILLOT, F., HE, J., SUN, M., ZHU, L., DU, X., WANG, N. & HUANG, X. 2025. Reconstructed global monthly burned area maps from 1901 to 2020. *Earth Syst. Sci. Data,* 17**,** 3599-3618.

HAAS, O., PRENTICE, I. C. & HARRISON, S. P. 2026. Wildfires on a changing planet. *Nature Communications,* 17**,** 1599.

HALL, R. J., SKAKUN, R. S., METSARANTA, J. M., LANDRY, R., FRASER, R. H., RAYMOND, D., GARTRELL, M., DECKER, V. & LITTLE, J. 2020. Generating annual estimates of forest fire disturbance in Canada: the National Burned Area Composite. *International Journal of Wildland Fire,* 29**,** 878-891.

HANAN, E. J., KENNEDY, M. C., REN, J., JOHNSON, M. C. & SMITH, A. M. S. 2022. Missing Climate Feedbacks in Fire Models: Limitations and Uncertainties in Fuel

Loadings and the Role of Decomposition in Fine Fuel Accumulation. *Journal of Advances in Modeling Earth Systems,* 14**,** e2021MS002818.

HANES, C. C., WANG, X., JAIN, P., PARISIEN, M.-A., LITTLE, J. M. & FLANNIGAN, M. D. 2019. Fire-regime changes in Canada over the last half century. *Canadian Journal of Forest Research,* 49**,** 256-269.

HANSEN, M. C., DEFRIES, R. S., TOWNSHEND, J., CARROLL, M., DIMICELI, C. & SOHLBERG, R. 2003. Global percent tree cover at a spatial resolution of 500 meters: First results of the MODIS vegetation continuous fields algorithm. *Earth Interactions,* 7**,** 1-15.

HANTSON, S., ARNETH, A., HARRISON, S. P., KELLEY, D. I., PRENTICE, I. C., RABIN, S. S., ARCHIBALD, S., MOUILLOT, F., ARNOLD, S. R., ARTAXO, P., BACHELET, D., CIAIS, P., FORREST, M., FRIEDLINGSTEIN, P., HICKLER, T., KAPLAN, J. O., KLOSTER, S., KNORR, W., LASSLOP, G., LI, F., MANGEON, S., MELTON, J. R., MEYN, A., SITCH, S., SPESSA, A., VAN DER WERF, G. R., VOULGARAKIS, A. & YUE, C. 2016. The status and challenge of global fire modelling. *Biogeosciences,* 13**,** 3359-3375.

HANTSON, S., PADILLA, M., CORTI, D. & CHUVIECO, E. 2013. Strengths and weaknesses of MODIS hotspots to characterize global fire occurrence. *Remote Sensing of Environment,* 131**,** 152-159.

HART, S. A. & CHEN, H. Y. H. 2006. Understory Vegetation Dynamics of North American Boreal Forests. *Critical Reviews in Plant Sciences,* 25**,** 381-397.

HAUSFATHER, Z. & PETERS, G. P. 2020. Emissions–the 'business as usual'story is misleading. *Nature,* 577**,** 618-620.

HAWBAKER, T. J., RADELOFF, V. C., SYPHARD, A. D., ZHU, Z. & STEWART, S. I. 2008. Detection rates of the MODIS active fire product in the United States. *Remote Sensing of Environment,* 112**,** 2656-2664.

HEIJMANS, M. M. P. D., MAGNÚSSON, R. Í., LARA, M. J., FROST, G. V., MYERS-SMITH, I. H., VAN HUISSTEDEN, J., JORGENSON, M. T., FEDOROV, A. N., EPSTEIN, H. E., LAWRENCE, D. M. & LIMPENS, J. 2022. Tundra vegetation change and impacts on permafrost. *Nature Reviews Earth & Environment,* 3**,** 68-84.

HERMOSILLA, T., WULDER, M. A., WHITE, J. C., COOPS, N. C. & HOBART, G. W. 2015. An integrated Landsat time series protocol for change detection and generation of annual gap-free surface reflectance composites. *Remote Sensing of Environment,* 158**,** 220-234.

HERMOSILLA, T., WULDER, M. A., WHITE, J. C., COOPS, N. C., HOBART, G. W. & CAMPBELL, L. B. 2016. Mass data processing of time series Landsat imagery: pixels to data products for forest monitoring. *International Journal of Digital Earth,* 9**,** 1035-1054.

HERRMANN, P. B., NASCIMENTO, V. F., CASAGRANDE, F., DE FREITAS, M. W. D. & KLUG, A. C. 2023. Spatial modeling of fire in the atlantic forest considering future climate change scenarios in Rio Grande do Sul state – Brazil. *Journal of South American Earth Sciences,* 131**,** 104614.

HERSBACH, H. 2022. *RE: ERA5 snow depth assimilation in Russia.* Type to CLELLAND, A. A.

HERSBACH, H., BELL, B., BERRISFORD, P., BIAVATI, G., HORÁNYI, A., MUÑOZ-SABATER, J., NICOLAS, J., PEUBEY, C., RADU, R., ROZUM, I., SCHEPERS, D., SIMMONS, A., SOCI, C., DEE, D. & THÉPAUT, J. N. 2023. *ERA5 hourly data on pressure levels from 1940 to present* [Online]. Copernicus Climate Change Service (C3S). [Accessed 04 July 2023 2023].

HERSBACH, H., BELL, B., BERRISFORD, P., HIRAHARA, S., HORÁNYI, A., MUÑOZ-SABATER, J., NICOLAS, J., PEUBEY, C., RADU, R., SCHEPERS, D., SIMMONS, A., SOCI, C., ABDALLA, S., ABELLAN, X., BALSAMO, G., BECHTOLD, P., BIAVATI, G., BIDLOT, J., BONAVITA, M., DE CHIARA, G., DAHLGREN, P., DEE, D., DIAMANTAKIS, M., DRAGANI, R., FLEMMING, J., FORBES, R., FUENTES, M., GEER, A., HAIMBERGER, L., HEALY, S., HOGAN, R. J., HÓLM, E., JANISKOVÁ, M., KEELEY, S., LALOYAUX, P., LOPEZ, P., LUPU, C., RADNOTI, G., DE ROSNAY, P., ROZUM, I., VAMBORG, F., VILLAUME, S. & THÉPAUT, J.-N. 2020. The ERA5 global reanalysis. *Quarterly Journal of the Royal Meteorological Society,* 146**,** 1999-2049.

HILL, D. F., BRUHIS, N., CALOS, S. E., ARENDT, A. & BEAMER, J. 2015. Spatial and temporal variability of freshwater discharge into the Gulf of Alaska. *Journal of Geophysical Research: Oceans,* 120**,** 634-646.

HOBBIE, S. E., NADELHOFFER, K. J. & HÖGBERG, P. 2002. A synthesis: The role of nutrients as constraints on carbon balances in boreal and arctic regions. *Plant and Soil,* 242**,** 163-170.

HOFFMAN, K. M., CHRISTIANSON, A. C., DICKSON-HOYLE, S., COPES-GERBITZ, K., NIKOLAKIS, W., DIABO, D. A., MCLEOD, R., MICHELL, H. J., AL MAMUN, A., ZAHARA, A., MAURO, N., GILCHRIST, J., ROSS, R. M. & DANIELS, L. D. 2022. The right to burn: barriers and opportunities for Indigenous-led fire stewardship in Canada. *FACETS,* 7**,** 464-481.

HOLBEN, B. N. 1986. Characteristics of maximum-value composite images from temporal AVHRR data. *International Journal of Remote Sensing,* 7**,** 1417-1434.

HU, G., ZHAO, L., WU, T., WU, X., PARK, H., LI, R., ZHU, X., NI, J., ZOU, D., HAO, J. & LI, W. 2022. Continued Warming of the Permafrost Regions Over the Northern Hemisphere Under Future Climate Change. *Earth's Future,* 10**,** e2022EF002835.

HUANG, X., XUE, L., WANG, Z., LIU, Y., DING, K. & DING, A. 2024. Escalating Wildfires in Siberia Driven by Climate Feedbacks Under a Warming Arctic in the 21st Century. *AGU Advances,* 5**,** e2023AV001151.

HUMBER, M. L., BOSCHETTI, L., GIGLIO, L. & JUSTICE, C. O. 2019. Spatial and temporal intercomparison of four global burned area products. *International Journal of Digital Earth,* 12**,** 460-484.

HUSSAIN, M. M. & MAHMUD, I. 2019. pyMannKendall: a python package for non parametric Mann Kendall family of trend tests. *Journal of Open Source Software,* 4**,** 1556.

IPCC 2023. Future Global Climate: Scenario-based Projections and Near-term Information. *In:* INTERGOVERNMENTAL PANEL ON CLIMATE, C. (ed.) *Climate Change 2021 – The Physical Science Basis: Working Group I Contribution to the Sixth Assessment Report of the Intergovernmental Panel on Climate Change.* Cambridge, UK, and New York, USA: Cambridge University Press.

IRANNEZHAD, M., LIU, J., AHMADI, B. & CHEN, D. 2020. The dangers of Arctic zombie wildfires. *Science,* 369**,** 1171-1171.

JAFAROV, E. E., MARCHENKO, S. S. & ROMANOVSKY, V. E. 2012. Numerical modeling of permafrost dynamics in Alaska using a high spatial resolution dataset. *The Cryosphere,* 6**,** 613-624.

JAFAROV, E. E., ROMANOVSKY, V. E., GENET, H., MCGUIRE, A. D. & MARCHENKO, S. S. 2013. The effects of fire on the thermal stability of permafrost in lowland and upland black spruce forests of interior Alaska in a changing climate. *Environmental Research Letters,* 8**,** 035030.

JAIN, P., BARBER, Q. E., TAYLOR, S. W., WHITMAN, E., CASTELLANOS ACUNA, D., BOULANGER, Y., CHAVARDÈS, R. D., CHEN, J., ENGLEFIELD, P., FLANNIGAN, M., GIRARDIN, M. P., HANES, C. C., LITTLE, J., MORRISON, K., SKAKUN, R. S., THOMPSON, D. K., WANG, X. & PARISIEN, M.-A. 2024. Drivers and Impacts of the Record-Breaking 2023 Wildfire Season in Canada. *Nature Communications,* 15**,** 6764.

JANSSEN, T. A. J., JONES, M. W., FINNEY, D., VAN DER WERF, G. R., VAN WEES, D., XU, W. & VERAVERBEKE, S. 2023. Extratropical forests increasingly at risk due to lightning fires. *Nature Geoscience,* 16**,** 1136-1144.

JANSSEN, T. A. J. & VERAVERBEKE, S. 2025. What Are the Limits to the Growth of Boreal Fires? *Global Change Biology,* 31**,** e70130.

JOHNSTONE, J. F., ALLEN, C. D., FRANKLIN, J. F., FRELICH, L. E., HARVEY, B. J., HIGUERA, P. E., MACK, M. C., MEENTEMEYER, R. K., METZ, M. R., PERRY, G. L. W., SCHOENNAGEL, T. & TURNER, M. G. 2016. Changing disturbance regimes, ecological memory, and forest resilience. *Frontiers in Ecology and the Environment,* 14**,** 369-378.

JONES, M. W., ABATZOGLOU, J. T., VERAVERBEKE, S., ANDELA, N., LASSLOP, G., FORKEL, M., SMITH, A. J. P., BURTON, C., BETTS, R. A., VAN DER WERF, G. R., SITCH, S., CANADELL, J. G., SANTÍN, C., KOLDEN, C., DOERR, S. H. & LE QUÉRÉ, C. 2022. Global and Regional Trends and Drivers of Fire Under Climate Change. *Reviews of Geophysics,* 60**,** e2020RG000726.

JUSTICE, C. O., GIGLIO, L., KORONTZI, S., OWENS, J., MORISETTE, J. T., ROY, D., DESCLOITRES, J., ALLEAUME, S., PETITCOLIN, F. & KAUFMAN, Y. 2002a. The MODIS fire products. *Remote Sensing of Environment,* 83**,** 244-262.

JUSTICE, C. O., TOWNSHEND, J. R. G., VERMOTE, E. F., MASUOKA, E., WOLFE, R. E., SALEOUS, N., ROY, D. P. & MORISETTE, J. T. 2002b. An overview of MODIS Land data processing and product status. *Remote Sensing of Environment,* 83**,** 3-15.

KAYES, I. & MALLIK, A. 2020. Boreal forests: distributions, biodiversity, and management. *Life on land***,** 1-12.

KELLEY, D. I., BISTINAS, I., WHITLEY, R., BURTON, C., MARTHEWS, T. R. & DONG, N. 2019. How contemporary bioclimatic and human controls change global fire regimes. *Nature Climate Change,* 9**,** 690-696.

KELLEY, D. I., BURTON, C., HUNTINGFORD, C., BROWN, M. A. J., WHITLEY, R. & DONG, N. 2021. Technical note: Low meteorological influence found in 2019 Amazonia fires. *Biogeosciences,* 18**,** 787-804.

KENDALL, M. G. 1975. *Rank correlation methods,* London, Charles Griffin.

KHAIROUN, A., MOUILLOT, F., CHEN, W., CIAIS, P. & CHUVIECO, E. 2024. Coarse-resolution burned area datasets severely underestimate fire-related forest loss. *Science of The Total Environment,* 920**,** 170599.

KHARUK, V. I., PONOMAREV, E. I., IVANOVA, G. A., DVINSKAYA, M. L., COOGAN, S. C. P. & FLANNIGAN, M. D. 2021. Wildfires in the Siberian taiga. *Ambio,* 50**,** 1953-1974.

KHARYUTKINA, E., PUSTOVALOV, K., MORARU, E. & NECHEPURENKO, O. 2022. Analysis of Spatio-Temporal Variability of Lightning Activity and Wildfires in Western Siberia during 2016–2021. *Atmosphere,* 13**,** 669.

KLEHMET, K., GEYER, B. & ROCKEL, B. 2013. A regional climate model hindcast for Siberia: analysis of snow water equivalent. *The Cryosphere,* 7**,** 1017-1034.

KLEIN TANK, A. M. G., WIJNGAARD, J. B., KÖNNEN, G. P., BÖHM, R., DEMARÉE, G., GOCHEVA, A., MILETA, M., PASHIARDIS, S., HEJKRLIK, L., KERN-HANSEN, C., HEINO, R., BESSEMOULIN, P., MÜLLER-WESTERMEIER, G., TZANAKOU,

M., SZALAI, S., PÁLSDÓTTIR, T., FITZGERALD, D., RUBIN, S., CAPALDO, M., MAUGERI, M., LEITASS, A., BUKANTIS, A., ABERFELD, R., VAN ENGELEN, A. F. V., FORLAND, E., MIETUS, M., COELHO, F., MARES, C., RAZUVAEV, V., NIEPLOVA, E., CEGNAR, T., ANTONIO LÓPEZ, J., DAHLSTRÖM, B., MOBERG, A., KIRCHHOFER, W., CEYLAN, A., PACHALIUK, O., ALEXANDER, L. V. & PETROVIC, P. 2002. Daily dataset of 20th-century surface air temperature and precipitation series for the European Climate Assessment. *International Journal of Climatology,* 22**,** 1441-1453.

KOCHEEVA, N. A., CHANKIBAEVA, M. H., MINAEV, A. I., SUKHOVA, M. G. & MODOROV, A. A. 2018. Peculiarities of Thunderstorms' Occurrences on the Border of the Western Siberia Plains and Altai Mountains. *Journal of Environmental Management and Tourism***,** 1061-1068%V 8.

KOENIGK, T., BERG, P. & DÖSCHER, R. 2015. Arctic climate change in an ensemble of regional CORDEX simulations. *Polar Research,* 34.

KOLDEN, C. A. & WEISBERG, P. J. 2007. Assessing Accuracy of Manually-mapped Wildfire Perimeters in Topographically Dissected Areas. *Fire Ecology,* 3**,** 22-31.

KREBS, P., PEZZATTI, G. B., MAZZOLENI, S., TALBOT, L. M. & CONEDERA, M. 2010. Fire regime: history and definition of a key concept in disturbance ecology. *Theory in Biosciences,* 129**,** 53-69.

KWAK, H., LEE, W.-K., SABOROWSKI, J., LEE, S.-Y., WON, M.-S., KOO, K.-S., LEE, M.-B. & KIM, S.-N. 2012. Estimating the spatial pattern of human-caused forest fires using a generalized linear mixed model with spatial autocorrelation in South Korea. *International Journal of Geographical Information Science,* 26**,** 1589-1602.

LAKE, F. K. & CHRISTIANSON, A. C. 2019. Indigenous Fire Stewardship. *In:* MANZELLO, S. L. (ed.) *Encyclopedia of Wildfires and Wildland-Urban Interface (WUI) Fires.* Cham, Switzerland: Springer International Publishing.

LAMPE, S., GUDMUNDSSON, L., KRAFT, B., HANTSON, S., KELLEY, D., HUMPHREY, V., LE SAUX, B., CHUVIECO, E. & THIERY, W. 2026. BuRNN (v1.0): a data-driven fire model. *Geosci. Model Dev.,* 19**,** 955-988.

LAN, H., GUO, D., HUA, W., PEPIN, N. & SUN, J. 2023. Evaluation of reanalysis air temperature and precipitation in high-latitude Asia using ground-based observations. *International Journal of Climatology,* 43**,** 1621-1638.

LANGFORD, Z., KUMAR, J. & HOFFMAN, F. Wildfire Mapping in Interior Alaska Using Deep Neural Networks on Imbalanced Datasets. 2018 IEEE International Conference on Data Mining Workshops (ICDMW), 17-20 Nov. 2018 2018. 770-778.

LATIFOVIC, R., HOMER, C., RESSL, R., POULIOT, D. A., HOSSIAN, S., COLDITZ, R., OLTHOF, I., CHANDRA, G. & VICTORIA, A. 2012. North American Land Change Monitoring System. *Remote Sensing of Land Use and Land Cover: Principles and Applications.* CRC Press.

LAVOIE, L. & SIROIS, L. 1998. Vegetation changes caused by recent fires in the northern boreal forest of eastern Canada. *Journal of Vegetation Science,* 9**,** 483-492.

LECUN, Y. & BENGIO, Y. 1995. Convolutional networks for images, speech, and time series. *The handbook of brain theory and neural networks,* 3361**,** 1995.

LI, X.-Y., JIN, H.-J., WANG, H.-W., MARCHENKO, S. S., SHAN, W., LUO, D.-L., HE, R.-X., SPEKTOR, V., HUANG, Y.-D., LI, X.-Y. & JIA, N. 2021. Influences of forest fires on the permafrost environment: A review. *Advances in Climate Change Research,* 12**,** 48-65.

LI, Y., JANSSEN, T. A. J., CHEN, R., HE, B. & VERAVERBEKE, S. 2024. Trends and drivers of Arctic-boreal fire intensity between 2003 and 2022. *Science of The Total Environment,* 926**,** 172020.

LIN, S., LIU, Y. & HUANG, X. 2021. Climate-induced Arctic-boreal peatland fire and carbon loss in the 21st century. *Science of The Total Environment,* 796**,** 148924.

LIU, J., HAGAN, D. F. T. & LIU, Y. 2021. Global Land Surface Temperature Change (2003–2017) and Its Relationship with Climate Drivers: AIRS, MODIS, and ERA5-Land Based Analysis. *Remote Sensing,* 13**,** 44.

LIU, T., MARLIER, M., KARAMBELAS, A., JAIN, M., SINGH, S., SINGH, M., GAUTAM, R. & DEFRIES, R. S. 2019. Missing emissions from post-monsoon agricultural fires in northwestern India: regional limitations of MODIS burned area and active fire products. *Environmental Research Communications,* 1.

LIU, Z., LIU, Y., WANG, S., YANG, X., WANG, L., BAIG, M. H. A., CHI, W. & WANG, Z. 2018. Evaluation of Spatial and Temporal Performances of ERA-Interim Precipitation and Temperature in Mainland China. *Journal of Climate,* 31**,** 4347-4365.

LIZUNDIA-LOIOLA, J., FRANQUESA, M., KHAIROUN, A. & CHUVIECO, E. 2022. Global burned area mapping from Sentinel-3 Synergy and VIIRS active fires. *Remote Sensing of Environment,* 282**,** 113298.

LIZUNDIA-LOIOLA, J., OTÓN, G., RAMO, R. & CHUVIECO, E. 2020. A spatio-temporal active-fire clustering approach for global burned area mapping at 250 m from MODIS data. *Remote Sensing of Environment,* 236**,** 111493.

LOBANOV, V. A. & KIRILLINA, K. S. 2019. *The modern and future climate changes in the Republic of Sakha (Yakutia),* St. Petersburg, RSHU.

LOBODA, T. V., HALL, J. V., CHEN, D., HOFFMAN-HALL, A., SHEVADE, V. S., ARGUETA, F. & LIANG, X. 2024. Arctic Boreal Annual Burned Area, Circumpolar Boreal Forest and Tundra, V2, 2002-2022. ORNL Distributed Active Archive Center.

LOBODA, T. V., HOY, E. E., GIGLIO, L. & KASISCHKE, E. S. 2011. Mapping burned area in Alaska using MODIS data: a data limitations-driven modification to the regional burned area algorithm. *International Journal of Wildland Fire,* 20**,** 487-496.

LONG, T., ZHANG, Z., HE, G., JIAO, W., TANG, C., WU, B., ZHANG, X., WANG, G. & YIN, R. 2019. 30 m Resolution Global Annual Burned Area Mapping Based on Landsat Images and Google Earth Engine. *Remote Sensing,* 11**,** 489.

LUND, M. T., NORDLING, K., GJELSVIK, A. B. & SAMSET, B. H. 2023. The influence of variability on fire weather conditions in high latitude regions under present and future global warming. *Environmental Research Communications,* 5**,** 065016.

LUNDBERG, S. M. & LEE, S.-I. 2017. A Unified Approach to Interpreting Model Predictions. *In:* GUYON, I., LUXBURG, U. V., BENGIO, S., WALLACH, H., FERGUS, R., VISHWANATHAN, S. & GARNETT, R. (eds.).

MAGNUS, G. 1844. Versuche über die Spannkräfte des Wasserdampfs. *Annalen der Physik,* 137**,** 225-247.

MANN, H. B. 1945. Nonparametric Tests Against Trend. *Econometrica,* 13**,** 245-259.

MARSOUIN, A., LE BORGNE, P., LEGENDRE, G., PÉRÉ, S. & ROQUET, H. 2015. Six years of OSI-SAF METOP-A AVHRR sea surface temperature. *Remote Sensing of Environment,* 159**,** 288-306.

MATVEEVA, T. & SIDORCHUK, A. 2020. Modelling of Surface Runoff on the Yamal Peninsula, Russia, Using ERA5 Reanalysis. *Water,* 12**,** 2099.

MCCARTY, J. L., AALTO, J., PAUNU, V. V., ARNOLD, S. R., ECKHARDT, S., KLIMONT, Z., FAIN, J. J., EVANGELIOU, N., VENÄLÄINEN, A., TCHEBAKOVA, N. M., PARFENOVA, E. I., KUPIAINEN, K., SOJA, A. J., HUANG, L. & WILSON, S. 2021. Reviews and syntheses: Arctic fire regimes and emissions in the 21st century. *Biogeosciences,* 18**,** 5053-5083.

MCCARTY, J. L., SMITH, T. E. L. & TURETSKY, M. R. 2020. Arctic fires re-emerging. *Nature Geoscience,* 13**,** 658-660.

MEINSHAUSEN, M., LEWIS, J., MCGLADE, C., GÜTSCHOW, J., NICHOLLS, Z. R. J., BURDON, R., COZZI, L. & HACKMANN, B. 2022. Realization of Paris Agreement pledges may limit warming just below 2 °C. *Nature,* 604**,** 304-309.

MEINSHAUSEN, M., NICHOLLS, Z. R. J., LEWIS, J., GIDDEN, M. J., VOGEL, E., FREUND, M., BEYERLE, U., GESSNER, C., NAUELS, A., BAUER, N., CANADELL, J. G., DANIEL, J. S., JOHN, A., KRUMMEL, P. B., LUDERER, G., MEINSHAUSEN, N., MONTZKA, S. A., RAYNER, P. J., REIMANN, S., SMITH, S. J., VAN DEN BERG, M., VELDERS, G. J. M., VOLLMER, M. K. & WANG, R. H. J. 2020. The shared socio-economic pathway (SSP) greenhouse gas concentrations and their extensions to 2500. *Geosci. Model Dev.,* 13**,** 3571-3605.

MEKONNEN, Z. A., RILEY, W. J., BERNER, L. T., BOUSKILL, N. J., TORN, M. S., IWAHANA, G., BREEN, A. L., MYERS-SMITH, I. H., CRIADO, M. G., LIU, Y., EUSKIRCHEN, E. S., GOETZ, S. J., MACK, M. C. & GRANT, R. F. 2021. Arctic tundra shrubification: a review of mechanisms and impacts on ecosystem carbon balance. *Environmental Research Letters,* 16**,** 053001.

MICHAEL, Y., HELMAN, D., GLICKMAN, O., GABAY, D., BRENNER, S. & LENSKY, I. M. 2021. Forecasting fire risk with machine learning and dynamic information derived from satellite vegetation index time-series. *Science of The Total Environment,* 764**,** 142844.

MILES, M. W., MILES, V. V. & ESAU, I. 2019. Varying climate response across the tundra, forest-tundra and boreal forest biomes in northern West Siberia. *Environmental Research Letters,* 14**,** 075008.

MINER, K. R., TURETSKY, M. R., MALINA, E., BARTSCH, A., TAMMINEN, J., MCGUIRE, A. D., FIX, A., SWEENEY, C., ELDER, C. D. & MILLER, C. E. 2022. Permafrost carbon emissions in a changing Arctic. *Nature Reviews Earth & Environment,* 3**,** 55-67.

MINNETT, P. J., ALVERA-AZCÁRATE, A., CHIN, T. M., CORLETT, G. K., GENTEMANN, C. L., KARAGALI, I., LI, X., MARSOUIN, A., MARULLO, S., MATURI, E., SANTOLERI, R., SAUX PICART, S., STEELE, M. & VAZQUEZ-CUERVO, J. 2019. Half a century of satellite remote sensing of sea-surface temperature. *Remote Sensing of Environment,* 233**,** 111366.

MOHAJANE, M., COSTACHE, R., KARIMI, F., BAO PHAM, Q., ESSAHLAOUI, A., NGUYEN, H., LANEVE, G. & OUDIJA, F. 2021. Application of remote sensing and machine learning algorithms for forest fire mapping in a Mediterranean area. *Ecological Indicators,* 129**,** 107869.

MOREIRA, F., VIEDMA, O., ARIANOUTSOU, M., CURT, T., KOUTSIAS, N., RIGOLOT, E., BARBATI, A., CORONA, P., VAZ, P., XANTHOPOULOS, G., MOUILLOT, F. & BILGILI, E. 2011. Landscape – wildfire interactions in southern Europe: Implications for landscape management. *Journal of Environmental Management,* 92**,** 2389-2402.

MORENO-RUIZ, J.-A., GARCÍA-LÁZARO, J.-R., ARBELO, M. & HERNÁNDEZ-LEAL, P. A. 2023. A satellite-based burned area dataset for the northern boreal region from 1982 to 2020. *International Journal of Wildland Fire,* 32**,** 854-871.

MORITZ, M. A., PARISIEN, M.-A., BATLLORI, E., KRAWCHUK, M. A., VAN DORN, J., GANZ, D. J. & HAYHOE, K. 2012. Climate change and disruptions to global fire activity. *Ecosphere,* 3**,** art49.

MUÑOZ-SABATER, J., DUTRA, E., AGUSTÍ-PANAREDA, A., ALBERGEL, C., ARDUINI, G., BALSAMO, G., BOUSSETTA, S., CHOULGA, M., HARRIGAN, S., HERSBACH, H., MARTENS, B., MIRALLES, D. G., PILES, M., RODRÍGUEZ-FERNÁNDEZ, N. J., ZSOTER, E., BUONTEMPO, C. & THÉPAUT, J. N. 2021.

ERA5-Land: a state-of-the-art global reanalysis dataset for land applications. *Earth Syst. Sci. Data,* 13**,** 4349-4383.

NAGOL, J. R., VERMOTE, E. F. & PRINCE, S. D. 2009. Effects of atmospheric variation on AVHRR NDVI data. *Remote Sensing of Environment,* 113**,** 392-397.

NATEKIN, A. & KNOLL, A. 2013. Gradient boosting machines, a tutorial. *Frontiers in Neurorobotics,* 7.

NATURAL RESOURCES CANADA 2022. Canadian National Fire Database. Edmonton, Alberta: Natural Resources Canada, Canadian Forest Service, Northern Forestry Centre.

NCAR. 2023. *ERA-Interim* [Online]. UCAR. Available: https://climatedataguide.ucar.edu/climate-data/era-interim [Accessed 31 May 2023 2023].

NEFEDOVA, T. 2021. The 2010 Catastrophic Forest Fires in Russia: Consequence of Rural Depopulation? *The Demography of Disasters: Impacts for Population and Place***,** 71-79.

NOËL, B., VAN KAMPENHOUT, L., VAN DE BERG, W. J., LENAERTS, J. T. M., WOUTERS, B. & VAN DEN BROEKE, M. R. 2020. Brief communication: CESM2 climate forcing (1950–2014) yields realistic Greenland ice sheet surface mass balance. *The Cryosphere,* 14**,** 1425-1435.

O'NEILL, B. C., TEBALDI, C., VAN VUUREN, D. P., EYRING, V., FRIEDLINGSTEIN, P., HURTT, G., KNUTTI, R., KRIEGLER, E., LAMARQUE, J. F., LOWE, J., MEEHL, G. A., MOSS, R., RIAHI, K. & SANDERSON, B. M. 2016. The Scenario Model Intercomparison Project (ScenarioMIP) for CMIP6. *Geosci. Model Dev.,* 9**,** 3461-3482.

OBU, J., WESTERMANN, S., BARTSCH, A., BERDNIKOV, N., CHRISTIANSEN, H. H., DASHTSEREN, A., DELALOYE, R., ELBERLING, B., ETZELMÜLLER, B., KHOLODOV, A., KHOMUTOV, A., KÄÄB, A., LEIBMAN, M. O., LEWKOWICZ, A. G., PANDA, S. K., ROMANOVSKY, V. E., WAY, R. G., WESTERGAARD-NIELSEN, A., WU, T., YAMKHIN, J. & ZOU, D. 2019. Northern Hemisphere permafrost map based on TTOP modelling for 2000–2016 at 1 km2 scale. *Earth-Science Reviews,* 193**,** 299-316.

OLIVA, P. & SCHROEDER, W. 2015. Assessment of VIIRS 375m active fire detection product for direct burned area mapping. *Remote Sensing of Environment,* 160**,** 144-155.

OLSSON, R. 2009. *Boreal Forest and Climate Change,* Goteborg, Air Pollution & Climate Secretariat & Taiga Rescue Network.

OLSSON, R. 2011. *To Manage or Protect? - Boreal Forests from a Climate Perspective,* Goteborg, Air Pollution & Climate Secretariat (Reinhold Pape).

ORIS, F., ASSELIN, H., ALI, A. A., FINSINGER, W. & BERGERON, Y. 2014. Effect of increased fire activity on global warming in the boreal forest. *Environmental Reviews,* 22**,** 206-219.

OTÓN, G., LIZUNDIA-LOIOLA, J., PETTINARI, M. L. & CHUVIECO, E. 2021. Development of a consistent global long-term burned area product (1982–2018) based on AVHRR-LTDR data. *International Journal of Applied Earth Observation and Geoinformation,* 103**,** 102473.

PARK, T., WANG, W., THRASHER, B., HASHIMOTO, H., MICHAELIS, A., MADRAZO, M., LEE, H., RYOO, J.-M., LEE, T., NEMANI, R. & BROSNAN, I. 2023. Downscaled 21st century global fire weather projections (v1.1). *In:* ZENODO (ed.).

PAUSAS, J. G. & KEELEY, J. E. 2021. Wildfires and global change. *Frontiers in Ecology and the Environment,* 19**,** 387-395.

PAYETTE, S. 1992. Fire as a controlling process in the North American boreal forest. *A systems analysis of the global boreal forest***,** 144-169.

PEDREGOSA, F., VAROQUAUX, G., GRAMFORT, A., MICHEL, V., THIRION, B., GRISEL, O., BLONDEL, M., PRETTENHOFER, P., WEISS, R. & DUBOURG, V. 2011. Scikit-learn: Machine learning in Python. *the Journal of machine Learning research,* 12**,** 2825-2830.

PEKEL, J.-F., COTTAM, A., GORELICK, N. & BELWARD, A. S. 2016. High-resolution mapping of global surface water and its long-term changes. *Nature,* 540**,** 418-422.

PESSÔA, A. C. M., ANDERSON, L. O., CARVALHO, N. S., CAMPANHARO, W. A., JUNIOR, C. H. L. S., ROSAN, T. M., REIS, J. B. C., PEREIRA, F. R. S., ASSIS, M., JACON, A. D., OMETTO, J. P., SHIMABUKURO, Y. E., SILVA, C. V. J., PONTES-LOPES, A., MORELLO, T. F. & ARAGÃO, L. E. O. C. 2020. Intercomparison of Burned Area Products and Its Implication for Carbon Emission Estimations in the Amazon. *Remote Sensing,* 12**,** 3864.

PETERSON, D., WANG, J., ICHOKU, C. & REMER, L. A. 2010. Effects of lightning and other meteorological factors on fire activity in the North American boreal forest: implications for fire weather forecasting. *Atmos. Chem. Phys.,* 10**,** 6873-6888.

PHILLIPS, C. A., ROGERS, B. M., ELDER, M., COOPERDOCK, S., MOUBARAK, M., RANDERSON, J. T. & FRUMHOFF, P. C. 2022. Escalating carbon emissions from North American boreal forest wildfires and the climate mitigation potential of fire management. *Science Advances,* 8**,** eabl7161.

POTTER, S., COOPERDOCK, S., VERAVERBEKE, S., WALKER, X., MACK, M. C., GOETZ, S. J., BALTZER, J. L., BOURGEAU-CHAVEZ, L., BURRELL, A., DIELEMAN, C., FRENCH, N., HANTSON, S., HOY, E. E., JENKINS, L., JOHNSTONE, J. F., KANE, E. S., NATALI, S. M., RANDERSON, J. T., TURETSKY, M. R., WHITMAN, E., WIGGINS, E. & ROGERS, B. M. 2023. Burned area and carbon emissions across northwestern boreal North America from 2001–2019. *Biogeosciences,* 20**,** 2785-2804.

POTTER, S., SOLVIK, K., ERB, A., GOETZ, S. J., JOHNSTONE, J. F., MACK, M. C., RANDERSON, J. T., ROMÁN, M. O., SCHAAF, C. L., TURETSKY, M. R., VERAVERBEKE, S., WALKER, X. J., WANG, Z., MASSEY, R. & ROGERS, B. M. 2020. Climate change decreases the cooling effect from postfire albedo in boreal North America. *Global Change Biology,* 26**,** 1592-1607.

QUILCAILLE, Y., BATIBENIZ, F., RIBEIRO, A. F. S., PADRÓN, R. S. & SENEVIRATNE, S. I. 2023. Fire weather index data under historical and shared socioeconomic pathway projections in the 6th phase of the Coupled Model Intercomparison Project from 1850 to 2100. *Earth Syst. Sci. Data,* 15**,** 2153-2177.

RABIN, S. S., MELTON, J. R., LASSLOP, G., BACHELET, D., FORREST, M., HANTSON, S., KAPLAN, J. O., LI, F., MANGEON, S., WARD, D. S., YUE, C., ARORA, V. K., HICKLER, T., KLOSTER, S., KNORR, W., NIERADZIK, L., SPESSA, A., FOLBERTH, G. A., SHEEHAN, T., VOULGARAKIS, A., KELLEY, D. I., PRENTICE, I. C., SITCH, S., HARRISON, S. & ARNETH, A. 2017. The Fire Modeling Intercomparison Project (FireMIP), phase 1: experimental and analytical protocols with detailed model descriptions. *Geosci. Model Dev.,* 10**,** 1175-1197.

RAMON, J., LLEDÓ, L., TORRALBA, V., SORET, A. & DOBLAS-REYES, F. J. 2019. What global reanalysis best represents near-surface winds? *Quarterly Journal of the Royal Meteorological Society,* 145**,** 3236-3251.

RANDERSON, J. T., CHEN, Y., VAN DER WERF, G. R., ROGERS, B. M. & MORTON, D. C. 2012. Global burned area and biomass burning emissions from small fires. *Journal of Geophysical Research: Biogeosciences,* 117.

RANDERSON, J. T., LIU, H., FLANNER, M. G., CHAMBERS, S. D., JIN, Y., HESS, P. G., PFISTER, G., MACK, M. C., TRESEDER, K. K., WELP, L. R., CHAPIN, F. S.,

HARDEN, J. W., GOULDEN, M. L., LYONS, E., NEFF, J. C., SCHUUR, E. A. G. & ZENDER, C. S. 2006. The Impact of Boreal Forest Fire on Climate Warming. *Science,* 314**,** 1130-1132.

RANTANEN, M., KARPECHKO, A. Y., LIPPONEN, A., NORDLING, K., HYVÄRINEN, O., RUOSTEENOJA, K., VIHMA, T. & LAAKSONEN, A. 2022. The Arctic has warmed nearly four times faster than the globe since 1979. *Communications Earth & Environment,* 3**,** 168.

REES, W. G., HOFGAARD, A., BOUDREAU, S., CAIRNS, D. M., HARPER, K., MAMET, S., MATHISEN, I., SWIRAD, Z. & TUTUBALINA, O. 2020. Is subarctic forest advance able to keep pace with climate change? *Global Change Biology,* 26**,** 3965-3977.

RIAHI, K., VAN VUUREN, D. P., KRIEGLER, E., EDMONDS, J., O'NEILL, B. C., FUJIMORI, S., BAUER, N., CALVIN, K., DELLINK, R., FRICKO, O., LUTZ, W., POPP, A., CUARESMA, J. C., KC, S., LEIMBACH, M., JIANG, L., KRAM, T., RAO, S., EMMERLING, J., EBI, K., HASEGAWA, T., HAVLIK, P., HUMPENÖDER, F., DA SILVA, L. A., SMITH, S., STEHFEST, E., BOSETTI, V., EOM, J., GERNAAT, D., MASUI, T., ROGELJ, J., STREFLER, J., DROUET, L., KREY, V., LUDERER, G., HARMSEN, M., TAKAHASHI, K., BAUMSTARK, L., DOELMAN, J. C., KAINUMA, M., KLIMONT, Z., MARANGONI, G., LOTZE-CAMPEN, H., OBERSTEINER, M., TABEAU, A. & TAVONI, M. 2017. The Shared Socioeconomic Pathways and their energy, land use, and greenhouse gas emissions implications: An overview. *Global Environmental Change,* 42**,** 153-168.

RIAZANOVA, A. A., VOROPAY, N. N., OKLADNIKOV, I. G. & GORDOV, E. P. 2016. Development of computational module of regional aridity for web-GIS "Climate". *IOP Conference Series: Earth and Environmental Science,* 48**,** 012032.

RIFFLER, M., LIEBERHERR, G. & WUNDERLE, S. 2015. Lake surface water temperatures of European Alpine lakes (1989–2013) based on the Advanced Very High Resolution Radiometer (AVHRR) 1 km data set. *Earth Syst. Sci. Data,* 7**,** 1-17.

ROGERS, B. M., BALCH, J. K., GOETZ, S. J., LEHMANN, C. E. R. & TURETSKY, M. 2020. Focus on changing fire regimes: interactions with climate, ecosystems, and society. *Environmental Research Letters,* 15**,** 030201.

ROGERS, B. M., SOJA, A. J., GOULDEN, M. L. & RANDERSON, J. T. 2015. Influence of tree species on continental differences in boreal fires and climate feedbacks. *Nature Geoscience,* 8**,** 228-234.

ROGERS, B. M., SOJA, A. J., GOULDEN, M. L. & RANDERSON, J. T. 2017. Fire Intensity and Burn Severity Metrics for Circumpolar Boreal Forests, 2001-2013. ORNL Distributed Active Archive Center.

ROMANOV, A. A., TAMAROVSKAYA, A. N., GLOOR, E., BRIENEN, R., GUSEV, B. A., LEONENKO, E. V., VASILIEV, A. S. & KRIKUNOV, E. E. 2022. Reassessment of carbon emissions from fires and a new estimate of net carbon uptake in Russian forests in 2001–2021. *Science of The Total Environment,* 846**,** 157322.

ROTETA, E., BASTARRIKA, A., IBISATE, A. & CHUVIECO, E. 2021. A Preliminary Global Automatic Burned-Area Algorithm at Medium Resolution in Google Earth Engine. *Remote Sensing,* 13**,** 4298.

ROWE, J. S. & SCOTTER, G. W. 1973. Fire in the boreal forest. *Quaternary research,* 3**,** 444-464.

ROY, D. P., BOSCHETTI, L., JUSTICE, C. O. & JU, J. 2008. The collection 5 MODIS burned area product — Global evaluation by comparison with the MODIS active fire product. *Remote Sensing of Environment,* 112**,** 3690-3707.

RUBÍ, J. N. S., DE CARVALHO, P. H. P. & GONDIM, P. R. L. 2023. Application of machine learning models in the behavioral study of forest fires in the Brazilian Federal District region. *Engineering Applications of Artificial Intelligence,* 118**,** 105649.

RUCKSTUHL, K. E., JOHNSON, E. A. & MIYANISHI, K. 2008. Introduction. The boreal forest and global change. The Royal Society London.

SAHIN, E. K. 2020. Assessing the predictive capability of ensemble tree methods for landslide susceptibility mapping using XGBoost, gradient boosting machine, and random forest. *SN Applied Sciences,* 2**,** 1308.

SAN-MIGUEL, I., COOPS, N. C., CHAVARDÈS, R. D., ANDISON, D. W. & PICKELL, P. D. 2020. What controls fire spatial patterns? Predictability of fire characteristics in the Canadian boreal plains ecozone. *Ecosphere,* 11**,** e02985.

SCAFETTA, N. 2024. Impacts and risks of "realistic" global warming projections for the 21st century. *Geoscience Frontiers,* 15**,** 101774.

SCHEFFER, M., HIROTA, M., HOLMGREN, M., VAN NES, E. H. & CHAPIN, F. S. 2012. Thresholds for boreal biome transitions. *Proceedings of the National Academy of Sciences,* 109**,** 21384-21389.

SCHMIDT, J. I., ZIEL, R. H., CALEF, M. P. & VARVAK, A. 2024. Spatial distribution of wildfire threat in the far north: exposure assessment in boreal communities. *Natural Hazards,* 120**,** 4901-4924.

SCHOLTEN, R. C., COUMOU, D., LUO, F. & VERAVERBEKE, S. 2022. Early snowmelt and polar jet dynamics co-influence recent extreme Siberian fire seasons. *Science,* 378**,** 1005-1009.

SCHOLTEN, R. C., JANDT, R. R., MILLER, E. A., ROGERS, B. M. & VERAVERBEKE, S. 2021. Overwintering fires in boreal forests. *Nature,* 593**,** 399-404.

SCHOLTEN, R. C., VERAVERBEKE, S., CHEN, Y. & RANDERSON, J. T. 2024. Spatial variability in Arctic–boreal fire regimes influenced by environmental and human factors. *Nature Geoscience,* 17**,** 866-873.

SCHROEDER, W., OLIVA, P., GIGLIO, L. & CSISZAR, I. A. 2014. The New VIIRS 375m active fire detection data product: Algorithm description and initial assessment. *Remote Sensing of Environment,* 143**,** 85-96.

SHABANOV, N., MARSHALL, G. J., REES, W. G., BARTALEV, S. A., TUTUBALINA, O. & GOLUBEVA, E. 2021. Climate-driven phenological changes in the Russian Arctic derived from MODIS LAI time series 2000-2019. *Environmental Research Letters*.

SHAO, Y., FAN, G., FENG, Z., SUN, L., YANG, X., MA, T., LI, X., FU, H. & WANG, A. 2023. Prediction of forest fire occurrence in China under climate change scenarios. *Journal of Forestry Research,* 34**,** 1217-1228.

SHAPIRO, S. S. & WILK, M. B. 1965. An analysis of variance test for normality (complete samples)†. *Biometrika,* 52**,** 591-611.

SHESTAKOVA, A. A., FEDOTOVA, E. V. & LYULYUKIN, V. S. 2024. Relevance of ERA5 Reanalysis for Wind Energy Applications: Comparison With Sodar Observations. *Geography, Environment, Sustainability,* 17**,** 54-66.

SHIVE, K. L., PREISLER, H. K., WELCH, K. R., SAFFORD, H. D., BUTZ, R. J., O'HARA, K. L. & STEPHENS, S. L. 2018. From the stand scale to the landscape scale: predicting the spatial patterns of forest regeneration after disturbance. *Ecological Applications,* 28**,** 1626-1639.

SHVETSOV, E. G., GOLYUKOV, A. S. & KHARUK, V. I. 2023. Long-Term Dynamics of Forest Fires in Southern Siberia. *Contemporary Problems of Ecology,* 16**,** 205-216.

SHVETSOV, E. G., KUKAVSKAYA, E. A., BURYAK, L. V. & BARRETT, K. 2019. Assessment of post-fire vegetation recovery in Southern Siberia using remote sensing observations. *Environmental Research Letters,* 14.

SHVIDENKO, A. Z. & SCHEPASCHENKO, D. G. 2013. Climate Change and Wildfires in Russia. *Contemporary Problems of Ecology,* 6, 683-692.

SHVIDENKO, A. Z., SCHEPASCHENKO, D. G., SUKHININ, A., MCCALLUM, I. & MAKSYUTOV, S. Carbon emissions from forest fires in boreal Eurasia between 1998-2010. Proceedings, 5th International Wildland Fire Conference, 9-13 May 2011.

SIMMONS, A., UPPALA, S., DEE, D. & KOBAYASHI, S. 2007. ERA-Interim: New ECMWF reanalysis products from 1989 onwards. *Newsletter Number 110 - Winter 2006/07*, 25-35.

SIMPSON, J. J., STITT, J. R. & SIENKO, M. 1998. Improved estimates of the areal extent of snow cover from AVHRR data. *Journal of Hydrology,* 204, 1-23.

SIRCA, C., SALIS, M., ARCA, B., DUCE, P. & SPANO, D. 2018. Assessing the performance of fire danger indexes in a Mediterranean area. *iForest - Biogeosciences and Forestry,* 11, 563-571.

SKAKUN, R. S., CASTILLA, G., METSARANTA, J. M., WHITMAN, E., RODRIGUE, S., LITTLE, J., GROENEWEGEN, K. & COYLE, M. 2022. Extending the National Burned Area Composite Time Series of Wildfires in Canada. *Remote Sensing,* 14, 3050.

SKAKUN, S., KUSSUL, N., SHELESTOV, A. & KUSSUL, O. 2014. Flood Hazard and Flood Risk Assessment Using a Time Series of Satellite Images: A Case Study in Namibia. *Risk Analysis,* 34, 1521-1537.

SOHL, T. L., WIMBERLY, M. C., RADELOFF, V. C., THEOBALD, D. M. & SLEETER, B. M. 2016. Divergent projections of future land use in the United States arising from different models and scenarios. *Ecological Modelling,* 337, 281-297.

SOJA, A. J., COFER, W. R., SHUGART, H. H., SUKHININ, A. I., STACKHOUSE JR., P. W., MCRAE, D. J. & CONARD, S. G. 2004a. Estimating fire emissions and disparities in boreal Siberia (1998–2002). *Journal of Geophysical Research: Atmospheres,* 109.

SOJA, A. J., SUKHININ, A. I., CAHOON JR, D. R., SHUGART, H. H. & STACKHOUSE JR, P. W. 2004b. AVHRR-derived fire frequency, distribution and area burned in Siberia. *International Journal of Remote Sensing,* 25, 1939-1960.

STEPHENS, C. W., IVES, A. R. & RADELOFF, V. C. 2025. Substantial increases in burned area in circumboreal forests from 1983 to 2020 captured by the AVHRR record and a new autoregressive burned area detection algorithm. *Remote Sensing of Environment,* 325, 114789.

STOCKS, B. J., MASON, J. A., TODD, J. B., BOSCH, E. M., WOTTON, B. M., AMIRO, B. D., FLANNIGAN, M. D., HIRSCH, K. G., LOGAN, K. A., MARTELL, D. L. & SKINNER, W. R. 2002. Large forest fires in Canada, 1959–1997. *Journal of Geophysical Research: Atmospheres,* 107, FFR 5-1-FFR 5-12.

STOREY, J. C., SCARAMUZZA, P. L. & SCHMIDT, G. L. Landsat 7 Scan Line Corrector-Off Gap-Filled Product Development. 2005.

SULLA-MENASHE, D. & FRIEDL, M. A. 2018. User guide to collection 6 MODIS land cover (MCD12Q1 and MCD12C1) product. *Usgs: Reston, Va, Usa,* 1, 18.

SUN, Q., BURRELL, A. L., BARRETT, K., KUKAVSKAYA, E. A., BURYAK, L. V., KADUK, J. & BAXTER, R. 2021. Climate Variability May Delay Post-Fire Recovery of Boreal Forest in Southern Siberia, Russia. *Remote Sensing,* 13, 2247.

SUNG, J. H., SEO, S. B. & RYU, Y. 2022. Deep Learning-Based Projection of Occurrence Frequency of Forest Fires under SSP Scenario: Exploring the Link between Drought Characteristics and Forest Fires. *Sustainability,* 14, 5494.

TALUCCI, A. C., LORANTY, M. M. & ALEXANDER, H. D. 2022. Siberian taiga and tundra fire regimes from 2001–2020. *Environmental Research Letters,* 17, 025001.

TANG, H. & LI, Z.-L. 2014. Applications of Thermal Remote Sensing in Agriculture Drought Monitoring and Thermal Anomaly Detection. *Quantitative Remote Sensing in Thermal Infrared: Theory and Applications*, 203-256.

TANGNEY, R., PAROISSIEN, R., LE BRETON, T. D., THOMSEN, A., DOYLE, C. A. T., ONDIK, M., MILLER, R. G., MILLER, B. P. & OOI, M. K. J. 2022. Success of post-fire plant recovery strategies varies with shifting fire seasonality. *Communications Earth & Environment,* 3, 126.

TAREK, M., BRISSETTE, F. & ARSENAULT, R. 2019. Evaluation of the ERA5 reanalysis as a potential reference dataset for hydrological modeling over North-America. *Hydrology and Earth System Sciences Discussions*, 1-35.

THRASHER, B., WANG, W., MICHAELIS, A., MELTON, F., LEE, T. & NEMANI, R. 2022. NASA Global Daily Downscaled Projections, CMIP6. *Scientific Data,* 9, 262.

THRASHER, B., WANG, W., MICHAELIS, A. & NEMANI, R. 2021. NEX-GDDP-CMIP6. *In:* SIMULATION, N. C. F. C. (ed.).

TIAN, C., PENG, D. & YUE, X. 2025. Projection of Future Fire Weather in Eurasia by Mid-21st Century. *Journal of Geophysical Research: Atmospheres,* 130, e2025JD043686.

TITKOVA, T. B. & ANANICHEVA, M. D. 2024. Using ERA5-Land Reanalysis and Data from Weather Stations in the Mountainous Regions of Russia to Assess Changes in the Glacial Systems of Eastern Siberia and the Far East. *Izvestiya, Atmospheric and Oceanic Physics,* 60, S227-S239.

TURCO, M., HERRERA, S., TOURIGNY, E., CHUVIECO, E. & PROVENZALE, A. 2019. A comparison of remotely-sensed and inventory datasets for burned area in Mediterranean Europe. *International Journal of Applied Earth Observation and Geoinformation,* 82, 101887.

TURETSKY, M. R., KANE, E. S., HARDEN, J. W., OTTMAR, R. D., MANIES, K. L., HOY, E. E. & KASISCHKE, E. S. 2011. Recent acceleration of biomass burning and carbon losses in Alaskan forests and peatlands. *Nature Geoscience,* 4, 27-31.

ULBRICHT, K. A. & HECKENDORFF, W. D. 1998. Satellite images for recognition of landscape and landuse changes. *ISPRS Journal of Photogrammetry and Remote Sensing,* 53, 235-243.

URRACA, R. & GOBRON, N. 2023. Temporal stability of long-term satellite and reanalysis products to monitor snow cover trends. *The Cryosphere,* 17, 1023-1052.

VALENCIA, G. M., ANAYA, J. A., VELÁSQUEZ, É. A., RAMO, R. & CARO-LOPERA, F. J. 2020. About Validation-Comparison of Burned Area Products. *Remote Sensing,* 12, 3972.

VAN DER WERF, G. R., RANDERSON, J. T., GIGLIO, L., COLLATZ, G. J., KASIBHATLA, P. S. & ARELLANO JR, A. F. 2006. Interannual variability in global biomass burning emissions from 1997 to 2004. *Atmos. Chem. Phys.,* 6, 3423-3441.

VAN DER WERF, G. R., RANDERSON, J. T., GIGLIO, L., VAN LEEUWEN, T. T., CHEN, Y., ROGERS, B. M., MU, M., VAN MARLE, M. J. E., MORTON, D. C., COLLATZ, G. J., YOKELSON, R. J. & KASIBHATLA, P. S. 2017. Global fire emissions estimates during 1997–2016. *Earth Syst. Sci. Data,* 9, 697-720.

VAN WAGNER, C. E. 1987. *Development and structure of the Canadian forest fire weather index system*, Canadian Forestry Service.

VERAVERBEKE, S., DELCOURT, C. J. F., KUKAVSKAYA, E. A., MACK, M. C., WALKER, X., HESSILT, T. D., ROGERS, B. M. & SCHOLTEN, R. C. 2021. Direct and longer-term carbon emissions from arctic-boreal fires: A short review of recent advances. *Current Opinion in Environmental Science & Health,* 23, 100277.

VERAVERBEKE, S., ROGERS, B. M., GOULDEN, M. L., JANDT, R. R., MILLER, C. E., WIGGINS, E. B. & RANDERSON, J. T. 2017. Lightning as a major driver of recent large fire years in North American boreal forests. *Nature Climate Change,* 7**,** 529-534.

VERMOTE, E. F. 2015. MOD09A1 MODIS/Terra Surface Reflectance 8-Day L3 Global 500m SIN Grid V006. NASA EOSDIS Land Processes Distributed Active Archive Center.

VERMOTE, E. F., EL SALEOUS, N. Z. & JUSTICE, C. O. 2002. Atmospheric correction of MODIS data in the visible to middle infrared: first results. *Remote Sensing of Environment,* 83**,** 97-111.

VERMOTE, E. F., KOTCHENOVA, S. Y. & RAY, J. P. 2011. MODIS surface reflectance user's guide. *MODIS Land Surface Reflectance Science Computing Facility, version,* 1**,** 1-40.

VIRTANEN, P., GOMMERS, R., OLIPHANT, T. E., HABERLAND, M., REDDY, T. R., COURNAPEAU, D., BUROVSKI, E., PETERSON, P., WECKESSER, W., BRIGHT, J., VAN DER WALT, S. J., BRETT, M., WILSON, J., MILLMAN, K. J., MAYOROV, N., NELSON, A. R. J., JONES, E., KERN, R., LARSON, E., CAREY, C. J., POLAT, İ., FENG, Y., MOORE, E. W., VANDERPLAS, J., LAXALDE, D., PERKTOLD, J., CIMRMAN, R., HENRIKSEN, I., QUINTERO, E. A., HARRIS, C. R., ARCHIBALD, A. M., RIBEIRO, A. H., PEDREGOSA, F., VAN MULBREGT, P., VIJAYKUMAR, A., BARDELLI, A. P., ROTHBERG, A., HILBOLL, A., KLOECKNER, A., SCOPATZ, A., LEE, A., ROKEM, A., WOODS, C. N., FULTON, C., MASSON, C., HÄGGSTRÖM, C., FITZGERALD, C., NICHOLSON, D. A., HAGEN, D. R., PASECHNIK, D. V., OLIVETTI, E., MARTIN, E., WIESER, E., SILVA, F., LENDERS, F., WILHELM, F., YOUNG, G., PRICE, G. A., INGOLD, G.-L., ALLEN, G. E., LEE, G. R., AUDREN, H., PROBST, I., DIETRICH, J. P., SILTERRA, J., WEBBER, J. T., SLAVIČ, J., NOTHMAN, J., BUCHNER, J., KULICK, J., SCHÖNBERGER, J. L., DE MIRANDA CARDOSO, J. V., REIMER, J., HARRINGTON, J., RODRÍGUEZ, J. L. C., NUNEZ-IGLESIAS, J., KUCZYNSKI, J., TRITZ, K., THOMA, M., NEWVILLE, M., KÜMMERER, M., BOLINGBROKE, M., TARTRE, M., PAK, M., SMITH, N. J., NOWACZYK, N., SHEBANOV, N., PAVLYK, O., BRODTKORB, P. A., LEE, P., MCGIBBON, R. T., FELDBAUER, R., LEWIS, S., TYGIER, S., SIEVERT, S., VIGNA, S., PETERSON, S., MORE, S., PUDLIK, T., OSHIMA, T., et al. 2020. SciPy 1.0: fundamental algorithms for scientific computing in Python. *Nature Methods,* 17**,** 261-272.

VITOLO, C., DI GIUSEPPE, F., BARNARD, C., COUGHLAN, R., SAN-MIGUEL-AYANZ, J., LIBERTÁ, G. & KRZEMINSKI, B. 2020. ERA5-based global meteorological wildfire danger maps. *Scientific Data,* 7**,** 216.

VOROPAY, N., RYAZANOVA, A. & DYUKAREV, E. 2021. High-resolution bias-corrected precipitation data over South Siberia, Russia. *Atmospheric Research,* 254**,** 105528.

WALKER, X. J., BALTZER, J. L., CUMMING, S. G., DAY, N. J., EBERT, C., GOETZ, S. J., JOHNSTONE, J. F., POTTER, S., ROGERS, B. M., SCHUUR, E. A. G., TURETSKY, M. R. & MACK, M. C. 2019. Increasing wildfires threaten historic carbon sink of boreal forest soils. *Nature,* 572**,** 520-523.

WALSH, J. E., BHATT, U. S., LITTELL, J. S., LEONAWICZ, M., LINDGREN, M., KURKOWSKI, T. A., BIENIEK, P. A., THOMAN, R., GRAY, S. & RUPP, T. S. 2018. Downscaling of climate model output for Alaskan stakeholders. *Environmental Modelling & Software,* 110**,** 38-51.

WANG, Y.-R., HESSEN, D. O., SAMSET, B. H. & STORDAL, F. 2022. Evaluating global and regional land warming trends in the past decades with both MODIS and ERA5-Land land surface temperature data. *Remote Sensing of Environment,* 280**,** 113181.

WANG, Z., WANG, Z., ZOU, Z., CHEN, X., WU, H., WANG, W., SU, H., LI, F., XU, W., LIU, Z. & ZHU, J. 2024. Severe Global Environmental Issues Caused by Canada's Record-Breaking Wildfires in 2023. *Advances in Atmospheric Sciences,* 41**,** 565-571.

WATANABE, T., MATSUYAMA, H., KUZHEVSKAIA, I. V., NECHEPURENKO, O., CHURSIN, V. & ZEMTSOV, V. 2023. Long-Term Trends of Extreme Climate Indexes in the Southern Part of Siberia in Comparison with Those of Surrounding Regions. *Atmosphere,* 14**,** 1131.

WILCZAK, J. M., AKISH, E., CAPOTONDI, A. & COMPO, G. P. 2024. Evaluation and Bias Correction of the ERA5 Reanalysis over the United States for Wind and Solar Energy Applications. *Energies,* 17**,** 1667.

WILLIAMS, A. P. & ABATZOGLOU, J. T. 2016. Recent Advances and Remaining Uncertainties in Resolving Past and Future Climate Effects on Global Fire Activity. *Current Climate Change Reports,* 2**,** 1-14.

WOTTON, B. M., NOCK, C. A. & FLANNIGAN, M. D. 2010. Forest fire occurrence and climate change in Canada. *International Journal of Wildland Fire,* 19**,** 253-271.

WULDER, M. A., ROY, D. P., RADELOFF, V. C., LOVELAND, T. R., ANDERSON, M. C., JOHNSON, D. M., HEALEY, S., ZHU, Z., SCAMBOS, T. A., PAHLEVAN, N., HANSEN, M. C., GORELICK, N., CRAWFORD, C. J., MASEK, J. G., HERMOSILLA, T., WHITE, J. C., BELWARD, A. S., SCHAAF, C., WOODCOCK, C. E., HUNTINGTON, J. L., LYMBURNER, L., HOSTERT, P., GAO, F., LYAPUSTIN, A., PEKEL, J.-F., STROBL, P. & COOK, B. D. 2022. Fifty years of Landsat science and impacts. *Remote Sensing of Environment,* 280**,** 113195.

XU, W., SCHOLTEN, R. C., HESSILT, T. D., LIU, Y. & VERAVERBEKE, S. 2022. Overwintering fires rising in eastern Siberia. *Environmental Research Letters,* 17**,** 045005.

YAO, Q., FANG, K., OU, T., ZHOU, F., HE, M., ZHENG, B., LIU, J., XING, H. & TROUET, V. 2022. Reply to: Fire activity as measured by burned area reveals weak effects of ENSO in China. *Nature Communications,* 13**,** 4317.

YILMAZ, M. 2023. Accuracy assessment of temperature trends from ERA5 and ERA5-Land. *Science of The Total Environment,* 856**,** 159182.

YUKIMOTO, S., KAWAI, H., KOSHIRO, T., OSHIMA, N., YOSHIDA, K., URAKAWA, S., TSUJINO, H., DEUSHI, M., TANAKA, T., HOSAKA, M., YABU, S., YOSHIMURA, H., SHINDO, E., MIZUTA, R., OBATA, A., ADACHI, Y. & ISHII, M. 2019. The Meteorological Research Institute Earth System Model Version 2.0, MRI-ESM2.0: Description and Basic Evaluation of the Physical Component. *Journal of the Meteorological Society of Japan. Ser. II,* 97**,** 931-965.

ZHANG, G., WANG, M. & LIU, K. 2019. Forest Fire Susceptibility Modeling Using a Convolutional Neural Network for Yunnan Province of China. *International Journal of Disaster Risk Science,* 10**,** 386-403.

ZHANG, G., WANG, M. & LIU, K. 2021. Deep neural networks for global wildfire susceptibility modelling. *Ecological Indicators,* 127**,** 107735.

ZHANG, G., WANG, M., YANG, B. & LIU, K. 2024a. Current and Future Patterns of Global Wildfire Based on Deep Neural Networks. *Earth's Future,* 12**,** e2023EF004088.

ZHANG, J.-H., YAO, F.-M., LIU, C., YANG, L.-M. & BOKEN, V. K. 2011a. Detection, Emission Estimation and Risk Prediction of Forest Fires in China Using Satellite Sensors and Simulation Models in the Past Three Decades—An Overview. *International Journal of Environmental Research and Public Health,* 8**,** 3156-3178.

ZHANG, T., WOOSTER, M. J., DE JONG, M. C. & XU, W. 2018. How Well Does the 'Small Fire Boost' Methodology Used within the GFED4.1s Fire Emissions Database

Represent the Timing, Location and Magnitude of Agricultural Burning? *Remote Sensing,* 10**,** 823.

ZHANG, X., KONDRAGUNTA, S. & QUAYLE, B. 2011b. Estimation of Biomass Burned Areas Using Multiple-Satellite-Observed Active Fires. *IEEE Transactions on Geoscience and Remote Sensing,* 49**,** 4469-4482.

ZHANG, Y., WANG, J. A., BERNER, L. T., GOETZ, S. J., ZHAO, K. & LIU, Y. 2024b. Warming and disturbances affect Arctic-boreal vegetation resilience across northwestern North America. *Nature Ecology & Evolution,* 8**,** 2265-2276.

ZHAO, H., ZHANG, Z., WANG, X., ZHEN, S., ZHANG, H., BU, Z.-J., ZHAO, J., GUO, X., WEI, K. & DONG, L. 2025. Future enhanced threshold effects of wildfire drivers could increase burned areas in northern mid- and high latitudes. *Communications Earth & Environment,* 6**,** 224.

ZYRYANOVA, O. A., MILYUTIN, L. I., MURATOVA, E. N., RYZHKOVA, V. A., LARIONOVA, A. Y., SEDELNIKOVA, T. S., KORETS, M. A. & MIKHAILOVA, I. A. 2008. Boreal Forests of Siberia: Genetic, Species and Ecosystem Diversity. *Contemporary Problems of Ecology,* 1**,** 22-28.